

# DOUBLY-HEAVY TETRAQUARKS FROM LATTICE QCD

Dissertation  
zur Erlangung des Doktorgrades  
der Naturwissenschaften

vorgelegt beim Fachbereich Physik  
der Johann Wolfgang Goethe-Universität  
in Frankfurt am Main

von Martin Alexander Pflaumer  
aus Offenbach am Main

Frankfurt 2023  
D 30

Vom Fachbereich Physik der  
Johann Wolfgang Goethe-Universität als Dissertation angenommen.

Dekan: Prof. Dr. Roger Erb

Gutachter: Prof. Dr. Marc Wagner  
Prof. Dr. Stefan Meinel

Datum der Disputation:

---

# DEUTSCHE ZUSAMMENFASSUNG

---

Seit Langem ist die Menschheit fasziniert von der Frage, was die elementaren Bausteine unserer Materie sind. Bereits der griechische Philosoph Demokrit postulierte, dass kleinste unteilbare Elemente existieren, aus denen alle bekannten Substanzen aufgebaut sind. Gegen Ende des 19. Jahrhunderts hatte man etwa 100 der heute als chemische Elemente bekannten Teilchen entdeckt und nahm an, dass es sich hierbei um Elementarteilchen handelt. Um 1900 stellte sich jedoch heraus, dass all diese Atome wiederum aus drei kleineren Bestandteilen, Protonen, Neutronen und Elektronen, aufgebaut sind. In Beschleuniger-Experimenten in den 50er und 60er Jahren des 20. Jahrhunderts wurde eine Vielzahl weiterer Teilchen entdeckt, die in ihren Eigenschaften Protonen und Neutronen ähneln. Dies warf erneut die Frage auf, ob all diese Teilchen wiederum auf kleinere elementare Bestandteile zurückgeführt werden können. Die Antwort auf diese Frage lieferten Mitte der 1960er Jahre Gell-Mann und Zweig, die die Existenz kleinster elementarer Teilchen, den Quarks, postulierten. Heute wissen wir, dass es sechs verschiedene Arten von Quarks gibt, sogenannte Flavours, die sich in ihrer Masse stark unterscheiden und in drei Generationen eingeteilt werden können. Die erste besteht aus den leichten up ( $u$ ) und down ( $d$ ) Quarks, welche die Konstituenten aller gegenständlichen Materie bilden. Hinzu kommen die Quarks der zweiten Generation, das strange ( $s$ ) und charm ( $c$ ) Quark, sowie abschließend die schweren bottom ( $b$ ) und top ( $t$ ) Quarks der dritten Generation. Teilchen, die aus Quarks aufgebaut sind, bezeichnet man als Hadronen, und man unterscheidet zwischen Baryonen, die halbzahligen Spin besitzen, und Mesonen mit ganzzahligem Spin. Hierbei sind gewöhnliche Baryonen aus drei Quarks oder Antiquarks aufgebaut, während gewöhnliche Mesonen aus einem Quark-Antiquark Paar bestehen. Da alle beobachteten Hadronen eine ganzzahlige elektrische Ladung aufweisen, müssen Quarks eine fraktionale Ladung von  $+2/3$  ( $u, c, t$ ) oder  $-1/3$  ( $d, s, b$ ) besitzen.

In der Praxis stand das Quarkmodell in seinen Anfängen jedoch vor zwei großen Problemen. Erstens konnten experimentell keine freien Teilchen mit nicht-ganzzahliger Ladung, sprich Quarks, nachgewiesen werden. Zweitens stand die Entdeckung des Spin  $3/2$  Baryons  $\Delta^{++}$  mit Quark-Struktur  $uuu$  im Widerspruch zum Pauli-Prinzip, da die drei Quarks in allen bekannten Quantenzahlen übereinstimmten und demnach die Gesamtwellenfunktion damit symmetrisch wäre, obwohl Baryonen als Fermionen eine antisymmetrische Gesamtwellenfunktion haben müssen. Dies führte zur Einführung eines weiteren Freiheitsgrades, der sogenannten Farbladung, welche drei verschiedene Werte (blau, grün, rot) annehmen kann. Ordnet man jedem der drei Quarks im  $\Delta^{++}$  eine andere Farbladung zu, so unterscheiden sie sich in einer Quantenzahl, das Pauli-Prinzip ist erfüllt und die Gesamt-Wellenfunktion ist antisymmetrisch. Alle frei-

---

en Teilchen, und somit auch Hadronen, sind farbneutral. Dies löst auch das zweite Problem des Quarkmodells, da freie Quarks eine Farbladung tragen und somit entsprechend dieser Forderung in der Natur nicht einzeln auftreten. Mathematisch lässt sich das Konzept der Farbladung mithilfe einer zusätzlichen globalen  $SU(3)$ -Symmetrie beschreiben, unter der die Wellenfunktion der freien Teilchen invariant ist.

Dies führt zur grundlegenden Theorie der starken Wechselwirkung, welche durch die Farbladung erzeugt wird und die Interaktion von Quarks (und Gluonen) sowie die Bildung von Hadronen charakterisiert. Formal beschrieben wird die starke Wechselwirkung durch eine nicht-abelsche  $SU(3)$ -Eichtheorie, die *Quantenchromodynamik* (QCD) genannt wird. Eine Besonderheit dieser Theorie ist, dass ihre Austauschteilchen, die Gluonen, selbst ebenfalls Farbladung tragen und somit nicht nur mit Quarks, sondern auch untereinander wechselwirken. Dies hat beispielsweise zur Folge, dass ein Quark-Antiquark Paar nicht separiert werden kann. Versucht man, ein solches Paar zu trennen, so bildet sich eine Art Schlauch aus Gluonen, und die Energie, die für eine weitere Vergrößerung des Abstandes benötigt wird, wächst proportional an. Zu einem gewissen Zeitpunkt ist diese Energie so groß, dass der Schlauch bricht (“string breaking”) und ein weiteres Quark-Antiquark Paar entsteht. Dieses Prinzip bezeichnet man auch als Confinement und verkörpert, dass Hadronen farbneutral sind und Quarks nicht als freie Teilchen vorliegen können. Gleichzeitig sind die Kräfte bei kleinen Abständen bzw. für große Energien gering, was auch asymptotische Freiheit genannt wird und eine Berechnung von QCD-Observablen innerhalb der Störungstheorie ermöglicht. Für nieder-energetische Messgrößen, wie beispielsweise die Massen von Hadronen, ist dies aufgrund der starken Kopplung jedoch nicht möglich.

Eine nicht-perturbative, numerische Methode zur Berechnung von QCD-Observablen bietet die Gitter-QCD, auch Lattice QCD genannt. Die Grundidee ist hierbei, das kontinuierliche und unendlich ausgedehnte Raum-Zeit Volumen durch eine vierdimensionale Box und diskretisierte Raum-Zeit zu approximieren. Neben dem Gittervolumen  $L^3 \times T$  ist hierbei die Gitterkonstante  $a$ , die den Abstand zweier Gitterpunkte quantifiziert, ein wichtiger Parameter. Mithilfe des Pfadintegralformalismus, welcher aufgrund des endlichen Gitterabstandes mathematisch wohldefiniert ist, können somit QCD-Erwartungswerte auch im niederenergetischen Bereich verlässlich berechnet werden. Diese Berechnungen sind jedoch so aufwendig, dass sie nur mithilfe moderner Hochleistungsrechner und unter Verwendung von statistischen Methoden wie Monte-Carlo Simulationen durchgeführt werden können. Gleichzeitig verwendet man häufig unphysikalisch schwere Massen für die leichten up und down Quarks, repräsentiert durch die Masse des Pions, da die numerischen Methoden, die innerhalb der Gitter-QCD verwendet werden, für die sehr kleine physikalische Pion-Masse sehr rechenintensiv werden.

Ein großer Vorteil der Gitter-QCD ist jedoch, dass sie außer den genannten Näherungen direkt auf der QCD aufbaut und keine weiteren Annahmen getroffen werden müssen. Zusätzlich können der nicht-verschwindende Gitterabstand, das räumliche Volumen und die Pion-Masse variiert werden, was es erlaubt, die Abhängigkeit der Messgrößen von diesen Parametern zu untersuchen. Darauf aufbauend können Ergebnisse

---

von Gitter-QCD Rechnungen somit in das Kontinuum, in das unendliche Volumen und zu physikalischen Pion-Massen extrapoliert werden. Dementsprechend sind mögliche systematische Fehler kontrollierbar, können relativ genau quantifiziert und somit im finalen Ergebnis berücksichtigt werden.

Während die Gitter-QCD eine sehr genaue Bestimmung der Massen von stabilen Hadronen ermöglicht, ist die Untersuchung von Resonanzen deutlich schwieriger. Ein prominentes Beispiel für solch eine Resonanz ist das  $\rho$ -Meson, welches bei der Streuung zweier Pionen entstehen kann und nach einer kurzen Zeitspanne auch wieder in zwei Pionen zerfällt. Um solche Resonanzen umfassend zu beschreiben, müssen daher sowohl die physikalischen Prozesse, die zur Bindung führen, wie auch die Zerfallsprozesse korrekt behandelt werden. Eine große Schwierigkeit ergibt sich dabei aus dem endlichen Volumen des Gitters. Während stabile Teilchen Eigenzustände des Hamilton-Operators sind, tauchen Resonanzen im Spektrum der kontinuierlichen Streuzustände auf und sind durch ihre Streuamplitude charakterisiert. Durch das endliche Gittervolumen ist dieses eigentlich kontinuierliche Energiespektrum jedoch auch diskretisiert. Die große Herausforderung ist deshalb, diese diskreten Energieniveaus mit dem kontinuierlichen Energiespektrum der physikalischen Streuzustände in Verbindung zu bringen. Der Durchbruch bei der Betrachtung von Streuprozessen in der Gitter-QCD gelang in den 1990er Jahren Martin Lüscher, der einen Formalismus entwickelte, mit dessen Hilfe die Streuamplitude im unendlichen Raum basierend auf den diskreten Energien, die im endlichen Gitter-Volumen berechnet wurden, bestimmt werden kann. Auf dieser Grundlage können, ähnlich wie bei der Analyse experimenteller Daten, Größen wie die Masse oder Zerfallsbreite einer Resonanz extrahiert werden. Neben der Berechnung von Resonanzen ist diese Methode auch dann hilfreich, wenn man gebundene Zustände mit kleinen Bindungsenergien betrachtet, da auch in diesem Fall signifikante Effekte aufgrund des endlichen Volumens auftreten können.

Ein Schwerpunkt aktueller experimenteller und theoretischer Forschung im Bereich der Elementarteilchenphysik liegt inzwischen auf der Untersuchung exotischer Hadronen. Hierunter versteht man Teilchen, die aus mehr als drei Quarks aufgebaut sind, z.B. Tetraquarks und Pentaquark, aber auch Zustände mit angeregten Gluonen, sogenannte hybride Mesonen, oder Teilchen, die nur aus Gluonen bestehen und als Glueballs bezeichnet werden. Im Rahmen dieser Arbeit beschäftige ich mich mit Tetraquarks, welche als Vier-Quark-Systeme aus zwei Quarks und zwei Antiquarks bestehen. Erste Anhaltspunkte für die tatsächliche Existenz von Tetraquarks lieferten Beschleuniger-Experimente, die ein Teilchen detektierten, dessen Masse der eines  $\bar{c}c$  Mesons ähnelte, das allerdings nicht elektrisch neutral war. Somit konnten die Quantenzahlen nicht mit einem einfachen Quark-Antiquark Paar beschrieben werden, was auf die Präsenz eines zusätzlichen leichten Quark-Antiquark Paares schließen ließ. Inzwischen wurden mithilfe großer Beschleuniger-Experimente wie LHCb, Belle oder BES III eine Vielzahl möglicher Tetraquarks entdeckt, wobei insbesondere Systeme, die zwei schwere Quarks (charm oder bottom Quarks) beinhalten, vielversprechende Kandidaten sind. In dieser Arbeit fokussiere ich mich auf Tetraquark-Systeme, die aus zwei schweren

---

Antiquarks aufgebaut sind, wobei mindestens eines der beiden Antiquarks ein bottom Quark ist. Im Gegensatz zu Tetraquarks, die aus einem schweren Quark-Antiquark Paar bestehen, konnten diese Teilchen bisher zwar experimentell nicht nachgewiesen werden, sind in einer theoretischen Betrachtung aber besser zugänglich. Man erwartet zudem, dass diese Systeme stabile Zustände hinsichtlich der starken Wechselwirkung bilden können.

Im Rahmen numerischer Gitter-QCD Simulationen berechne ich die Massen dieser potentiellen Tetraquarks und untersuche, ob sie tatsächlich gebundene Zustände formen oder möglicherweise Kandidaten für Resonanzen sind. Da die Implementierung von bottom Quarks auf dem Gitter aufgrund ihrer großen Masse mit einigen Problemen verbunden ist, verwende ich für sie eine nicht-relativistische Formulierung (NRQCD), die es erlaubt, auch schwere Quarks mit aktuell verfügbaren Gitterabständen und -größen zu betrachten. Ein entscheidender Punkt bei der Berechnung des Massenspektrums eines Hadrons, der sogenannten Hadronenspektroskopie, ist die sorgfältige Auswahl geeigneter Erzeugungsoperatoren, wobei die generierten Zustände möglichst ähnlich zu den tatsächlichen physikalischen Zuständen sein sollten. Für meine Gitter-QCD Berechnungen der Tetraquark-Energiespektren verwende ich zusätzlich zu Operatoren, die alle vier Quarks an der gleichen räumlichen Position platzieren, auch Streuoperatoren, die zwei räumlich separierte Mesonen repräsentieren. Neben einer besseren Auflösung des Energiespektrums erlaubt dies auch, eine Streuanalyse mithilfe des Lüscher-Formalismus durchzuführen und somit mögliche Effekte aufgrund des endlichen räumlichen Volumens genau betrachten zu können.

Das Hauptaugenmerk meiner Arbeit liegt darauf, die Vier-Quark Systeme  $\bar{b}bud$  mit Quantenzahlen  $I(J^P) = 0(1^+)$ ,  $\bar{b}bus$  mit  $J^P = 1^+$  und  $\bar{b}cud$  mit  $I(J^P) = 0(0^+)$  und  $I(J^P) = 0(1^+)$  hinsichtlich der Existenz eines gebundenen Zustandes zu untersuchen. Hierfür habe ich zwei unterschiedliche Gitter-Setups betrachtet. Im ersten Setup, das von der RBC und UKQCD Kollaboration generiert wurde, verwende ich Streuoperatoren lediglich als Vernichtungsoperatoren, während ich für die Rechnungen auf den Eichfeldkonfigurationen des zweiten Setups, die mit der HISQ-Wirkung von der MILC Kollaboration erzeugt wurden, Streuoperatoren vollständig berücksichtige.

Sowohl für das  $\bar{b}bud$  als auch für das  $\bar{b}bus$  System wurde in beiden Rechnungen jeweils exakt die gleiche Operator-Basis verwendet, wobei wie erwähnt für das erste Setup Streuoperatoren nicht als Erzeugungsoperatoren verwendet wurden. Für beide Systeme zeigte sich, dass die Berücksichtigung von Streuoperatoren essentiell ist, um den Grundzustand bestmöglich aufzulösen. Angeregte Zustände werden jedoch nur dann gut wiedergegeben, wenn Streuoperatoren komplett, d.h. als Erzeugungs- und Vernichtungsoperatoren in die Berechnungen einbezogen werden.

Für das  $\bar{b}bud$  System finde ich für beide Rechnungen einen Grundzustand, der deutlich unterhalb der  $BB^*$ -Threshold liegt. Dies deutet auf die Existenz eines gebundenen Zustandes hin. Basierend auf den beiden niedrigsten Energieniveaus ist es möglich, eine Ein-Kanal Streuanalyse mithilfe der Lüscher-Methode durchzuführen und die Bindungsenergie im unendlichen Volumen zu bestimmen. Im Fall des  $\bar{b}bud$  Systems zeigt sich jedoch, dass diese Bindungsenergien identisch zu den aus der Gitter-QCD

---

Rechnung erhaltenen Grundzustandsenergien sind und Effekte aufgrund des endlichen Volumens dementsprechend klein sind. Für beide Setups wurden die Rechnungen für verschiedene Gitter Ensembles durchgeführt, die sich in der Pion-Masse und dem Gitterabstand unterscheiden. Dies ermöglicht es, die Bindungsenergie zum Punkt physikalischer Pion-Masse zu extrapolieren. Außerdem kann der Einfluss von Diskretisierungseffekten abgeschätzt werden, wobei ich im Fall der MILC Ensembles die Ergebnisse explizit im Kontinuumslimit betrachtet habe. Es ergeben sich damit die Bindungsenergien für das  $\bar{b}b\bar{u}d$  System von  $-128(24)(10)$  MeV bzw.  $-101(11)(25)$  MeV, was mit der Vorhersage eines gebundenen  $\bar{b}b\bar{u}d$  Zustand mit  $I(J^P) = 0(1^+)$  einher geht.

Qualitativ ähnliche Ergebnisse konnte ich auch für das  $\bar{b}b\bar{u}s$  System mit Quantenzahlen  $J^P = 1^+$  finden. Auch hier liegt die Grundzustandsenergie unterhalb der relevanten Threshold. Eine Streuanalyse gestaltet sich in diesem System jedoch komplizierter, da zwei Streukanäle mit ähnlicher Energie relevant sind und somit einbezogen werden müssen. Folglich ist eine Zwei-Kanal Streuung für eine rigorose Betrachtung des  $\bar{b}b\bar{u}s$  Systems notwendig. Es stellte sich jedoch heraus, dass dies nur möglich ist, wenn Streuoperatoren vollständig implementiert sind, da anderenfalls die niedrigsten Energieniveaus nicht ausreichend aufgelöst werden können. Aus diesem Grund habe ich nur für die Rechnungen, die auf den MILC Konfigurationen durchgeführt wurden, gemäß der Lüscher-Methode die Bindungsenergien im unendlichen räumlichen Volumen bestimmt. Hierbei wurden die drei niedrigsten Energieniveaus in einer Zwei-Kanal Streuung berücksichtigt, und die Streuamplitude bestimmt. Es zeigte sich jedoch auch für das  $\bar{b}b\bar{u}s$  System, dass die Bindungsenergien im unendlichen Volumen den Energiedifferenzen zur Threshold im endlichen Volumen entsprechen. Auch hier traten somit keine entscheidenden Effekte durch das endliche Gittervolumen auf. Aus diesem Grund kann man annehmen, dass auch die Ergebnisse der Gitter-Rechnung basierend auf den Konfigurationen der RBC und UKQCD Kollaboration verlässlich die Bindungsenergien widerspiegeln. Deshalb habe ich für beide Fälle die Ergebnisse zum physikalischen Punkt extrapoliert und für die MILC Konfigurationen zusätzlich das Kontinuumslimit betrachtet. Die gefundenen Bindungsenergien von  $-86(22)(10)$  MeV bzw.  $-28(5)(10)$  MeV legen die Interpretation nahe, dass es sich bei dem  $\bar{b}b\bar{u}s$  Grundzustand um ein Tetraquark handelt, das bezüglich der starken Wechselwirkung stabil ist.

Für die  $\bar{b}c\bar{u}d$  Vier-Quark Systeme zeigte sich sowohl im  $I(J^P) = 0(0^+)$  wie auch im  $I(J^P) = 0(1^+)$  Kanal ein qualitativ anderes Bild. Die Rechnungen, basierend auf den Konfigurationen der RBC und UKQCD Kollaboration, bei denen die Streuoperatoren lediglich als Vernichtungsoperatoren berücksichtigt wurden, lieferten keinen Hinweis darauf, dass gebundene Tetraquark-Zustände vorliegen, da das niedrigste Energieniveau im endlichen Volumen konsistent mit der Threshold ist. Allerdings lassen sich auf diese Weise keine Aussagen über die mögliche Existenz eines nur schwach gebundenen Zustandes oder gar einer Resonanz treffen. Hierzu ist es erforderlich, mithilfe der Lüscher-Methode die Streuamplitude zu bestimmen. Dies erfolgte daraufhin im Rahmen der Rechnungen basierend auf den MILC-Konfigurationen. Hierzu habe ich die Operator-Basis um einige Streuoperatoren erweitert, wodurch es möglich wurde,

---

das niederenergetische Energiespektrum vollständig aufzulösen. Es zeigt sich hierbei, dass im Vergleich zu den nicht-interagierenden Meson-Meson Energieniveaus das Energiespektrum verschoben ist und ein zusätzliches Energieniveau auftritt. Dies ist ein Hinweis auf nicht-triviale Interaktionen, die auf einen zusätzlichen Zustand hindeuten können. Mithilfe einer Ein-Kanal Streuanalyse lässt sich aus diesen Energieniveaus die Streuamplitude bestimmen. Diese weist charakteristische Pole auf, die mit einer Resonanz assoziiert werden können und folglich darauf hindeuten, dass zwar keine gebundenen Zustände in den beide  $\bar{b}\bar{c}ud$  Kanälen vorliegen, jedoch jeweils eine breite Tetraquark-Resonanz.

Schlussendlich habe ich eine vereinfachte Analyse des  $\bar{b}\bar{b}ud$  Systems mit Quantenzahlen  $I(J^P) = 0(1^-)$  auf den MILC-Konfigurationen durchgeführt. Dieses System ist ein möglicher Kandidat für eine Tetraquark-Resonanz, jedoch ist eine rigorose theoretische Untersuchung herausfordernd. Unter Verwendung von Daten einer Born-Oppenheimer Rechnung, mit denen ich mögliche Ergebnisse einer Gitter-QCD Rechnung simuliert habe, konnte ich zeigen, dass eine Lüscher-Analyse basierend auf Energieniveaus, die im endlichen Gitter Volumen bestimmt wurden, prinzipiell möglich sein sollte. Eine erste volle Gitter-QCD Betrachtung, die sich lediglich auf eine kleine Zahl von Streuoperatoren begründet, sowie eine anschließende Ein-Kanal Streuanalyse konnten die mögliche Existenz einer Resonanz jedoch nicht bestätigen. Gleichzeitig lässt die Genauigkeit der Ergebnisse allerdings auch nicht zu, eine Resonanz zuverlässig auszuschließen.

Abschließend lässt sich sagen, dass in dieser Arbeit die Existenz von gebundenen  $\bar{b}\bar{b}ud$  und  $\bar{b}\bar{b}us$  Tetraquark Zuständen vorhergesagt wird und zusätzlich eine Resonanz für die  $\bar{b}\bar{c}ud$  Kanäle mit  $J = 0$  und  $J = 1$  postuliert wird. Diese theoretischen Befunde können einen wichtigen Beitrag für die experimentelle Suche nach exotischen Hadronen liefern und somit helfen, neue physikalische Teilchen zu entdecken.



---

# CONTENTS

---

<b>1. Introduction</b>	<b>1</b>
<b>2. Lattice QCD</b>	<b>5</b>
2.1. The Formulation of QCD on the Lattice . . . . .	5
2.1.1. From Continuum to Lattice Theory . . . . .	6
2.1.2. The Path Integral Formulation for Lattice QCD . . . . .	7
2.1.3. Generation of Gauge Link Configurations . . . . .	9
2.2. Gauge Actions . . . . .	9
2.3. Fermion Actions . . . . .	10
2.3.1. Wilson Fermions . . . . .	10
2.3.2. Wilson-Clover Fermions . . . . .	11
2.3.3. Domain-Wall Fermions . . . . .	12
2.3.4. Staggered Fermions . . . . .	14
2.3.5. Mixed Action Setup . . . . .	15
2.4. Effective Theories for Heavy Quarks . . . . .	16
2.4.1. Dynamics of Heavy Quark Systems . . . . .	16
2.4.2. Foldy-Wouthuysen-Tani Transformation . . . . .	17
2.4.3. Power Counting . . . . .	20
2.4.4. Euclidean Green Function . . . . .	21
2.5. Relativistic Heavy Quark Action . . . . .	23
2.6. Statistical and Systematic Uncertainties . . . . .	24
2.6.1. Estimating Statistical Uncertainties . . . . .	24
2.6.2. Systematic Uncertainties . . . . .	25
<b>3. Two-Particle States in the Finite Volume</b>	<b>29</b>
3.1. Derivation of Scattering Phase Shift Formula . . . . .	30
3.1.1. Non-Interacting Particles . . . . .	30
3.1.2. $d$ -Periodic Boundary Conditions of the Wave Function . . . . .	31
3.1.3. Interacting Particles . . . . .	32
3.2. Symmetry Properties of the Lattice . . . . .	36
3.3. Coupled Channel Scattering . . . . .	38
<b>4. Hadron Spectroscopy for Tetraquark States</b>	<b>41</b>
4.1. The Correlation Function and Physical Observables . . . . .	42
4.2. Interpolation Operators . . . . .	43
4.2.1. Construction of Interpolating Operators on the Lattice . . . . .	44

4.2.2.	Interpolating Operators and Correlation Function for Mesons . . . . .	47
4.2.3.	Interpolating Operators for $\bar{Q}\bar{Q}'qq'$ Four-Quark Systems . . . . .	49
4.3.	Techniques to Extract Energy Levels from Correlation Matrices . . . . .	54
4.3.1.	Variational Method . . . . .	54
4.3.2.	Multi-exponential Matrix Fitting . . . . .	55
4.4.	Techniques to Compute Quark Propagators . . . . .	56
4.4.1.	Point-to-all Propagators . . . . .	56
4.4.2.	Stochastic Timeslice-to-all Propagators . . . . .	57
4.4.3.	The One-End-Trick for Stochastic Propagators . . . . .	58
4.5.	Smearing Techniques . . . . .	61
4.5.1.	Smearing of Gauge Fields . . . . .	61
4.5.2.	Smearing of Quark Fields at Sinks and Sources . . . . .	63
4.6.	Scattering Analysis . . . . .	63
4.6.1.	Lattice Dispersion Relation . . . . .	64
4.6.2.	Scattering Momenta and Infinite Volume Scattering Amplitude . . . . .	64
4.6.3.	The Left-Hand Cut . . . . .	68
<b>5.</b>	<b>The Ground-State Energy for <math>\bar{Q}\bar{Q}'qq'</math> Tetraquarks</b>	<b>71</b>
5.1.	Lattice Setup . . . . .	72
5.1.1.	Gauge Field Configurations . . . . .	72
5.1.2.	Light and Strange Quark Propagators . . . . .	72
5.1.3.	Charm Quark Propagators . . . . .	73
5.1.4.	Bottom Quark Propagators . . . . .	73
5.1.5.	Smearing of Quark Fields . . . . .	74
5.2.	Energies for Antiheavy-Light Pseudoscalar and Vector Mesons . . . . .	75
5.3.	Results on $\bar{Q}\bar{Q}'qq'$ Tetraquark Systems . . . . .	76
5.3.1.	Results for the Case of $\bar{b}\bar{b}ud$ with $I(J^P) = 0(1^+)$ . . . . .	77
5.3.2.	Results for the Case of $\bar{b}\bar{b}us$ with $J^P = 1^+$ . . . . .	80
5.3.3.	Results for the Case of $\bar{b}\bar{c}ud$ with $I(J^P) = 0(0^+)$ . . . . .	85
5.3.4.	Results for the Case of $\bar{b}\bar{c}ud$ with $I(J^P) = 0(1^+)$ . . . . .	86
5.4.	Final Results and Chiral Extrapolation . . . . .	88
<b>6.</b>	<b>The Low-Lying Energy Spectrum for <math>\bar{b}\bar{b}ud</math> and <math>\bar{b}\bar{b}us</math> Tetraquarks</b>	<b>93</b>
6.1.	Lattice Setup . . . . .	94
6.1.1.	Gauge Link Configurations . . . . .	94
6.1.2.	Light and Strange Quark Propagators . . . . .	94
6.1.3.	Bottom Quark Propagators . . . . .	95
6.1.4.	Techniques to Compute Quark Propagators and Smearing of Quark Fields . . . . .	96
6.2.	Energies and Kinetic Masses for $B$ and $B_s$ Mesons . . . . .	97
6.3.	Finite Volume $\bar{b}\bar{b}qq'$ Energy Levels . . . . .	99
6.3.1.	Energy Spectrum for the Case of $\bar{b}\bar{b}ud$ with $I(J^P) = 0(1^+)$ . . . . .	100
6.3.2.	Energy Spectrum for the Case of $\bar{b}\bar{b}us$ with $J^P = 1^+$ . . . . .	106

6.4.	Scattering Analysis . . . . .	111
6.4.1.	Scattering Analysis for the Case of $\bar{b}b\bar{u}d$ with $I(J^P) = 0(1^+)$ . .	111
6.4.2.	Scattering Analysis for the Case of $\bar{b}b\bar{u}s$ with $J^P = 1^+$ . . . . .	116
6.5.	Final Results and Investigation of Systematic Uncertainties . . . . .	118
<b>7.</b>	<b>Investigation of <math>\bar{b}\bar{c}ud</math> Tetraquark States in <math>BD</math> and <math>B^*D</math> Scattering</b>	<b>127</b>
7.1.	Lattice Setup and Tuning of the Charm Quark Mass . . . . .	128
7.2.	Interpolating Operators for $\bar{b}\bar{c}ud$ Four-Quark Systems . . . . .	129
7.2.1.	Symmetry Groups and Irreps . . . . .	129
7.2.2.	Interpolating Operators for $\bar{b}\bar{c}ud$ with $I(J^P) = 0(0^+)$ . . . . .	131
7.2.3.	Interpolating Operators for $\bar{b}\bar{c}ud$ with $I(J^P) = 0(1^+)$ . . . . .	133
7.2.4.	Techniques to Compute Quark Propagators and Smearing of Quark Fields . . . . .	136
7.3.	Energies and Kinetic Masses for $D$ and $D^*$ Mesons . . . . .	136
7.4.	Finite Volume $\bar{b}\bar{c}ud$ Energy Levels . . . . .	138
7.4.1.	Energy Spectrum for the Case of $\bar{b}\bar{c}ud$ with $I(J^P) = 0(0^+)$ . . .	138
7.4.2.	Energy Spectrum for the Case of $\bar{b}\bar{c}ud$ with $I(J^P) = 0(1^+)$ . . .	140
7.5.	Scattering Analysis . . . . .	143
7.5.1.	Scattering Analysis for the Case of $\bar{b}\bar{c}ud$ with $I(J^P) = 0(0^+)$ . .	144
7.5.2.	Scattering Analysis for the Case of $\bar{b}\bar{c}ud$ with $I(J^P) = 0(1^+)$ . .	149
<b>8.</b>	<b>Investigation of the <math>\bar{b}b\bar{u}d</math> Resonance Candidate with <math>I(J^P) = 0(1^-)</math></b>	<b>155</b>
8.1.	Preparatory Investigation of $BB$ Scattering Based on Born-Oppenheimer Setup . . . . .	156
8.1.1.	Parametrization of the Scattering Phase Shift . . . . .	156
8.1.2.	T-Matrix Pole Based on Born-Oppenheimer Data . . . . .	157
8.2.	Lattice Setup . . . . .	159
8.3.	Interpolating Operators for $\bar{b}b\bar{u}d$ with $I(J^P) = 0(1^-)$ . . . . .	160
8.4.	Finite Volume Energy Levels for $\bar{b}b\bar{u}d$ with $I(J^P) = 0(1^-)$ . . . . .	162
8.5.	Strategy for the Scattering Analysis for $\bar{b}b\bar{u}d$ with $I(J^P) = 0(1^-)$ . . . .	164
<b>9.</b>	<b>Conclusions</b>	<b>167</b>
<b>A.</b>	<b>Conventions</b>	<b>175</b>
<b>B.</b>	<b>Group Theoretical Background of Symmetry Considerations</b>	<b>177</b>
B.1.	Basics of Representation Theory . . . . .	177
B.2.	Decomposition of Rotational Group into Irreducible Representations . .	179
B.3.	Simplification of $M$ -Matrix due to Group Symmetries . . . . .	181
B.3.1.	Group $D_{4h}$ . . . . .	181
B.3.2.	Group $D_{2h}$ . . . . .	182
B.3.3.	Group $C_{4v}$ . . . . .	182
B.3.4.	Group $C_{2v}$ . . . . .	182

<b>C. Correlation Functions for Four-Quark Operators</b>	<b>185</b>
C.1. Derivation of Correlation Matrix Elements . . . . .	186
C.1.1. Type I Correlation Matrix Elements . . . . .	186
C.1.2. Type II Correlation Matrix Elements . . . . .	187
C.1.3. Type III Correlation Matrix Elements . . . . .	188
C.1.4. Type IV Correlation Matrix Elements . . . . .	189
C.2. Quark Propagator Types for Correlation Matrix Elements . . . . .	190
<b>D. Computing Weighted Average Including Statistical Uncertainties</b>	<b>193</b>
<b>E. Tuning of Parameters for the MILC-HISQ Setup</b>	<b>195</b>
E.1. Determination of Smearing Parameters for Fermion Fields . . . . .	195
E.2. Determination of GEVP Normalization $t_0$ . . . . .	197
<b>F. Plots of Single-Exponential Fits to Determine the Energy Levels for the HISQ-Ensembles</b>	<b>201</b>
<b>Bibliography</b>	<b>209</b>
<b>Acknowledgements</b>	<b>229</b>

# 1

---

## INTRODUCTION

---

The theory that describes the strong interaction of quarks and gluons is called Quantum Chromodynamics (QCD). It is formulated as a non-abelian  $SU(3)$  gauge theory where the color charge serves as the associated conserved quantity. Originating from the non-abelian structure of the theory, the gluons, which are the mediators of QCD, also carry color and thus experience self-interactions. These interactions are one reason why the coupling constant of QCD depends on the energy regime and decreases for increasing energies. For high energies, this leads to only weakly interacting quarks and gluons which is called *asymptotic freedom*. In the low-energy regime, however, the coupling becomes large so that quarks and gluons are strongly interacting and appear only as color-neutral states like hadrons. This is called *confinement*.

While the high-energy region of QCD can be studied perturbatively thanks to the small coupling constant, this is not feasible for low energies where the coupling constant becomes large. Accordingly, studying low-energy observables like hadron masses requires a different approach which is non-perturbative.

Lattice QCD, initially introduced by K. Wilson [1], provides such an approach. Here, QCD is considered on a discretized Euclidean lattice of space-time points with finite size  $L^3 \times T$  where the distance between two neighboring points is called lattice spacing  $a$ . A reasonable approach to computing QCD observables on this grid is to utilize the path integral formalism of quantum field theory. On the lattice, the path integral becomes finite-dimensional and can be evaluated numerically using stochastic integration methods like Monte-Carlo simulations on high performance computers. Note that introducing the discretized finite grid represents an approximation to QCD which is, however, controllable. The dependence of QCD observables on the non-zero lattice spacing and the finite space-time volume can be studied, and an appropriate continuum and infinite volume limit can be established.

One branch of particular interest in modern QCD calculations is hadron spectroscopy. Computing masses of particles which are experimentally well-established is an excellent test of QCD. Moreover, predicting new states that have not been detected yet provides valuable input for ongoing experimental research.

While decades of experimental efforts discovered a zoo of hadrons, it was Gell-Mann and Zweig in the 1960s who introduced quarks as point-like elementary particles which are, together with gluons, the building blocks of all hadrons [2, 3]. There are six different types of quarks, called flavors: the up ( $u$ ), down ( $d$ ), strange ( $s$ ), charm ( $c$ ),

bottom ( $b$ ) and top ( $t$ ) quarks. Hadrons are divided into two categories: mesons, which have integer spin, and baryons, which have half-integer spin. Generally, an ordinary meson corresponds to a quark-antiquark pair, whereas an ordinary baryon is built of three quarks or three antiquarks. However, QCD also allows for the formation of color-neutral hadrons consisting of more than three quarks or antiquarks like tetraquarks<sup>1</sup> or pentaquarks which are summarized as *exotic hadrons*.

In the last few years, a large number of hadrons that cannot be explained by ordinary, i.e., non-exotic, quark content have been experimentally discovered. Such exotic hadrons are summarized as XYZ states. One prominent example is the  $Z_c(3900)$ , which has been simultaneously discovered by the Belle and BES III collaborations [4, 5] as an enhancement in the process  $e^+e^- \rightarrow \pi^+\pi^- J/\psi$  and is the first independently found tetraquark candidate. This discovery has been followed by the detection of further quarkonium-like  $Z_c$  and  $Z_b$  states by the Belle [6, 7], BES III [8–11] and LHCb [12] collaborations while by now a large number of tetraquark candidates have been found, many of them in the heavy quark sector [13–19]. Quite recently, the LHCb collaboration has found the  $T_{cc}$ , which is the first tetraquark state with a mass below the relevant two-meson threshold corresponding to  $DD^*$  [20, 21]. In contrast to the  $Z_c$  states, which have a charmonium-like structure, the  $T_{cc}$  consists of two anticharm quarks and two light quarks and is therefore obviously a flavor exotic state.

Lattice QCD provides an excellent framework to investigate the spectrum of hadrons and study exotic states. Using carefully chosen creation operators, the energy spectra of interest are computed from Euclidean correlation functions. The energies of stable hadrons are then governed by the energies well below the threshold of strong decay and can be computed in current lattice calculations extremely precisely. However, the variety of hadrons covers not only stable particles but also resonances with short lifetimes. Unfortunately, the vast majority of flavor exotic states is expected to be either a stable state close to the threshold of strong decay or a resonance so that theoretical investigations are facing big challenges. The treatment of resonances is sophisticated as they are not eigenstates of QCD with distinct energies but excitations in the continuous spectrum of scattering states. The essential challenge is to relate the discrete spectrum of states in the finite volume to the continuum of scattering states in the infinite volume. This has been facilitated by the pioneering work of M. Lüscher who established a formalism that relates the finite volume energy spectrum to the infinite volume scattering amplitude [22, 23] from which resonance parameters like the hadron mass can be extracted. Nevertheless, this is a sophisticated task as a large number of energy levels need to be resolved precisely. Also the energies of stable hadrons that are close to the threshold of strong decay may not be directly extracted from the finite volume energy spectra as couplings to the threshold of strong decay might play an important role. This issue can also be addressed by resorting to Lüscher’s method.

---

<sup>1</sup>The term *tetraquark* is used ambiguously in literature. While sometimes it is used exclusively for diquark-antidiquark structures, I will follow the more general nomenclature where all bound states and resonances that have a strong four-quark contribution are labeled as tetraquarks.

---

Four-quark structures  $\bar{Q}\bar{Q}'qq'$  that consist of two heavy antiquarks and two light quarks are promising candidates for bound tetraquarks or resonances and are theoretically easier to examine than their  $\bar{Q}Q'\bar{q}q'$  counterpart, since they can decay only in two heavy-light mesons whose masses are in general of similar order [24].  $\bar{Q}Q'\bar{q}q'$  systems, however, have an additional decay channel corresponding to a light meson and a heavy quarkonium. Additionally, it can be shown that the  $\bar{Q}\bar{Q}'qq'$  tetraquark is hadronically stable in the infinite mass limit for heavy quarks,  $m_{Q,Q'} \rightarrow \infty$  [25–27]. In this case, a color-antitriplet is formed by the two heavy antiquarks, while the associated binding energy is of order  $\alpha_s^2 m_Q$  [26]. As the binding is weakened for decreasing heavy quark masses, the essential question is now if such antiheavy-antiheavy-light-light tetraquarks  $\bar{Q}\bar{Q}'qq'$  exist also for physical bottom or charm quark masses and, if so, whether as a QCD-stable bound state below or as a resonance above the two meson threshold  $\bar{Q}q\text{-}\bar{Q}'q'$ .

First lattice QCD computations of doubly-antiheavy doubly-light tetraquark systems have been carried out for the  $\bar{b}\bar{b}ud$  four-quark system with quantum numbers  $I(J^P) = 0(1^+)$  using static  $\bar{b}$  quarks and the Born-Oppenheimer approximation, predicting a  $\bar{b}\bar{b}ud$  tetraquark bound state with respect to the strong interaction [28–32]. Using the same approach, a  $\bar{b}\bar{b}ud$  tetraquark resonance with quantum numbers  $I(J^P) = 0(1^-)$  has been found [33], while a more recent study questions this [34]. The existence of the bound  $\bar{b}\bar{b}ud$  tetraquark with  $I(J^P) = 0(1^+)$  has been confirmed by calculations with  $\bar{b}$  quarks of finite mass which are treated in a non-relativistic framework (NRQCD) [35–40]. Furthermore, lattice calculations carried out by several groups agree about the existence of a bound  $\bar{b}\bar{b}us$  tetraquark with  $J^P = 1^+$  [24, 35, 36, 40], while for the  $\bar{b}\bar{c}ud$  system with  $I(J^P) = 0(1^+)$ , recent results are still inconclusive if a stable tetraquark exists or not [41–43].

So far, there has been no experimental observation of  $\bar{Q}\bar{Q}'qq'$  tetraquarks with at least one heavy  $\bar{b}$  quark, but the prospects of discovering such states have been examined in Refs. [44–46]. However, in the closely related sector of doubly-charmed tetraquarks, major progress has recently been made via the discovery of the  $T_{cc}$  tetraquark by the LHCb collaboration as stated above [20, 21], while a lattice QCD calculation investigating this system can be found in Ref. [47].

In this thesis, I will investigate doubly-antiheavy doubly-light tetraquark systems with at least one heavy antibottom quark using lattice QCD. I focus on four-quark systems, which are promising candidates for stable or nearly stable tetraquarks. In order to investigate such structures, the correlation functions are constructed using two different types of creation operators. In addition to local creation operators, where all four quarks are located at the same space-time position, I utilize also scattering operators which resemble two spatially separated mesons. According to Refs. [48, 49], such scattering operators are mandatory to rigorously resolve the energy of ground states in exotic systems. Thus, I expand on previous research in Refs. [35, 36, 41]

where doubly-antiheavy doubly-light tetraquarks were investigated without considering scattering operators. In addition to that, including scattering operators allows me to apply Lüscher's method by analyzing the relevant meson-meson scattering and subsequently to determine the scattering amplitude in the infinite volume. I use this method for two different cases. First, I investigate possible effects due to couplings to the threshold of strong decay for tetraquarks which are expected to be stable under the strong interaction. Second, I apply this approach to study tetraquark candidates which might be bound states, resonances or neither of the two. As none of the investigated states has been experimentally observed yet, these results might be a valuable starting point for the experimental search of such exotic hadrons.

This thesis is structured as follows: In Chapter 2, I introduce the theoretical foundations of lattice QCD. I present the different fermion actions that are utilized in the following calculations and, in particular, I discuss the framework of non-relativistic QCD (NRQCD) that is used for implementing  $b$  quarks throughout this work. Chapter 3 focuses on the theoretical description of two-particle states on the lattice. As an essential part I recapitulate the derivation of Lüscher's formula and discuss implications of the lattice symmetries for actual calculations. Basic aspects of hadron spectroscopy on the lattice that are required for the following computations are covered in Chapter 4. Here, I also describe the construction of the relevant interpolating operators and provide the techniques that are used for computing and evaluating correlation functions. I also explicate the employed strategy for the scattering analysis. In Chapter 5, I present results for the ground-state energies of the four-quark systems  $\bar{b}\bar{b}ud$  with  $I(J^P) = 0(1^+)$ ,  $\bar{b}\bar{b}us$  with  $J^P = 1^+$  and  $\bar{b}\bar{c}ud$  with  $I(J^P) = 0(0^+)$  and  $I(J^P) = 0(1^+)$ . Here I use scattering operators at the sink and identify two candidates for a stable tetraquark. A more elaborated study of the  $\bar{b}\bar{b}ud$  system with  $I(J^P) = 0(1^+)$  and the  $\bar{b}\bar{b}us$  system with  $J^P = 1^+$  is carried out in Chapter 6. Using scattering operators at the sink and the source, the low-lying energy spectrum is extracted, and I perform a rigorous scattering analysis using Lüscher's method. In Chapter 7, I exploratively study the  $\bar{b}\bar{c}ud$  systems with  $I(J^P) = 0(0^+)$  and  $I(J^P) = 0(1^+)$  in a scattering analysis relying on energy spectra obtained from large operator bases including scattering operators. Chapter 8 focuses on the  $\bar{b}\bar{b}ud$  system with  $I(J^P) = 0(1^-)$  which is a candidate for a tetraquark resonance. Here, I initially discuss the prospects of studying this system in lattice QCD, followed by the results of a first rough lattice calculation. I will end with my conclusions and an outlook on further work in Chapter 9.



# 2

---

## LATTICE QCD

---

Lattice QCD provides a powerful numerical approach to studying QCD and particularly allows computing low-energy observables like hadron masses for which perturbation theory is not applicable. In this chapter I will recapitulate the theoretical foundations of lattice QCD based on Ref. [50] and discuss some special techniques that are applied in this work. I start with a short overview of the basic concepts of lattice QCD and illustrate the derivation of the naive fermion action as well as the gauge action from the continuum theory in Sec. 2.1. Here, I also briefly discuss the path integral formulation which is a suitable approach to computing observables on the lattice. In Sec. 2.2, I introduce an improved gauge action which reduces lattice discretization errors, while in the subsequent Sec. 2.3, I present several fermion actions which are utilized to include light and strange quarks in the lattice computations carried out in this thesis. Considering heavy quarks in lattice QCD is more sophisticated as they cannot be reliably resolved on currently used lattices. One option to incorporate them is using an effective field theory corresponding to a non-relativistic expansion of the Dirac Lagrangian which is discussed in Sec. 2.4. In Sec. 2.5 I present a relativistic heavy quark action which depicts another possible approach to including heavy quarks in lattice simulations. Finally, in Sec. 2.6 I give an overview of statistical and systematic uncertainties occurring in lattice calculations. A more complete introduction to lattice QCD can be found in standard text books like Refs. [50, 51].

### 2.1 The Formulation of QCD on the Lattice

The fundamental idea of lattice QCD is to replace the continuous Euclidean space-time by a four-dimensional grid of finite size. This hypercubic lattice with spatial extent  $L$  and temporal extent  $T$  is characterized by the set of lattice points

$$\Gamma = \{x \in \mathbb{Z}^4 \mid x_1, x_2, x_3 = 0, \dots, N_s - 1 \text{ and } x_4 = 0, \dots, N_t - 1\} \quad (2.1)$$

which are separated by a lattice spacing  $a$ . Here  $N_s$  and  $N_t$  equal the total number of lattice points in the spatial and temporal direction. As a consequence of the finite spatial volume, the lattice momenta are discrete obeying

$$p_i = n_i \frac{2\pi}{L}, \quad n_i \in \mathbb{Z}, \quad i = 1, 2, 3. \quad (2.2)$$

Additionally, due to the discretized space-time, the momentum is bounded from above and the maximal momentum is given by  $2\pi/a$ . Therefore, the lattice serves as a

natural regulator of the theory. It introduces a momentum cutoff which renders the ultraviolet divergence that appears for QCD as a quantum field theory and sets a finite energy region. Moreover, the discretization of the space-time makes the path integral formalism of QCD mathematically well-defined (see Sec. 2.1.2). One drawback is, however, that the continuous translational and rotational symmetry is broken. I will discuss the implications of this in Secs. 3.2 and 4.2 in more detail.

### 2.1.1 From Continuum to Lattice Theory

The QCD action in the continuum for four-dimensional Euclidean space-time is given by

$$S_{\text{QCD}}[\psi, \bar{\psi}, A] = S_F[\psi, \bar{\psi}, A] + S_G[A], \quad (2.3)$$

with the fermion action

$$S_F[\psi, \bar{\psi}, A] = \sum_{f=1}^{N_f} \int d^4x \bar{\psi}^{(f)}(x) \left( \gamma_\mu D_\mu + m^{(f)} \right) \psi^{(f)}(x), \quad (2.4)$$

and the gluon action

$$S_G[A] = \frac{1}{2g^2} \int d^4x \text{Tr} [F_{\mu\nu}(x) F_{\mu\nu}(x)], \quad (2.5)$$

with the bare coupling  $g$ . Here, the spinors  $\psi^{(f)a}_A(x)$ ,  $\bar{\psi}^{(f)a}_A(x)$  denote a quark field of flavor  $f$  at space-time position  $x$  with Dirac index  $A = 1, \dots, 4$  and color index  $a = 1, 2, 3$ . The field strength tensor  $F_{\mu\nu}(x)$  is defined as

$$F_{\mu\nu}(x) = \partial_\mu A_\nu(x) - \partial_\nu A_\mu(x) + i[A_\mu(x), A_\nu(x)]. \quad (2.6)$$

The covariant derivative writes  $D_\mu = \partial_\mu + iA_\mu(x)$  and is introduced to maintain gauge invariance of the action, while the  $3 \times 3$  matrices  $A_\mu(x)$  represent the gluon fields with the Lorentz index  $\mu = 1, \dots, 4$  labeling the direction of its components in Euclidean space-time. The  $\gamma_\mu$  are the Euclidean gamma matrices as defined in Appendix A. Note that the last term of the field-strength tensor is not vanishing, as the  $A_\mu(x)$  matrices are not commuting. This is a consequence of the non-abelian structure of QCD and incorporates the gluons' self-interactions.

In order to construct the QCD action on the lattice, all terms appearing in Eq. (2.3) must be converted to a discretized formulation. As the fermion fields  $\psi(x)$ ,  $\bar{\psi}(x)$  are placed on the lattice points, a discretized version of the fermion fields' derivative must be established. One possible symmetric expression is

$$\partial_\mu \psi(x) = \frac{\psi(x + \hat{\mu}) - \psi(x - \hat{\mu})}{2a}, \quad (2.7)$$

where  $\hat{\mu}$  stands for one step on the lattice in  $\mu$ -direction. However, using a discretized derivative like Eq. (2.7) in the fermion action introduces terms like  $\bar{\psi}(x) \psi(x + \hat{\mu})$  which

are not invariant under gauge transformations according to  $\psi(x) \rightarrow \psi'(x) = \Omega(x) \psi(x)$  with  $\Omega(x) \in \text{SU}(3)$ . To preserve the gauge invariance of the action, new gauge fields  $U_\mu(x) \in \text{SU}(3)$  are introduced. These fields carry a directorial index  $\mu$  and are located at the links between two lattice points. They are related to the continuum gauge fields  $A_\mu(x)$  by

$$U_\mu(x) = \exp(iaA_\mu(x)). \quad (2.8)$$

Their transformation behavior under a gauge transformation  $\Omega(x)$  is governed by

$$U_\mu(x) \rightarrow U'_\mu(x) = \Omega(x) U_\mu(x) \Omega^\dagger(x + \hat{\mu}) \quad (2.9)$$

and is designed such that the terms appearing in the discretized derivative can be formulated in a gauge invariant way. Using the gauge fields to formulate a gauge invariant lattice derivative, the naive lattice fermion action is given by

$$S_F[\psi, \bar{\psi}, U] = a^4 \sum_{f=1}^{N_f} \sum_{x \in \Gamma} \bar{\psi}^{(f)}(x) D^{(f)}(x; y) \psi^{(f)}(y), \quad (2.10)$$

with the Dirac operator

$$D^{(f)}(x; y) = \frac{1}{2a} \sum_{\mu=1}^4 \gamma_\mu \left( U_\mu(x) \delta_{x+\hat{\mu}, y} - U_{-\mu}(x) \delta_{x-\hat{\mu}, y} \right) + m^{(f)} \delta_{x, y}, \quad (2.11)$$

where  $U_{-\mu}(x) \equiv U_\mu(x - \hat{\mu})^\dagger$ .

A lattice version of the gauge action is obtained by using closed loops of gauge links, while these loops are gauge invariant objects (e.g., see Ref. [50]). The smallest possible loop is the so-called plaquette  $U_{\mu, \nu}(x)$  which is defined as

$$U_{\mu, \nu}(x) = U_\mu(x) U_\nu(x + \hat{\mu}) U_{-\mu}(x + \hat{\mu} + \hat{\nu}) U_{-\nu}(x + \hat{\nu}). \quad (2.12)$$

The first version of a lattice gauge action has been introduced by Wilson [1] and is constructed via a sum over all plaquettes of the lattice, while every loop is only counted once,

$$S_G[U] = \frac{2}{g^2} \sum_{x \in \Gamma} \sum_{\mu < \nu} \text{ReTr} \left[ \mathbf{1} - U_{\mu, \nu}(x) \right]. \quad (2.13)$$

Using Eq. (2.8), it can be shown that this gauge action recovers the continuum action Eq. (2.5) in the naive continuum limit  $a \rightarrow 0$ .

### 2.1.2 The Path Integral Formulation for Lattice QCD

The Euclidean path integral is a fundamental tool to compute observables of QCD on the lattice. Using the lattice gauge action and fermion action discussed in the previous paragraph, expectation values of observables are given by

$$\langle \mathcal{O} \rangle = \frac{1}{Z} \int \mathcal{D}[\psi, \bar{\psi}] \mathcal{D}[U] e^{-S_F[\psi, \bar{\psi}, U] - S_G[U]} \mathcal{O}[\psi, \bar{\psi}, U] \quad (2.14)$$

with the partition function

$$Z = \int \mathcal{D}[\psi, \bar{\psi}] \mathcal{D}[U] e^{-S_F[\psi, \bar{\psi}, U] - S_G[U]}. \quad (2.15)$$

The path integral on the lattice is formulated as an integral over all possible fermion and gluon field configurations. The measures are consequently products over all fields and all associated indices,

$$\mathcal{D}[\Phi] = \prod_{x \in \Gamma} \prod_{\alpha} d\Phi_{\alpha}, \quad (2.16)$$

where  $\Phi$  is a generic field and  $\alpha$  labels all internal indices of  $\Phi$ . Every possible path is weighted by the exponential  $e^{-S_F[\psi, \bar{\psi}, U] - S_G[U]}$  which serves as the Boltzmann factor of the QCD action. Note that the operator  $\mathcal{O}$  is translated from a Hilbert-space operator to a functional of the fields.

As the lattice consists of a finite number of points, the number of possible field configurations is also finite and the path integral is mathematically well-defined on the lattice. This makes lattice QCD an excellent tool to evaluate the path integral.

The expectation values for observables can also be written in a form separating the fermionic from the gauge field part of the path integral,

$$\langle \mathcal{O} \rangle = \langle \langle \mathcal{O} \rangle_F \rangle_G = \frac{1}{Z} \int \mathcal{D}[U] e^{-S_G[U]} \left( \int \mathcal{D}[\psi, \bar{\psi}] e^{-S_F[\psi, \bar{\psi}, U]} \mathcal{O}[\psi, \bar{\psi}, U] \right). \quad (2.17)$$

Using anti-commuting Grassmann numbers to express the fermion fields  $\psi, \bar{\psi}$ , the fermionic part of the path integral can be integrated out. This yields the expectation value

$$\langle \mathcal{O} \rangle = \frac{1}{Z} \int \mathcal{D}[U] e^{-S_G[U]} \det(D[U]) \langle \mathcal{O} \rangle_F, \quad (2.18)$$

where  $\det(D[U]) = \prod_{f=1}^{N_f} \det(D^{(f)}[U])$  is the fermion determinant and  $\langle \mathcal{O} \rangle_F$  the fermionic expectation value.

In order to compute correlation functions of hadron operators as it will be discussed in Sec. 4.1, it is necessary to compute the fermionic expectation values for fermion fields, i.e., Grassmann valued numbers,

$$\langle \psi^{(f)}(x) \bar{\psi}^{(f)}(y) \rangle_F. \quad (2.19)$$

This expectation value can be evaluated using *Wick's theorem* (e.g., see Ref. [50]) as

$$\langle \psi^{(f)a}_A(x) \bar{\psi}^{(f)b}_B(y) \rangle_F = (D^{(f)})^{-1}_{A,B}{}^{a,b}(x; y), \quad (2.20)$$

where  $(D^{(f)})^{-1}$  is the inverse of the Dirac operator given, for example, by Eq. (2.11). This is also referred to as fermion contractions, and the inverse Dirac operator  $(D^{(f)})^{-1}$  is also called *quark propagator*. I will discuss different techniques of how to determine the quark propagator in Sec. 4.4.

### 2.1.3 Generation of Gauge Link Configurations

Using modern computing systems, it is not possible to calculate Eq. (2.14) in its entirety. Such path integrals are instead evaluated by Monte Carlo simulations which replace the integral by a sum over  $N$  samples of gauge field configurations  $U_n$  that are distributed according to the Boltzmann weight  $e^{-S[\psi, \bar{\psi}, U]}$ . The expectation value for an observable  $\mathcal{O}$  is then approximated by

$$\langle \mathcal{O} \rangle \approx \frac{1}{N} \sum_{U_n} \mathcal{O}[U_n] \quad (2.21)$$

where  $U_n$  has a probability  $\propto e^{-S[\psi, \bar{\psi}, U]}$ . For a sufficiently large number of sample gauge configurations  $N$ , Eq. (2.21) approaches Eq. (2.14) and describes the expectation values quite accurately. The set of sample gauge configurations is generated by Monte Carlo algorithms. Hereby, Markov chains provide a reasonable way to obtain a sequence of gauge configurations which respect the probability distribution introduced by the Boltzmann factor. For more details about the generation of gauge link configurations see, for example, Sec. 4 of Ref. [50].

## 2.2 Gauge Actions

The Wilson gauge action given in Eq. (2.13) approximates the continuum gauge action in Eq. (2.5) up to  $\mathcal{O}(a^2)$ , which can be easily seen if Eq. (2.8) is inserted in the Wilson action and expanded in orders of  $a$ . While the discretization effects are already quite small, further improvement can be achieved using the so-called *Lüscher-Weisz gauge action*. [52, 53] Hereby, in addition to the plaquette term known from Wilsons gauge action, one adds a sum over all closed rectangular  $2 \times 1$  loops,  $U_{\mu, \nu}^{\text{rect.}}$ , and a sum over all parallelogram loops of lengths 6 along the contour of all three-dimensional cubes,  $U_{\mu, \nu, \rho}^{\text{par.}}$

$$S_G^{\text{Lüscher-Weisz}}[U] = \frac{2}{g^2} \sum_{x \in \Gamma} \left( c_0 \sum_{\mu < \nu} \text{Re Tr} \left[ \mathbb{1} - U_{\mu, \nu}(x) \right] + c_1 \sum_{\mu \neq \nu} \text{Re Tr} \left[ \mathbb{1} - U_{\mu, \nu}^{\text{rect.}}(x) \right] + c_2 \sum_{\mu \neq \nu \neq \rho} \text{Re Tr} \left[ \mathbb{1} - U_{\mu, \nu, \rho}^{\text{par.}}(x) \right] \right). \quad (2.22)$$

The coefficients  $c_i$  obey the relation  $c_0 + 8c_1 + 8c_2 = 1$ , so that for  $c_1 = c_2 = 0$  the Wilson gauge action is recovered. Tree-level improvement in perturbation theory is obtained by  $c_1 = -\frac{1}{12}$ ,  $c_2 = 0$  and consequently  $c_0 = \frac{5}{3}$ . Another prominent gauge scheme is the Iwasaki gauge action which uses  $c_1 = -0.331$ ,  $c_2 = 0$  and accordingly  $c_0 = 3.468$  [54, 55].

### 2.3 Fermion Actions

The naive fermion discretization given in Eq. (2.11) suffers from lattice artifacts, the so-called doublers. Considering the naive fermion action in Eqs. (2.10) and (2.11) for free fermions, e.g.,  $U_\mu(x) = \mathbf{1}$ , and a single flavor, the Fourier transformed Dirac operator is given by

$$\tilde{D}(p; q) = \frac{1}{\Gamma} \sum_{x, y \in \Gamma} e^{-ipx} D(x; y) e^{iqy} = \delta_{p, q} \tilde{D}(p) \quad (2.23)$$

with

$$\tilde{D}(p) = m\mathbb{1} + \frac{i}{a} \sum_{\mu=1}^4 \gamma_\mu \sin(p_\mu a). \quad (2.24)$$

In the case of massless fermions,  $m = 0$ , the inverse Dirac operator, the so-called quark propagator, can be easily determined. First, one observes that the correct naive continuum limit is obtained,

$$\tilde{D}^{-1}(p)|_{m=0} = \frac{-\frac{i}{a} \sum_{\mu=1}^4 \gamma_\mu \sin(p_\mu a)}{\frac{1}{a^2} \sum_{\mu=1}^4 \sin^2(p_\mu a)} \xrightarrow{a \rightarrow 0} \frac{-i \sum_{\mu=1}^4 \gamma_\mu p_\mu}{p^2}. \quad (2.25)$$

Second, the continuum propagator has one pole at  $p = (0, 0, 0, 0)$ . In the lattice version, this pole is also present, however, there are also poles for all other combinations of  $p_\mu \in [0, \pi/a]$ , so there appear 15 additional unphysical poles which are called doublers. These doublers should be removed from the theory.

In the following paragraphs, I will present several lattice fermion discretizations, so-called fermion actions, which essentially remove or partially remove the doublers, while fulfilling the correct continuum limit.

#### 2.3.1 Wilson Fermions

One common formulation of lattice fermions has been introduced by Wilson (e.g., see Ref. [50]). He added an extra term, the Wilson term

$$O_{\text{Wilson}} = \frac{1}{a} \sum_{\mu=1}^4 (1 - \cos(p_\mu a)), \quad (2.26)$$

to the Dirac operator in momentum space  $\tilde{D}(p)$  in order to distinguish the unphysical poles from the physical pole and to remove the doublers. This term vanishes in the continuum limit  $a \rightarrow 0$  and gives rise to an additional mass for the doublers,

$$m = \frac{2l}{a}, \quad l : \text{Number of momentum components } p_\mu = \pi/a, \quad (2.27)$$

so only one massless pole remains. Sending  $a \rightarrow 0$ , the mass of all other poles diverges and they decouple from the theory.

In position space, the Wilson Dirac operator is given by

$$D_{\text{Wilson}}^{(f)}(x; y) = \left(m^{(f)} + \frac{4}{a}\right) \mathbb{1} \delta_{x,y} - \frac{1}{2a} \sum_{\mu=\pm 1}^{\pm 4} (\mathbb{1} - \gamma_{\mu}) U_{\mu}(x) \delta_{x+\hat{\mu},y}, \quad (2.28)$$

where  $\gamma_{-\mu} \equiv -\gamma_{\mu}$ . Note that the Wilson Dirac operator is invariant with respect to crucial symmetry transformations like charge conjugation and parity and obeys  $\gamma_5$ -hermiticity, which means that it fulfills

$$(\gamma_5 D)^{\dagger} = \gamma_5 D \quad \text{or} \quad D^{\dagger} = \gamma_5 D \gamma_5. \quad (2.29)$$

However, one big disadvantage of Wilson's discretization is that the Wilson term breaks chiral symmetry explicitly, even for massless fermions. This can easily be seen, as the Wilson Dirac operator does not satisfy the equation (e.g., see Ref. [50])

$$\{D, \gamma_5\} = 0. \quad (2.30)$$

Restoring the chiral symmetry is a quite delicate issue and cannot be fully achieved, while obtaining a theory free of any doublers. This is formulated by the Nielsen-Ninomiya theorem [56–58] which states that for a lattice regularization which is hermitian, local and translational invariant, fermion doublers cannot be totally removed without breaking the chiral symmetry for massless fermions.

Implementing chiral symmetry on the lattice has been an unresolved issue for many years. Progress was only achieved when it was recognized that the Ginsparg-Wilson equation,

$$\{D, \gamma_5\} = a D \gamma_5 D, \quad (2.31)$$

provides a way of implementing chiral symmetry in a milder and better controllable way on the lattice [59, 60]. As the lattice spacing  $a$  appears on the right-hand side of Eq. (2.31), the continuum expression for chiral symmetry in Eq. (2.30) is recovered for  $a \rightarrow 0$ . Based on the Ginsparg-Wilson equation, fermion actions which restore chiral symmetry have been developed. Two frequently used discretizations obeying the Ginsparg-Wilson equation are *overlap fermions* [61–65] and *domain wall fermions* (see Sec. 2.3.3). Another formulation of fermions on the lattice that can recover chiral symmetry are the so-called *staggered fermions* (see Sec. 2.3.4). Here, the number of doublers is reduced while in the meantime a remnant chiral symmetry is maintained.

### 2.3.2 Wilson-Clover Fermions

While the Wilson formulation of fermions discussed in Sec. 2.3.1 matches the continuum fermion action in Eq. (2.4) when taking the continuum limit  $a \rightarrow 0$ , discretization errors of  $\mathcal{O}(a)$  appear for non-zero lattice spacing  $a$ . Using the Symanzik improvement scheme [52, 66, 67], the discretization errors can be further reduced from  $\mathcal{O}(a)$  to  $\mathcal{O}(a^2)$  by adding an additional term to the Wilson action,

$$S_{\text{Wilson-Clover}} = S_{\text{Wilson}} + c_{\text{sw}} a^5 \sum_{x \in \Gamma} \sum_{\mu < \nu} \bar{\psi}(x) \frac{1}{2} \sigma_{\mu\nu} \hat{F}_{\mu\nu}(x) \psi(x), \quad (2.32)$$

with the Sheikholeslami-Wohlert coefficient  $c_{\text{sw}}$  and  $\sigma_{\mu\nu} = \frac{1}{2}[\gamma_\mu, \gamma_\nu]$ . This term is called the clover term as its shape looks like a clover leaf. The term  $\hat{F}_{\mu\nu}(x)$  is expressed by

$$\hat{F}_{\mu\nu}(x) = \frac{-i}{8a^2}(Q_{\mu\nu}(x) - Q_{\nu\mu}(x)) \quad (2.33)$$

with  $Q_{\mu\nu}(x) = U_{\mu,\nu}(x) + U_{\mu,-\nu}(x) + U_{-\mu,-\nu}(x) + U_{-\mu,\nu}(x)$

where  $Q_{\mu\nu}$  is the sum over plaquettes in the  $\mu - \nu$  plane.

For removing all contributions of  $\mathcal{O}(a)$ , the  $c_{\text{sw}}$  coefficient must be tuned in an appropriate way. This can be done non-perturbatively using the chiral symmetry of QCD [68–70]. Another feasible approach is the tadpole improvement [71] which reduces radiative corrections. Consequently, adding the clover term with a reasonably tuned  $c_{\text{sw}}$ , the Wilson-clover action is  $\mathcal{O}(a)$  improved.

### 2.3.3 Domain-Wall Fermions

Domain-wall fermions [72–75] provide an opportunity to implement chiral symmetry on the lattice. The basic concept is to introduce a fifth dimension, while chiral zero modes are located at the domain walls of this dimension, i.e., the four-dimensional boundaries. Following the approach of Ref. [76], one considers a five-dimensional continuum Dirac equation with a mass term depending on the fifth dimension,

$$\left[ D + \gamma_5 \partial_s + m(s) \right] \Psi(x, s) = 0, \quad (2.34)$$

where  $D$  is a four-dimensional massless Dirac operator and  $s$  is the coordinate for the fifth dimension. The mass term is given by

$$m(s) = \begin{cases} m & \text{for } s > 0 \\ -m & \text{for } s < 0 \end{cases} \quad (m > 0). \quad (2.35)$$

The spinor  $\Psi(x, s)$  can be expanded in modes  $n$  and factorized in left- and right-handed parts according to

$$\Psi(x, s) = \sum_{n \in \mathbb{Z}} \left[ g_n(s) P_R + f_n(s) P_L \right] \psi_n(x), \quad (2.36)$$

with the chiral projectors  $P_{R/L} = (\mathbf{1} \pm \gamma_5)/2$  and the  $s$ -dependent prefactors  $g_n$  and  $f_n$ . Eq. (2.36) needs to fulfill the Dirac equation in Eq. (2.34), which yields

$$\begin{aligned} [\partial_s + m(s)] f_n(s) &= \mu_n g_n(s), \\ [-\partial_s + m(s)] g_n(s) &= \mu_n f_n(s), \\ [D + \mu_n] \psi_n(x) &= 0. \end{aligned} \quad (2.37)$$

The value  $\mu_n$  can be understood as a coupling of the left- and right-handed parts of  $\Psi$  and consequently must be zero for a chiral zero mode where both parts are decoupled.



Solving Eq. (2.37) for  $\mu_0 = 0$ , we observe that the solution  $f_0(s)$  is not normalizable, so the left-handed spinor  $\Psi_L(x, s)$  vanishes. Consequently, the chiral fermion which appears at the four-dimensional boundary is right-handed. Note that the location of this zero mode corresponds to the position where the mass changes sign, i.e.,  $s = 0$ . If the fifth dimension  $L_s$  is finite as required for lattice calculations, the mass must change its sign once more. Thus, another zero mode with opposite chirality appears, located at the other domain wall. These two chiralities decouple only if the length of the fifth dimension is sent to infinity. For a finite sized fifth dimension, left- and right-handed modes are coupled and exact chiral symmetry is broken. However, their interactions are exponentially suppressed by the length of the fifth dimension so an approximated chiral symmetry is maintained.

This description of chiral symmetry allows the formulation of the domain-wall action on the lattice given by [73, 74]

$$S_F^{\text{dw}}[\Psi, \bar{\Psi}, U] = \sum_{x, y \in \Gamma} \sum_{s, r=0}^{N_5} \bar{\Psi}(x, s) D^{\text{dw}}(x, s; y, r) \Psi(y, r), \quad (2.38)$$

with the domain wall Dirac operator

$$D^{\text{dw}}(x, s; y, r) = \delta_{s,r} D(x; y) + \delta_{x,y} D_5^{\text{dw}}(s; r). \quad (2.39)$$

Here,  $D(x; y)$  is the known Wilson Dirac operator as defined in Eq. (2.28), but the mass term is replaced by a new parameter  $-M_5$  which should be chosen between 0 and 1 to avoid doublers [75]. The domain-wall term  $D_5^{\text{dw}}(s; r)$  is given by

$$D_5^{\text{dw}}(s; r) = \delta_{s,r} - (1 - \delta_{s, N_5-1}) P_L \delta_{s+1, r} - (1 - \delta_{s, 0}) P_R \delta_{s-1, r} \\ + m (P_L \delta_{s, N_5-1} \delta_{0, r} + P_R \delta_{s, 0} \delta_{N_5-1, r}). \quad (2.40)$$

where  $N_5$  is the number of lattice points in the fifth dimension and  $m$  is the mass appearing in the four-dimensional theory [50]. The form of the operator  $D_5^{\text{dw}}$  in Eq. (2.40) guarantees that the boundary conditions in the fifth dimension are fulfilled. Consequently, the five-dimensional fields  $\Psi(x, s)$  obey

$$P_L \Psi(x, N_5) = -m P_L \Psi(x, 0), \\ P_R \Psi(x, -1) = -m P_R \Psi(x, N_5 - 1). \quad (2.41)$$

Note that for large values of  $N_5$  heavy degrees of freedom appear which are removed by introducing pseudofermion fields, also called Pauli-Villars fields [50, 75]. A convenient choice for the associated Dirac operator has the same form as Eq. (2.39), but with

$$D_5^{\text{pf}}(s, r) = D_5^{\text{dw}}(s, r) \Big|_{m=1} \quad (2.42)$$

replacing  $D_5^{\text{dw}}(s, r)$  [75]. For more details about the pseudofermion fields, I refer to Ref. [50].

The powerful property of domain-wall fermions is that fermion doublers can be removed, while simultaneously chiral symmetry breaking is kept exponentially small [77]. However, the additional fifth dimension increases the number of lattice points by a factor of  $N_5$  so that numerical computations become extremely expensive.

### 2.3.4 Staggered Fermions

The staggered formulation of fermions, established by Kogut and Susskind [78], reduces the number of doublers to 4 while in the meantime a remnant chiral symmetry is maintained. The fundamental step is to transform the fermion fields according to

$$\psi(x) = \Gamma(x) \psi'(x), \quad \text{with} \quad \Gamma(x) = \gamma_1^{x_1} \gamma_2^{x_2} \gamma_3^{x_3} \gamma_4^{x_4}, \quad (2.43)$$

which mixes spinor and space-time indices (see Ref. [50]). Inserting the transformed fields governed by Eq. (2.43) in the naive fermion action given in Eq. (2.10), we obtain

$$S_F[\psi', \bar{\psi}'] = a^4 \sum_{x \in \Gamma} \bar{\psi}'(x) \left( \sum_{\mu=1}^4 \eta_\mu(x) \frac{U_\mu(x) \psi'(x + \hat{\mu}) - U_{-\mu}(x) \psi'(x - \hat{\mu})}{2a} + m \psi'(x) \right), \quad (2.44)$$

where  $\eta_\mu$  are scalars which are defined as

$$\eta_1(x) = 1, \quad \eta_2(x) = (-1)^{x_1}, \quad \eta_3(x) = (-1)^{x_1+x_2}, \quad \eta_4(x) = (-1)^{x_1+x_2+x_3}. \quad (2.45)$$

Consequently, Eq. (2.44) is diagonal in Dirac space, while all four components are identical copies. The staggered action is now obtained by keeping only one of the four identical components, e.g.,  $\psi'_1(x)$ , while the other three are discarded. The number of fermion doublers decreases therefore from 16 to 4.

To better understand their physical interpretation and to recover the familiar 4-spinor structure for staggered fermions, one can introduce hypercubes of length 2 which group together 16 lattice sites [79, 80]. Labeling each hypercube by  $h$  and the corners by  $s$ , these new coordinates are related to the original ones by

$$x_\mu = 2h_\mu + s_\mu, \quad (2.46)$$

with  $x_\mu = 0, \dots, N_\mu - 1, \quad h_\mu = 0, \dots, N_\mu/2 - 1, \quad s_\mu = 0, 1,$

where  $N_\mu$  is the number of lattice points in  $\mu$ -direction. Considering the free case, we can now introduce new fields  $\psi_A^{(t)}$  which live on the grid of hypercubes and are defined as

$$\psi_A^{(t)}(h) = \frac{1}{8} \sum_s \Gamma_{At}(s) \psi'_1(2h + s), \quad \bar{\psi}_A^{(t)}(h) = \frac{1}{8} \sum_s \bar{\psi}'_1(2h + s) \Gamma_{At}^*(s), \quad (2.47)$$

where  $A$  is a spinor index and  $t$  will be identified as the taste of the fermion. This gives rise to the free staggered action

$$S_F[q, \bar{q}] = b^2 \sum_h \left( \sum_{t=1}^4 \left( m \bar{\psi}^{(t)}(h) \psi^{(t)}(h) + \sum_\mu \bar{\psi}^{(t)}(h) \gamma_\mu \nabla_\mu \psi^{(t)}(h) \right) - \frac{b}{2} \sum_{t,t'=1}^4 \sum_\mu \bar{\psi}^{(t)}(h) \gamma_5 (\tau_5 \tau_\mu)_{tt'} \nabla_\mu^{(2)} \psi^{(t')}(h) \right), \quad (2.48)$$

with  $\tau_\mu = \gamma_\mu^T$  and  $\nabla_\mu$  and  $\nabla_\mu^{(2)}$  being the first and second lattice derivative as defined in Appendix A but with the hypercubic lattice spacing  $b = 2a$ . Here, we observe four different types of quarks, called tastes of staggered fermions, labeled by  $t = 1, \dots, 4$ . While the first two terms of Eq. (2.48), corresponding to a mass and kinetic term, are diagonal in taste, the third term mixes the different tastes of quarks and subsequently breaks the taste symmetry. Remember that taste originates from doublers and thus is unphysical. However, the major problem is not the presence of several tastes as long as these are decoupled [81, 82], but rather the existence of large taste changing interactions which are absent in real QCD.

The discretization errors of the staggered action are  $\mathcal{O}(a^2)$  as chiral symmetry is maintained [81]. These  $\mathcal{O}(a^2)$  errors are, however, unusually large and have two different sources, first the discretization of the derivatives, and second taste exchange interactions associated to the taste mixing term in Eq. (2.48). While the errors originating from discretizing the derivatives can be easily removed exploiting the Naik term [83], a rigorous treatment of  $\mathcal{O}(a^2)$  taste exchange terms has been carried out in Refs. [81, 82] to remove also errors arising due to taste mixing. A quite accurate formulation of staggered quarks is the *highly improved staggered quark* (HISQ) action which is derived in Ref. [82] and used for computations with staggered quarks in this work (see Chapters 6 to 8).

A huge advantage of the staggered fermion action is that it can be simulated faster than other fermion actions, while relying on the HISQ formulation it is still a quite accurate discretization [82]. The preservation of chiral symmetry, however, comes at the cost of introducing additional tastes of fermions which must be treated in a proper way as discussed above.

### 2.3.5 Mixed Action Setup

In QCD one distinguishes between sea quarks and valence quarks. Sea quarks describe virtual quark-antiquark pairs which are permanently created and annihilated, while valence quarks are those quarks which are the constituents of the hadron. In lattice QCD, sea quarks are incorporated by including a specific fermion action in the QCD action that is utilized to generate the gauge link configurations as discussed in Secs. 2.1.2 and 2.1.3. The valence quarks are introduced directly as fermion fields in lattice observables. As these fields, which appear in fermionic expectation values, are contracted according to Wick's theorem in Eq. (2.20), they are expressed by quark propagators. The quark propagators in turn are computed by inverting the Dirac operator of a specific fermion action.

In general, the same fermion action is used for incorporating the sea and valence quarks. However, it is also possible to use different fermion actions for the generation of gauge link configurations and the computation of the quark propagator. This is called a *mixed action* setup. In order to obtain a well-defined continuum limit, the two actions must be matched. This can be achieved by demanding that the pion mass is equal in both actions [84, 85]. Even if this matching is done properly, the eigen-

value spectrum of the sea and valence Dirac operators differ. For small quark masses this can cause problems arising from so-called exceptional configurations. These are configurations for which the valence Dirac operator has small eigenvalues and consequently the numerical inversion breaks down. In a setup with same sea and valence quark action, such exceptional configurations are suppressed during the generation of the gauge configurations [86]. For computations using mixed-action setups in practice, it is thus mandatory to ensure that the used ensemble does not suffer from such exceptional configurations for the given valence quark action.

## 2.4 Effective Theories for Heavy Quarks

Lattice computations facing heavy quarks like the bottom quark require some special techniques since the Compton wavelength  $\lambda_{\text{Compton}} \propto 1/m_Q$  of a heavy quark is in general smaller than a typical lattice spacing and thus heavy quarks cannot be resolved reliably. For example, for a bottom quark with mass  $m_b = 4.18_{-0.02}^{+0.03}$  GeV in the  $\overline{\text{MS}}$  scheme [87], one would require a lattice spacing  $a < 0.04$  fm, while nowadays commonly used lattices have lattice spacings of order 0.05 fm to 0.2 fm. Accordingly, relativistic fermion actions as discussed in Sec. 2.3 are only applicable for quarks fulfilling  $am_Q < 1$  which is obviously not the case for bottom quarks.

One major contribution to the masses of heavy mesons are the valence quark masses themselves. Thus, the basic strategy of an effective theory for heavy quarks is to separate the different energy scales  $|\mathbf{p}_Q| \ll m_Q$ , where  $m_Q$  denotes the heavy quark mass and  $|\mathbf{p}_Q|$  the relevant spatial momentum. In this way, the valence quark mass contribution can be removed and higher energy contributions can be treated perturbatively so that numerical calculations involving heavy quarks are feasible on recent lattices. One successful way to describe heavy quarks on the lattice is constructing an effective non-relativistic Lagrangian. The subsequent discussion of this effective Lagrangian is based on Refs. [88–90].

### 2.4.1 Dynamics of Heavy Quark Systems

In order to understand how to separate the energy scales, it is essential to consider the dynamics of heavy quarks. The power counting differs for systems containing only one heavy quark and systems containing at least two heavy quarks [89, 90]. The dynamics of the light degrees of freedom and gluons is described by the QCD scale  $\Lambda_{\text{QCD}}$ , while heavy quarks introduce another scale as their dynamics is mainly governed by their mass  $m_Q$ .

In systems containing only one heavy quark, the momentum transfer is of order  $\Lambda_{\text{QCD}}$ . As  $\Lambda_{\text{QCD}} \ll m_Q$ , the dynamics of the heavy quark is hardly influenced by the light degrees of freedom, and the motion of the heavy quark is suppressed by  $(\Lambda_{\text{QCD}}/m_Q)$ . This makes  $(\Lambda_{\text{QCD}}/m_Q)$  a good expansion parameter for these systems.

For systems consisting of at least two heavy quarks, their dynamics is different as their movement is mainly governed by their orbital movement around their center of masses. The orbital velocity  $v$  is given for bottomonium by  $v^2 \sim 0.1$  and for charmonium by

$v^2 \sim 0.3$ , which is based on the  $2S - 1S$  energy splitting [88]. Hence the dynamics of the quarks is described by three different energy scales: the mass of the heavy quarks  $m_Q$ , their spatial momentum  $|\mathbf{p}_Q| \sim m_Q v$ , and the kinetic energy scale  $E_{\text{kin}} \sim m_Q v^2$ . The appropriate expansion coefficient for such systems is therefore  $v$ .

I will continue this discussion of the power counting in Sec. 2.4.3 after recapitulating the derivation of the NRQCD Lagrangian in the next paragraph.

### 2.4.2 Foldy-Wouthuysen-Tani Transformation

The heavy quark effective Lagrangian for the continuum can be derived using the Foldy-Wouthuysen-Tani (FWT) transformation. In this section, I will follow the derivation in Ref. [91] which has also been carried out in detail in Refs. [90,92,93]. The underlying idea is to transform the fermion fields in such a way that contributions of  $\mathcal{O}(1/m_Q^n)$  in the Lagrangian are removed up to desired order  $n$ . Note that expanding in orders of  $1/m_Q$  is only formal. As discussed in the previous section, the power counting and consequently the expansion parameter depends on the actual number of heavy quarks. For systems with a single heavy quark where the expansion parameter is  $(\Lambda_{\text{QCD}}/m_Q)$ , it is obviously a convenient choice to expand in orders of  $1/m_Q$ . Even though the power counting is different for heavy-heavy systems, expanding in orders of  $1/m_Q$  is still adequate. I will illustrate this in more detail in Sec. 2.4.3.

The Foldy-Wouthuysen-Tani transformation decouples particle and antiparticle components of the Dirac Lagrangian  $\mathcal{L}$  up to a given order of  $1/m_Q$ . As the particle/antiparticle projectors are given by

$$P_{\pm} = \frac{1}{2}(1 \pm \gamma_0), \quad (2.49)$$

a transformation decoupling particle and antiparticle components must remove all terms that do not commute with  $\gamma_0$ . Accordingly, considering the Dirac Lagrangian in Minkowski space,

$$\mathcal{L} = \bar{\psi} \left( i\hat{\gamma}_0 D^0 + i\hat{\gamma}_j D^j - m_Q \right) \psi, \quad (2.50)$$

the term  $i\hat{\gamma}_j D^j$  needs to vanish. This is achieved by the first field transformation which writes

$$\begin{aligned} \psi &= \exp\left(\frac{1}{2m_Q} i\hat{\gamma}_j D^j\right) \psi_{(1)}, \\ \bar{\psi} &= \bar{\psi}_{(1)} \exp\left(\frac{1}{2m_Q} i\hat{\gamma}_j D^j\right). \end{aligned} \quad (2.51)$$

This transformation cancels the non-commuting term  $i\hat{\gamma}_j D^j$  but introduces an infinite number of terms in higher powers of  $1/m_Q$ . Consequently, the Lagrangian expressed in terms of the new fields is given by

$$\mathcal{L} = \bar{\psi}_{(1)} \left( i\hat{\gamma}_0 D^0 - m \right) \psi_{(1)} + \sum_{n=1}^{\infty} \frac{1}{m_Q^n} \bar{\psi}_{(1)} \mathcal{O}_{(1),n} \psi_{(1)}. \quad (2.52)$$

Eq. (2.52) is obtained by expanding the exponentials in Eq. (2.51) in Taylor series. In this manner, the sub-leading term of  $\mathcal{O}(1/m_Q)$  is found to be

$$O_{(1),1} = -\frac{1}{2}D_j D^j - \frac{ig}{8} [\hat{\gamma}_\mu, \hat{\gamma}_\nu] F^{\mu\nu}, \quad (2.53)$$

with the field strength tensor  $F^{\mu\nu}$  defined as

$$[D^\mu, D^\nu] = ig F^{\mu\nu}. \quad (2.54)$$

For a step-by-step derivation of Eqs. (2.52) and (2.53), I refer to Ref. [92].

In order to further improve the Lagrangian up to  $\mathcal{O}(1/m_Q^2)$ , non-commuting terms appearing in  $O_{(1),1}$  need to be canceled. I split  $O_{(1),1}$  in a commuting part  $O_{(1),1}^C$  and an anti-commuting part  $O_{(1),1}^A$ ,

$$O_{(1),1} = \underbrace{-\frac{1}{2}D_j D^j - \frac{ig}{8} [\hat{\gamma}_i, \hat{\gamma}_j] F^{ij}}_{=O_{(1),1}^C} - \underbrace{\frac{ig}{2} [\hat{\gamma}_j, \hat{\gamma}_0] F^{j0}}_{=O_{(1),1}^A}. \quad (2.55)$$

To cancel the anti-commuting term  $O_{(1),1}^A$ , a second field transformation according to

$$\begin{aligned} \psi_{(1)} &= \exp\left(\frac{1}{2m_Q^2} O_{(1),1}^A\right) \psi_{(2)}, \\ \bar{\psi}_{(1)} &= \bar{\psi}_{(2)} \exp\left(\frac{1}{2m_Q^2} O_{(1),1}^A\right), \end{aligned} \quad (2.56)$$

is performed. The Lagrangian for the fields  $\psi_{(2)}$ ,  $\bar{\psi}_{(2)}$  consequently reads

$$\mathcal{L} = \bar{\psi}_{(2)} \left( i\hat{\gamma}_0 D^0 - m \right) \psi_{(2)} + \frac{1}{m_Q} \bar{\psi}_{(2)} O_{(1),1}^C \psi_{(2)} + \sum_{n=2}^{\infty} \frac{1}{m_Q^n} \bar{\psi}_{(2)} \mathcal{O}_{(2),n} \psi_{(2)}. \quad (2.57)$$

The anti-commuting term of  $\mathcal{O}(1/m_Q)$  has vanished, and the next anti-commuting term appears in  $\mathcal{O}(1/m_Q^2)$ . To cancel also the  $\mathcal{O}(1/m_Q^2)$  contributions, one proceeds in the same way as for  $\mathcal{O}(1/m_Q)$ . First, the operator  $\mathcal{O}_{(2),2}$  is expressed in terms of a commuting part  $\mathcal{O}_{(2),2}^C$  and an anti-commuting part  $\mathcal{O}_{(2),2}^A$ . Then, another field transformation defined by

$$\begin{aligned} \psi_{(2)} &= \exp\left(\frac{1}{2m_Q^3} O_{(2),2}^A\right) \psi_{(3)}, \\ \bar{\psi}_{(2)} &= \bar{\psi}_{(3)} \exp\left(\frac{1}{2m_Q^3} O_{(2),2}^A\right), \end{aligned} \quad (2.58)$$

is carried out, yielding a Lagrangian which contains only commuting terms up to  $\mathcal{O}(1/m_Q^2)$ . This procedure can be repeated up to the desired order in  $1/m_Q^n$ . Here, I

stop at the given order of  $\mathcal{O}(1/m_Q^2)$ . In a final step, the mass term in the Lagrangian can be eliminated by the field transformation

$$\begin{aligned}\psi_{(3)} &= \exp(-im_Q \hat{\gamma}_0 x_0) \tilde{\psi}, \\ \bar{\psi}_{(3)} &= \tilde{\bar{\psi}} \exp(im_Q \hat{\gamma}_0 x_0),\end{aligned}\tag{2.59}$$

since the operators  $O_{(n),n}^C$  commute with  $\hat{\gamma}_0$  and apart from  $i\hat{\gamma}_0 D^0$  no time derivatives appear. Consequently, the resulting Lagrangian is given by

$$\begin{aligned}\mathcal{L} = \tilde{\bar{\psi}} &\left[ i\hat{\gamma}_0 D^0 - \frac{1}{2m_Q} D_j D^j - \frac{ig}{8m_Q} [\hat{\gamma}_i, \hat{\gamma}_j] F^{ij} \right. \\ &\left. - \frac{g}{8m_Q^2} \hat{\gamma}_0 \left( (D^j)^* F^{j0} - \frac{1}{2} [\hat{\gamma}_i, \hat{\gamma}_j] \{D^i, F^{j0}\} \right) \right] \tilde{\psi} + \mathcal{O}\left(\frac{1}{m_Q^3}\right),\end{aligned}\tag{2.60}$$

where I inserted  $O_{(1),1}^C$  and  $O_{(2),2}^C$  explicitly.

It can be observed that Eq. (2.60) is block-diagonal, so consequently the particle and antiparticle solution decouple as desired. We can write the fields  $\tilde{\psi}$ ,  $\tilde{\bar{\psi}}$  in a two component representation using

$$\tilde{\psi} = \begin{pmatrix} \psi_h \\ \chi_h \end{pmatrix}, \quad \tilde{\bar{\psi}} = \left( \psi_h^\dagger, \quad -\chi_h^\dagger \right),\tag{2.61}$$

where  $\psi_h$  are the quark fields and  $\chi_h$  are the antiquark fields. Moreover, identifying the chromoelectric and chromomagnetic fields as

$$E_i = F_{0i} \quad \text{and} \quad B_i = -\frac{1}{2} \epsilon_{ijk} F_{jk}\tag{2.62}$$

and using

$$[\hat{\gamma}_i, \hat{\gamma}_j] = -2i \epsilon_{ijk} \Sigma_k \quad \text{with} \quad \Sigma_k = \begin{pmatrix} \sigma_k & 0 \\ 0 & \sigma_k \end{pmatrix},\tag{2.63}$$

the Lagrangian is finally given by

$$\begin{aligned}\mathcal{L} = &\psi_h^\dagger \left[ iD^0 + \frac{\mathbf{D}^2}{2m_Q} + \frac{g \boldsymbol{\sigma} \cdot \mathbf{B}}{2m_Q} + \frac{g}{8m_Q^2} \left( \mathbf{D}^* \cdot \mathbf{E} + i \boldsymbol{\sigma} \cdot (\mathbf{D} \times \mathbf{E} - \mathbf{E} \times \mathbf{D}) \right) \right] \psi_h \\ &+ \chi_h^\dagger \left[ iD^0 - \frac{\mathbf{D}^2}{2m_Q} - \frac{g \boldsymbol{\sigma} \cdot \mathbf{B}}{2m_Q} + \frac{g}{8m_Q^2} \left( \mathbf{D}^* \cdot \mathbf{E} + i \boldsymbol{\sigma} \cdot (\mathbf{D} \times \mathbf{E} - \mathbf{E} \times \mathbf{D}) \right) \right] \chi_h \\ &+ \mathcal{O}\left(\frac{1}{m_Q^3}\right).\end{aligned}\tag{2.64}$$

### 2.4.3 Power Counting

As the expansion parameter  $1/m_Q$  which has been used deriving the effective Lagrangian Eq. (2.64) in Sec. 2.4.2 is purely formal, one needs to distinguish between systems containing one heavy quark and systems with at least two heavy quarks as discussed in Sec. 2.4.1.

Remember that the motion of a heavy quark at rest in heavy-light systems is suppressed by  $(\Lambda_{\text{QCD}}/m_Q)$ . Additionally, the momentum transfer as well as the gluon dynamics are governed by  $\Lambda_{\text{QCD}}$ , so that the covariant derivatives are of order

$$|D^0| \sim |\mathbf{D}| \sim \Lambda_{\text{QCD}}, \quad (2.65)$$

and the gauge field potentials as well,

$$|g A^0| \sim |g \mathbf{A}| \sim \Lambda_{\text{QCD}}. \quad (2.66)$$

The chromoelectric and chromomagnetic fields are hence of order

$$|g \mathbf{E}| \sim |g \mathbf{B}| \sim \Lambda_{\text{QCD}}^2. \quad (2.67)$$

Comparing Eqs. (2.65) to (2.67) with the effective Lagrangian in Eq. (2.64) reveals that a term which appears in order  $1/m_Q^n$  is indeed suppressed by  $(\Lambda_{\text{QCD}}/m_Q)^n$  compared to the leading contribution.

For systems with at least two heavy quarks, their motion is mainly governed by the orbital movement around the center of masses with velocity  $v$ , while the relevant scales are the spatial momentum and the kinetic energy

$$|\mathbf{p}_Q| \sim m_Q v, \quad E_{\text{kin}} \sim m_Q v^2. \quad (2.68)$$

The spatial and temporal covariant derivatives acting on gauge fields are of order [94]

$$|\mathbf{D}| \sim m_Q v \quad \text{and} \quad |D^0| \sim m_Q v^2. \quad (2.69)$$

Using the lowest order field equation in Coulomb gauge, it is found that the potential energy is of same order as the kinetic energy [94], so

$$|g A^0| \sim m_Q v^2. \quad (2.70)$$

Finally, the vector potential is found to be of order [94]

$$|g \mathbf{A}| \sim m_Q v^3 \quad (2.71)$$

and consequently

$$|g \mathbf{E}| \sim m_Q^2 v^3 \quad \text{and} \quad |g \mathbf{B}| \sim m_Q^2 v^4. \quad (2.72)$$

Comparing these expressions with the terms appearing in the Lagrangian in Eq. (2.64), we observe that all contributions to the Lagrangian are suppressed by certain orders



of  $v^2$ . Thus, the formal expansion in  $1/m_Q$  is suited for systems with more than one heavy quark and  $v^2$  is proved to be the correct expansion parameter as discussed in Sec. 2.4.1. Eq. (2.64) contains only terms up to  $\mathcal{O}(v^4)$ , however, one term is missing. This can easily be seen by expanding the relativistic expression of the kinetic energy in terms of the momentum,

$$E_{\text{kin}} = \sqrt{m_Q^2 + \mathbf{p}_Q^2} - m_Q = \frac{\mathbf{p}_Q^2}{2m_Q} - \frac{\mathbf{p}_Q^4}{8m_Q^3} + \mathcal{O}(\mathbf{p}_Q^6). \quad (2.73)$$

While the first term is included in Eq. (2.64), the second term, which is  $\mathcal{O}(v^4)$ , is missing. Including this term yields the non-relativistic (NRQCD) Lagrangian for quark fields

$$\begin{aligned} \mathcal{L}_{\text{NRQCD}} = \psi_h^\dagger & \left[ iD^0 + \frac{\mathbf{D}^2}{2m_Q} + \frac{g\boldsymbol{\sigma} \cdot \mathbf{B}}{2m_Q} + \frac{\mathbf{D}^4}{8m_Q^3} \right. \\ & \left. + \frac{g}{8m_Q^2} \left( \mathbf{D}^* \cdot \mathbf{E} + i\boldsymbol{\sigma} \cdot (\mathbf{D} \times \mathbf{E} - \mathbf{E} \times \mathbf{D}) \right) \right] \psi_h + \mathcal{O}(v^6), \end{aligned} \quad (2.74)$$

which includes all terms up to corrections of  $\mathcal{O}(v^6)$ . A detailed discussion of power counting and contributions in higher order in  $v^2$  can be found in Ref. [94]. Note that Eq. (2.74) can be applied for heavy-light as well as heavy-heavy systems. As discussed above, Eq. (2.74) is accurate up to  $\mathcal{O}(v^4)$  for systems with at least two quarks and still up to order  $(\Lambda_{\text{QCD}}/m_Q)^2$  for heavy-light systems.

#### 2.4.4 Euclidean Green Function

To apply the NRQCD formalism in lattice calculations, the Euclidean formulation of the NRQCD Lagrangian is required. This is obtained by replacing the derivatives and chromoelectric and chromomagnetic fields expressed in Minkowski space by their Euclidean counterparts. The only two terms that introduce additional factors are

$$D_{(M)}^0 = iD_{(E)}^0 \quad \text{and} \quad E_{(M)}^j = -iE_{(E)}^j, \quad (2.75)$$

where the index  $(M)$  labels Minkowski space and  $(E)$  Euclidean space. Consequently, the Euclidean lattice NRQCD Lagrangian (omitting the index  $(E)$ ) reads

$$\begin{aligned} \mathcal{L}_{\text{NRQCD}} = \psi_h^\dagger & \left[ \nabla_0 - \frac{\Delta^{(2)}}{2m_Q} - \frac{g\boldsymbol{\sigma} \cdot \mathbf{B}}{2m_Q} - \frac{(\Delta^{(2)})^2}{8m_Q^3} \right. \\ & \left. + \frac{ig}{8m_Q^2} \left( \nabla^* \cdot \mathbf{E} + i\boldsymbol{\sigma} \cdot (\nabla \times \mathbf{E} - \mathbf{E} \times \nabla) \right) \right] \psi_h + \mathcal{O}(v^6). \end{aligned} \quad (2.76)$$

This Lagrangian can be written in short as

$$\mathcal{L}_{\text{NRQCD}} = \psi_h^\dagger \left[ \nabla_0 + H \right] \psi_h, \quad (2.77)$$

so that the associated Green function must obey

$$\left[ \nabla_0 + H \right] G_{\psi_h}(x; x') = \delta^4(x, x'). \quad (2.78)$$

A convenient way to solve Eq. (2.78) is the temporal Green function evolution equation given by [90, 94]

$$\begin{aligned} G_{\psi_h}(\mathbf{x}, x_0; \mathbf{y}, y_0) &= \left( 1 - \frac{\delta H|_{x_0}}{2} \right) \left( 1 - \frac{H_0|_{x_0}}{2n} \right)^n U_0^\dagger(\mathbf{x}, x_0 - a) \\ &\times \left( 1 - \frac{H_0|_{x_0-a}}{2n} \right)^n \left( 1 - \frac{\delta H|_{x_0-a}}{2} \right) G_{\psi_h}(\mathbf{x}, x_0 - a; \mathbf{y}, y_0). \end{aligned} \quad (2.79)$$

This is the so-called retarded Green function as it describes quark fields and vanishes for  $x_0 < y_0$ . The Green function for antiquark fields can be easily obtained from Eq. (2.79) via [90]

$$G_{\psi_h}(\mathbf{x}, x_0; \mathbf{y}, y_0) = -G_{\chi_h}(\mathbf{y}, y_0; \mathbf{x}, x_0)^\dagger. \quad (2.80)$$

Combining the quark and antiquark Green function, the heavy quark propagator in 4-spinor notation is consequently given by

$$G_h(\mathbf{x}, x_0; \mathbf{y}, y_0) = \Theta(x_0 - y_0) \begin{pmatrix} G_{\psi_h}(\mathbf{x}, x_0; \mathbf{y}, y_0) & 0 \\ 0 & 0 \end{pmatrix} - \Theta(-x_0 + y_0) \begin{pmatrix} 0 & 0 \\ 0 & G_{\chi_h}(\mathbf{x}, x_0; \mathbf{y}, y_0) \end{pmatrix}. \quad (2.81)$$

Let us have a closer look at the Green function in Eq. (2.79).  $H_0$  contains the kinetic term of leading order  $\mathcal{O}(v^2)$  and is given by

$$H_0 = -\frac{\Delta^{(2)}}{2m_Q}. \quad (2.82)$$

The integer  $n$  is introduced to avoid instabilities due to high momenta [94]. The term  $\delta H$  contains all contributions in higher order of  $v$  including also Symanzik improvement terms. Splitting the contributions in  $\mathcal{O}(v^4)$  and  $\mathcal{O}(v^6)$  terms, we obtain

$$\delta H = \delta H_{v^4} + \delta H_{v^6} \quad (2.83)$$

with

$$\begin{aligned} \delta H_{v^4} &= -c_1 \frac{(\Delta^{(2)})^2}{8m_Q^3} + c_2 \frac{ig}{8m_Q^2} (\nabla \cdot \tilde{\mathbf{E}} - \tilde{\mathbf{E}} \cdot \nabla) - c_3 \frac{g}{8m_Q^2} \boldsymbol{\sigma} (\tilde{\nabla} \times \tilde{\mathbf{E}} - \tilde{\mathbf{E}} \times \tilde{\nabla}) \\ &\quad - c_4 \frac{g}{2m_Q} \boldsymbol{\sigma} \cdot \tilde{\mathbf{B}} + c_5 \frac{\Delta^{(4)}}{24m_Q} - c_6 \frac{(\Delta^{(2)})^2}{16nm_Q^2} \end{aligned} \quad (2.84)$$

and

$$\begin{aligned} \delta H_{v^6} = & -c_7 \frac{g}{8m_Q^3} \left\{ \Delta^{(2)}, \boldsymbol{\sigma} \cdot \tilde{\mathbf{B}} \right\} - c_8 \frac{3g}{64m_Q^4} \left\{ \Delta^{(2)}, \boldsymbol{\sigma} \left( \tilde{\nabla} \times \tilde{\mathbf{E}} - \tilde{\mathbf{E}} \times \tilde{\nabla} \right) \right\} \\ & - c_9 \frac{ig^2}{8m_Q^3} \boldsymbol{\sigma} \tilde{\mathbf{E}} \times \tilde{\mathbf{E}}. \end{aligned} \quad (2.85)$$

The chromoelectric and chromomagnetic fields  $\mathbf{E}$  and  $\mathbf{B}$  are replaced by their Symanzik improved counterparts  $\tilde{\mathbf{E}}$  and  $\tilde{\mathbf{B}}$  as defined in Appendix A of Ref. [90]. The same holds for the improved derivatives  $\tilde{\nabla}$  which can be also found in Appendix A of Ref. [90]. The coefficients  $c_i$  are the matching coefficients which should be chosen such that the effective theory matches full QCD. A reasonable way of matching the parameters perturbatively is using tadpole improvement for the underlying gauge fields [71]. This is achieved by dividing all gauge links by the tadpole parameter  $u_0$ , while a convenient choice for  $u_0$  is the mean link in Landau gauge  $u_{0L}$  [71, 95]. Using tadpole improvement, one possibility is to set the matching coefficients to their tree-level value  $c_i = 1$ . Throughout this work, I use a heavy quark Green function, which is accurate up to  $\mathcal{O}(v^4)$ , so the matching coefficients associated with  $\delta H_{v^6}$  are set to zero,  $c_7 = c_8 = c_9 = 0$ . The actual choice of the other matching coefficients that are used for the investigations carried out in this work is discussed in the corresponding chapter (see Chapters 5 and 6).

## 2.5 Relativistic Heavy Quark Action

Nowadays, there exist also approaches that treat heavy quarks in a relativistic framework. As lattice discretization effects become large for  $am_Q \gtrsim 1$  while the non-relativistic expansion breaks down for  $am_Q \lesssim 1$ , this is especially useful for charm quarks where  $am_Q \approx 1$  on commonly used lattices but also for heavier quarks when moving to smaller lattice spacings. A well-established approach to treating heavy quarks relativistically is the so-called *Fermilab method* [96, 97], where the basic idea is to tune the bare quark mass and the coupling of spatial and temporal terms in the heavy quark action such that the heavy quark dispersion relation is correctly reproduced. The Fermilab method has been applied in several slightly different variants [49, 96–106], while the general form of the Fermilab action is an anisotropic clover action according to

$$\begin{aligned} S_{\text{rel. heavy}} = & a^4 \sum_{x \in \Gamma} \bar{\psi}(x) \left[ m_Q + \gamma_0 \nabla_0 - \frac{a}{2} \nabla_0^{(2)} + \zeta \sum_{i=1}^3 \left( \gamma_i \nabla_i - \frac{a}{2} \nabla_i^{(2)} \right) \right. \\ & \left. - c_e \frac{a}{2} \sum_{i=1}^3 \sigma_{0i} \hat{F}_{0i}(x) - c_B \frac{a}{4} \sum_{i,j=1}^3 \sigma_{ij} \hat{F}_{ij}(x) \right] \psi(x). \end{aligned} \quad (2.86)$$

Here,  $\nabla_\mu$  and  $\nabla_\mu^{(2)}$  denote the first and second covariant lattice derivative in direction  $\mu$  as defined in Eq. (A.3). In contrast to the isotropic clover action given in Eq. (2.32)

which has two parameters, the anisotropic clover action has four parameters which are the bare quark mass  $m_Q$ , the anisotropy  $\zeta$ , and the chromoelectric and chromomagnetic coefficients  $c_E$  and  $c_B$ . Considering the coefficients  $\zeta$ ,  $c_E$  and  $c_B$  as functions of  $am_Q$  and tuning all four parameters appropriately, discretization errors of order  $a|\mathbf{p}|$ ,  $(am_Q)^n$  and  $a|\mathbf{p}|(am_Q)^n$  can be eliminated [105].

In this work, I rely on two different variations of the Fermilab action. The first variant uses the same parameter for the chromoelectric and chromomagnetic coefficients,  $c_E = c_B = c_P$ , and tunes the remaining three parameters, the mass  $am_Q$ , the anisotropy parameter  $\zeta$ , and the clover coefficient  $c_P$  in an appropriate way. This approach has been utilized, e.g., in Refs. [96, 101, 105]. The second approach which is the simplest variant of the Fermilab action fixes the anisotropy to unity and sets the clover coefficient to its tree-level value with tadpole improvement,  $c_E = c_B = c_{\text{sw}} = 1/u_0^3$ , where  $u_0$  is the mean link. The single remaining parameter is the bare quark mass  $am_Q$  which is related to the so-called hopping parameter  $\kappa_Q$  according to  $2\kappa_Q = 1/(am_Q + 4)$  and is finally tuned non-perturbatively. This has been applied, e.g., in Refs. [49, 103, 104, 106].

## 2.6 Statistical and Systematic Uncertainties

Lattice calculations provide a first principle approach to computing QCD observables. While the path integral formulation in the continuum discussed in Sec. 2.1.2 is exact, computing observables in lattice QCD introduces statistical and systematic errors which can, however, be estimated or controlled.

### 2.6.1 Estimating Statistical Uncertainties

Statistical uncertainties arise as only a limited number of possible paths of the path integral formulation are considered. Those paths are governed by the gauge field configurations which are generated according to a Monte-Carlo sampling (see Sec. 2.1.3). Using this set of gauge field configurations, one can determine the expectation value of an observable and its statistical error. Reasonable approaches to computing this statistical uncertainty are the jackknife or the bootstrap methods, which are closely related to each other. In both cases, one considers the  $N$  measurements of an observable  $X$  which are given by the data set  $\{X_i\}$ . The mean value  $\hat{X}$  obtained from these  $N$  measurements is given by

$$\hat{X} = \frac{1}{N} \sum_{i=1}^N X_i. \quad (2.87)$$

#### 2.6.1.1. Jackknife method

In order to compute the Jackknife error of the observable  $X$ , one draws  $N$  so-called Jackknife samples  $\tilde{X}_n$  by removing the  $n$ -th entry of the data set  $\{X_i\}$  and computing the mean value of this reduced sample,

$$\tilde{X}_n = \frac{1}{N-1} \sum_{i \neq n}^N X_i. \quad (2.88)$$

An estimate for the statistical error  $\sigma_{\hat{X}}$  is finally obtained via

$$\sigma_{\hat{X}}^2 = \frac{N-1}{N} \sum_{n=1}^N (\tilde{X}_n - \hat{X})^2 \quad (2.89)$$

so that the expectation value for the observable  $X$  can be expressed as  $\langle X \rangle = \hat{X} \pm \sigma_{\hat{X}}$ .

### 2.6.1.2. Bootstrap method

An alternative approach to estimating the statistical uncertainty is provided by the bootstrap method. In this case a set of  $K$  samples is created by choosing randomly  $N$  data points from the original set  $\{X_i\}$ . For each of the  $K$  new samples, the mean value  $\tilde{X}_k$  is determined. An estimate for the expectation value of  $X$  is computed as

$$\tilde{X} = \frac{1}{K} \sum_{k=1}^K \tilde{X}_k \quad (2.90)$$

with the associated bootstrap error

$$\sigma_{\tilde{X}}^2 = \frac{1}{K} \sum_{k=1}^K (\tilde{X}_k - \tilde{X})^2. \quad (2.91)$$

In analogy to the jackknife method, the expectation value for the observable is then quoted as  $\langle X \rangle = \tilde{X} \pm \sigma_{\tilde{X}}$ .

Both methods assume that the data set  $\{X_i\}$  is uncorrelated. If this is not the case, an efficient method is to bin the data by dividing it into sub-blocks of fixed size and computing their mean values. These means serve then as a new data set which is used to compute the statistical error.

If the number of uncorrelated data points  $N$  is increased, which is equivalent to increasing the number of gauge field configurations, the statistical error decreases like  $1/\sqrt{N}$ .

## 2.6.2 Systematic Uncertainties

The formulation of QCD on the lattice introduces systematic errors due to the finite volume, the discretized space-time, and unphysical heavy quark masses. In principle, these sources of systematic error can be controlled. This can be done by investigating the dependence of a QCD observable, e.g., the mass of a hadron, on the spatial volume, the lattice spacing and the pion mass.

### 2.6.2.1. Discretization Errors

The first source of systematic errors arises due to the discretized space-time. The lattice actions for the gluon and fermion fields which have been discussed in Secs. 2.2

and 2.3 are only accurate up to a specific order in the lattice spacing  $a$ . Consequently, the same holds also for a lattice observable computed with these actions, so the lattice QCD result depends on the lattice spacing  $a$ . Results for continuum space-time are obtained if one approaches the limit  $a \rightarrow 0$ , which is the so-called continuum limit. Decreasing the lattice spacing, however, shrinks also the physical volume of the box if the number of lattice points  $N_s$  and  $N_t$  is kept constant. To maintain the physical volume when approaching the continuum limit, the number of lattice points must be increased accordingly which results in increasing the numerical costs. A reasonable way to study the  $a$ -dependence of an observable is to compute the expectation value for different lattice spacings  $a$ , while the physical volume is preserved and perform a continuum extrapolation to  $a = 0$ .

### 2.6.2.2. Finite Volume Effects

Systematic errors are also introduced by the finite size of the lattice. Due to the periodic boundary conditions, interactions around the spatial torus appear. These are governed by the mass of the lightest meson, the pion, and are exponentially suppressed according to  $\exp(-m_\pi L)$  [107]. In general, these effects are negligible if  $m_\pi L \gtrsim 4$ , which is the case for most modern lattices. Additionally, for a hadronically stable state the spatial volume must be large enough to accommodate this particle. If the volume were too small, the wave function would be influenced by the boundaries of the box and the energy spectrum would change. In practice, a physical box size  $\gtrsim 3$  fm turned out to be sufficiently large.

For multi-particle states, however, finite volume effects play a crucial role and influence the energy levels also for rather large box sizes. The energy spectrum for such states differs significantly from the infinite volume case as the finite box discretizes the previously continuous spectrum of scattering states. This problem has been addressed by M. Lüscher, who related the finite spectrum to infinite volume quantities [22], and will be exhaustively discussed in Chapter 3.

### 2.6.2.3. Unphysical heavy quark masses

A further adjustment that is usually applied in lattice calculations is choosing a heavier than physical light quark mass. In practice, a good indicator for the light quark masses is the pion since it consists exclusively of two light quarks. While at the physical point, the pion mass is given by  $m_{\pi,\text{phys.}} \simeq 135$  MeV, lattice calculations often use pion masses in the region of 200 MeV to 300 MeV.

Whereas the first two sources of systematic errors originate directly from establishing QCD on the lattice, this adjustment is motivated by practical reasons as computations for small pion masses are expensive or in some cases even problematic. Choosing a small pion mass requires extremely large lattices to keep finite size effects due to interactions around the torus negligible. Additionally, the computation of the quark propagator which involves inverting the Dirac operator (see Sec. 4.4) is numerically

more expensive for small quark masses. Finally, small quark masses can also lead to problematic gauge field configurations, the so-called exceptional configurations (see Sec. 2.3.5). These can appear for some fermion discretizations if small pion masses lead to zero eigenvalues of the Dirac operator.

In order to avoid such problems and keep the numerical costs within acceptable limits, it is a common strategy to determine the expectation value of an observable for several heavier-than-physical pion masses and extrapolate the results to the physical point, which is often referred to as chiral extrapolation.

Throughout this work all three sources of systematic errors will be addressed. All computations are performed on several gauge link ensembles which differ in the pion mass, the lattice spacing, and the physical volume. For all systems considered in this work, I will perform a chiral extrapolation to the physical point if feasible and discuss possible implications of discretization effects. Additionally, I apply Lüscher's method to extrapolate results to the infinite volume, if necessary.





# 3

---

## TWO-PARTICLE STATES IN THE FINITE VOLUME

---

Within the last decades, a large number of previously unknown hadrons have been found in experiments. While some of them are stable with respect to the strong interaction, the majority are resonances with rather short lifetimes. This poses new challenges for a theoretical formulation of such unstable states as additionally to the binding also the decay process must be encoded. Lattice QCD as a non-perturbative approach provides a framework for dealing with both stable and resonant states. However, the finite volume of the lattice complicates studying resonances. While hadronically stable states appear as eigenstates of QCD with a discrete energy, resonances are enhancements in the continuous spectrum of scattering states [108]. The crucial quantity to describe the elastic scattering of two hadrons is the phase shift  $\delta_l$ . It describes the shift of the phase between the incoming and the outgoing  $l$ -wave outside the interaction range and it encodes the relevant information of the two-particle interaction.

In the finite volume of the lattice, the previously continuous spectrum of scattering states becomes discrete. Thus the main challenge is to relate the discrete energy levels of the lattice to the infinite volume phase shift which allows us to draw conclusions about a possibly existing resonance.

This problem has been solved by Lüscher who developed an approach that relates the discrete two-particle energies in a cubic box to the scattering phase shift in the infinite volume [22, 107, 109–111]. Lüscher’s formalism, often referred to as *Lüscher’s method*, has been originally developed for the scattering of two particles with equal masses  $m$  and zero total momentum  $\mathbf{P} = 0$ . This formalism has been extended to non-zero momenta  $\mathbf{P} \neq 0$ , so-called *moving frames*, by Rummukainen and Gottlieb [112] and Feng *et al.* [113, 114] and generalized for particles with different masses by Fu [115] and Leskovec *et al.* [116]. On the lattice, the phase shift  $\delta_l(s)$  can only be computed for the discrete energies  $s$  where  $s = E^2 - \mathbf{P}^2$  is the squared center-of-momentum energy and  $E$  are the discrete lattice energies. Considering also moving frames with  $\mathbf{P} \neq 0$  consequently enlarges the number of accessible energies  $s$  for which the phase shift  $\delta_l(s)$  can be computed. This allows a more precise determination of the phase shift’s energy dependence and facilitates extracting resonance parameters.

In this chapter I will first present the derivation of the scattering phase shift formula for two-particle elastic scattering in Sec. 3.1. In the subsequent Sec. 3.2 I will focus

on the reduced rotational symmetry of the lattice and the resulting consequences for two-particle scattering. This is followed by a brief discussion of the theoretical foundations of coupled channel scattering, describing processes with more than one scattering channel involved in Sec. 3.3.

### 3.1 Derivation of Scattering Phase Shift Formula

In this section, I recapitulate the derivation of Lüscher's formula that relates the finite volume energies to the infinite volume phase shift. Deriving the phase shift formula for moving frames and particles with different masses is conceptually similar to the original work by Lüscher [22] for  $\mathbf{P} = 0$  and equal masses. Since the phase shift is naturally defined in the center-of-mass frame (CMF), the major overhead to establish a phase shift formula for moving frames (MF) is to transform the scattering system back to the CMF. This is accomplished by a Lorentz transformation and has been carried out for the scattering of two particles with both equal masses [112–114, 117] and unequal masses [115, 116]. Here, I will illustrate the derivation of the phase shift formula in the most general form considering moving frames and particles of different masses following the discussion in Refs. [115, 116].

#### 3.1.1 Non-Interacting Particles

We consider two non-interacting particles with masses  $m_1$  and  $m_2$ , momenta  $\mathbf{p}_1$  and  $\mathbf{p}_2$ , and total momentum  $\mathbf{P}$  in a finite box of size  $L^3$ . As a consequence of the periodic boundary conditions, the momenta obey

$$\mathbf{P} = \mathbf{p}_1 + \mathbf{p}_2 = \frac{2\pi}{L} \mathbf{d}, \quad \text{with } \mathbf{d} \in \mathbb{Z}^3. \quad (3.1)$$

The energy  $E$  of the two particles in the lattice frame, which is also called moving frame (MF) for  $\mathbf{P} \neq 0$ , is given by the sum of the single particle energies,

$$E = \sqrt{m_1^2 + \mathbf{p}_1^2} + \sqrt{m_2^2 + \mathbf{p}_2^2}, \quad \text{with } \mathbf{p}_1 = \frac{2\pi}{L} \mathbf{n}_1, \quad \mathbf{p}_2 = \frac{2\pi}{L} \mathbf{n}_2, \quad \mathbf{n}_1, \mathbf{n}_2 \in \mathbb{Z}^3. \quad (3.2)$$

The center-of-momentum frame (CMF) moves relatively to the lattice frame with a velocity  $\mathbf{v}$  given by

$$\mathbf{v} = \frac{\mathbf{P}}{E}, \quad \gamma = \frac{1}{\sqrt{1 - \mathbf{v}^2}}, \quad (3.3)$$

where  $\gamma$  is the Lorentz factor. Note that a Lorentz boost only affects the component of a vector  $\mathbf{y}$  that is parallel to  $\mathbf{v}$  while the perpendicular component is unaffected,

$$\gamma \mathbf{y} = \gamma \mathbf{y}_{\parallel} + \mathbf{y}_{\perp}, \quad \text{with } \mathbf{y}_{\parallel} = \frac{\mathbf{v} \cdot \mathbf{y}}{|\mathbf{v}|^2} \mathbf{v}, \quad \mathbf{y}_{\perp} = \mathbf{y} - \mathbf{y}_{\parallel}. \quad (3.4)$$

As the total momentum vanishes in the CMF, the single particle momenta obey

$$\mathbf{p}_{1,\text{cm}} = \mathbf{p}_{\text{cm}} = -\mathbf{p}_{2,\text{cm}}. \quad (3.5)$$

Using a Lorentz transformation to relate  $\mathbf{p}_{i,\text{cm}}$  and  $\mathbf{p}_i$  one obtains

$$\mathbf{p}_1 = \gamma(\mathbf{p}_{\text{cm}} + \mathbf{v}E_{1,\text{cm}}) \quad \text{and} \quad \mathbf{p}_2 = \gamma(-\mathbf{p}_{\text{cm}} + \mathbf{v}E_{2,\text{cm}}), \quad (3.6)$$

where  $E_{i,\text{cm}}$  is the center-of-momentum energy of the  $i$ -th particle given by

$$E_{1,\text{cm}} = \frac{E_{\text{cm}}}{2} \left( 1 + \frac{m_1^2 - m_2^2}{(E_{\text{cm}})^2} \right) \quad \text{and} \quad E_{2,\text{cm}} = \frac{E_{\text{cm}}}{2} \left( 1 + \frac{m_2^2 - m_1^2}{(E_{\text{cm}})^2} \right). \quad (3.7)$$

Here,  $E_{\text{cm}} = \sqrt{s}$  denotes the two-particle energy in the CMF which is related to  $E$  via

$$E_{\text{cm}} = \sqrt{s} = \gamma^{-1}E = \sqrt{E^2 - \mathbf{P}^2}. \quad (3.8)$$

Finally, we can express the momentum  $\mathbf{p}_{\text{cm}}$  in the CMF as

$$\mathbf{p}_{\text{cm}} = \gamma^{-1}(\mathbf{p}_1 - \gamma\mathbf{v}E_{1,\text{cm}}) = \gamma^{-1} \left( \mathbf{p}_1 - \frac{2\pi\mathbf{d}}{L} \frac{1}{2} \left[ 1 + \frac{m_1^2 - m_2^2}{(E_{\text{cm}})^2} \right] \right) \equiv \frac{2\pi}{L} \mathbf{r}. \quad (3.9)$$

In the last step, a short notation for  $\mathbf{p}_{\text{cm}}$  has been introduced [116] using  $\mathbf{r} \in P_{\mathbf{d}}$ , where  $P_{\mathbf{d}}$  describes the set of all lattice points after the Lorentz transformation from the MF to the CMF according to

$$P_{\mathbf{d}} = \left\{ \mathbf{r} \mid \mathbf{r} = \gamma^{-1} \left( \mathbf{n} - \frac{1}{2} A \mathbf{d} \right) \right\}, \quad \mathbf{n} \in \mathbb{Z}^3 \quad (3.10)$$

with the abbreviation

$$A \equiv 1 + \frac{m_1^2 - m_2^2}{(E_{\text{cm}})^2}. \quad (3.11)$$

The mesh  $P_{\mathbf{d}}$  and especially the symmetry transformations under which this set of points is invariant play a crucial role for the scattering formalism on the lattice [116] and will be discussed in detail in Sec. 3.2.

### 3.1.2 $d$ -Periodic Boundary Conditions of the Wave Function

The wave function for the system of two spinless particles  $\psi(x_1, x_2)$  transforms under a Lorentz transformation according to

$$\psi(x_1, x_2) = \psi'(x'_1, x'_2) = \psi'(\Lambda x_1, \Lambda x_2), \quad (3.12)$$

where  $(x')^\mu = \lambda^\mu{}_\nu x^\nu$  denotes the Lorentz transformation of the space-time argument. In Ref. [112], Rummukainen and Gottlieb derived for two particles with equal masses an expression that relates the wave function  $\psi_{\text{MF}}(x_1, x_2)$  in the moving frame to the wave function  $\phi_{\text{CM}}(\mathbf{x}_{\text{cm}})$  in the center-of-momentum frame depending only on the relative coordinate  $\mathbf{x}_{\text{cm}} = \mathbf{x}_{1,\text{cm}} - \mathbf{x}_{2,\text{cm}}$ . In a finite box with size  $L^3$  and periodic boundary conditions, the wave function  $\psi_{\text{MF}}$  in the moving frame fulfills

$$\psi_{\text{MF}}(\mathbf{x}_1, \mathbf{x}_2) = \psi_{\text{MF}}(\mathbf{x}_1 + \mathbf{n}_1 L, \mathbf{x}_2 + \mathbf{n}_2 L), \quad \mathbf{n}_1, \mathbf{n}_2 \in \mathbb{Z}^3. \quad (3.13)$$

Using their relation between the MF and CMF wave functions, Rummukainen and Gottlieb determined the so-called  $\mathbf{d}$ -periodic boundary conditions for the wave function  $\phi_{\text{CM}}$  in the CMF [112]. This has been generalized by Fu [115] for the case of two particles with different masses, yielding

$$\phi_{\text{CM}}(\mathbf{x}_{\text{cm}}) = (-1)^{A\mathbf{nd}} \phi_{\text{CM}}(\mathbf{x}_{\text{cm}} + \gamma\mathbf{n}L), \quad \mathbf{n} \in \mathbb{Z}^3, \quad (3.14)$$

with  $A$  as defined in Eq. (3.11).

### 3.1.3 Interacting Particles

In the case of two interacting particles, the interaction will change the energy eigenvalues compared to the non-interacting case, and the individual momenta of the particles do not obey anymore the quantization condition in Eq. (3.2). To provide a clear distinction between quantized and non-quantized momenta, I will label the momenta appearing for interacting particles with  $\mathbf{k}$ , while I will continue to use  $\mathbf{p}$  for momenta obeying a quantization condition like Eq. (3.2) or Eq. (3.10).

The center-of-momentum energy for two interacting particles is consequently given by

$$E_{\text{cm}} = \sqrt{s} = \sqrt{m_1^2 + \mathbf{k}_{\text{cm}}^2} + \sqrt{m_2^2 + \mathbf{k}_{\text{cm}}^2}, \quad \text{with } \mathbf{k}_{\text{cm}} = \frac{2\pi}{L}\mathbf{q}, \quad (3.15)$$

where the entries of  $\mathbf{q}$  are arbitrary numbers. The subsequent discussion will be carried out in the CMF, and to increase readability, I will omit from now on the index  $cm$  indicating CMF quantities.

Following the discussion in Refs. [112, 115, 116], the two-particle interaction is characterized by a short-range potential  $V(x)$  with  $x = |\mathbf{x}|$ , which vanishes in an exterior region  $|\mathbf{x}| > R$ , while  $R < L/2$ . Before I consider the wave function in a finite box, let us go back to the infinite volume. We know that the wave function for a spherical symmetric potential can be expanded in spherical harmonics  $Y_{lm}$ ,

$$\phi_{\text{CM}}(\mathbf{x}) = \sum_{l=0}^{\infty} \sum_{m=-l}^l Y_{lm}(\theta, \varphi) \phi_{lm}(x). \quad (3.16)$$

In the exterior range  $|\mathbf{x}| > R$ ,  $\phi_{\text{CM}}(\mathbf{x})$  solves the Helmholtz equation

$$\left(\Delta_{\mathbf{x}} + k^2\right) \phi_{\text{CM}}(\mathbf{x}) = 0, \quad (3.17)$$

with  $k = |\mathbf{k}|$ , and the free radial wave function is found to be

$$\phi_{lm}(x) = c_{lm} \left[ a_l(k) j_l(kx) + b_l(k) n_l(kx) \right], \quad (3.18)$$

where  $j_l$  and  $n_j$  are the spherical Bessel and Neumann functions. The interactions in the interior region affect the free solution in the exterior region only by a phase shift  $\delta_l(k)$  between the incoming wave  $j_l - in_l$  and the outgoing wave  $j_l + in_l$ . Comparing

this shifted wave function with the free solution in Eq. (3.18) yields the well-known relation [22, 37, 112]

$$e^{2i\delta_l(k)} = \frac{a_l(k) + ib_l(k)}{a_l(k) - ib_l(k)}. \quad (3.19)$$

In the finite box, the proceeding is similar, but additionally to the Helmholtz equation given in Eq. (3.17),  $\phi_{\text{CM}}$  must also satisfy the  $\mathbf{d}$ -periodic boundary condition in Eq. (3.14). One possible choice for  $\phi_{\text{CM}}$  is the Green function

$$G^{\mathbf{d}}(\mathbf{x}, k^2) = \frac{1}{\gamma L^3} \sum_{\mathbf{p}=\frac{2\pi}{L}\mathbf{r}, \mathbf{r} \in P_{\mathbf{d}}} \frac{e^{i\mathbf{p}\mathbf{x}}}{\mathbf{p}^2 - k^2}, \quad (3.20)$$

where the sum runs over all possible lattice momenta  $\mathbf{p} = 2\pi\mathbf{r}/L$  which are defined by the mesh  $P_{\mathbf{d}}$  given in Eq. (3.10). Note that we assume that  $k$  is not a ‘‘singular’’ value, which means that for  $k = 2\pi|\mathbf{q}|/L$  it holds that  $\mathbf{q} \notin P_{\mathbf{d}}$ . Considering singular values requires a special treatment which has been discussed in detail in Ref. [22] for the CMF and equal masses and can be generalized for moving frames as shown in Ref. [112]. Around the origin  $\mathbf{x} = 0$ , the Green function must be governed by a power of  $1/|\mathbf{x}|$  to satisfy the Helmholtz equation [22]. Thus, a convenient way to express  $G^{\mathbf{d}}(\mathbf{x}, k^2)$  is to split off the singular part at the origin and write the Green function as

$$G^{\mathbf{d}}(\mathbf{x}, k^2) = \frac{k}{4\pi} n_0(kx) + \hat{G}^{\mathbf{d}}(\mathbf{x}, k^2), \quad (3.21)$$

where  $\hat{G}^{\mathbf{d}}(\mathbf{x}, k^2)$  contains all regular parts of  $G^{\mathbf{d}}(\mathbf{x}, k^2)$  [22, 112]. A complete set of linear independent solutions of the Helmholtz equation is given by

$$G_{lm}^{\mathbf{d}}(\mathbf{x}, k^2) = \mathcal{Y}_{lm}(\nabla) G^{\mathbf{d}}(\mathbf{x}, k^2), \quad (3.22)$$

where  $\mathcal{Y}_{lm}(\mathbf{x}) = x^l Y_{lm}(\theta, \varphi)$  are the harmonic polynomials [22, 112, 116]. Accordingly, the wave function  $\phi_{\text{CM}}$  can be written as a linear combination of the functions  $G_{lm}^{\mathbf{d}}$ ,

$$\phi_{\text{CM}}(\mathbf{x}) = \sum_{l=0}^{\infty} \sum_{m=-l}^l v_{lm} G_{lm}^{\mathbf{d}}(\mathbf{x}, k^2). \quad (3.23)$$

In analogy to the continuum case, we expand Eq. (3.23) and thus the functions  $G_{lm}^{\mathbf{d}}(\mathbf{x}, k^2)$  in spherical harmonics. This has been initially done by Lüscher for the CMF [22], and the generalization to moving frames is straightforward [112, 116], yielding

$$G_{lm}^{\mathbf{d}}(\mathbf{x}, k^2) = \frac{(-1)^l k^{l+1}}{4\pi} \left[ n_l(kx) Y_{lm}(\theta, \varphi) + \sum_{l'=0}^{\infty} \sum_{m'=-l'}^{l'} \mathcal{M}_{lm, l'm'}^{\mathbf{d}}(q^2) j_{l'}(kx) Y_{l'm'}(\theta, \varphi) \right]. \quad (3.24)$$

The first term is the singular part at the origin which can be derived from  $\mathcal{Y}_{lm}(\nabla) n_0(kx)$  as done in Ref. [22]. The matrix  $\mathcal{M}^{\mathbf{d}}$  appearing in the regular term is essential to determine the two-particle phase shift. It is governed by an analytic expression which

was first derived in Ref. [22] for the CMF, while its generalization to moving frames was deduced in Refs. [112, 116] and is given by

$$\mathcal{M}_{lm,l'm'}^d(q^2) = \frac{(-1)^l}{\gamma\pi^{3/2}} \sum_{j=|l-l'|}^{l+l'} \sum_{s=-j}^j \frac{i^j}{q^{j+1}} \mathcal{Z}_{js}^d(1; q^2) C_{lm,js,l'm'}, \quad (3.25)$$

where the tensor  $C_{lm,js,l'm'}$  can be expressed in terms of the Wigner  $3j$ -symbols,

$$C_{lm,js,l'm'} = (-1)^{m'} i^{l-j+l'} \sqrt{(2l+1)(2j+1)(2l'+1)} \begin{pmatrix} l & j & l' \\ m & s & -m' \end{pmatrix} \begin{pmatrix} l & j & l' \\ 0 & 0 & 0 \end{pmatrix}. \quad (3.26)$$

The generalized Zeta function  $\mathcal{Z}_{js}^d(1; q^2)$  is given by [115, 116]

$$\mathcal{Z}_{lm}^d(s; q^2) = \sum_{\mathbf{x} \in P_d} \frac{\mathcal{Y}_{lm}(\mathbf{x})}{(\mathbf{x}^2 - q^2)^s}. \quad (3.27)$$

The sum in Eq. (3.27) diverges for  $\text{Re}(2s) < l + 3$ , but the divergence can be removed by analytically continuing to the complex plane [116]. A more elaborated discussion of this analytic continuation as well as an approach to numerically evaluating the Zeta function can be found in Refs. [22, 116].

In practice, not the complete matrix  $\mathcal{M}^d$  but only the elements with the lowest coefficients  $l$  are relevant. Consequently, we can write  $\mathcal{M}^d$  for  $l \leq 1$  and  $-1 \leq m \leq 1$  explicitly as

$$M = \mathcal{M}_{lm,l'm'}^d = \begin{matrix} & \begin{matrix} 00 & 10 & 11 & 1-1 \end{matrix} \\ \begin{matrix} 00 \\ 10 \\ 11 \\ 1-1 \end{matrix} & \begin{pmatrix} w_{00} & i\sqrt{3}w_{10} & i\sqrt{3}w_{11} & i\sqrt{3}w_{1-1} \\ -i\sqrt{3}w_{10} & w_{00} + 2w_{20} & \sqrt{3}w_{21} & \sqrt{3}w_{2-1} \\ i\sqrt{3}w_{1-1} & -\sqrt{3}w_{2-1} & w_{00} - w_{20} & -\sqrt{6}w_{2-2} \\ i\sqrt{3}w_{11} & -\sqrt{3}w_{21} & -\sqrt{6}w_{22} & w_{00} - w_{20} \end{pmatrix} \end{matrix} \quad (3.28)$$

with the abbreviation

$$w_{lm} = \frac{1}{\pi^{3/2} \sqrt{2l+1} \gamma q^{l+1}} \mathcal{Z}_{lm}^d(1; q^2). \quad (3.29)$$

In a last step, we compare the wave function  $\phi_{\text{CM}}(\mathbf{x})$  expressed in Eq. (3.23) using the expansion of the functions  $G_{lm}^d$  in Eq. (3.24) with  $\phi_{\text{CM}}(\mathbf{x})$  given in Eqs. (3.16) and (3.18). Matching the factors in front of the spherical Bessel and Neumann functions  $j_l$  and  $n_l$ , respectively, one obtains

$$c_{lm} b_l(k) = \frac{(-1)^l k^{l+1}}{4\pi} v_{lm}, \quad c_{lm} a_l(k) = \sum_{l',m'} \frac{(-1)^{l'} k^{l'+1}}{4\pi} v_{l'm'} \mathcal{M}_{l'm',lm}^d(q^2), \quad (3.30)$$

which can be rewritten by inserting the first into the second equation as

$$\sum_{l',m'} c_{l'm'} \left[ b_{l'}(k) \mathcal{M}_{l'm',lm}^d(q^2) - a_{l'}(k) \delta_{ll'} \delta_{mm'} \right] = 0. \quad (3.31)$$

This is a system of homogeneous linear equations which has only non-zero solutions if the determinant of the coefficient matrix vanishes. Accordingly, this gives rise to the determinant condition

$$\det [B M - A] = 0, \quad (3.32)$$

where the matrices  $A$  and  $B$  are related to the coefficients  $a_l$  and  $b_l$  [22] and  $M$  is a short notation for the matrix  $\mathcal{M}^d$ ,

$$M_{lm,l'm'} = \mathcal{M}_{lm,l'm'}^d(q^2), \quad A_{lm,l'm'} = a_{l'}(k) \delta_{ll'} \delta_{mm'}, \quad B_{lm,l'm'} = b_{l'}(k) \delta_{ll'} \delta_{mm'}. \quad (3.33)$$

Identifying the phase shift in the same way as in Eq. (3.19) as

$$e^{2i\delta_l(k)} = \frac{A + iB}{A - iB}, \quad (3.34)$$

the determinant condition in Eq. (3.32) is given by

$$\det \left[ \cot(\delta_l(k)) - M(q^2) \right] = 0. \quad (3.35)$$

This is the key equation for describing two-particle scattering in a box as it relates the energy levels  $E_{\text{cm}}$  (or equivalently the momenta  $k$ ) which are computed on the lattice to the infinite volume scattering phase shift  $\delta_l(k)$ . Note that according to Eq. (3.15), the center-of-momentum energy  $E_{\text{cm}} = \sqrt{s}$  and the momentum  $k$  are directly related to each other. Consequently, it is equivalent to expressing the phase shift  $\delta_l$  as a function of the energy  $s$  or the momentum  $k$ , while in some cases, for example, in coupled channel systems, it is more convenient to choose  $\delta_l(s)$ .

The scattering phase shift  $\delta_l(s)$  is directly related to the scattering amplitude  $T^{(l)}(s)$  as

$$T^{(l)}(s) = \frac{1}{\rho(s)} \sin(\delta_l(s)) e^{i\delta_l(s)} = \frac{1}{\rho(s)} \frac{1}{\cot(\delta_l(s)) - i}, \quad (3.36)$$

where  $\rho(s) = 2k/\sqrt{s}$  is the phase space. In modern lattice scattering studies, this scattering amplitude plays a central role. Analytically continuing  $T^{(l)}(s)$  to complex energies, physical states appear as poles of this  $T$ -matrix in the complex energy plane and thus allow to deduce the parameters of resonances.

Note that Eq. (3.35) describes two particles with different masses and non-zero total momentum  $\mathbf{P} \neq 0$ . For  $m_1 = m_2$ , the parameter  $A$  given in Eq. (3.11) becomes unity and the result for equal masses [112] is recovered. Setting additionally  $\mathbf{P} = 0$  and  $\gamma = 1$  reproduces Lüscher's original version of the phase shift formula [22].

### 3.2 Symmetry Properties of the Lattice

In contrast to the infinite volume with continuous space-time where rotations are governed by the continuous orthogonal group  $O(3)$ , the lattice has a reduced rotational symmetry. This is a consequence of the discrete grid of lattice points which is given by the mesh  $P_{\mathbf{d}}$  defined in Eq. (3.10). Note that  $P_{\mathbf{d}}$  describes the grid of lattice points for arbitrary total momenta  $\mathbf{P} = 2\pi\mathbf{d}/L$ , while the factor  $A$  in Eq. (3.10) also allows us to distinguish between systems with two particles of equal or different masses. We introduce now a group  $\mathbb{G}$  which contains all symmetry transformations  $\hat{R}$  that leave the points in  $P_{\mathbf{d}}$  invariant. A short discussion of its relevant group theoretical properties can be found in Appendix B.1.

If the lattice is at rest, it has the symmetry of a cube, while the corresponding symmetry group is the cubic group  $O_h$ . For moving frames, however, where a Lorentz transformation to the CMF is required, the volume of the box is Lorentz contracted along the direction of  $\mathbf{P}$  and the previously cubic form of the box is deformed [112]. As a consequence, the symmetry is further reduced, and the corresponding symmetry group becomes a subgroup of the cubic group  $O_h$ . The actual shape of the box and thus the relevant symmetry group depends on the total momentum  $\mathbf{P}$ . Moreover, for moving frames, the symmetry group also depends on whether the masses of the two particles are equal or not. According to Eq. (3.10), for different masses the cubic mesh is first shifted by  $-1/2A\mathbf{d}$ , while  $A \neq 1$  for  $m_1 \neq m_2$ . Thus, the origin of the mesh  $P_{\mathbf{d}}$  is not anymore in the center of a unit cell, and several symmetries like an inversion with respect to the origin are lost [116]. Consequently, the symmetry groups for moving frames and two particles with different mass have less elements than in the case of equal masses. I list the symmetry groups for the lowest total momenta  $\mathbf{P}$ , distinguishing the case of equal and different masses, in Table 3.1.

$\mathbf{d} = \frac{L}{2\pi}\mathbf{P}$	Symmetry group	Classification	$N_{\text{elements}}$
$(0, 0, 0)^T$	$O_h$	cubic	48
equal masses $m_1 = m_2$			
$(0, 0, 1)^T$	$D_{4h}$	tetragonal	16
$(1, 1, 0)^T$	$D_{2h}$	orthorhombic	8
different masses $m_1 \neq m_2$			
$(0, 0, 1)^T$	$C_{4v}$	tetragonal	8
$(1, 1, 0)^T$	$C_{2v}$	orthorhombic	4

Table 3.1.: Classification of Lorentz boosts, associated symmetry group, cubic classification and number of elements for the center-of-momentum frame and moving frames with  $|\mathbf{P}|^2 \leq 2(2\pi/L)^2$ .



The two-particle wave function in Eq. (3.23) transforms under a symmetry transformation  $\hat{R}$  according to

$$\hat{R} \phi_{\text{CM}}(\mathbf{x}) = \sum_{l,m,m'} v_{lm} \Gamma_{mm'}^{(l)}(\hat{R}) G_{lm'}^d(\mathbf{x}, p^2), \quad (3.37)$$

where  $\Gamma_{mm'}^{(l)}(\hat{R})$  is the representation matrix of the transformation  $\hat{R}$  in the basis of  $Y_{lm}$  [114] and originates from

$$Y_{lm}(\hat{R}\mathbf{x}) = \sum_{m'=-l}^l \Gamma_{mm'}^{(l)}(\hat{R}) Y_{lm'}(\mathbf{x}). \quad (3.38)$$

For the rotational group  $O(3)$ , the spherical harmonics  $Y_{lm}$  form an orthogonal basis, and the representations  $\Gamma_{mm'}^{(l)}(\hat{R})$  are irreducible representations of the group  $O(3)$  [114]. For the group  $\mathbb{G}$ , the  $\Gamma_{mm'}^{(l)}(\hat{R})$  are in general reducible and can be decomposed into the irreducible representations (irreps)  $\Lambda$  of group  $\mathbb{G}$ . In the case of the cubic group  $O_h$  there are 10 different irreps, namely  $A_1^\pm$ ,  $A_2^\pm$ ,  $E^\pm$ ,  $T_1^\pm$ ,  $T_2^\pm$  where  $\pm$  distinguishes the transformation behavior under reflections [22, 118].

The representations  $\Gamma^{(l)}$  of the rotational group  $O(3)$  are formed by the  $2l+1$  functions  $Y_{lm}$ . The decomposition of  $\Gamma^{(l)}$  into the irreducible representations  $\Lambda$  can be performed by exploiting the transformation behavior of  $Y_{lm}$  under the transformations  $\hat{R} \in \mathbb{G}$ . I carry this out exemplarily for  $O_h$  in Appendix B.2 where the resulting decomposition up to  $l \leq 2$  is found to be

$$\begin{aligned} \Gamma^{(0)} &= A_1^+, \\ \Gamma^{(1)} &= T_1^-, \\ \Gamma^{(2)} &= E^+ \oplus T_2^+. \end{aligned} \quad (3.39)$$

The symmetry transformations of group  $\mathbb{G}$  that result in the decomposition of the representations  $\Gamma^{(l)}$  into irreps also lead to a block-diagonal form of the matrix  $M$  defined in Eq. (3.28). To recognize this, we consider the transformation behavior under transformations  $\hat{R}$  of the Zeta function  $\mathcal{Z}_{lm}^d(s; q^2)$  given in Eq. (3.27) which is the main building block of the matrix  $M$ . Relying on the fact that all transformations  $\hat{R} \in \mathbb{G}$  leave the mesh  $P_d$  invariant, the Zeta function can be rewritten as

$$\begin{aligned} \mathcal{Z}_{lm}^d(s; q^2) &= \sum_{\mathbf{x} \in P_d} \frac{\mathcal{Y}_{lm}(\mathbf{x})}{(\mathbf{x}^2 - q^2)^s} = \sum_{\mathbf{x}' = \hat{R}\mathbf{x} \in P_d} \frac{\mathcal{Y}_{lm}(\mathbf{x}')}{(\mathbf{x}'^2 - q^2)^s} = \sum_{\mathbf{x} \in P_d} \frac{|\mathbf{x}|^l Y_{lm}(\hat{R}\mathbf{x})}{(\mathbf{x}^2 - q^2)^s} \\ &= \sum_{\mathbf{x} \in P_d} \sum_{m'=-l}^l \Gamma_{mm'}^{(l)}(\hat{R}) \frac{\mathcal{Y}_{lm'}(\mathbf{x})}{(\mathbf{x}^2 - q^2)^s} = \sum_{m'=-l}^l \Gamma_{mm'}^{(l)}(\hat{R}) \mathcal{Z}_{lm'}^d(s; q^2), \end{aligned} \quad (3.40)$$

where  $|\mathbf{x}'| = |\mathbf{x}|$  and the transformation relation for  $Y_{lm}$  in Eq. (3.38) has been used [116]. This set of linear relations for  $\mathcal{Z}_{lm}^d$  can be used to determine if a specific  $\mathcal{Z}_{lm}^d$  is purely real, imaginary or zero [22]. For example, in the case of the group  $O_h$  the inversion  $i \in O_h$  which transforms  $\mathbf{x} \rightarrow -\mathbf{x}$  leads to

$$\mathcal{Z}_{1m}^d = -\mathcal{Z}_{1m}^d, \quad m = -1, 0, 1, \quad (3.41)$$

and consequently  $\mathcal{Z}_{1m}^d = 0$ . Hereby, the representation matrices  $\Gamma_{mm'}^{(l)}(\hat{R})$  are obtained from the transformation of the spherical harmonics  $Y_{lm}$  according to Eq. (3.38) as listed in Table B.3. In the case of  $O_h$ , all  $\mathcal{Z}_{lm}^d$  with  $l < 4$  vanish besides  $\mathcal{Z}_{00}^d$  [22]. Consequently, the matrix  $M$  in Eq. (3.28) becomes block diagonal,

$$M = \mathcal{M}_{lm,l'm'}^d = \begin{array}{c} \\ 00 \\ 10 \\ 11 \\ 1-1 \end{array} \begin{pmatrix} 00 & 10 & 11 & 1-1 \\ w_{00} & 0 & 0 & 0 \\ 0 & w_{00} & 0 & 0 \\ 0 & 0 & w_{00} & 0 \\ 0 & 0 & 0 & w_{00} \end{pmatrix}. \quad (3.42)$$

The quantization condition in Eq. (3.35) now allows us to extract the  $S$ -wave scattering phase shift  $\delta_0$  from the  $A_1^+$  irrep of  $O_h$  as

$$\cot(\delta_0(k)) = \omega_{00} = \frac{\mathcal{Z}_{00}(1; q^2)}{\pi^{3/2} q}, \quad (3.43)$$

and the  $P$ -wave scattering phase shift  $\delta_1$  from the  $T_1^-$  irrep of  $O_h$  as

$$\cot(\delta_1(k)) = \omega_{00} = \frac{\mathcal{Z}_{00}(1; q^2)}{\pi^{3/2} q}. \quad (3.44)$$

Here I utilized  $\mathcal{Z}_{00}(1; q^2) \equiv \mathcal{Z}_{00}^{d=0}(1; q^2)$  and  $\gamma = 1$ . For the other symmetry groups  $\mathbb{G} \in \{D_{4h}, D_{2h}, C_{4v}, C_{2v}\}$ , the matrix  $M$  in Eq. (3.28) can also be simplified following the same proceeding, which means utilizing the symmetry transformations of the relevant symmetry group  $\mathbb{G}$  to study the transformation behavior of  $\mathcal{Z}_{lm}^d$ . The final forms of the  $M$  matrices are collected in Appendix B.3 for all groups  $\mathbb{G} \in \{D_{4h}, D_{2h}, C_{4v}, C_{2v}\}$ .

### 3.3 Coupled Channel Scattering

In practice, it is often not sufficient to describe a resonance by the scattering of two particles. Many hadrons have several decay channels leading to different final states which are all of similar importance. In order to study such resonances, all decay channels must be taken into account, which requires a theoretical treatment of such coupled channel scattering processes [119–125]. What complicates this is the fact that these channels interact with each other, so the scalar potential introduced at the beginning of Sec. 3.1.3 must be replaced by a matrix potential containing also effective two-body interactions [124]. As a consequence, also the scattering amplitude  $T^{(l)}$  that is scalar for a single channel scattering process becomes a matrix for the coupled channel scattering formalism. Note that the scattering amplitude  $T^{(l)}$  is the crucial quantity for scattering processes in coupled channels, while a scalar phase shift is not suited to capture all information about the scattering process.

A relation between the finite volume energies and the infinite volume scattering amplitude for coupled-channel scattering has been derived in Ref. [124] by generalizing the

partial-wave decomposition using separate wave functions for the different channels. The resulting determinant condition is given by

$$\det \left[ \delta_{ll'} \delta_{mm'} \delta_{\alpha\beta} + i\rho_\alpha(s) T_{\alpha\beta}^{(l)}(s) \left( \delta_{ll'} \delta_{mm'} + i\mathcal{M}_{lm,l'm'}^d(q_\alpha^2) \right) \right] = 0, \quad (3.45)$$

where the indices  $\alpha, \beta$  denote the different channels [124].  $\rho_\alpha(s) = 2k_\alpha/\sqrt{s}$  is the relativistic phase-space for channel  $\alpha$ , and  $T_{\alpha\beta}^{(l)}(s)$  is the coupled channel scattering amplitude as a function of the center-of-momentum energy  $\sqrt{s}$ . Note that for a single channel, the quantization condition given in Eq. (3.35) is recovered. This can easily be shown by inserting the definition of the scattering amplitude  $T^{(l)}$  in Eq. (3.36) into the coupled channel quantization condition in Eq. (3.45).



# 4

---

## HADRON SPECTROSCOPY FOR TETRAQUARK STATES

---

A major field of application for lattice QCD is hadron spectroscopy. As a non-perturbative approximation of QCD, lattice QCD is perfectly suited to compute low-energy observables like hadron masses. Therefore, hadron spectroscopy in lattice QCD is an excellent framework to test the theory of QCD by comparing hadron masses determined in lattice simulations with existing experimental measurements. Moreover, theoretical predictions of hadron masses for states which have not been experimentally measured yet provide valuable input for upcoming experimental investigations.

Candidates for such exotic hadrons that have not been observed in experiment so far are the antiheavy-antiheavy-light-light four-quark systems with quark content  $\bar{b}b\bar{u}d$ ,  $\bar{b}b\bar{u}s$  and  $\bar{b}c\bar{u}d$  which are investigated in this work. As I am mainly interested in whether these tetraquark systems form hadronically stable states, the ground-state energies are of particular importance. However, in general such tetraquarks are expected to be rather weakly bound with ground-state energies close to the threshold of strong decay. Hence, a faithful treatment of finite volume effects is advisable. This can be done by performing a scattering analysis using Lüscher's method, which requires to resolve also higher energy levels sufficiently precisely.

In this chapter, I illustrate how the low-lying energy spectrum for these four-quark systems is extracted and present the methods that are employed in the associated lattice computations. The relevant lattice observables to compute hadron masses are two-point correlation functions of interpolating operators which are introduced in Sec. 4.1. As the essential components of these correlation functions are carefully chosen interpolating operators, I discuss them extensively in Sec. 4.2. Especially, I illustrate how to construct interpolating operators on the lattice and establish the interpolating operators for the four-quark systems of interest. In Sec. 4.3, I present two techniques that are applied to extract the energy spectrum from a matrix of correlation functions. Quark propagators play a central role when computing correlation functions. In Sec. 4.4, I illustrate several numerical methods to estimate the quark propagator by inverting the Dirac operator. In order to improve the overlap generated by creation operators with physical states, one employs smearing methods for both the gauge fields and the fermion fields, which is explained in Sec. 4.5. Finally, in Sec. 4.6, I discuss the essential steps of a scattering analysis that can be utilized to investigate doubly-heavy doubly-light tetraquark systems.

## 4.1 The Correlation Function and Physical Observables

In order to compute hadron masses, Euclidean correlation functions of two hadron interpolating operators  $\mathcal{O}_1(t)$  and  $\mathcal{O}_2^\dagger(0)$ ,

$$C(t) = \langle \mathcal{O}_1(t) \mathcal{O}_2^\dagger(0) \rangle, \quad (4.1)$$

are employed, while the temporal locations  $t$  and  $0$  can be chosen without loss of generality due to the periodicity of the lattice. Such two-point correlation functions can be evaluated via the path integral formalism according to Eq. (2.14). In a lattice calculation, the path integral is calculated by first generating a set of gauge link configurations according to the probability distribution given by the Boltzmann factor as discussed in Sec. 2.1.3. Then, if such an ensemble of gauge link configurations is available, the correlation function is computed on each single gauge link configuration, and the expectation value is obtained by averaging these results according to Eq. (2.21). To extract physical observables like hadron masses from a correlation function, Eq. (4.1) is written in its spectral representation. Starting with the time evolution of the operator  $\mathcal{O}_1(t)$  on the periodic lattice, Eq. (4.1) can be expressed as

$$\langle \mathcal{O}_1(t) \mathcal{O}_2^\dagger(0) \rangle_T = \frac{1}{Z_T} \text{Tr} \left[ e^{-(T-t)\hat{H}} \mathcal{O}_1 e^{-t\hat{H}} \mathcal{O}_2 \right], \quad Z_T = \text{Tr} \left[ e^{-T\hat{H}} \right], \quad (4.2)$$

where  $\hat{H}$  is the Hamilton operator of the system and  $Z_T$  is the partition function [50]. Using the eigenvector equation

$$\hat{H}|n\rangle = E_n|n\rangle, \quad (4.3)$$

where  $E_n$  is the energy of the  $n$ -th state and  $|n\rangle$  is the associated eigenstate, the correlation function can be written as

$$\langle \mathcal{O}_1(t) \mathcal{O}_2^\dagger(0) \rangle_T = \frac{1}{Z_T} \sum_{n,m=0}^{\infty} \langle m|\mathcal{O}_1|n\rangle \langle n|\mathcal{O}_2^\dagger|m\rangle e^{-E_m(T-t)} e^{-E_n t}. \quad (4.4)$$

Taking the limit  $T \rightarrow \infty$ , the sum over  $m$  breaks down and only the vacuum state  $|m\rangle = |0\rangle$  remains. Defining the energy difference to the vacuum as  $\Delta E_n = E_n - E_0$  consequently yields

$$\lim_{T \rightarrow \infty} \langle \mathcal{O}_1(t) \mathcal{O}_2^\dagger(0) \rangle_T = \sum_{n=0}^{\infty} \langle 0|\mathcal{O}_1|n\rangle \langle n|\mathcal{O}_2^\dagger|0\rangle e^{-\Delta E_n t}. \quad (4.5)$$

The energy differences to the vacuum are exactly those observables that are measurable in experiment and thus are the quantities of interest in a lattice computation. From now on, the energy difference to the vacuum is labeled by  $E_n$  instead of  $\Delta E_n$ , which means that the ground-state energy is given by  $E_0$ .

Studying stable hadrons, this ground-state energy  $E_0$  is of particular interest. As  $E_0 < E_n$  for  $n \geq 1$ , the contributions of excited states in the sum in Eq. (4.5) are

exponentially suppressed for sufficiently large times  $t$ , and the correlation function is then dominated by the ground-state contribution. In order to extract the ground-state energy, one defines the *effective energy* as

$$aE_{\text{eff}}(t) = \ln \left( \frac{C(t)}{C(t+a)} \right), \quad (4.6)$$

which can be identified with the ground-state energy in the limit of large times  $t$ ,

$$aE_0 = \lim_{t \rightarrow \infty} aE_{\text{eff}}(t). \quad (4.7)$$

In practice, the effective energy reaches a plateau already at finite values of  $t$ . This corresponds to a temporal separation where mainly the ground-state energy contributes to the correlation function, while all higher contributions are sufficiently small. Consequently, the effective energy in the plateau region corresponds to the ground-state energy.

## 4.2 Interpolation Operators

The essential ingredients to compute hadron masses from correlation functions are carefully selected interpolating operators that first describe the correct quark content and second generate the desired quantum numbers. For the sake of simplicity, I label the quark fields appearing in interpolating operators according to their flavors ( $u$ ,  $d$ ,  $s$ ,  $c$ ,  $b$ , or  $t$ ), while I additionally distinguish between heavy quarks  $Q \in \{b, c\}$  and light quarks  $q \in \{u, d, s\}$ . The relevant quantum numbers characterizing the four-quark states of interest in this work are the isospin  $I$ , the spin  $J$  and the parity  $P$ . Only the  $u$  and  $d$  quarks carry isospin, while both have a value of  $I = 1/2$ . Accordingly, the isospin of a state containing two of these light quarks can be either  $I = 0$  or  $I = 1$ . An operator that creates a state with isospin  $I = 0$  is constructed such that it is antisymmetric under the flavor exchange  $u \leftrightarrow d$ , while  $I = 1$  is obtained if the operator is symmetric under flavor exchange. Spin  $J$  and parity  $P$  are governed by an appropriate combination  $\Gamma$  of the gamma matrices  $\gamma_\mu$ . In Table 4.1, I list the quantum numbers  $J^P$  for several states and show the associated combinations  $\Gamma$  that generate these quantum numbers.

State	$J^P$	$\Gamma$
Scalar	$0^+$	$\mathbb{1}, \gamma_4$
Pseudoscalar	$0^-$	$\gamma_5, \gamma_4\gamma_5$
Vector	$1^-$	$\gamma_j, \gamma_4\gamma_j$
Pseudovector	$1^+$	$\gamma_j\gamma_5$

Table 4.1.: Quantum numbers for commonly used combinations of gamma matrices and the associated states.

The ground-state energy of most ordinary mesons built of two quarks can be extracted precisely from a correlation function consisting of a single interpolating operator. However, this is not the case for exotic states like tetraquarks where a single interpolating operator is not sufficient to reliably obtain the ground-state energy. Especially if also higher energy levels should be resolved, a large basis of interpolating operators  $\mathcal{O}_j$  with  $j = 1, \dots, N$  is required. Thus, the correlation function in Eq. (4.1) is replaced by a correlation matrix,

$$C_{jk}(t) = \langle \mathcal{O}_j(t) \mathcal{O}_k^\dagger(0) \rangle, \quad j, k = 1, \dots, N. \quad (4.8)$$

In this work, the low-lying energy spectra of  $\bar{Q}\bar{Q}'qq'$  four-quark systems with quark content  $\bar{b}bud$ ,  $\bar{b}bus$  and  $\bar{b}\bar{c}ud$  are of particular interest. Hereby, I am especially interested in whether a hadronically stable tetraquark is formed, which means that the ground-state energy is below the lowest corresponding meson-meson threshold. Thus, reasonably chosen sets of interpolating operators describing the four-quark structures are crucial. I will discuss the four-quark interpolating operators that are employed in this work in detail in Sec. 4.2.3. In order to assess if a stable tetraquark state  $\bar{Q}\bar{Q}'qq'$  exists, its ground-state energy is compared to the lowest meson-meson threshold corresponding to the two mesons  $\bar{Q}q$  and  $\bar{Q}'q'$ . Consequently, also the associated meson masses must be determined within the lattice calculation. Therefore, I discuss the mesonic interpolating operators in Sec. 4.2.2, and illustrate how to evaluate a correlation function by using the example of the rather simple mesonic operators. I will start, however, with a more general discussion in Sec. 4.2.1, focusing on the construction of lattice interpolating operators with distinct quantum numbers taking into account the reduced rotational symmetry of the lattice.

### 4.2.1 Construction of Interpolating Operators on the Lattice

The overall objective of hadron spectroscopy is to study the energy spectrum of particles with distinct quantum numbers  $J^P$ . However, introducing the discretized space-time lattice reduces the rotational symmetry that is present in the continuum to the symmetry of the cubic group  $O_h$  as discussed in Sec. 3.2. Consequently, states cannot be classified by their spin  $J$  but rather according to the associated irreps of the symmetry group. The infinite number of spins  $J$  are therefore *subduced* into a finite number of lattice irreps  $\Lambda$  [118]. I list the spins up to  $J = 4$  that appear in each irrep of the group  $O_h$  in Table 4.2. Accordingly, also continuum interpolating operators with distinct spin  $J$  must be subduced into the appropriate lattice irrep. The crucial property of such a lattice operator is that it transforms accordingly to the relevant irrep,

$$\hat{R} \mathcal{O} \hat{R}^{-1} = \chi^{(\Lambda)}(\hat{R}) \mathcal{O}. \quad (4.9)$$

Here  $\hat{R} \in O_h$  are transformations that leave the mesh of lattice points  $P_d$  (see Eq. (3.10)) invariant, and  $\chi^{(\Lambda)}(\hat{R})$  is the associated character of irrep  $\Lambda$  which can be found in the group's character table (e.g., see Table B.2 for the characters of  $O_h$ ).



Symmetry group	Irrep $\Lambda^P$	$J^P$
$O_h$ $\mathbf{d} = (0, 0, 0)^T$	$A_1^\pm$	$0^\pm, 4^\pm, \dots$
	$T_1^\pm$	$1^\pm, 3^\pm, 4^\pm, \dots$
	$T_2^\pm$	$2^\pm, 3^\pm, 4^\pm, \dots$
	$E^\pm$	$3^\pm, 4^\pm, \dots$
	$A_2^\pm$	$3^\pm, \dots$

Table 4.2.: Lattice irreps  $\Lambda^P$  for the symmetry group  $O_h$  together with the quantum numbers  $J^P$  that are subduced into these irreps.

For example, according to Table 4.2 a lattice interpolating operator for a vector meson with  $J^P = 1^-$  is constructed in the  $T_1^-$  irrep. This is achieved by choosing  $\Gamma = \gamma_j$  (see Table 4.1) as, e.g., the operator with  $\gamma_1$  transforms like the polynomial  $x$  which in turn transforms like the first row of the  $T_1^-$  irrep, so the correct transformation behavior is confirmed.

For moving frames the situation gets even more complicated. Already in the continuum, the  $z$ -component  $M$  of the spin  $J$  is only well-defined if  $\mathbf{P} = 0$  or  $\mathbf{P} \propto e_z$  but not for arbitrary  $\mathbf{P}$ . For moving frames it is therefore more convenient to use the helicity  $\lambda$  instead of the spin  $J$  which is defined as the projection of the vectored spin  $\mathbf{J}$  on the direction of the total momentum  $\mathbf{P}$ ,

$$\lambda = \frac{\mathbf{J} \cdot \mathbf{P}}{|\mathbf{P}|}. \quad (4.10)$$

Additionally, also parity  $P$  is in general not a good quantum number in moving frames since the reflection at a plane perpendicular to  $\mathbf{P}$  also inverts the direction of the total momentum  $\mathbf{P}$ . In Ref. [126] it was shown that a helicity state with  $\lambda = 0$  is an eigenstate of a reflection at a plane with associated eigenvalue  $\tilde{\eta} = P(-1)^J$  which can be interpreted as the equivalent of parity in moving frames. Note that for  $\lambda \neq 0$  a helicity state is no eigenstate of a reflection at a plane and consequently  $\tilde{\eta}$  cannot be defined. Similar to the spin  $J$ , also the helicity  $\lambda$  is only a good quantum number in the continuum, so it also has to be subduced into the irreps of the relevant symmetry group. As the helicity  $\lambda$  for a given spin  $J$  can take values according to  $0 \leq \lambda \leq J$ , it is obvious that each value of  $\lambda$  refers to a bunch of spins  $J$  and consequently even more continuum spins  $J$  are subduced into the same irrep  $\Lambda$ . In Table 4.3 I list which helicities  $\lambda$  and which  $\tilde{\eta}$  can appear in each irrep of the symmetry groups  $C_{4v}$  and  $C_{2v}$ . In the last column I also give the associated quantum numbers  $J^P$  in the rest frame for each irrep. Note that the groups  $C_{4v}$  and  $C_{2v}$  describe the lattice symmetry for two particles with different masses in the moving frames with  $\mathbf{P}/(2\pi/L) = (0, 0, 1)^T$  and  $\mathbf{P}/(2\pi/L) = (1, 1, 0)^T$ , respectively. In the case of two particles with equal masses, the

Symmetry group	Irrep $\Lambda$	$\lambda^{\tilde{\eta}}$	$J^P$ (at rest)
$C_{4v}$ $\mathbf{d} = (0, 0, 1)^T$	$A_1$	$0^+, 4, \dots$	$0^+, 1^-, 2^+, 3^-, 4^+ \dots / 4^\pm, \dots$
	$A_2$	$0^-, 4, \dots$	$0^-, 1^+, 2^-, 3^+, 4^- \dots / 4^\pm, \dots$
	$E$	$1, 3, \dots$	$1^\pm, 2^\pm, 3^\pm, 4^\pm, \dots$
	$B_1$	$2, \dots$	$2^\pm, 3^\pm, 4^\pm, \dots$
	$B_2$	$2, \dots$	$2^\pm, 3^\pm, 4^\pm, \dots$
$C_{2v}$ $\mathbf{d} = (1, 1, 0)^T$	$A_1$	$0^+, 2, 4, \dots$	$0^+, 1^-, 2^+, 3^-, 4^+ \dots / 2^\pm, 3^\pm, 4^\pm, \dots$
	$A_2$	$0^-, 2, 4, \dots$	$0^-, 1^+, 2^-, 3^+, 4^- \dots / 2^\pm, 3^\pm, 4^\pm, \dots$
	$B_1$	$1, 3, \dots$	$1^\pm, 2^\pm, 3^\pm, 4^\pm, \dots$
	$B_2$	$1, 3, \dots$	$1^\pm, 2^\pm, 3^\pm, 4^\pm, \dots$

Table 4.3.: Lattice irreps  $\Lambda$  for the symmetry groups  $C_{4v}$  and  $C_{2v}$  together with the quantum numbers that are subduced into these irreps. The second column lists which helicities  $\lambda$  and which  $\tilde{\eta} = P(-1)^J$  can appear for each irrep, while the third column shows the associated  $J^P$  at rest.

relevant symmetry groups are  $D_{4h}$  for  $\mathbf{P}/(2\pi/L) = (0, 0, 1)^T$  and  $D_{2h}$  for  $\mathbf{P}/(2\pi/L) = (1, 1, 0)^T$ . Here, the subduction of continuum quantum numbers is slightly different. As discussed in Sec. 3.2, the symmetry groups  $D_{4h}$  and  $D_{2h}$  contain additional symmetry transformations like the inversion with respect to the origin. In particular, the irreps  $\Lambda^P$  of  $D_{4h}$  and  $D_{2h}$  are also characterized by the parity  $P$  so that a quantum number  $J^+$  cannot be subduced into an irrep  $\Lambda^-$  and vice versa. Accordingly, quantum numbers  $J^P$  with different parities cannot appear in the same irrep. For example, the quantum numbers  $1^-$  and  $3^-$  appearing in the irrep  $A_1$  of  $C_{4v}$  cannot appear in the  $A_1^+$  irrep of  $D_{4h}$ . Thus, only the quantum numbers  $0^+, 2^+$  and  $4^+$  are subduced into this irrep. I list the quantum numbers  $J^P$  with  $J \leq 4$  for each irrep  $\Lambda^P$  of the groups  $D_{4h}$  and  $D_{2h}$  in Table 4.4. Note that this subduction is also obtained by considering the decomposition of the representations  $\Gamma^{(l)}$  into irreps as done in Appendix B.2. More details on how to construct interpolating operators on the lattice can be found in Refs. [126–131].

Symmetry group	Irrep $\Lambda^P$	$J^P$ (at rest)
$D_{4h}$ $\mathbf{d} = (0, 0, 1)^T$	$A_1^\pm$	$0^\pm, 2^\pm, 4^\pm \dots$
	$A_2^\pm$	$1^\pm, 3^\pm, 4^\pm \dots$
	$E^\pm$	$1^\pm, 2^\pm, 3^\pm, 4^\pm, \dots$
	$B_1^\pm$	$2^\pm, 3^\pm, 4^\pm, \dots$
	$B_2^\pm$	$2^\pm, 3^\pm, 4^\pm, \dots$
$D_{2h}$ $\mathbf{d} = (1, 1, 0)^T$	$A^\pm$	$0^\pm, 2^\pm, 3^\pm, 4^\pm \dots$
	$B_1^\pm$	$1^\pm, 2^\pm, 3^\pm, 4^\pm \dots$
	$B_2^\pm$	$1^\pm, 2^\pm, 3^\pm, 4^\pm \dots$
	$B_3^\pm$	$1^\pm, 2^\pm, 3^\pm, 4^\pm \dots$

Table 4.4.: Lattice irreps  $\Lambda^P$  for the symmetry groups  $D_{4h}$  and  $D_{2h}$  together with the quantum numbers  $J^P$  at rest that are subduced into these irreps.

#### 4.2.2 Interpolating Operators and Correlation Function for Mesons

The interpolating operator for an ordinary meson built of a quark-antiquark pair  $\bar{Q}q$  whose quantum numbers are determined by the monomial of gamma matrices  $\Gamma$  is given by

$$\mathcal{O}_M(t) = \frac{1}{\sqrt{V_S}} \sum_{\mathbf{x}} \bar{Q}(\mathbf{x}, t) \Gamma q(\mathbf{x}, t) e^{i\mathbf{p}\mathbf{x}}. \quad (4.11)$$

Here, a Fourier transformation running over the spatial coordinates  $\mathbf{x}$  is performed to project the operator to a distinct momentum  $\mathbf{p}$ , while the normalization factor  $V_S = L^3$  indicates the spatial lattice volume. Accordingly, this operator describes a meson with definite spatial momentum  $\mathbf{p} = 2\pi\mathbf{n}/L$  with  $\mathbf{n} \in \mathbb{Z}^3$  located at the timeslice  $t$ , and the special case  $\mathbf{p} = 0$  is called zero momentum projection. The associated conjugated operator is given by

$$\mathcal{O}_M^\dagger(t) = \frac{1}{\sqrt{V_S}} \sum_{\mathbf{x}} \bar{q}(\mathbf{x}, t) \Gamma' Q(\mathbf{x}, t) e^{-i\mathbf{p}\mathbf{x}} \quad (4.12)$$

with  $\Gamma' = \gamma_0 \Gamma^\dagger \gamma_0$ . According to Eq. (4.1), the correlation function for a meson can be computed using the operators  $\mathcal{O}_M(t)$  and  $\mathcal{O}_M^\dagger(0)$ . Here, I will discuss the case of zero momentum projection, while the approach is similar for non-vanishing momenta. The

correlation function is then given by

$$\begin{aligned}
 C(t) &= \langle \mathcal{O}_M(t) \mathcal{O}_M^\dagger(0) \rangle = \frac{1}{V_S} \sum_{\mathbf{x}, \mathbf{y}} \left\langle \left( \bar{Q}(\mathbf{x}, t) \Gamma q(\mathbf{x}, t) \right) \left( \bar{q}(\mathbf{y}, 0) \Gamma' Q(\mathbf{y}, 0) \right) \right\rangle_{F,U} \\
 &= \frac{1}{V_S} \sum_{\mathbf{x}, \mathbf{y}} \Gamma_{AB} \Gamma'_{CD} \left\langle \bar{Q}_A^a(\mathbf{x}, t) q_B^a(\mathbf{x}, t) \bar{q}_C^b(\mathbf{y}, 0) Q_D^b(\mathbf{y}, 0) \right\rangle_{F,U} \\
 &= -\frac{1}{V_S} \sum_{\mathbf{x}, \mathbf{y}} \Gamma_{AB} \Gamma'_{CD} \left\langle \langle q_B^a(\mathbf{x}, t) \bar{q}_C^b(\mathbf{y}, 0) \rangle_F \langle Q_D^b(\mathbf{y}, 0) \bar{Q}_A^a(\mathbf{x}, t) \rangle_F \right\rangle_U \\
 &= -\frac{1}{V_S} \sum_{\mathbf{x}, \mathbf{y}} \Gamma_{AB} \Gamma'_{CD} \left\langle \left( (D^{(q)})^{-1}{}^{ab}{}_{BC}(x; y) \right) \left( (D^{(Q)})^{-1}{}^{ba}{}_{DA}(y; x) \right) \right\rangle_U.
 \end{aligned} \tag{4.13}$$

In the last step, Wick's theorem has been applied to compute the fermionic expectation value of two fermion fields according to Eq. (2.20), giving rise to the quark propagators. These can be estimated by inverting the Dirac operator of the fermion action. I present several inversion techniques applied in this work in Sec. 4.4. Exploiting the structure of the spin and color indices, Eq. (4.13) can be written as a trace. Using finally  $\gamma_5$ -hermiticity to get rid of backwards propagators yields

$$C(t) = -\frac{1}{V_S} \sum_{\mathbf{x}, \mathbf{y}} \left\langle \text{Tr} \left[ (D^{(q)})^{-1}(x; y) \Gamma' \gamma_5 \left( (D^{(Q)})^{-1}(x; y) \right)^\dagger \gamma_5 \Gamma \right] \right\rangle_U. \tag{4.14}$$

Here,  $\langle \dots \rangle_U$  denotes the path integral expectation value over the gauge fields. As already mentioned, in lattice calculations, one computes Eq. (4.14) for each gauge link configuration separately, while the final estimate for the correlation function is governed by averaging these results according to Eq. (2.21).

To investigate whether the  $\bar{Q}\bar{Q}'qq'$  four-quark systems of interest in this work are hadronically stable, their ground-state energies must be compared to the lowest meson-meson thresholds. Thus, the masses of the pseudoscalar and vector  $B$ ,  $B_s$  and  $D$  mesons are required which are determined using the interpolating operators

$$\mathcal{O}_B(\mathbf{p}) = \frac{1}{\sqrt{V_S}} \sum_{\mathbf{x}} \bar{b}(\mathbf{x}) \gamma_5 u(\mathbf{x}) e^{i\mathbf{p}\mathbf{x}}, \tag{4.15}$$

$$\mathcal{O}_{B^*}(\mathbf{p}) = \frac{1}{\sqrt{V_S}} \sum_{\mathbf{x}} \bar{b}(\mathbf{x}) \gamma_j u(\mathbf{x}) e^{i\mathbf{p}\mathbf{x}}, \tag{4.16}$$

$$\mathcal{O}_{B_s}(\mathbf{p}) = \frac{1}{\sqrt{V_S}} \sum_{\mathbf{x}} \bar{b}(\mathbf{x}) \gamma_5 s(\mathbf{x}) e^{i\mathbf{p}\mathbf{x}}, \tag{4.17}$$

$$\mathcal{O}_{B_s^*}(\mathbf{p}) = \frac{1}{\sqrt{V_S}} \sum_{\mathbf{x}} \bar{b}(\mathbf{x}) \gamma_j s(\mathbf{x}) e^{i\mathbf{p}\mathbf{x}}, \tag{4.18}$$

$$\mathcal{O}_D(\mathbf{p}) = \frac{1}{\sqrt{V_S}} \sum_{\mathbf{x}} \bar{c}(\mathbf{x}) \gamma_5 u(\mathbf{x}) e^{i\mathbf{p}\mathbf{x}}, \tag{4.19}$$

$$\mathcal{O}_{D^*}(\mathbf{p}) = \frac{1}{\sqrt{V_S}} \sum_{\mathbf{x}} \bar{c}(\mathbf{x}) \gamma_j u(\mathbf{x}) e^{i\mathbf{p}\mathbf{x}}, \tag{4.20}$$

while I omit from now on the time coordinate.

### 4.2.3 Interpolating Operators for $\bar{Q}\bar{Q}'qq'$ Four-Quark Systems

In order to compute the low-lying energy spectrum of the  $\bar{Q}\bar{Q}'qq'$  four-quark systems of interest, an appropriate operator basis that describes the correct quantum numbers and generates good overlap with the physical states is required.

In the case of the  $\bar{b}\bar{b}ud$  system, I consider the quantum numbers  $I(J^P) = 0(1^+)$ . The choice of isospin  $I = 0$  is motivated by previous studies where it has been found that the  $I = 0$  channel is more attractive than the  $I = 1$  channel [27, 31]. The spin  $J$  is then fixed due to symmetry considerations of the wave functions of the antiquark  $\bar{b}\bar{b}$  and the diquark  $ud$  [30]. Since both, diquark and antiquark are assumed to be in a symmetric  $S$ -wave and to form an antisymmetric color antitriplet and triplet, respectively, the flavor-spin wave function must be symmetric following the Pauli principle. As for the antiquark  $\bar{b}\bar{b}$  the flavor is symmetric, its spin must be 1, while for the flavor-antisymmetric light quarks  $ud$ , spin 0 follows. Consequently, the total spin is  $J = 1$ .

For the  $\bar{b}\bar{b}us$  system, the only channel that is expected to be sufficiently attractive to form a bound state has quantum numbers  $J^P = 1^+$  [32]. This can be motivated by assuming an  $SU(3)$  flavor symmetry for the three lightest quarks  $u, d, s$  which holds reasonably well for elementary particles [132, 133]. Then, the same chain of reasoning as discussed for the  $\bar{b}\bar{b}ud$  system also applies to the  $\bar{b}\bar{b}us$  system. Consequently, the most attractive channel is found to have total spin  $J = 1$ .

For quark content  $\bar{b}\bar{c}ud$ , I consider again isospin  $I = 0$  following the same arguments as discussed for the  $\bar{b}\bar{b}ud$  system. However, two promising channels exist for the  $\bar{b}\bar{c}ud$  system since the heavy antiquark can be arranged either in a symmetric or in an antisymmetric flavor combination. For the flavor symmetric heavy antiquark, the quantum numbers are given by  $I(J^P) = 0(1^+)$  so this channel is conceptually similar to the  $\bar{b}\bar{b}ud$  channel with  $I(J^P) = 0(1^+)$  and the  $\bar{b}\bar{b}us$  channel with  $J^P = 1^+$ . The antisymmetric flavor combination of the heavy antiquark leads to the total spin  $J = 0$ , and accordingly the quantum numbers for this channel are given by  $I(J^P) = 0(0^+)$ .

For all four-quark states, I employ local interpolating operators as well as scattering interpolating operators. Local operators are built of four quarks which are all located at the same position in space while the total momentum of the four quarks is projected to zero. Meanwhile, scattering operators describe a pair of two heavy-light mesons which are placed at different locations in space. The momentum of each meson is separately projected to zero. In the case of local operators, I distinguish between meson-meson and diquark-antiquark operators. A schematic representation of the different operator types can be found in Fig. 4.1.

Both types of meson-meson operators correspond to pairs of mesons whose overall quantum numbers coincide with those of the investigated four-quark state. For every local meson-meson operator a scattering operator rendering the same two mesons is included in the operator basis [24]. The diquark-antiquark operators resemble a substructure consisting of a heavy antiquark  $\bar{Q}\bar{Q}'$  and a light diquark  $qq'$  and have been

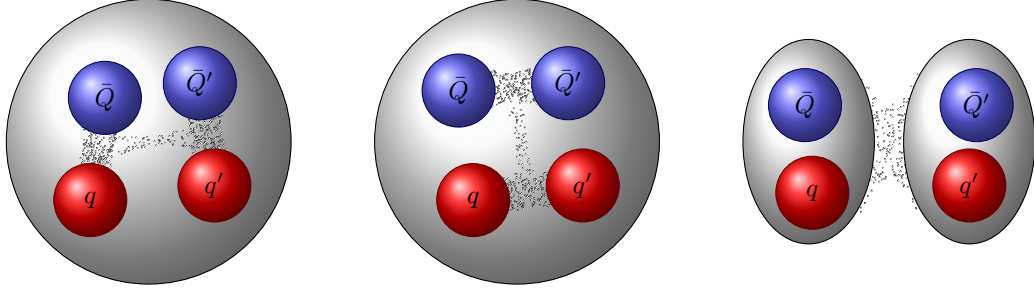


Figure 4.1.: Schematic representation of a local meson-meson operator (left), a local diquark-antidiquark operator (center) and a scattering meson-meson operator (right). Heavy quarks are depicted by blue balls while light quarks are represented by red balls. The small white circles illustrate exchange gluons indicating the dominant interactions of each structure.

shown to play an important role for four-quark states [134–136]. Sticking to Jaffe’s characterization of “good” and “bad” diquarks [134], a “good” diquark has quantum numbers  $J^P = 0^+$ , while a “bad” diquark is characterized by  $J^P = 1^+$ . The scalar “good” diquark is expected to lead to a smaller mass and thus is favorable. This mass splitting between “good” and “bad” diquark gets milder for heavier quarks. Therefore, I construct the diquark-antidiquark operators in all cases such that the light diquarks ( $ud$  or  $us$ ) correspond to a “good” diquark. If possible, also the heavy antidiquark is constructed as a “good” diquark (which is only possible for quantum numbers  $I(J^P) = 0(0^+)$  in the case of  $\bar{b}cud$ ), otherwise I use the “bad” diquark.

As the main objective of this work is to study the low-lying energy levels of the previously mentioned four-quark systems with a particular interest in the ground-state energy, it is mandatory to resolve all low-lying energy levels in sufficiently precise way. I expect that a trial state generated by a local interpolating operator will have good overlap with the ground state which might be a bound four-quark state. Moreover, the scattering operators should describe meson-meson scattering states close to the lowest meson-meson threshold quite well. If a bound four-quark state exists which might be close to this threshold, resolving those meson-meson scattering states will eliminate their contributions to the ground state and improve the fit results for the ground-state energy [24].

For the bound state analysis carried out in Chapters 5 and 6, I consider only the center-of-momentum frame with total momentum  $\mathbf{P} = 0$ , so the associated symmetry group describing the lattice symmetry is  $O_h$ . According to Sec. 4.2.1, the interpolating operators for the four-quark systems with quantum numbers  $J^P = 1^+$  are constructed in the  $T_1^+$  irrep of  $O_h$ , while the operators for four-quark systems with  $J^P = 0^+$  are designed to transform like the  $A_1^+$  irrep of  $O_h$  [118].

#### 4.2.3.1. Interpolating Operators for $\bar{b}\bar{b}ud$ with $I(J^P) = 0(1^+)$

In the case of  $\bar{b}\bar{b}ud$  with quantum numbers  $I(J^P) = 0(1^+)$  we consider the two lowest meson-meson thresholds  $BB^*$  and  $B^*B^*$  which differ only by approximately 45 MeV. The first three-particle threshold with correct quark content is  $BB\pi$  which is 44 MeV above the  $B^*B^*$  threshold. Note, however, that this three-meson channel would have to appear as  $P$ -wave to render the quantum numbers correctly so it is further suppressed. Additionally, I assume that the coupling to three-particle channels is negligible compared to the coupling to two-particle channels and hence I do not consider three-meson thresholds. I also exclude baryon-antibaryon thresholds as according to Ref. [137] the mass of  $\bar{\Xi}_{bb}N$  is more than 500 MeV higher than the  $B^*B^*$  mass.

Consequently, I use three local interpolating operators, two meson-meson operators and one diquark-antidiquark operator, given by

$$\mathcal{O}_1 = \mathcal{O}_{[BB^*](0)} = \frac{1}{\sqrt{V_S}} \sum_{\mathbf{x}} \bar{b}\gamma_5 u(\mathbf{x}) \bar{b}\gamma_j d(\mathbf{x}) - (d \leftrightarrow u), \quad (4.21)$$

$$\mathcal{O}_2 = \mathcal{O}_{[B^*B^*](0)} = \frac{1}{\sqrt{V_S}} \epsilon_{jkl} \sum_{\mathbf{x}} \bar{b}\gamma_k u(\mathbf{x}) \bar{b}\gamma_l d(\mathbf{x}) - (d \leftrightarrow u), \quad (4.22)$$

$$\mathcal{O}_3 = \mathcal{O}_{[Dd](0)} = \frac{1}{\sqrt{V_S}} \sum_{\mathbf{x}} \bar{b}^a \gamma_j \mathcal{C} \bar{b}^{b,T}(\mathbf{x}) u^{a,T} \mathcal{C} \gamma_5 d^b(\mathbf{x}) - (d \leftrightarrow u). \quad (4.23)$$

The operator basis is completed by the two scattering operators

$$\mathcal{O}_4 = \mathcal{O}_{B(0)B^*(0)} = \frac{1}{V_S} \left( \sum_{\mathbf{x}} \bar{b}\gamma_5 u(\mathbf{x}) \right) \left( \sum_{\mathbf{y}} \bar{b}\gamma_j d(\mathbf{y}) \right) - (d \leftrightarrow u), \quad (4.24)$$

$$\mathcal{O}_5 = \mathcal{O}_{B^*(0)B^*(0)} = \frac{1}{V_S} \epsilon_{jkl} \left( \sum_{\mathbf{x}} \bar{b}\gamma_k u(\mathbf{x}) \right) \left( \sum_{\mathbf{y}} \bar{b}\gamma_l d(\mathbf{y}) \right) - (d \leftrightarrow u). \quad (4.25)$$

Hereby, summation over the color indices  $a, b$  as well as the spacial vector indices  $j, k, l$  is implied. For open spatial indices, I average over all three directions. The matrix  $\mathcal{C}$  appearing in the diquark-antidiquark operator  $\mathcal{O}_{[Dd](0)}$  is the charge conjugation matrix defined as  $\mathcal{C} = \gamma_0 \gamma_5$ . To take account of the isospin  $I = 0$ , the operators are constructed using the antisymmetric light flavor combination  $ud - du$ .

At first glance, one might argue that the operator  $\mathcal{O}_{[B^*B^*](0)}$  is negligible as the two  $B^*$  mesons are heavier than one  $B$  and one  $B^*$  meson. However, an investigation using static heavy quarks [32] showed that the operator resembling the  $B^*B^*$  structure contributes similarly to the ground-state wave function as a  $BB^*$  structure. Therefore, I consider both operators as important.

#### 4.2.3.2. Interpolating Operators for $\bar{b}\bar{b}us$ with $J^P = 1^+$

The  $\bar{b}\bar{b}us$  four-quark system with  $J^P = 1^+$  does not exhibit the  $SU(2)$  flavor symmetry that is observed for  $\bar{b}\bar{b}ud$ . For this reason, instead of two, there are three relevant meson-meson thresholds that should be taken into account. The two lowest thresholds

$BB_s^*$  and  $B^*B_s$  differ only by 3 MeV, and the following threshold  $B^*B_s^*$  is also only 49 MeV above the  $BB_s^*$  threshold. Similar to  $\bar{b}b\bar{u}d$ , the lowest three-particle threshold  $BB_s\pi$  in  $P$ -wave and the lowest baryon-antibaryon threshold  $\bar{\Xi}_{bb}\Sigma$  (which is approximately 600 MeV above the  $B^*B_s^*$  threshold) are negligible.

Accordingly, I use three local meson-meson operators and one local diquark-antidiquark operator,

$$\mathcal{O}_1 = \mathcal{O}_{[BB_s^*](0)} = \frac{1}{\sqrt{V_S}} \sum_{\mathbf{x}} \bar{b}\gamma_5 u(\mathbf{x}) \bar{b}\gamma_j s(\mathbf{x}), \quad (4.26)$$

$$\mathcal{O}_2 = \mathcal{O}_{[B^*B_s](0)} = \frac{1}{\sqrt{V_S}} \sum_{\mathbf{x}} \bar{b}\gamma_j u(\mathbf{x}) \bar{b}\gamma_5 s(\mathbf{x}), \quad (4.27)$$

$$\mathcal{O}_3 = \mathcal{O}_{[B^*B_s^*](0)} = \frac{1}{\sqrt{V_S}} \epsilon_{jkl} \sum_{\mathbf{x}} \bar{b}\gamma_k u(\mathbf{x}) \bar{b}\gamma_l s(\mathbf{x}), \quad (4.28)$$

$$\mathcal{O}_4 = \mathcal{O}_{[Dd](0)} = \frac{1}{\sqrt{V_S}} \sum_{\mathbf{x}} \bar{b}^a \gamma_j \mathcal{C} \bar{b}^{b,T}(\mathbf{x}) u^{a,T} \mathcal{C} \gamma_5 s^b(\mathbf{x}), \quad (4.29)$$

and three scattering operators given by

$$\mathcal{O}_5 = \mathcal{O}_{B(0)B_s^*(0)} = \frac{1}{V_S} \left( \sum_{\mathbf{x}} \bar{b}\gamma_5 u(\mathbf{x}) \right) \left( \sum_{\mathbf{y}} \bar{b}\gamma_j s(\mathbf{y}) \right), \quad (4.30)$$

$$\mathcal{O}_6 = \mathcal{O}_{B^*(0)B_s(0)} = \frac{1}{V_S} \left( \sum_{\mathbf{x}} \bar{b}\gamma_j u(\mathbf{x}) \right) \left( \sum_{\mathbf{y}} \bar{b}\gamma_5 s(\mathbf{y}) \right), \quad (4.31)$$

$$\mathcal{O}_7 = \mathcal{O}_{B^*(0)B_s^*(0)} = \frac{1}{V_S} \epsilon_{jkl} \left( \sum_{\mathbf{x}} \bar{b}\gamma_k u(\mathbf{x}) \right) \left( \sum_{\mathbf{y}} \bar{b}\gamma_l s(\mathbf{y}) \right). \quad (4.32)$$

As already mentioned, I do not utilize an antisymmetric flavor combination for  $\bar{b}b\bar{u}s$  so also the operators are not designed accordingly. Note, however, that the operators  $\mathcal{O}_3$ ,  $\mathcal{O}_4$  and  $\mathcal{O}_7$  are by construction antisymmetric in the light quark flavors. The operators  $\mathcal{O}_1$  and  $\mathcal{O}_2$  as well as  $\mathcal{O}_5$  and  $\mathcal{O}_6$  can be linearly combined such that one flavor symmetric and one flavor antisymmetric operator is obtained [24].

#### 4.2.3.3. Interpolating Operators for $\bar{b}\bar{c}ud$ with $I(J^P) = 0(0^+)$

The two lowest meson-meson thresholds for the case of  $\bar{b}\bar{c}ud$  with  $I(J^P) = 0(0^+)$  are given by  $BD$  and  $B^*D^*$ . As the  $B^*D^*$  threshold is approximately 190 MeV above the  $BD$  threshold, I expect that the associated  $B^*D^*$  meson-meson operator is not required to study a possibly existing tetraquark bound state below the  $BD$  threshold. Following the argumentation for the  $\bar{b}b\bar{u}d$  system, the lowest three-meson threshold  $B^*D\pi$  in  $P$ -wave and the lowest baryon-antibaryon threshold  $\bar{\Xi}_{cb}N$  are not considered.



The two local operators that I use are

$$\mathcal{O}_1 = \mathcal{O}_{[BD](0)} = \frac{1}{\sqrt{V_S}} \sum_{\mathbf{x}} \bar{b} \gamma_5 u(\mathbf{x}) \bar{c} \gamma_5 d(\mathbf{x}) - (d \leftrightarrow u), \quad (4.33)$$

$$\mathcal{O}_2 = \mathcal{O}_{[Dd](0)} = \frac{1}{\sqrt{V_S}} \sum_{\mathbf{x}} \bar{b}^a \gamma_5 \mathcal{C} \bar{c}^{b,T}(\mathbf{x}) u^{a,T} \mathcal{C} \gamma_5 d^b(\mathbf{x}) - (d \leftrightarrow u), \quad (4.34)$$

and the single scattering operator is

$$\mathcal{O}_3 = \mathcal{O}_{B(0)D(0)} = \frac{1}{V_S} \left( \sum_{\mathbf{x}} \bar{b} \gamma_5 u(\mathbf{x}) \right) \left( \sum_{\mathbf{y}} \bar{c} \gamma_5 d(\mathbf{y}) \right) - (d \leftrightarrow u). \quad (4.35)$$

As for  $\bar{b}\bar{c}ud$ , the light quarks  $ud$  are arranged in an antisymmetric flavor combination to ensure isospin  $I = 0$ . The heavy antiquarks  $\bar{b}\bar{c}$  are also in an antisymmetric flavor combination allowing total spin  $J = 0$ . Note that this is not possible for the heavy antiquark  $\bar{b}\bar{b}$  which is always flavor symmetric.

#### 4.2.3.4. Interpolating Operators for $\bar{b}\bar{c}ud$ with $I(J^P) = 0(1^+)$

For the  $\bar{b}\bar{c}ud$  four-quark system with  $I(J^P) = 0(1^+)$ , the three lowest meson-thresholds are  $B^*D$ ,  $BD^*$  and  $B^*D^*$ . As in the case of  $J = 0$ , I do not consider the  $B^*D^*$  threshold while the remaining two lowest thresholds  $B^*D$  and  $BD^*$  are separated by approximately 100 MeV. As before, the relevant three-meson threshold  $BD\pi$  in  $P$ -wave is expected to be strongly suppressed and the lowest baryon-antibaryon threshold  $\bar{\Xi}_{cb}N$  is significantly above the lowest meson-meson threshold [137]. This leads to the three local operators

$$\mathcal{O}_1 = \mathcal{O}_{[B^*D](0)} = \frac{1}{\sqrt{V_S}} \sum_{\mathbf{x}} \bar{b} \gamma_j u(\mathbf{x}) \bar{c} \gamma_5 d(\mathbf{x}) - (d \leftrightarrow u), \quad (4.36)$$

$$\mathcal{O}_2 = \mathcal{O}_{[BD^*](0)} = \frac{1}{\sqrt{V_S}} \sum_{\mathbf{x}} \bar{b} \gamma_5 u(\mathbf{x}) \bar{c} \gamma_j d(\mathbf{x}) - (d \leftrightarrow u), \quad (4.37)$$

$$\mathcal{O}_3 = \mathcal{O}_{[Dd](0)} = \frac{1}{\sqrt{V_S}} \sum_{\mathbf{x}} \bar{b}^a \gamma_j \mathcal{C} \bar{c}^{b,T}(\mathbf{x}) u^{a,T} \mathcal{C} \gamma_5 d^b(\mathbf{x}) - (d \leftrightarrow u), \quad (4.38)$$

and the two scattering operators

$$\mathcal{O}_4 = \mathcal{O}_{B^*(0)D(0)} = \frac{1}{V_S} \left( \sum_{\mathbf{x}} \bar{b} \gamma_j u(\mathbf{x}) \right) \left( \sum_{\mathbf{y}} \bar{c} \gamma_5 d(\mathbf{y}) \right) - (d \leftrightarrow u), \quad (4.39)$$

$$\mathcal{O}_5 = \mathcal{O}_{B(0)D^*(0)} = \frac{1}{V_S} \left( \sum_{\mathbf{x}} \bar{b} \gamma_5 u(\mathbf{x}) \right) \left( \sum_{\mathbf{y}} \bar{c} \gamma_j d(\mathbf{y}) \right) - (d \leftrightarrow u). \quad (4.40)$$

Isospin  $I = 0$  is realized by an antisymmetric flavor combination for the light quarks  $ud$ , while the heavy quarks are in a symmetric flavor combination which yields a total spin of  $J = 1$ .

Finally constructing the correlation matrix elements as defined in Eq. (4.8) for the four-quark interpolating operators follows the same approach as discussed in Sec. 4.2.2 for meson interpolating operators. Some more details about the correlation matrices of the tetraquark systems can be found in Appendix C while I illustrate the derivation of the correlation functions for some selected operator combinations in Appendix C.1. Note that some beneficial analytical properties of lattice QCD like charge conjugation and time reversal can be employed to improve the results of a lattice QCD calculation. In fact, the correlation matrix  $C(t)$  is found to be real and symmetric and the matrix elements  $C_{jk}(+t)$  and  $C_{jk}(-t)$  can be related, so that the statistical uncertainties can be reduced by averaging related correlation functions appropriately.

### 4.3 Techniques to Extract Energy Levels from Correlation Matrices

As discussed in the previous section, a large basis of interpolating operators is used to describe the investigated four-quark states. Thus, the correlation function in Eq. (4.1) is replaced by a correlation matrix according to Eq. (4.8),

$$C_{jk}(t) = \langle \mathcal{O}_j(t) \mathcal{O}_k^\dagger(0) \rangle. \quad (4.41)$$

As a consequence, more elaborated techniques are required to extract the low-lying energy levels from the correlation matrix. The starting point is a spectral decomposition analogous to the scalar case (see Sec. 4.1) yielding

$$C_{jk}(t) = \sum_{n=0}^{\infty} \langle 0 | \mathcal{O}_j | n \rangle \langle n | \mathcal{O}_k^\dagger | 0 \rangle e^{-E_n t} = \sum_{n=0}^{\infty} Z_j^n (Z_k^n)^* e^{-E_n t}, \quad (4.42)$$

with the overlap factors

$$Z_j^n = \langle 0 | \mathcal{O}_j | n \rangle. \quad (4.43)$$

Extracting the low-lying energy spectrum from this correlation matrix can be achieved using special techniques. In this work, I apply two different methods, first the variational method and second a multi-exponential matrix fitting. The actual choice which method is used depends on the shape of the correlation matrix.

#### 4.3.1 Variational Method

The variational method provides a well-established way to extract the low-lying energy spectrum from a correlation matrix  $C(t)$ . The basic idea of this approach is that the eigenvalues  $\lambda_n(t)$  of the correlation matrix behave like

$$\lambda_n(t) \propto e^{-E_n t} \left[ 1 + \mathcal{O}(e^{-\bar{\Delta} E_n t}) \right], \quad (4.44)$$

where  $E_n$  is the  $n$ -th energy level and  $\bar{\Delta} E_n$  its distance to nearby energy levels of the spectrum [50]. Thus, corrections to the energy level  $E_n$  decrease exponentially for large times  $t$  [110, 138, 139]. As in practice the correlation matrix  $C(t)$  cannot be

computed very accurately for arbitrary large times  $t$ , the error in Eq. (4.44) might not be negligible. It has been found that better results are obtained if the eigenvalues  $\lambda_n(t, t_0)$  of the generalized eigenvalue problem (GEVP)

$$C(t) v_n(t, t_0) = \lambda_n(t, t_0) C(t_0) v_n(t, t_0), \quad n = 1, \dots, N, \quad t > t_0 \quad (4.45)$$

are considered [139] where  $N$  denotes the number of operators, i.e., the size of the correlation matrix. The normalization at time  $t_0$  improves the signal as contributions of higher excited states are suppressed and the eigenvalues  $\lambda_n(t, t_0)$  behave like

$$\lambda_n(t, t_0) \propto e^{-E_n(t-t_0)} \quad (4.46)$$

for sufficiently large times  $t$ . The energy levels  $E_n$  can be extracted from the eigenvalues  $\lambda_n(t, t_0)$  either by computing the effective energy according to

$$aE_{\text{eff},n}(t) = \ln \left( \frac{\lambda_n(t, t_0)}{\lambda_n(t+a, t_0)} \right) \quad (4.47)$$

and fitting a constant to its plateau-like region in  $t$  or by performing a correlated  $\chi^2$ -minimizing single exponential fit using Eq. (4.46) as the fit function. In this work the energy levels are primarily determined using single exponential fits, while in all cases agreement with the results obtained from a constant fit to the effective energy is found. The parameter  $t_0$  is always chosen rather small as the correlation functions become noisier for large temporal separations but still sufficiently large so that the energies  $E_n$  are independent of the actual choice of  $t_0$ .

### 4.3.2 Multi-exponential Matrix Fitting

An alternative approach to extracting the energy levels  $E_n$  and the overlap factors  $Z_j^n$  from a correlation matrix as given in Eq. (4.42) is a correlated  $\chi^2$ -minimizing multi-exponential matrix fit. The associated fit function is given by a truncated version of Eq. (4.42),

$$C_{jk}^{\text{fit}}(t) = \sum_{n=0}^{N-1} Z_j^n (Z_k^n)^* e^{-E_n t}, \quad (4.48)$$

while the temporal fit range  $t_{\min} \leq t \leq t_{\max}$  must be chosen in such a way that contributions of excited states with  $n \geq N$  can be neglected.

The multi-exponential fits in this work are carried out with the QMBF application [140]. Here, the overlap factors for  $n > 0$  are written as  $Z_j^n = B_j^n Z_j^0$ , while the  $B_j^n$  are used as fit parameters. Moreover, in order to guarantee that the energies  $E_n$  obtained in the fit are ordered, the logarithms of the energy differences  $g_n = \ln(aE_n - aE_{n-1})$  are used as fit parameters for  $n > 0$ .

Note that if the size of the correlation matrix increases, the number of fit parameters will grow significantly, which makes multi-exponential matrix fits much more challenging. Thus, for large square correlation matrices, the variational method is preferable. However, multi-exponential fits are not restricted to square matrices so that also non-square correlation matrices can be analyzed using this approach.

## 4.4 Techniques to Compute Quark Propagators

Quark propagators are the essential ingredient to calculate correlation functions as discussed in Sec. 4.2.2. In the subsequent paragraphs, I will present the techniques that are employed in this work to compute the quark propagators which are required to determine correlation matrices for tetraquark systems. The entries of a quark propagator  $G_{AB}^{(f)ab}(x; y) \equiv (D^{(f)})^{-1ab}_{AB}(x; y)$  connect two points  $(x, a, A)$  and  $(y, b, B)$  which are often labeled as the source and sink position. We obtain the all-to-all quark propagator  $G^{(f)}$  as the inverse of the Dirac operator  $D^{(f)}$  according to

$$\sum_{y,b,B} D_{AB}^{(f)ab}(x; y) G_{BC}^{(f)bc}(y; z) = \delta_{ac} \delta_{AC} \delta(x, z) \quad (4.49)$$

for a particular flavor  $f$  [50]. This equation needs to be evaluated  $12 \times N_s^3 \times N_t$  times<sup>1</sup> to obtain the full quark propagator. For modern lattice sizes,  $G^{(f)}$  has  $\mathcal{O}(10^{13})$  entries. This makes an exact inversion impossible as storing this large matrix would require too much memory and its computation would be numerically too expensive. Moreover, the quark propagator describes the propagation in one particular gauge link configuration which means that the entries of the matrix are highly correlated [50]. Therefore, attempting to determine the full propagator is not reasonable, whereas a suitable approach is to compute only those parts which are required for an appropriate estimate of the quark propagator with respect to the correlation functions of interest. The starting point for most techniques is to consider the system of linear equations,

$$\sum_{y,b,B} D_{AB}^{(f)ab}(x; y) \phi_B^{(f)b}(y) = \xi_A^a(x) \quad (4.50)$$

and determine the solution  $\phi^{(f)}$  for a given source term  $\xi$ . This solution  $\phi^{(f)}$  is an estimate for a column of the quark propagator  $G^{(f)}$  as shown in the following sections. Solving Eq. (4.50) for a particular choice of indices is often called an ‘‘inversion’’. Numerically,  $\phi$  is determined up to certain precision using iterative methods such as a conjugate gradient solver (CG) [141], the bi-conjugate gradient stabilized solver (Bi-CGStab) [142] or a multi grid solver (MG) [143–147].

### 4.4.1 Point-to-all Propagators

Since QCD is spatially translational invariant, in many cases it is sufficient to compute the quark propagator from a fixed space-time position to all other points on the lattice. This propagator is obtained by solving

$$\sum_{y,b,B} D_{AB}^{(f)ab}(x; y) \phi_B^{(f)b}(y)[c, C, z] = \xi_A^a(x)[c, C, z], \quad (4.51)$$

where  $\xi_A^a(x)[c, C, z]$  is a point source given by

$$\xi_A^a(x)[c, C, z] = \delta_{ac} \delta_{AC} \delta(x, z). \quad (4.52)$$

---

<sup>1</sup>The integer 12 is obtained by number of color components times number of Dirac components.

The indices in the square brackets  $[c, C, z]$  denote the fixed color, spin and space-time indices, i.e., the location of the point source. Taking the spin and color structure into account, Eq. (4.51) must be solved for all 12 spin-color indices to obtain the 12 solutions  $\phi^{(f)b}_B(y)[c, C, z]$  connecting the space-time position  $z$  with all other points. Multiplying both sides of Eq. (4.51) with the quark propagator  $G^{(f)}$ , we can identify

$$\phi^{(f)b}_B(y)[c, C, z] = G^{(f)bc}_{BC}(y; z), \quad (4.53)$$

which is referred to as a so-called point-to-all propagator. For example, expressing the correlation function in Eq. (4.14) in terms of point-to-all propagators yields

$$C(t) = - \sum_{\mathbf{x}} \left\langle \text{Tr} \left[ (\Gamma' \gamma_5)_{AB} \left( \phi^{(f)}(x)[b, B, y] \gamma_5 \Gamma \phi^{(f)\dagger}(x)[b, A, y] \right) \right] \right\rangle_U. \quad (4.54)$$

Using translational invariance, the sum over  $\mathbf{y}$  has been replaced by a factor  $V_s$  and  $\mathbf{y}$  is fixed to the arbitrary source location.

While point-to-all propagators provide a rather straightforward way of computing quark propagators, there is one severe disadvantage: This method can only be used if all propagators of a particular correlation function start at the same point  $\mathbf{y}$ . Especially for four-quark systems so-called scattering operators (see Sec. 4.2.3), which rely on quark propagators starting at different positions in space-time, become important. Consequently, an effective method to calculate also all-to-all propagators is required.

#### 4.4.2 Stochastic Timeslice-to-all Propagators

Even if it is numerically not feasible to exactly compute the full all-to-all propagator from any space-time position  $x$  to any other position  $y$ , it is possible to make a stochastic estimate [148–151]. One method which is commonly used are so-called stochastic timeslice-to-all propagators. Hereby, a stochastic estimate of a propagator from all spatial positions  $\mathbf{x}$  of a fixed timeslice  $t_0$  to any other space-time point  $y$  is computed. To that end, we introduce  $N_R$  stochastic sources

$$\xi_A^a(\mathbf{x})[t_0, r] = \delta(x_0, t_0) \eta_A^a(\mathbf{x})[r], \quad (4.55)$$

where  $\eta_A^a(\mathbf{x})[r]$  with  $r = 1, \dots, N_R$  denotes a random number and the set of random numbers must obey

$$\frac{1}{N_R} \sum_{r=1}^{N_R} \eta_A^a(\mathbf{x})[r] \eta_B^{*b}(\mathbf{y})[r] = \delta_{ab} \delta_{AB} \delta(\mathbf{x}, \mathbf{y}) + \text{unbiased noise}. \quad (4.56)$$

Commonly one uses so-called  $\mathbb{Z}(2)$  noise, which means that the complex random numbers are given by  $\eta_A^a(\mathbf{x})[r] \in \mathbb{Z}(2) \times \mathbb{Z}(2)$ . The introduced unbiased noise for this choice is  $\mathcal{O}(1/\sqrt{N_R})$ . The resulting  $N_R$  systems of linear equations that need to be solved for the given stochastic sources are found to be

$$\sum_{y,b,B} D^{(f)ab}_{AB}(x; y) \phi^{(f)b}_B(y)[t_0, r] = \xi_A^a(x)[t_0, r]. \quad (4.57)$$

Multiplying Eq. (4.57) with  $\xi_C^{*c}(z)[t_0, r]$  and  $G_{DA}^{(f)da}(u; x)$  and summing over all noise terms  $r$ , the quark propagator can be written in terms of the  $N_R$  stochastic sources  $\xi$  and the associated solutions  $\phi^{(f)}$  of Eq. (4.57):

$$\begin{aligned}
 & \frac{1}{N_R} \sum_{r=1}^{N_R} \sum_{x,a,A} \sum_{y,b,B} \xi_C^{*c}(z)[t_0, r] G_{DA}^{(f)da}(u; x) D_{AB}^{(f)ab}(x; y) \phi_B^{(f)b}(y)[t_0, r] \\
 &= \frac{1}{N_R} \sum_{r=1}^{N_R} \sum_{x,a,A} \xi_A^a(x)[t_0, r] \xi_C^{*c}(z)[t_0, r] G_{DA}^{(f)da}(u; x) \\
 \Leftrightarrow & \frac{1}{N_R} \sum_{r=1}^{N_R} \sum_{y,b,B} \delta(u, y) \delta_{db} \delta_{DB} \xi_C^{*c}(z)[t_0, r] \phi_B^{(f)b}(y)[t_0, r] \\
 &= \sum_{x,a,A} G_{DA}^{(f)da}(u; x) \left( \delta_{ac} \delta_{AC} \delta(x, z) \delta(z_0, t_0) + \text{unbiased noise} \right) \\
 \Leftrightarrow & \frac{1}{N_R} \sum_{r=1}^{N_R} \xi_C^{*c}(z)[t_0, r] \phi_D^{(f)d}(u)[t_0, r] \\
 &= G_{DC}^{(f)dc}(u; \mathbf{z}, t_0) + \sum_{x,a,A} G_{DA}^{(f)da}(u; x) \times \text{unbiased noise}.
 \end{aligned} \tag{4.58}$$

Consequently, a stochastic estimate for the quark propagator is given by

$$G_{AB}^{(f)ab}(x; \mathbf{y}, t_0) = \frac{1}{N_R} \sum_{r=1}^{N_R} \phi_A^{(f)a}(x)[t_0, r] \xi_B^{*b}(y)[t_0, r] + \text{unbiased noise}. \tag{4.59}$$

In practice, the number of stochastic sources  $N_R$  can be rather small as the sum over the sources commutes with the sum over the gauge link configurations. Nevertheless, for every stochastic propagator a different source term is required.

In contrast to point-to-all propagators, stochastic timeslice-to-all propagators do not rely on replacing a spatial sum using translational invariance so arbitrary sink and source positions are possible. This flexibility comes along with the severe drawback of introducing stochastic noise. The number of stochastic noise terms for each applied stochastic timeslice-to-all propagator is  $\approx V_s^2$  so the signal-to-noise ratio becomes rapidly worse if a large number of stochastic propagators is used for a single correlation function. Especially for tetraquark systems where four quark propagators are required the exclusive use of stochastic propagators is expected to yield an insufficient signal-to-noise ratio.

In Appendix C.2, I discuss which type of quark propagator is used to compute a particular correlation matrix element for the investigation of the four-quark systems.

#### 4.4.3 The One-End-Trick for Stochastic Propagators

As every stochastic source term  $\xi$  and the associated solution  $\phi^{(f)}$  of Eq. (4.57) introduces additional stochastic noise terms, it is desirable to reduce the number of required source terms. If exactly two quark propagators are connected at a space-time

point  $y$ , while no other quark propagator starts or ends at this point, the one-end-trick [152, 153] provides an efficient way to compute the product of those two quark propagators. One needs to solve the  $2N_R$  linear equations

$$\begin{aligned} \sum_y D_{AB}^{(f_1)ab}(x; y) \phi^{(f_1)b}_B(y)[t_0, r] &= \xi_A^a(x)[t_0, r], \\ \sum_y D_{AB}^{(f_2)ab}(x; y) \tilde{\phi}^{(f_2)b}_B(y)[t_0, \Gamma, r] &= (\gamma_5 \Gamma^\dagger \xi)_A^a(x)[t_0, r], \end{aligned} \quad (4.60)$$

where  $\xi$  is a stochastic source as defined in Eq. (4.55). If the solutions  $\phi^{(f_1)}$  and  $\tilde{\phi}^{(f_2)}$  are determined, the product of the two quark propagators is given by [151]

$$\begin{aligned} &\sum_{\mathbf{y}} G^{(f_1)}(x; \mathbf{y}, t_0) \Gamma G^{(f_2)}(\mathbf{y}, t_0; z) \\ &= \frac{1}{N_R} \sum_{r=1}^{N_R} \phi^{(f_1)}(x)[t_0, r] \tilde{\phi}^{(f_2)}(z)[t_0, \Gamma, r]^\dagger \gamma_5 + \text{unbiased noise}. \end{aligned} \quad (4.61)$$

Using the one-end-trick instead of two ordinary stochastic propagators has the advantage that only a single stochastic source term is needed. Consequently, the number of stochastic noise terms is reduced by a factor  $V_s$  which results in a significant improved signal-to-noise ratio [151].

Using only a single stochastic source term, however, also comes along with a disadvantage as it fixes the spin structure at space-time point  $y$  to  $\Gamma$ . Accordingly, the second linear equation in Eq. (4.60) must be solved separately for every required spin structure  $\Gamma$ . Especially for large sets of creation operators with different  $\Gamma$ s, this might be impractical.

#### 4.4.3.1. Spin Dilution

The linear equations in Eq. (4.60) can be formulated independent of  $\Gamma$  if one introduces additional spin dilution [154]. Hereby, spin indices are established at the source, so the spin-diluted stochastic source is given by

$$\xi_A^a(x)[t_0, B, r] = \delta(x_0, t_0) \delta_{AB} \eta_B^a(\mathbf{x})[r]. \quad (4.62)$$

Instead of solving a linear equation for every  $\Gamma$ , one needs to solve only four linear equations, one for each spin index, given by

$$\sum_y D_{AB}^{(f)ab}(x; y) \phi^{(f)b}_B(y)[t_0, C, r] = \xi_A^a(x)[t_0, C, r]. \quad (4.63)$$

The product of two quark propagators connected at the same space-time position in terms of the solutions  $\phi^{(f)}$  can then be written as

$$\begin{aligned} &\sum_{\mathbf{y}} G^{(f_1)ab}_{AB}(x; \mathbf{y}, t_0) \Gamma_{BC} G^{(f_2)bc}_{CD}(\mathbf{y}, t_0; z) \\ &= \frac{1}{N_R} \sum_{r=1}^{N_R} \phi^{(f_1)a}_A(x)[t_0, B, r] (\Gamma \gamma_5)_{BC} \phi^{(f_2)c}_E(z)[t_0, C, r]^\dagger (\gamma_5)_{ED} + \text{unbiased noise}. \end{aligned} \quad (4.64)$$



#### 4.4.3.2. One-End-Trick for Combinations of Heavy and Light Quark Propagators

Most of the products of two quark propagators that are relevant for the four-quark states discussed in this work are built of one light quark propagator using a fermion action presented in Sec. 2.3 and one heavy quark propagator computed in the framework of NRQCD (see Sec. 2.4). As NRQCD decouples the particle and antiparticle solutions, the associated propagators have only a 2-component spin structure which can be embedded in a 4-component spin structure as shown in Eq. (2.81). In order to use the one-end-trick for such a product of one heavy and one light quark propagator, the same source term  $\xi$  must be used for both cases, so

$$\phi^{(f)}(x)[t_0, B, r] = \sum_{\mathbf{y}} G^{(f)}(x; \mathbf{y}, t_0) \xi(\mathbf{y})[t_0, B, r] \quad (4.65)$$

for heavy and light flavors  $f = h, l$ . In the case of the heavy quark propagator, we can apply Eq. (2.81) to decouple the solution  $\phi^{(h)}$  in particle and antiparticle solutions,

$$\phi^{(h)}(x)[t_0, B, r] = \begin{cases} \Theta(x_0 - t_0) \begin{pmatrix} \phi_{\psi}^{(h)}(x)[t_0, B, r] \\ 0 \end{pmatrix}, & \text{for } B = 1, 2, \\ -\Theta(-x_0 + t_0) \begin{pmatrix} 0 \\ \phi_{\chi}^{(h)}(x)[t_0, B, r] \end{pmatrix}, & \text{for } B = 3, 4. \end{cases} \quad (4.66)$$

As I am using spin dilution for the stochastic sources (see Eq. (4.62)), only those entries of the source term for which the Dirac index agrees with the spin-dilution index are non-zero. Accordingly, the linear equations for the 2-spin component heavy quark propagators are written as

$$\begin{aligned} \phi_{\psi}^{(h)}(x)[t_0, B, r] &= \sum_{\mathbf{y}} G_{\psi}^{(h)}(x; \mathbf{y}) \xi(\mathbf{y})[t_0, B, r], & \text{with } B = 1, 2, \\ \phi_{\chi}^{(h)}(x)[t_0, B, r] &= \sum_{\mathbf{y}} G_{\chi}^{(h)}(x; \mathbf{y}) \xi(\mathbf{y})[t_0, B, r], & \text{with } B = 3, 4. \end{aligned} \quad (4.67)$$

Consequently, the 2-spin component forward quark propagator is computed using only the first two spin-diluted stochastic sources, while for the backward quark propagator only the last two spin-diluted stochastic sources are considered.

All stochastic timeslice-to-all propagators that are used in this work exploit the one-end-trick with spin dilution. Additionally, I also introduce color dilution which is analogous to spin dilution formulated as

$$\sum_{\mathbf{y}} D_{AB}^{(f)ab}(x; \mathbf{y}) \phi^{(f)b}(y)[t_0, C, c, r] = \xi_A^a(x)[t_0, C, c, r] \quad (4.68)$$

with a spin and color diluted source

$$\xi_A^a(x)[t_0, B, b, r] = \delta(x_0, t_0) \delta_{AB} \delta_{ab} \eta_B^b(\mathbf{x})[r]. \quad (4.69)$$

This requires a factor of 3 additional inversions and is expected to further reduce stochastic noise (see Ref. [155]). The main benefit, however, is that it drastically simplifies the numerical computation of correlation functions in the employed code framework.



## 4.5 Smearing Techniques

Energy levels that are extracted from correlation functions are governed by their behavior for large temporal separations  $t$  where the noise becomes large, while for small separations the signal suffers from contributions of higher excited states. In order to optimize the signal-to-noise ratio, one attempts to improve the overlap generated by the creation operators with the real physical states. Fermion fields which are placed at a single space-time point as well as gauge links are highly local and do not render the actual physical shape quite well. The overlap with real physical states can be improved by smearing the fields in only spatial or spatial and temporal direction. This is done by replacing a field with a field obtained by averaging over neighboring points.

### 4.5.1 Smearing of Gauge Fields

In a first step, the signal of the correlation function can be substantially improved by smearing the gauge links. The smeared gauge links are obtained by averaging over short paths connecting the start and endpoint of the gauge link. This removes fluctuations of the gauge fields at short distances. Moreover, smearing gauge link configurations also mitigates the appearance of exceptional configurations which have been mentioned in Sec. 2.3.5. As the new gauge links are in general not SU(3) matrices anymore, they are projected back to SU(3). In practice, there is a large number of different smearing algorithms using different approaches. I will shortly discuss those techniques that are applied in this work.

#### 4.5.1.1. APE Smearing

*APE smearing* [156] constructs the new links using so-called staples  $\tilde{S}_{\mu\nu}(x)$  which are the six paths with length 3 connecting the two endpoints of the gauge link. The smeared link is given by

$$U_{\mu}^{\text{APE}}(x) = P_{\text{SU}(3)} \left[ (1 - \alpha_{\text{APE}}) U_{\mu}(x) + \frac{\alpha_{\text{APE}}}{6} \sum_{\nu \neq \mu} \tilde{S}_{\mu\nu}(x) \right], \quad (4.70)$$

where the staples are defined as

$$\tilde{S}_{\mu\nu}(x) = U_{\nu}(x) U_{\mu}(x + \hat{\nu}) U_{\nu}^{\dagger}(x + \hat{\mu}) + U_{\nu}^{\dagger}(x - \hat{\nu}) U_{\mu}(x - \hat{\nu}) U_{\nu}(x - \hat{\nu} + \hat{\mu}). \quad (4.71)$$

$P_{\text{SU}(3)}$  indicates projection to SU(3), and  $\alpha_{\text{APE}}$  is the real-valued smearing parameter. In general, one performs  $N_{\text{APE}}$  smearing steps by iteratively repeating the smearing procedure described in Eq. (4.70).

#### 4.5.1.2. HYP Smearing

Another smearing approach is *HYP smearing* [157] where the gauge link is averaged over the hypercubes that contain the original gauge link. Mathematically this is

realized by

$$U_{\mu}^{\text{HYP}}(x) = P_{\text{SU}(3)} \left[ (1 - \alpha_1) U_{\mu}(x) + \frac{\alpha_1}{6} \sum_{\pm\nu \neq \mu} \tilde{V}_{\nu\mu}(x) \tilde{V}_{\mu\nu}(x + \hat{\nu}) \tilde{V}_{\nu\mu}^{\dagger}(x + \hat{\mu}) \right], \quad (4.72)$$

where only the so-called decorated links  $\tilde{V}_{\nu\mu}(x)$  that are perpendicular to the  $\mu$ -direction, i.e.,  $\nu \neq \mu$ , are taken into account. The links  $\tilde{V}_{\mu\nu}(x)$  are constructed from another set of decorated links as

$$\tilde{V}_{\mu\nu}(x) = P_{\text{SU}(3)} \left[ (1 - \alpha_2) U_{\mu}(x) + \frac{\alpha_2}{4} \sum_{\pm\rho \neq \nu, \mu} \bar{V}_{\rho\nu\mu}(x) \bar{V}_{\mu\rho\nu}(x + \hat{\rho}) \bar{V}_{\rho\nu\mu}^{\dagger}(x + \hat{\mu}) \right], \quad (4.73)$$

where the index  $\rho$  runs only over the directions  $\rho \neq \mu, \nu$ . Finally,  $\bar{V}_{\rho\nu\mu}(x)$  is governed by

$$\bar{V}_{\mu\nu\rho}(x) = P_{\text{SU}(3)} \left[ (1 - \alpha_3) U_{\mu}(x) + \frac{\alpha_3}{2} \sum_{\pm\eta \neq \rho, \nu, \mu} U_{\eta}(x) U_{\mu}(x + \hat{\eta}) U_{\eta}^{\dagger}(x + \hat{\mu}) \right]. \quad (4.74)$$

In this way, only links that are part of the hypercubes containing the original gauge link are considered where each single step uses a modified form of APE blocking. Note that  $P_{\text{SU}(3)}$  denotes again projection to  $\text{SU}(3)$ . A convenient choice for the smearing parameters is  $\alpha_1 = 0.75$ ,  $\alpha_2 = 0.6$  and  $\alpha_3 = 0.3$ , which is also applied in this work. In principle it is also possible to perform several HYP smearing steps iteratively. In most cases a single step is, however, sufficient.

#### 4.5.1.3. Stout Smearing

Using *Stout Smearing* [158], the new links are obtained by a projection of the old links according to

$$U_{\mu}^{\text{Stout}}(x) = e^{iQ_{\mu}(x)} U_{\mu}(x). \quad (4.75)$$

The hermitian and traceless matrix  $Q_{\mu}(x)$  is built of the staples  $\tilde{S}_{\mu\nu}(x)$  defined in Eq. (4.71) via

$$\begin{aligned} Q_{\mu}(x) &= \frac{i}{2} \left( \Omega_{\mu}^{\dagger}(x) - \Omega_{\mu}(x) - \frac{1}{3} \text{Tr} \left[ \Omega_{\mu}^{\dagger}(x) - \Omega_{\mu}(x) \right] \right), \\ \Omega_{\mu}(x) &= \left( \sum_{\nu \neq \mu} \rho_{\mu\nu} \tilde{S}_{\mu\nu}(x) \right) U_{\mu}^{\dagger}(x). \end{aligned} \quad (4.76)$$

The smearing parameters are commonly kept constant with  $\rho_{\mu\nu} = \rho$ . Again, the smearing procedure can be iteratively repeated up to a desired number of smearing steps  $N_{\text{Stout}}$ .

### 4.5.2 Smearing of Quark Fields at Sinks and Sources

A common practice in lattice QCD is to smear also the fermion fields thus improving the overlap of the trial state generated by an operator with low-lying energy eigenstates. A reasonable choice is a Gaussian shape. Therefore, smearing fermion fields is also referred to as Gaussian smearing [159–161], which I apply in two slightly different formulations in this work. First, I use the gauge-covariant Gaussian smearing in the form

$$\psi_{\text{smearred}}(x) = \left(1 + \frac{\sigma_{\text{Gauss}}^2}{4N_{\text{Gauss}}} \Delta^{(2)}\right)^{N_{\text{Gauss}}} \psi(x), \quad (4.77)$$

where  $N_{\text{Gauss}}$  is the number of smearing steps and  $\sigma_{\text{Gauss}}$  is the smearing parameter [37].  $\Delta^{(2)}$  is the spatial nearest-neighbor gauge covariant Laplacian as defined in Eq. (A.3), while the gauge fields  $U_j(x)$  are replaced by gauge fields  $\tilde{U}_j(x)$  that are smeared according to one of the gauge fields smearing techniques discussed in Sec. 4.5.1.

The second formulation for Gaussian smearing is given by

$$\psi_{\text{smearred}}(x) = \left[ \frac{1}{1 + 6\kappa_{\text{Gauss}}} \left(1 + \kappa_{\text{Gauss}} H\right) \right]^{N_{\text{Gauss}}} \psi(x), \quad (4.78)$$

with

$$H \psi(x) = \sum_{j=1}^3 \left[ \tilde{U}_j(x) \psi(x + \hat{j}) + \tilde{U}_j^\dagger(x - \hat{j}) \psi(x - \hat{j}) \right]. \quad (4.79)$$

This prescription is also called Gaussian/Wuppertal smearing [160, 162, 163]. Both formulations can be transferred into each other using

$$\sigma_{\text{Gauss}} = \sqrt{\frac{2N_{\text{Gauss}} \kappa_{\text{Gauss}}}{1 + 6\kappa_{\text{Gauss}}}}, \quad (4.80)$$

which relates  $\kappa_{\text{Gauss}}$  to the width  $\sigma_{\text{Gauss}}$  of the smeared fermion field [164].

Every fermion field that appears in a correlation function should be smeared. This means that the quark propagator which is obtained via Wick contraction of the quark fields must be multiplied by smearing operators from the left as well as the right side. If we consider the techniques to compute the quark propagator discussed in Sec. 4.4 and especially the general formula in Eq. (4.50), we recognize that both the source term  $\xi$  and the solution  $\phi$  must be smeared to obtain correctly smeared fermion fields.

## 4.6 Scattering Analysis

The finite volume energy spectrum that is extracted from a correlation matrix can only be associated to hadronic states well below the threshold of strong decay. To investigate states that are located in the elastic scattering region or close to  $S$ -wave thresholds, a more elaborated treatment is required as the finite volume energy spectrum needs to be related to the infinite volume scattering amplitude to reliably extract these hadron masses. Thus, performing a scattering analysis using Lüscher's method (see Ref. [22] and Chapter 3) provides a suitable approach to rigorously studying tetraquark states close to or above the threshold of strong decay.

### 4.6.1 Lattice Dispersion Relation

In order to apply Lüscher's method, we require the dispersion relation of the mesons that are involved in the scattering process. For relativistic mesons, the dispersion relation is given by

$$E(\mathbf{p}) = \sqrt{m^2 + \mathbf{p}^2}, \quad (4.81)$$

where  $m$  is the meson mass and  $\mathbf{p} = 2\pi\mathbf{n}/L$  is the quantized lattice momentum. For mesons where at least one heavy quark is treated in the framework of NRQCD, the dispersion relation needs to be modified since the heavy quark mass has been removed from the action as discussed in Sec. 2.4. The momentum dependent energy for mesons with one heavy quark obeys

$$E_M(\mathbf{p}) = E_{M,0} + \sqrt{m_{M,\text{kin}}^2 + \mathbf{p}^2} - m_{M,\text{kin}}, \quad (4.82)$$

where  $M$  can be, for example, the pseudoscalar and vector  $B$  or  $B_s$  mesons and  $m_{M,\text{kin}}$  is the kinetic mass of the meson  $M$  [37]. Computing the momentum dependent energy  $E_M(\mathbf{p})$  of a particular meson for several values of  $\mathbf{p}$ , the meson's kinetic mass can be extracted directly from Eq. (4.82) by solving it for the lowest momentum  $\mathbf{p}^2 = (2\pi/L)^2$  and verifying that the solution is also valid for higher momenta  $\mathbf{p}$ . Alternatively,  $m_{M,\text{kin}}$  can be also extracted from a  $\chi^2$ -minimizing fit to Eq. (4.82) using all energies  $E_M(\mathbf{p})$ .

### 4.6.2 Scattering Momenta and Infinite Volume Scattering Amplitude

According to Eq. (3.15), the low-lying finite volume energy levels  $E_n$  of a particular four-quark state can be related to the scattering momentum  $k_n$  by

$$E_n = E_{M_1}(k_n) + E_{M_2}(k_n), \quad (4.83)$$

where  $M_1$  and  $M_2$  indicate the two mesons that are involved in the scattering process. In the case of antiheavy-light mesons, the dispersion relations are given by Eq. (4.82). Solving Eq. (4.83) for  $k_n^2$ , one obtains

$$k_n^2 = \frac{1}{4s} \left( s - (m_{M_1,\text{kin}} + m_{M_2,\text{kin}})^2 \right) \left( s - (m_{M_1,\text{kin}} - m_{M_2,\text{kin}})^2 \right) \quad (4.84)$$

with the center-of-momentum energy  $\sqrt{s}$  given by

$$\sqrt{s} = E_n - E_{M_1}(0) - E_{M_2}(0) + m_{M_1,\text{kin}} + m_{M_2,\text{kin}}. \quad (4.85)$$

The scattering momenta  $k_n$ , which are governed directly from the finite volume energy levels  $E_n$  via Eq. (4.84) can be related to the infinite volume scattering amplitude  $T$  using Lüscher's method. This is done by constraining a suitable energy dependent parametrization of the  $T$ -matrix using the finite number of discrete momenta  $k_n$ . In practice, there are different ways how the  $T$ -matrix parametrization can be determined relying either on the quantization condition in Eq. (3.35) where the phase shift  $\delta_l$  is

considered or on the more general quantization condition in Eq. (3.45) where the  $T$ -matrix appears directly. Which approach is more appropriate depends on the number of scattering channels and the structure of the  $M$ -matrix defined in Eq. (3.28).

After the scattering amplitude has been successfully parametrized, it can be analytically continued into the complex energy plane. Here, one examines if pole singularities of the  $T$ -matrix appear. Such poles are related to physical states. Poles that are located on the real axis of the first Riemann sheet below the threshold correspond to bound states, while the location of the pole yields the bound state's binding energy. Resonances are governed by poles in the second Riemann sheet off the real axis and above the threshold. The pole position can be interpreted as the mass (real part) and width (imaginary part) of the resonance.

#### 4.6.2.1. Computing the Infinite Volume Phase Shift

For a scattering analysis using only a single scattering channel, a common method is to compute the phase shift  $\delta_l(k_n)$  for each scattering momenta  $k_n$  using the quantization condition in Eq. (3.35). This is possible as long as the  $M$ -matrix can be block-diagonalized for the relevant angular momentum  $l$ . For example, this approach is applicable for the scattering analysis of the  $\bar{b}b u d$  system with  $I(J^P) = 0(1^+)$  carried out in Chapter 5. In the center-of-momentum frame, the quantum numbers  $J^P = 1^+$  appear in the  $T_1^+$  irrep of group  $O_h$  and according to Sec. 3.2, the  $S$ -wave phase shift  $\delta_0$  for the  $T_1^+$  irrep is found to be

$$\cot(\delta_0(k_n)) = \frac{2\mathcal{Z}_{00}(1; (k_n L/2\pi)^2)}{\pi^{1/2} k_n L}. \quad (4.86)$$

For the tetraquark candidates that are studied in Chapter 7, where also moving frames are considered, different symmetry groups and irreps must be taken into account. Thus, the phase shift formulas might differ from Eq. (4.86). However, they are obtained in a similar way considering the block-diagonal part of the  $M$ -matrix that corresponds to the relevant irrep. The  $M$ -matrices for all symmetry groups of interest can be found in Eqs. (3.42) and (B.14) to (B.17).

In the next step a reasonable parametrization for  $\cot(\delta_l)$  is selected and the associated parameters are determined. Besides many possible parametrizations, two common choices are the effective-range expansion (ERE) and the Breit-Wigner parametrization.

According to Ref. [49], the effective-range expansion is a reasonable parametrization for  $k \cot(\delta_0)$  in the vicinity of the threshold, given by

$$k \cot(\delta_0(k)) = \frac{1}{a_0} + \frac{1}{2} r_0 k^2 + \mathcal{O}(k^4). \quad (4.87)$$

Using the scattering momenta  $k_n$  and the corresponding phase shifts  $\cot(\delta_0(k_n))$ , the two parameters  $a_0$  ( $S$ -wave scattering length) and  $r_0$  ( $S$ -wave effective range) can be

determined. Note that for the case of only two energy levels  $E_n$  with  $n = 0$  and  $n = 1$ , the parameters can be directly computed by solving the occurring system of linear equations. If more than two energy levels are involved, the parameters are determined via a  $\chi^2$ -minimizing fit.

Using the parametrization of  $k \cot(\delta_0)$ , the scattering amplitude is given via Eq. (3.36). In order to determine the pole positions of the  $T$ -matrix, one needs to find the solutions of  $\cot(\delta_0) = i$  in the complex energy plane.

For bound states, the pole is located at the real axis below threshold where  $-ik > 0$ . This simplifies the pole search, as we can introduce the bound state momentum  $k_{\text{BS}}$  according to  $k = i|k_{\text{BS}}|$ . Combining the pole condition  $\cot(\delta_0(k_{\text{BS}})) = i$  with the effective-range expansion yields

$$-|k_{\text{BS}}| = \frac{1}{a_0} - \frac{1}{2}r_0|k_{\text{BS}}|^2, \quad (4.88)$$

which can be easily solved for  $|k_{\text{BS}}|$ . The binding energy is then given by

$$\begin{aligned} E_{\text{bind}} &= E_{\text{BS}} - E_{M_1}(0) - E_{M_2}(0) = E_{M_1}(k_{\text{BS}}) + E_{M_2}(k_{\text{BS}}) - E_{M_1}(0) - E_{M_2}(0) \\ &= \sqrt{m_{M_1, \text{kin}}^2 - |k_{\text{BS}}|^2} - m_{M_1, \text{kin}} + \sqrt{m_{M_2, \text{kin}}^2 - |k_{\text{BS}}|^2} - m_{M_2, \text{kin}}, \end{aligned} \quad (4.89)$$

where  $E_{\text{BS}}$  denotes the bound state energy. This approach has been successfully applied in various previous work (e.g., see Refs. [48, 49, 165, 166]). I will follow this proceeding in Chapter 5 where I determine the infinite volume binding energy of the  $\bar{b}b\bar{u}d$  tetraquark state with  $I(J^P) = 0(1^+)$ . Additionally, I also utilize this approach in Chapter 7 to studying  $\bar{b}c\bar{u}d$  four-quark systems with  $I(J^P) = 0(0^+)$  and  $I(J^P) = 0(1^+)$ .

The Breit-Wigner parametrization is well-suited to describe narrow  $P$ -wave resonances (see Refs. [167, 168]). Here, the phase shift is parametrized as

$$\frac{k^3}{\sqrt{s}} \cot(\delta_1(s)) = \frac{6\pi}{g^2}(m_R^2 - s), \quad (4.90)$$

where the free parameters are the coupling  $g$  and the resonance mass  $m_R$ . As discussed for the effective-range expansion, using the lattice energy levels  $E_n$  (which are related to the scattering momenta  $k_n$  and the center-of-momentum energies  $\sqrt{s_n}$  according to Eqs. (4.84) and (4.85)) and the associated phase shifts  $\cot(\delta_1)$  allows us to determine the free parameters  $g$  and  $m_R$  by fitting the Breit-Wigner function in Eq. (4.90) to the data. Using the parametrization, the pole of the scattering amplitude (see Eq. (3.36)) in the complex energy plane is determined. Such a parametrization could be used to search for a  $\bar{b}b\bar{u}d$  tetraquark resonance with  $I(J^P) = 0(1^-)$  as discussed in Chapter 8.

#### 4.6.2.2. Parametrizing the Scattering Amplitude

If either the  $M$ -matrix cannot be block-diagonalized or several scattering channels are considered, the phase shift cannot be computed as easily as discussed in the previous section. Here, it is more appropriate to use the quantization condition given in

Eq. (3.45). The  $T$ -matrix can be written as

$$[T^{-1}(s)]_{\alpha\beta} = \frac{1}{(2k_\alpha)^l} [K^{-1}(s)]_{\alpha\beta} \frac{1}{(2k_\beta)^l} + I_{\alpha\beta}(s), \quad (4.91)$$

where  $K(s)$  is a symmetric matrix which is real for real  $s$ , and the factors  $1/(2k_\alpha)^l$  guarantee that the behavior at the kinematic thresholds is correct [129, 169–171]. The diagonal matrix  $I(s)$  ensures unitarity by claiming that  $\text{Im}(I_{\alpha\beta}(s)) = -\delta_{\alpha\beta}\rho_\alpha(s)$  above the threshold and  $\text{Im}(I_{\alpha\beta}(s)) = 0$  below the threshold [129, 170]. To determine the real part of  $I(s)$ , I follow the approach in Refs. [129, 170] and use the Chew-Mandelstam prescription [172] which ensures an analytically well-behaving scattering amplitude below threshold. The  $K$ -matrix parametrization that I use in this work for single channel scattering processes is given by

$$[K^{-1}(s)]_{\text{single}} = c^{(0)} + c^{(1)}s, \quad (4.92)$$

where  $c^{(k)}$  are the free parameters. Similarly, for a coupled channel scattering analysis, the associated  $K$ -matrix parametrization is given by

$$[K^{-1}(s)]_{\text{coupled}} = \begin{pmatrix} c_{00}^{(0)} & c_{01}^{(0)} \\ c_{10}^{(0)} & c_{11}^{(0)} \end{pmatrix} + \begin{pmatrix} c_{00}^{(1)} & c_{01}^{(1)} \\ c_{10}^{(1)} & c_{11}^{(1)} \end{pmatrix} s, \quad (4.93)$$

with the free parameters  $c_{ij}^{(k)}$  which has been applied, e.g., in Refs [129, 170, 171, 173]. As the  $K$ -matrix is supposed to be symmetric, it follows that  $c_{ij}^{(k)} = c_{ji}^{(k)}$ . Having chosen a reasonable ansatz for the parametrization of the energy dependent scattering amplitude  $T(s)$ , the quantization condition in Eq. (3.45) must be solved for the discrete finite volume energy spectrum obtained from the lattice QCD calculation in order to determine the free parameters of the  $T$ -matrix. In the most general case, one might have computed the energy spectrum not only for the center-of-momentum frame but also for several moving frames and possibly for different irreps. Additionally, also several lattice volumes might have been taken into account. All these energy levels can then be considered in a single scattering analysis. The discrete energy spectra are consequently denoted as  $E_{n,\text{cm}}(\mathbf{P}, \Lambda, L)$ , where  $\mathbf{P}, \Lambda$  labels the frame and irrep and  $L$  the spatial lattice extent. The index  $cm$  indicates that all energies obtained in moving frames are transferred back to the center-of-momentum frame according to  $E_{n,\text{cm}} = \sqrt{s} = \sqrt{E_n^2 - \mathbf{P}^2}$ . One approach to determining the  $T$ -matrix parametrization is to vary the free parameters such that the whole spectrum  $E_{n,\text{cm}}(\mathbf{P}, \Lambda, L)$  is described in an optimal way. Mathematically, this is achieved by minimizing a  $\chi^2$  function that describes the difference between the lattice energy levels  $E_{n,\text{cm}}$  and the energy levels  $E_{n,\text{cm}}^{\text{par.}}$  that are obtained from Eq. (3.45) for a specific choice of parameters  $\{c_j\}$ ,

$$\begin{aligned} \chi^2(\{c_j\}) = & \sum_L \sum_{n,n'} \sum_{\mathbf{P}, \Lambda, \mathbf{P}', \Lambda'} \left[ E_{n,\text{cm}}(\mathbf{P}, \Lambda, L) - E_{n,\text{cm}}^{\text{par.}}(\mathbf{P}, \Lambda, L, \{c_j\}) \right] \\ & \times \left( C^{-1} \right)_{n,n'}(\mathbf{P}, \Lambda, \mathbf{P}', \Lambda', L) \left[ E_{n',\text{cm}}(\mathbf{P}', \Lambda', L) - E_{n',\text{cm}}^{\text{par.}}(\mathbf{P}', \Lambda', L, \{c_j\}) \right]. \end{aligned} \quad (4.94)$$



Here, the matrix  $C$  is the data covariance matrix. For energy levels computed on the same ensemble, its off-diagonal elements can be non-zero, while a suitable way to estimate them is the jackknife method [129].

If the scattering amplitude is successfully parametrized, one searches for poles of the  $T$ -matrix in the complex energy plane to identify physical states. I apply the approach discussed in this paragraph for the scattering analysis carried out in Chapter 6.

### 4.6.3 The Left-Hand Cut

One major issue in modern scattering analyses is imposed by the so-called left-hand cut. This corresponds to a branch cut that originates from a one-particle exchange in two-body systems [174]. A detailed discussion of possible implications of the left-hand cut with respect to the parametrization of the scattering amplitude has been carried out for  $DD^*$  scattering in Ref. [174]. Here, I will give a short overview of the most important aspects and implications. Let us consider the scattering process of two hadronically stable particles, e.g.,  $BB^*$  scattering. The relevant threshold  $BB^*$  introduces a two-body branch point in the scattering amplitude, while a three-body branch point occurs from the three-meson threshold  $BB\pi$ . Both introduce branch cuts which are right-handed and located at the real axis. According to Ref. [174], the two-body branch point is located at

$$k_{\text{thc}_2}^2 = 0, \quad (4.95)$$

and the three-body branch point at

$$k_{\text{thc}_3}^2 = 2\mu(m_\pi - \Delta m) \quad (4.96)$$

with  $\Delta m = m_{M_2} - m_{M_1}$  and  $\mu = m_{M_1}m_{M_2}(m_{M_1} + m_{M_2})$ , where  $m_{M_{1/2}}$  denotes the masses of the mesons involved in the scattering process.

Additionally, also one-particle exchanges play a crucial role, while in the case of  $BB^*$  scattering the relevant interaction is one-pion exchange. This introduces an additional singularity of the amplitude and gives rise to a left-hand cut starting at this branch point. Following Ref. [174], its location can be determined as

$$(k_{\text{lh}_c}^{1\pi})^2 \approx \frac{1}{4}(\Delta m^2 - m_\pi^2). \quad (4.97)$$

Note that additional left-hand cuts are introduced by exchange of heavier mesons and two or more pions.

The actual practical implications for a scattering analysis concern the parametrization of the  $T$ -matrix or phase shift, respectively. The range of convergence for most parametrizations like the ERE is constrained by the nearest singularity which is given by the branch point of the left-hand cut. Thus for scattering systems, where the singularity appears in the relevant energy region, the physics behind the left-hand cut cannot be disregarded [174].



However, it is still an unresolved issue how to cover the left-hand cut rigorously in a scattering analysis. Moreover, it is unclear how to interpret a pole that has been found using a particular parametrization which exceeds its range of convergence. It is unknown if such a pole suffers from only mild corrections due to one-particle exchange or if it is totally unphysical as the parametrization is not valid to describe the physics in this energy region. It is the subject of ongoing research to investigate this subtle issue further [174–178].

In this thesis, I neglect effects due to the left-hand cut in my scattering analyses. Nevertheless, I determine the position of the branch point associated to the left-hand cut to judge if the  $T$ -matrix parametrization is reliable or if one-particle exchanges should be taken into account. In the case of a left-hand cut in the relevant energy region the results of a scattering analysis must be treated with caution since their truthfulness is unclear. Here, an improved scattering analysis formalism taking into account one-particle exchange would be desirable.



# 5

---

## COMPUTATION OF THE GROUND-STATE ENERGY FOR $\bar{Q}\bar{Q}'qq'$ TETRAQUARK STATES

---

One major interest of this work is to investigate if hadronically stable antiheavy-anti-heavy-light-light tetraquark states  $\bar{Q}\bar{Q}'qq'$  exist. In this chapter I will discuss the lattice computations that were carried out to determine the four-quark ground-state energy levels for the most promising tetraquark candidates with quark content  $\bar{b}b\bar{u}d$  in the  $I(J^P) = 0(1^+)$  channel,  $\bar{b}b\bar{u}s$  in the  $J^P = 1^+$  channel, and  $\bar{b}\bar{c}ud$  with  $I(J^P) = 0(0^+)$  and  $I(J^P) = 0(1^+)$ . While for the  $\bar{b}b\bar{u}d$  and  $\bar{b}b\bar{u}s$  tetraquarks evidence for a bound state has already been found in several lattice calculations [24, 35–40], the situation is less clear for  $\bar{b}\bar{c}ud$  four-quark states where first a bound state had been predicted in Ref. [41] but later revoked [42], while another group found indication for a stable tetraquark state [43].

In addition to local interpolating operators the lattice calculation presented in this chapter employs also scattering interpolating operators which have not been considered in previous calculations [35, 36, 41–43] and therefore expands these works accordingly. Since the computation of quark propagators is extremely expensive for the given lattice setup, already existing light and strange point-to-all propagators are used. Therefore, scattering operators can only be considered at the sink but not at the source, thus resulting in a non-square correlation matrix. All techniques that are applied to study the four-quark states in this chapter have been introduced in Chapter 4, while I have discussed the utilized interpolating operators in particular in Sec. 4.2.3.

In Sec. 5.1 I present the used lattice setup covering the gauge link ensembles, the applied techniques to compute the quark propagators, and the utilized smearing methods. In Sec. 5.2 I show the results for the energies of the heavy-light mesons which are constituents of the relevant meson-meson thresholds. Sec. 5.3 covers the main part of this chapter. Here I depict the lattice results for the four-quark ground-state energy levels. This is followed by a discussion of the final results in Sec. 5.4 including a chiral extrapolation of the binding energies to the physical pion mass.

Note that the results for the case of  $\bar{b}b\bar{u}d$  which are discussed in the following are part of a previous work in Refs. [37, 92], but I will nevertheless recapitulate them for the sake of completeness. All results that are presented in this chapter have been published in Refs. [24, 37].

## 5.1 Lattice Setup

In this section, I present the gauge field configurations, explain how the quark propagators are computed, and mention the applied smearing methods.

### 5.1.1 Gauge Field Configurations

The computations carried out in this chapter use gauge link configurations generated by the RBC and UKQCD collaborations [179, 180]. These ensembles are generated using the Iwasaki gauge action [54, 55] (see also Sec. 2.2) and domain-wall fermions with  $N_f = 2 + 1$  flavors [72–74, 181] (see also Sec. 2.3.3). The five ensembles that are utilized for this project differ in their lattice spacing, the spatial volume and the pion mass, while one ensemble is at the physical point. Details about the lattice ensembles are summarized in Table 5.1, and the lattice spacings have been determined in Ref. [180].

Ensemble	$N_s^3 \times N_t$	$a$ [fm]	$am_{u,d}^{(\text{sea;val})}$	$am_s^{(\text{sea})}$	$am_s^{(\text{val})}$	$m_\pi$ [MeV]	$N_{\text{conf}}$
C00078	$48^3 \times 96$	0.1141(3)	0.00078	0.0362	0.0362	139(1)	40
C005	$24^3 \times 64$	0.1106(3)	0.005	0.04	0.0323	340(1)	311
C01	$24^3 \times 64$	0.1106(3)	0.01	0.04	0.0323	431(1)	283
F004	$32^3 \times 64$	0.0828(3)	0.004	0.03	0.0248	303(1)	251
F006	$32^3 \times 64$	0.0828(3)	0.006	0.03	0.0248	360(1)	442

Table 5.1.: List of gauge link ensembles [179, 180] used in this work.  $N_s, N_t$ : number of lattice sites in spatial and temporal directions;  $a$ : lattice spacing;  $am_q^{(\text{sea})}$ : sea-quark mass for flavor  $q$ ;  $am_q^{(\text{val})}$ : valence-quark mass for flavor  $q$ ;  $m_\pi$ : pion mass;  $N_{\text{conf}}$ : number of gauge field configurations.

### 5.1.2 Light and Strange Quark Propagators

For the light and strange quark propagators, I use Gaussian smeared point-to-all propagators which are computed using a conjugate gradient solver in combination with low-mode deflation. A more detailed discussion of the numerical methods used to calculate the quark propagators can be found in Ref. [37].

As the numerical computation of the point-to-all propagators is quite expensive, I apply the so-called all-mode-averaging technique [182, 183] to reduce the numerical costs. Hereby, on each configuration only a small sample of *exact* quark propagators and associated *exact* correlation functions and a larger sample of *sloppy* quark propagators and correlation functions are computed. Exact and sloppy correlation functions are afterwards combined such that the expectation value of the exact sample is maintained while the large number of sloppy samples reduces the variance significantly,

$$(\text{AMA samp.})_e = (\text{ex. samp.})_e - (\text{slop. samp.})_{e,0} + \frac{1}{N_{\text{slop.}}} \sum_{s=0}^{N_{\text{slop.}}-1} (\text{slop. samp.})_{e,s}. \quad (5.1)$$

Here,  $e$  numerates the exact samples (ex. samp.), covering all gauge link configurations and source positions. The sloppy samples (slop. samp.) associated to an exact sample  $e$  are additionally indexed with  $s$  which labels a space-time displacement of the source relative to the exact source, while  $s = 0$  indicates no displacement. The number of exact and sloppy samples for each ensemble are listed in Table 5.2.

Ensemble	$N_{\text{samples, exact}}$	$N_{\text{samples, sloppy}}$
C00078	80	2560
C005	311	9952
C01	283	9056
F004	251	8032
F006	442	14144

Table 5.2.: Number of exact and sloppy samples used for all-mode-averaging [182,183]. Per configuration I use 1 or 2 exact samples with 32 or 64 sloppy samples.

### 5.1.3 Charm Quark Propagators

For the charm quarks I use point-to-all propagators which are computed using the first variant of the anisotropic clover action in Eq. (2.86) presented in Sec. 2.5. Following this approach, I use the same values for the chromoelectric and chromomagnetic coefficients, i.e.,  $c_P \equiv c_E = c_B$  (e.g., see Ref. [105]). The remaining three parameters  $am_Q$ ,  $\zeta$  and  $c_P$  are tuned for each ensemble such that the rest mass, the kinetic mass and the hyperfine splitting for the  $D_s$  meson match their experimental values [24,87]. I list all coefficients in Table 5.3.

Ensemble	$am_Q = am_c$	$\zeta$	$c_P$
C00078	0.2751	1.1883	2.0712
C005, C01	0.1541	1.2004	1.8407
F004, F006	-0.0517	1.1021	1.4483

Table 5.3.: Parameters used in the anisotropic clover action in Eq. (2.86) for the charm quarks.

### 5.1.4 Bottom Quark Propagators

The bottom quarks are treated in the framework of NRQCD which has been presented in Sec. 2.4 whereby the quark propagators are determined using the Green function evolution equation given in Eq. (2.76). The matching coefficients are all set to their tree-level value  $c_i = 1$  except for  $c_4$  which is taken from a computation in one-loop lattice perturbation theory in Ref. [184]. As discussed in Sec. 2.4.4, the gauge links

are divided by the mean link in Landau gauge  $u_{0L}$ . The bare bottom quark masses are tuned such that the spin-averaged kinetic mass of bottomonium matches its experimental value [37, 137]. I list all parameters in Table 5.4, while omitting the matching coefficients which are set to their tree-level value.

Ensemble	$am_b$	$u_{0L}$	$c_4$
C00078	2.52	0.8432	1.09389
C005, C01	2.52	0.8439	1.09389
F004, F006	1.85	0.8609	1.07887

Table 5.4.: Parameters used in the NRQCD action in Eq. (2.76) for the bottom quarks.

### 5.1.5 Smearing of Quark Fields

All quark fields that are used to compute the correlation functions in this chapter are smeared. I use Gaussian smearing for all five quark flavors as discussed in Sec. 4.5.2, while the smearing parameters and the number of Gaussian smearing steps are listed in Table 5.5. For the up, down and strange quarks, the Gaussian smearing is carried out on spatially APE smeared gauge links (see Sec. 4.5.1.1). Furthermore, for the charm quarks, the gauge links are initially stout smeared (see Sec. 4.5.1.3), while no gauge link smearing is used for the bottom quarks. All parameters for the gauge link smearing are also summarized in Table 5.5. As the computation of the quark propagators is numerically extremely expensive, I reuse existing quark propagators

Ensemble	Up and down quarks				Strange quarks			
	$N_{\text{Gauss}}$	$\sigma_{\text{Gauss}}$	$N_{\text{APE}}$	$\alpha_{\text{APE}}$	$N_{\text{Gauss}}$	$\sigma_{\text{Gauss}}$	$N_{\text{APE}}$	$\alpha_{\text{APE}}$
C00078	100	7.171	25	2.5	30	4.350	25	2.5
C005, C01	30	4.350	25	2.5	30	4.350	25	2.5
F004, F006	60	5.728	25	2.5	60	5.728	25	2.5
	Charm quarks				Bottom quarks			
	$N_{\text{Gauss}}$	$\sigma_{\text{Gauss}}$	$N_{\text{stout}}$	$\rho$	$N_{\text{Gauss}}$	$\sigma_{\text{Gauss}}$		
C00078	10	2.00	10	0.08	10	2.0		
C005, C01	10	2.00	10	0.08	10	2.0		
F004, F006	16	2.66	10	0.08	10	2.0		

Table 5.5.: Smearing parameters for the quark-fields used in the computation of the correlation functions. Gaussian smearing is carried out according to Eq. (4.77). A single gauge link smearing sweep is defined in Eq. (4.70) for APE smearing and in Eq. (4.75) for stout smearing.

from a previous project. This is the reason why a different gauge link smearing is applied for the charm quarks.

## 5.2 Energies for Antiheavy-Light Pseudoscalar and Vector Mesons

To make reliable statements about the binding of four-quark states, we require the masses of the mesons forming the lowest two-meson threshold in each channel. For this purpose, I compute the two-point correlation functions for the pseudoscalar and vector  $B$ ,  $B_s$  and  $D$  mesons using the interpolating operators presented in Eqs. (4.15) to (4.20) for zero momentum projection,  $\mathbf{p} = 0$ . The ground-state energy for each meson is determined by an uncorrelated  $\chi^2$ -minimizing fit of a constant to the effective energy given by Eq. (4.6) for sufficiently large temporal separations. Statistical uncertainties are calculated using jackknife resampling. I exemplarily depict the effective energies for all mesons computed on ensemble C005 in Fig. 5.1 together with a plateau fit for a suitable temporal fit range. The final results for the mesons' energies on all ensembles are collected in Table 5.6. Note that slightly different  $B$  and  $B^*$  masses have been used for studying the  $\bar{b}bud$  system (see Ref. [37]) due to a slightly different temporal fit range, though those masses are consistent within statistical uncertainties.

The energies for the pseudoscalar and vector  $B$  and  $B_s$  mesons do not correspond to their physical values but are shifted as a consequence of using NRQCD [24, 37]. This

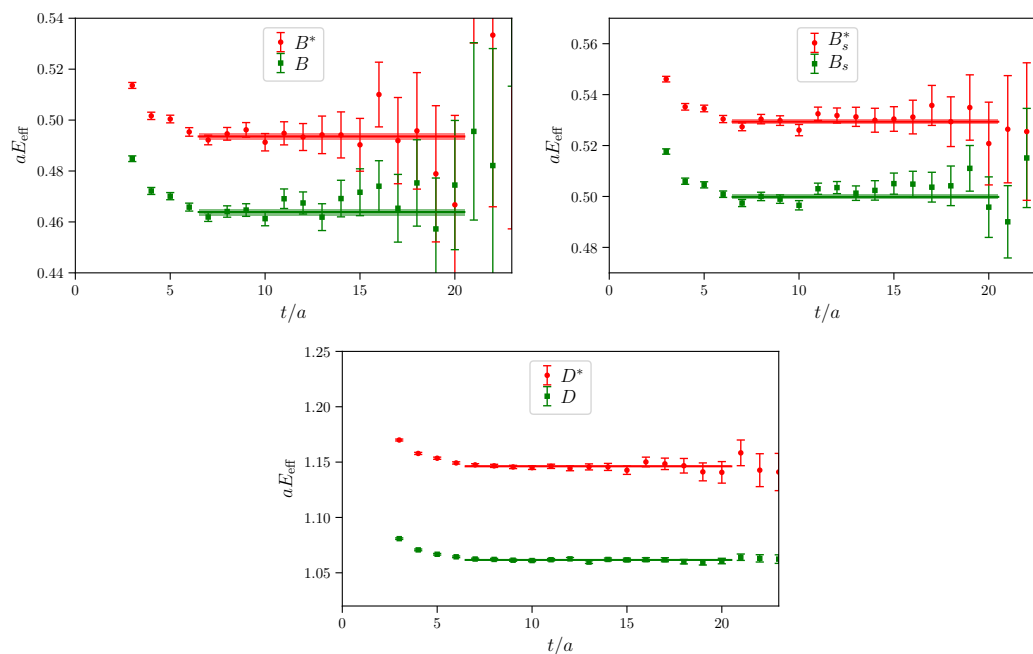


Figure 5.1.: Effective energies as defined in Eq. (4.6) at zero momentum for pseudoscalar and vector  $B$ ,  $B_s$  and  $D$  mesons computed on ensemble C005. The corresponding plateau fits in the range  $7 \leq t/a \leq 20$  are indicated by the horizontal lines.

Ensemble	$aE_B$	$aE_{B^*}$	$aE_{B_s}$	$aE_{B_s^*}$	$aE_D$	$aE_{D^*}$
C00078	0.4564(46)	0.4814(49)	0.5052(12)	0.5349(15)	1.0823(14)	1.1638(21)
C005	0.4639(12)	0.4936(14)	0.4998(8)	0.5294(9)	1.0616(4)	1.1462(8)
C01	0.4737(11)	0.5052(13)	0.5025(8)	0.5338(10)	1.0714(4)	1.1586(7)
F004	0.3757(10)	0.3976(11)	0.4031(6)	0.4256(7)	0.7944(4)	0.8566(6)
F006	0.3786(6)	0.4007(7)	0.4033(4)	0.4258(5)	0.7981(2)	0.8609(4)

 Table 5.6.: Energies of pseudoscalar and vector  $B$ ,  $B_s$  and  $D$  mesons at zero momentum.

shift is proportional to the number of  $b$  quarks  $n_b$ , and consequently it cancels if we consider energy differences with equal number of  $b$  quarks as it is the case for the difference of a four-quark energy level to the associated lowest two-meson threshold. For the case of  $\bar{b}bud$ , the finite volume ground-state energy is extrapolated to the infinite volume by performing a scattering analysis. Therefore, the momentum dependence for the  $B$  and  $B^*$  mesons' energy has been studied, and the kinetic masses have been determined using the dispersion relation given in Eq. (4.82). More details and the resulting kinetic masses can be found in Sec. IV of Ref. [37].

### 5.3 Results on $\bar{Q}\bar{Q}'qq'$ Tetraquark Systems

The four-quark correlation functions are computed using the interpolating operators in Eqs. (4.21) to (4.40), while scattering operators are applied only at the sink. Accordingly, the correlation matrices have a shape of  $(N_{\text{loc}} \times N_{\text{scatt}}) \times (N_{\text{loc}})$  where  $N_{\text{loc}}$  is the number of local operators and  $N_{\text{scatt}}$  the number of scattering operators for the respective four-quark system. The energies  $E_n$  are extracted from these non-square correlation matrices using fully correlated  $\chi^2$ -minimizing multi-exponential matrix fits as described in Sec. 4.3.2. I vary the number of exponentials  $N$  included in the fit as well as the temporal fit range and determine the energies  $E_n$  for the full correlation matrix and also for several sub-matrices.

As the number of exact samples is partly rather small compared to the degrees of freedom appearing in the matrix fit, the covariance matrix might be poorly determined, especially for the full correlation matrix. I prevent this by using a modified version of the all-mode-averaging where the modified AMA sample (mAMA) is governed as

$$(\text{mAMA samp.})_{e,s} = (\text{ex. samp.})_e - (\text{slop. samp.})_{e,0} + (\text{slop. samp.})_{e,0}. \quad (5.2)$$

This increases the number of samples by a factor  $N_{\text{sloppy}} = 32$  so that the covariance matrix is also well-defined for large correlation matrices. A drawback of this modified AMA method is, however, that additional correlations are introduced. This is covered by rescaling the uncertainties of the energy levels in an appropriate way. For more details about this procedure, I refer to Ref. [37].

In addition to the energies  $E_n$ , I also determine the overlap factors  $Z_j^n$  as defined in



Eq. (4.42). A trial state of a particular creation operator can be expanded in terms of the overlap factor  $Z_j^n$  according to

$$\mathcal{O}_j^\dagger|\Omega\rangle = \sum_{n=0}^{\infty} |n\rangle\langle n|\mathcal{O}_j^\dagger|\Omega\rangle = \sum_{n=0}^{\infty} Z_j^n |n\rangle. \quad (5.3)$$

Consequently, the overlap factor  $Z_j^n$  indicates how strongly the energy eigenstate  $|n\rangle$  contributes to the trial state  $\mathcal{O}_j^\dagger|\Omega\rangle$ . This makes it possible to draw certain conclusions about the composition of the eigenstate  $|n\rangle$ . If for a particular trial state  $\mathcal{O}_j^\dagger|\Omega\rangle$  one overlap factor  $|Z_j^m|$  is considerably larger than all other overlap factors  $|Z_j^n|$  for  $n \neq m$ , this suggests that  $|m\rangle$  is similar to the trial state  $\mathcal{O}_j^\dagger|\Omega\rangle$  [24]. In contrast to that, an overlap factor  $|Z_j^m|$  that is clearly smaller than at least one other overlap factor  $|Z_j^n|$  with  $n \neq m$  indicates that the states  $|m\rangle$  and  $\mathcal{O}_j^\dagger|\Omega\rangle$  are rather orthogonal to each other. In this section, I consider the normalized overlap factors defined as

$$\tilde{Z}_j^n = \frac{Z_j^n}{\max_m(|Z_j^m|)}. \quad (5.4)$$

### 5.3.1 Results for the Case of $\bar{b}\bar{b}ud$ with $I(J^P) = 0(1^+)$

The  $\bar{b}\bar{b}ud$  four-quark system with  $I(J^P) = 0(1^+)$  is the most promising candidate for a bound tetraquark state. In the following, I will summarize the results for this system, which have been published in Refs. [37, 92], to give a complete overview of all studies on doubly-heavy tetraquarks that have been carried out using the presented lattice setup. Parts of the analysis have been done by other members of our collaboration.

In Fig. 5.2, I present the fit results obtained from various sub-matrices for the ground-state energy level  $\Delta E_0$  (blue) and the first excited state  $\Delta E_1$  (green) relative to the  $BB^*$  threshold, i.e.,  $\Delta E_n = E_n - E_B - E_{B^*}$ , on ensemble C005. The boxes below the plot indicate which operators are included in the correlation matrix. The lowest box represents  $\mathcal{O}_1$  and the topmost  $\mathcal{O}_5$ . A filled/empty box indicates that the associated operator is included/excluded in the fit, while a black box represents a local operator and a red box a scattering operator. The final estimates for the energy levels  $\Delta E_n = E_n - E_B - E_{B^*}$  are depicted by the horizontal lines with shaded error bands. Looking at these fit results, we can make two essential observations [37]. First, including scattering operators has substantial impact on the fit results. This is characterized by the fact that, on the one hand, stable results are only obtained if at least one scattering operator is included and, on the other hand, that in this case the ground-state energy and the energy of the first excited state drop significantly. Second, the final estimate for the ground-state energy level is found approximately 120 MeV below the  $BB^*$  threshold which is an indication for a bound tetraquark state. Moreover, the first excited state is close to the  $BB^*$  threshold indicating a meson-meson scattering state.

These observations can be further supported by considering the normalized overlap factors  $\tilde{Z}_j^n$  as defined in Eq. (5.4). In Fig. 5.3, I show the normalized overlap factors

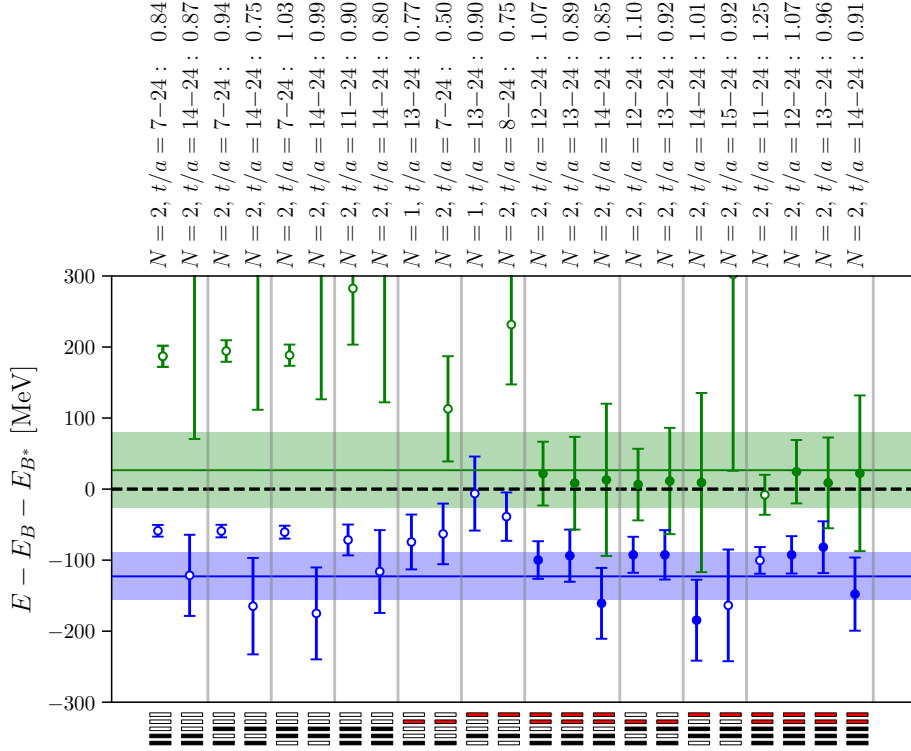


Figure 5.2.: Fit results for the two lowest energy levels  $\Delta E_0$  and  $\Delta E_1$  for the  $\bar{b}b u d$  system with  $I(J^P) = 0(1^+)$  relative to the  $BB^*$  threshold obtained on ensemble C005. The boxes below the plot indicate the utilized operator basis. Above each fit the number of exponentials, the temporal fit range and the value of  $\chi^2/\text{d.o.f.}$  are presented. The shaded horizontal lines correspond to the final estimates for  $\Delta E_0$  and  $\Delta E_1$  and are obtained by a bootstrap average of the fit results indicated by a filled symbol.

that have been extracted from a fit to the full  $5 \times 3$  correlation matrix on ensemble C005. Note that the mean values and uncertainties of  $\tilde{Z}_j^n$  are obtained via bootstrap resampling of the fits with the consequence that the largest value can be smaller than 1 [37]. According to Fig. 5.3, we observe that the overlap of the trial state generated by the operator  $\mathcal{O}_3$  with the ground state  $|0\rangle$  is significantly larger than the overlap with all other states, i.e.,  $\tilde{Z}_3^0 \gg \tilde{Z}_3^n$  for  $n \neq 0$ . Additionally, the trial states generated by the scattering operators  $\mathcal{O}_4$  and  $\mathcal{O}_5$  overlap mainly with the first excited state  $|1\rangle$ . This agrees with the interpretation of the ground state as a bound four-quark state and the first excited state as a meson-meson scattering state.

The estimates for the finite volume energy levels  $E_n$  presented in Fig. 5.2 can be related to the infinite volume scattering amplitude using Lüscher's method following the approach discussed in Sec. 4.6.2.1. In Ref. [37], we computed the parameters  $a_0$  and  $r_0$  of the effective-range expansion which is shown in Fig. 5.4. Using the ERE given in Eq. (4.87), the pole of the scattering amplitude below the threshold is determined according to Eqs. (4.88) and (4.89). This pole position corresponds to the binding

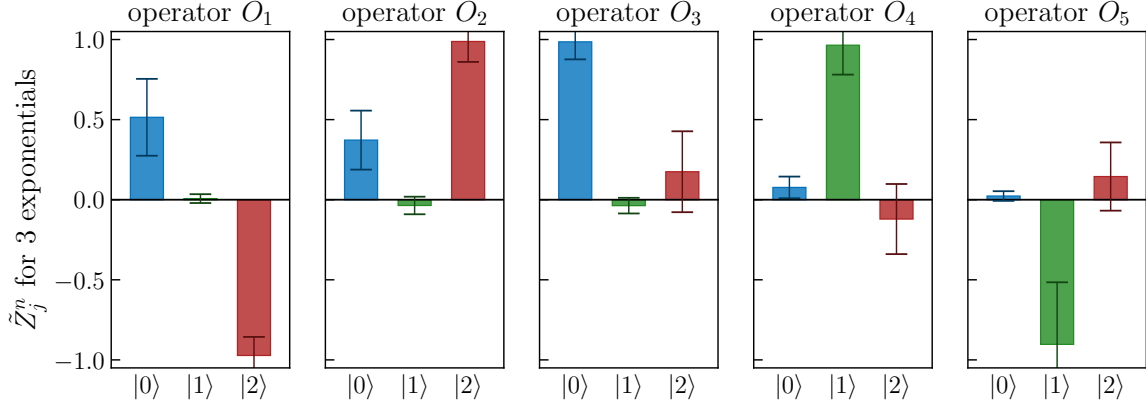


Figure 5.3.: Normalized overlap factors  $\tilde{Z}_j^n$  for the  $\bar{b}\bar{b}ud$  system obtained via a three-exponential fit to the full  $5 \times 3$  correlation matrix in the range  $12 \leq t/a \leq 24$  on ensemble C005. The index  $j$  corresponds to the index of the operator shown above each plot, the index  $n$  to the energy eigenstates shown below each plot.

energy  $E_{\text{bind}}$  of the  $\bar{b}\bar{b}ud$  tetraquark state and is found to be essentially identical to the finite-volume energy difference  $\Delta E_0$  [37]. Consequently, the interpretation of the  $\bar{b}\bar{b}ud$  ground state as a stable tetraquark is further supported. The results for the ground-state binding energies are collected for all ensembles in Table 5.8 in Sec. 5.4. For more details about the calculations studying the  $\bar{b}\bar{b}ud$  tetraquark system, I refer to Ref. [37].

Note that in the scattering analysis performed for the  $\bar{b}\bar{b}ud$  system possible effects due to the left-hand cut (see Sec. 4.6.3) are neglected. However, using Eq. (4.97),  $\Delta m = m_{B^*} - m_B \simeq 45 \text{ MeV}$  and  $m_\pi \simeq 310 \text{ MeV}$ , we find the left-hand cut branch point at  $(k_{\text{lh}}^{1\pi})^2 \approx -(153 \text{ MeV})^2$  which is much closer to the threshold than the bound

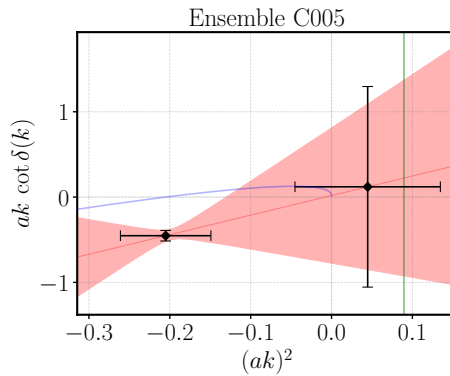


Figure 5.4.: Effective range expansion for ensemble C005 indicated by the red line based on the two lowest energy levels. The  $BB^*$  threshold is located at  $k = 0$ , the  $B^*B^*$  threshold is indicated by the green vertical line. The blue curve starting at  $k = 0$  corresponds to  $ak \cot(\delta(k)) + a|k|$  whose lowest zero gives the binding energy.

state pole located at  $k_{\text{BS}} \approx 800 \text{ MeV}$  [37]. Thus, the pole of the scattering amplitude lies outside the range of convergence of the ERE and consequently this parametrization might not be a valid choice for the scattering analysis. A rigorous understanding of the implications arising due to the left-hand cut is still subject of ongoing research and not further addressed in this chapter.

### 5.3.2 Results for the Case of $\bar{b}\bar{b}us$ with $J^P = 1^+$

Another promising candidate for a bound tetraquark state is the  $\bar{b}\bar{b}us$  four-quark system with quantum numbers  $J^P = 1^+$ . My results presented in this section have already been published in Ref. [24]. As discussed in Sec. 4.2.3.2, four local operators and three scattering operators are considered in this channel which leads to a rather large correlation matrix. This is disadvantageous as extracting the energies via multi-exponential matrix fits for large matrices is extremely challenging and the obtained fits might be unstable.

#### 5.3.2.1. Reducing the Size of the Correlation Matrix

A reasonable way to handle this disadvantage is reducing the size of the correlation matrix while maintaining all relevant information which is required to precisely describe the ground-state energy level. Accordingly, the size of the associated correlation matrix for the  $\bar{b}\bar{b}us$  system is reduced from  $7 \times 4$  to  $6 \times 3$ . To do so, the set of local interpolating operators  $\mathcal{O}_1$  to  $\mathcal{O}_4$  defined in Eqs. (4.26) to (4.29) is substituted by linear combinations of these operators given by

$$\mathcal{O}'_j = \sum_{k=1}^4 \bar{v}_{j-1}^k \mathcal{O}_k, \quad \text{with } j = 1, \dots, 4. \quad (5.5)$$

The coefficients  $\bar{v}_n^k$  are extracted from the eigenvectors  $v_n$  that are obtained by solving the GEVP for the  $4 \times 4$  correlation matrix built of the local operators  $\mathcal{O}_1$  to  $\mathcal{O}_4$ . Note that each eigenvector  $v_n$  associated to the  $n$ -th state is normalized according to  $\sum_{k=1}^4 |v_n^k|^2 = 1$ . I show the squared normalized eigenvector components  $|v_n^k(t)|^2$  obtained on ensemble C01 in Fig. 5.5. As one can see, for sufficiently large temporal separation, the eigenvectors become independent of  $t$ . A reasonable choice for the

$\bar{v}_n^k$	$k = 1$	$k = 2$	$k = 3$	$k = 4$
$n = 0$	+0.493	-0.501	-0.588	-0.399
$n = 1$	-0.708	-0.706	+0.002	+0.002
$n = 2$	-0.448	+0.446	-0.773	-0.056
$n = 3$	-0.351	+0.351	+0.529	-0.689

Table 5.7.: Coefficients  $\bar{v}_n^k$  that are applied in the linear combination of the local operators  $\mathcal{O}_1$  to  $\mathcal{O}_4$  to obtain the new interpolation operators  $\mathcal{O}'_j$  according to Eq. (5.5).

coefficients  $\bar{v}_n^k$  in Eq. (5.5) is found to be  $\bar{v}_n^k = v_n^k(t/a = 8)$  as for  $t/a = 8$  a plateau is reached, while statistical fluctuations are small [24]. I collect the results obtained for all  $\bar{v}_n^k$  in Table 5.7.

The new set of operators has some beneficial properties as the trial state generated by the operator  $\mathcal{O}_j$  acting on the vacuum state will have significant overlap with the eigenstate  $|j-1\rangle$ , while it will be almost orthogonal to all other eigenstates. Accordingly, the operator  $\mathcal{O}_1$  is crucial to describe the ground-state energy level, while operators whose trial states overlap mainly with higher excitations play a rather subordinate role and can possibly be discarded. This allows us to consider a small correlation matrix which is advantageous for performing multi-exponential fits whereas simultaneously all relevant contributions to the lowest energy levels are preserved. While additionally to  $\mathcal{O}_1$  also  $\mathcal{O}_2$  and  $\mathcal{O}_3$  have been found to be valuable to precisely determine the low-lying energy levels, the operator  $\mathcal{O}_4$  does not seem to provide any improvement and is

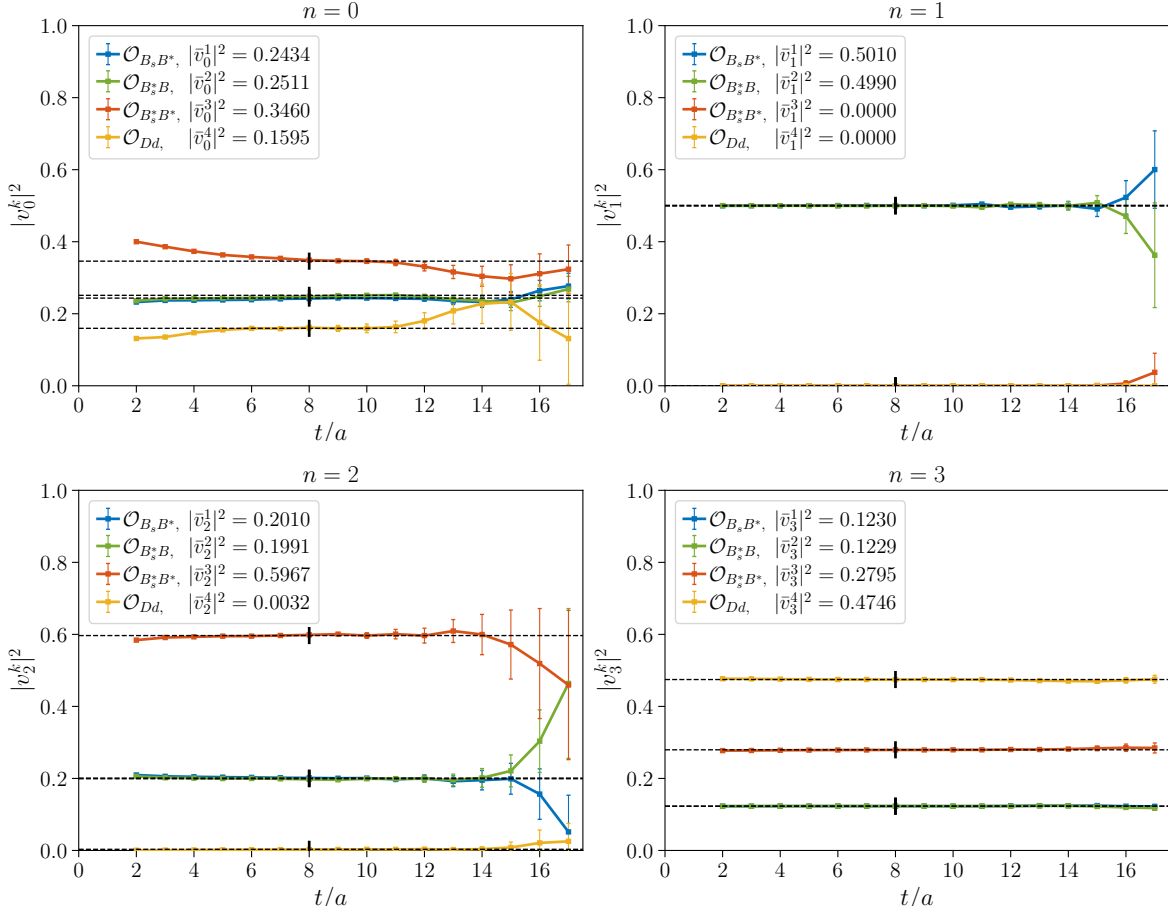


Figure 5.5.: Squared normalized eigenvector components  $|v_n^k(t)|^2$  as a function of  $t$  determined on ensemble C01 via a generalized eigenvalue problem using the  $4 \times 4$  correlation matrix for the local operators  $\mathcal{O}_1$  to  $\mathcal{O}_4$ . The squares of the coefficients  $\bar{v}_n^k = v_n^k(t/a = 8)$  are indicated by dashed horizontal lines.

therefore dropped [24].

In addition to the three new local interpolating operators  $\mathcal{O}'_1$ ,  $\mathcal{O}'_2$  and  $\mathcal{O}'_3$ , the operator basis is completed by the three scattering operators in Eqs. (4.30) to (4.32) which are renamed as

$$\mathcal{O}'_4 = \mathcal{O}_5, \quad \mathcal{O}'_5 = \mathcal{O}_6, \quad \mathcal{O}'_6 = \mathcal{O}_7, \quad (5.6)$$

resulting in a  $6 \times 3$  correlation matrix which will be analyzed in the following paragraph.

### 5.3.2.2. Energy Levels and Overlap Factors

I carried out correlated  $\chi^2$ -minimizing multi-exponential fits, as discussed in Sec. 4.3.2, for various sub-matrices of the correlation matrix discussed in the previous section [24]. The fit results are presented in Fig. 5.6 in the same way as for  $\bar{b}bud$  in Fig. 5.2.

First, we observe that for fits which consider only correlation matrices with local interpolating operators, each operator seems to be associated to one specific energy level (see the first seven fits in Fig. 5.6). This is expectable, as the local operator  $\mathcal{O}'_j$  is constructed such that its trial state overlaps mainly with the eigenstate  $|j-1\rangle$  and is orthogonal to all other eigenstates for sufficiently large temporal separations. As already pointed out in the previous paragraph, the operator  $\mathcal{O}'_1$  is mandatory to resolve

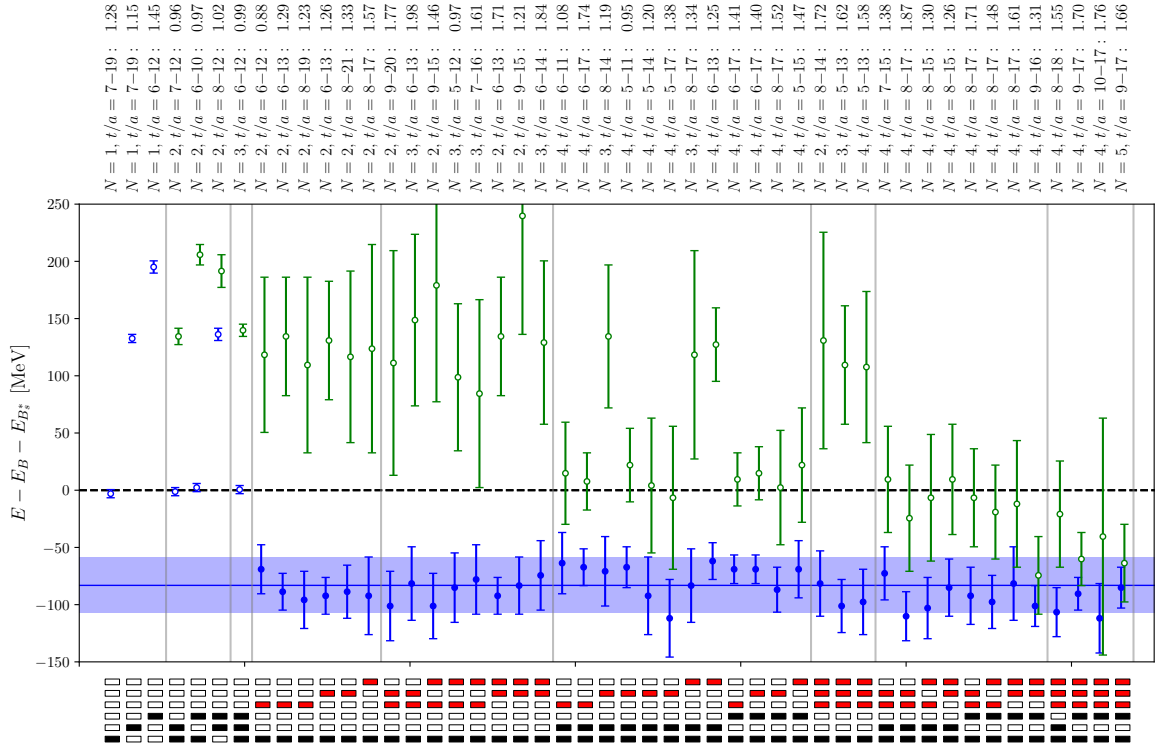


Figure 5.6.: Fit results for the two lowest energy levels  $\Delta E_0$  and  $\Delta E_1$  for the  $\bar{b}bus$  system with  $J^P = 1^+$  relative to the  $BB_s^*$  threshold obtained on ensemble C01. The notation is the same as for Fig. 5.2.

the ground-state energy level reliably and is consequently included in all subsequent fits [24].

If we consider now fits including  $\mathcal{O}'_1$ , at least one of the scattering operators  $\mathcal{O}'_4$  to  $\mathcal{O}'_6$ , and possibly further operators, we observe that the ground-state energy level as well as the result for  $E_1$  drop significantly. This is in agreement with the observations for the case of  $\bar{b}b\bar{u}d$  (see Sec. 5.3.1) where including scattering operators also lowers the energy levels. Here, we observe a ground-state energy level about 100 MeV below the lowest non-interacting meson-meson threshold  $BB_s^*$ , indicating the existence of a bound tetraquark state. The energy  $E_1$  is found in many cases at around 0 MeV, which agrees with the assumption that the first excited state is a meson-meson scattering state. Similar results are also obtained for the other ensemble for which the fit results can be found in Appendix A of Ref. [24].

The final estimate for the ground-state energy is obtained from all fits that are indicated by a filled symbol in Fig. 5.6. For all these fits, the ground-state energies agree within statistical uncertainties. Assuming fully correlated fit results, I compute the weighted average of the ground-state energies following the approach that is also used by the FLAG collaboration [185] (see also Appendix D). In the following I refer to this method as the *FLAG average*. The final estimate for the ground-state energy is illustrated in Fig. 5.6 by the horizontal blue line with error band.

I decided not to compute an average for the energy  $E_1$  as it is difficult to judge if this energy level indeed belongs to the first excited state [24]. Close to the  $BB_s^*$  threshold there are also two other two-meson thresholds appearing, namely the  $B^*B_s$  threshold which differs only by a few MeV and the  $B^*B_s^*$  threshold which is approximately 50 MeV above  $BB_s^*$ . Therefore it is difficult to make reliable statements if  $E_1$ , extracted from a particular fit, really belongs to the first excited state or if it is rather a mixture of the three states which are all expected at similar energy. For this reason I renounce giving a final estimate for  $E_1$  based on the fit results.

The normalized overlap factors obtained from a three-exponential fit of the full  $6 \times 3$  correlation matrix in the range  $16 \leq t/a \leq 24$  on ensemble F004 are shown in Fig. 5.7. First of all, for the overlap factors associated to  $\mathcal{O}'_1$ , we observe that  $|\tilde{Z}_1^0| \gg |\tilde{Z}_1^1|, |\tilde{Z}_1^2|$ . This indicates that the trial state which is generated by  $\mathcal{O}'_1$  is similar to the ground state  $|0\rangle$ . In principle, this is not surprising as  $\mathcal{O}'_1|\Omega\rangle$  has been constructed such that the overlap with the lowest state is large. Note that  $\mathcal{O}'_1$  is a linear combination of the four operators  $\mathcal{O}_1$  to  $\mathcal{O}_4$ . According to Table 5.7 the contributions of the local  $BB_s^*$  and  $B^*B_s$  components are equally large but the coefficients  $\bar{v}_0^1$  and  $\bar{v}_0^2$  differ in sign, which yields an antisymmetric combination in the flavors *us*. Additionally, there is a considerable contribution of operator  $\mathcal{O}_3$  resembling a local  $B^*B_s^*$  component which is also antisymmetric in the light flavors. As discussed in Ref. [24], this is not unexpected as the static-light lattice QCD computation in Ref. [32] found similar results for the ground state in the closely related  $\bar{b}b\bar{u}d$  system with  $I(J^P) = 0(1^+)$ . Finally, also the diquark-antidiquark operator  $\mathcal{O}_4$  has a substantial contribution to  $\mathcal{O}'_1$  which is slightly smaller than the meson-meson components.

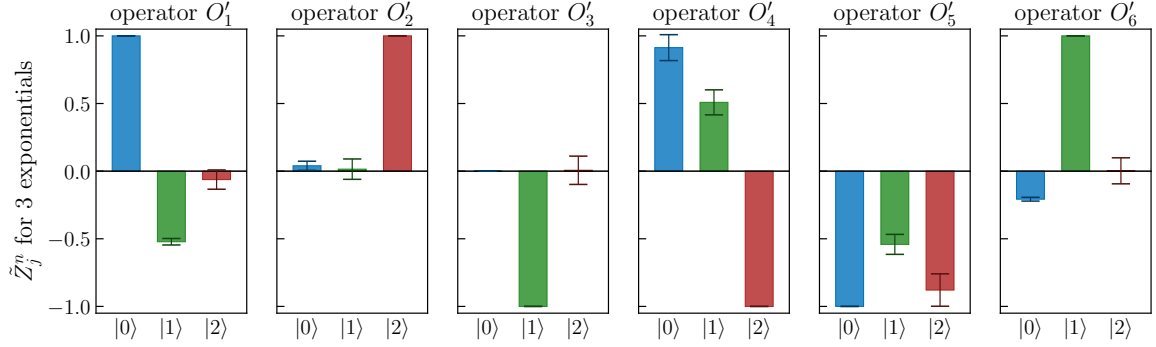


Figure 5.7.: Normalized overlap factors  $\tilde{Z}_j^n$  for the  $\bar{b}\bar{b}us$  system obtained via a three-exponential fit to the full  $6 \times 3$  correlation matrix in the range  $16 \leq t/a \leq 24$  on ensemble F004.

Additionally, we observe that  $|\tilde{Z}_2^0|, |\tilde{Z}_3^0| \approx 0$ , confirming that the trial states  $\mathcal{O}'_2|\Omega\rangle$  and  $\mathcal{O}'_3|\Omega\rangle$  are approximately orthogonal to the ground state  $|0\rangle$  as expected. Note that, according to Table 5.7, the operator  $\mathcal{O}'_2$  is essentially an equal weighted combination of  $\mathcal{O}_1$  and  $\mathcal{O}_2$  corresponding to a symmetric flavor combination in  $us$ , while operator  $\mathcal{O}'_3$  is, according to Table 5.7, antisymmetric in the flavors  $us$ .

The trial states generated by the two scattering operators  $\mathcal{O}'_4$  and  $\mathcal{O}'_5$  have sizable overlap with the ground state but also to higher excitations. Note that all terms of the local operators  $\mathcal{O}_1$  and  $\mathcal{O}_2$  also appear in  $\mathcal{O}'_4$  and  $\mathcal{O}'_5$ . Therefore, the large overlap factors  $|\tilde{Z}_4^0|, |\tilde{Z}_5^0|$  do not indicate that the ground state is a meson-meson scattering state but rather support the interpretation that it is a bound four-quark state with a large flavor antisymmetric  $BB_s^*$  and  $B^*B_s$  contribution [24].

Finally, it is worthwhile to take a brief look at the flavor symmetry of the different states. For the two lowest states  $|0\rangle$  and  $|1\rangle$ , the associated overlap factors  $|\tilde{Z}_j^0|$  and  $|\tilde{Z}_j^1|$  indicate that only the antisymmetric light flavor combination contributes to the associated state. In contrast to that, one can deduce from  $|\tilde{Z}_j^2|$  that the state  $|2\rangle$  is governed almost exclusively by contributions which are symmetric in the light flavors. This indicates that an approximated  $SU(3)$  flavor symmetry is preserved in the finite volume for the bound state as well as for the scattering states. Consequently, the  $\bar{b}\bar{b}us$  ground state, which is antisymmetric in the light flavors, has a flavor structure similar to that of the  $\bar{b}\bar{b}ud$  ground state with  $I = 0$ .



### 5.3.3 Results for the Case of $\bar{b}\bar{c}ud$ with $I(J^P) = 0(0^+)$

In the case of  $\bar{b}\bar{c}ud$  with  $I(J^P) = 0(0^+)$  the correlation matrix has size  $3 \times 2$  with the two local operators given in Eqs. (4.33) and (4.34) and the scattering operator in Eq. (4.35). The ground-state energy level is again extracted using multi-exponential matrix fits for several sub-matrices varying the number of exponentials and the fit range [24]. In Fig. 5.8 I show all fit results with  $\chi^2/\text{d.o.f.} < 2$  for ensemble C01. As in the case

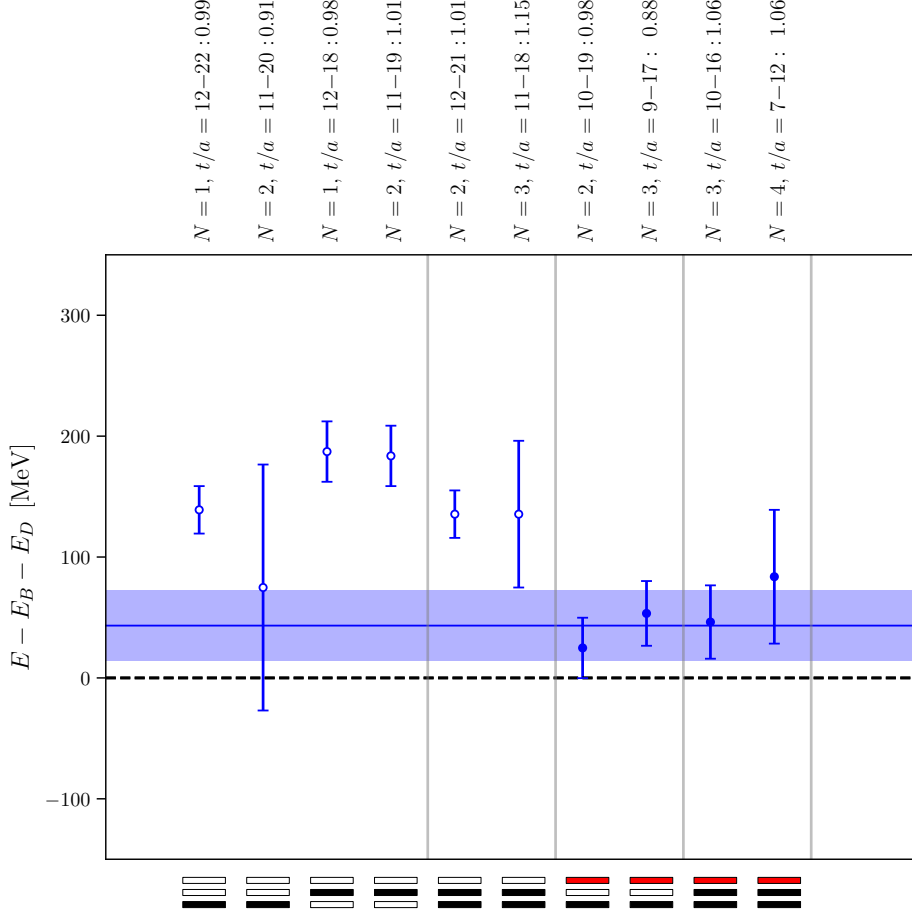


Figure 5.8.: Fit results for the lowest energy level  $\Delta E_0$  for the  $\bar{b}\bar{c}ud$  system with  $I(J^P) = 0(0^+)$  relative to the  $BD$  threshold obtained on ensemble C01. The notation is the same as for Fig. 5.2.

of  $\bar{b}\bar{b}ud$  and  $\bar{b}\bar{b}us$ , we observe that the ground-state energy level drops significantly if the scattering operator  $\mathcal{O}_3$  is included in the operator basis compared to fits relying only on local operators. The final estimate for the  $\bar{b}\bar{c}ud$  ground-state energy level with  $J = 0$  is determined via the FLAG average (see Appendix D) considering all fits that include the scattering operator  $\mathcal{O}_3$ . Here, we observe the ground-state energy slightly above but within uncertainties coinciding with the lowest meson-meson threshold  $BD$ . The results are qualitatively similar for all other ensembles as can be seen in Appendix

A of Ref. [24]. This indicates that the ground state is rather a  $BD$  scattering state than a bound four-quark state.

The normalized overlap factors  $\tilde{Z}_j^n$  support this interpretation. In Fig. 5.9 I present the  $\tilde{Z}_j^n$  obtained from a three-exponential fit to the full  $3 \times 2$  correlation matrix in the range  $6 \leq t/a \leq 10$  on ensemble F004. We clearly observe that the trial state  $\mathcal{O}_3^\dagger|\Omega\rangle$  generated by the  $BD$  scattering operator  $\mathcal{O}_3$  has dominating overlap with the ground state  $|0\rangle$ , while the overlap with higher excitations is negligible. This agrees with the interpretation of the ground state as a  $BD$  scattering state.

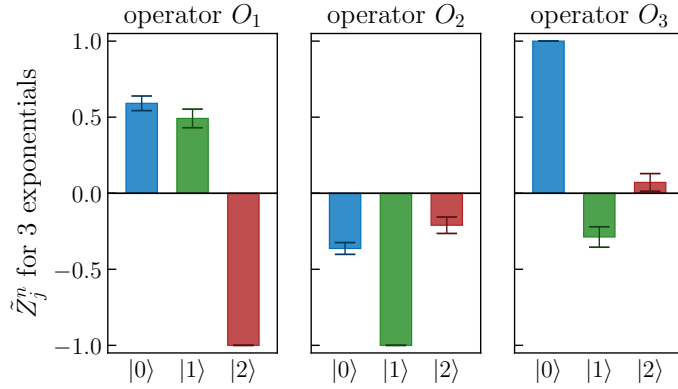


Figure 5.9.: Normalized overlap factors  $\tilde{Z}_j^n$  for the  $\bar{b}\bar{c}ud$  system with  $I(J^P) = 0(0^+)$  obtained via a three-exponential fit to the full  $3 \times 2$  correlation matrix in the range  $6 \leq t/a \leq 10$  on ensemble F004.

### 5.3.4 Results for the Case of $\bar{b}\bar{c}ud$ with $I(J^P) = 0(1^+)$

Finally, I consider the case of  $\bar{b}\bar{c}ud$  with  $I(J^P) = 0(1^+)$ . Note that the results discussed in this section have already been presented in Ref. [24]. The full correlation matrix has size  $5 \times 3$  and is composed of the three local operators defined in Eqs. (4.36) to (4.38) and the two scattering operators given in Eqs. (4.39) and (4.40). Again, I determine the ground-state energy and the energy of the first excitation via multi-exponential matrix fits and present the corresponding fit results in Fig. 5.10 for ensemble C01. Similar to the previous section, we observe that including scattering operators (in this case  $\mathcal{O}_4$  and  $\mathcal{O}_5$ ) in the operator basis results in a significant decrease in the energy levels  $E_0$  and  $E_1$ , while the operator  $\mathcal{O}_4$ , which creates a  $B^*D$  meson-meson scattering state, seems to be of particular importance. If  $\mathcal{O}_4$  is included in the operator basis,  $E_0$  is found to be considerably smaller compared to fits where  $\mathcal{O}_4$  is excluded. Since also the operator  $\mathcal{O}_1$  represents a  $B^*D$ -like structure, all fits that include  $\mathcal{O}_1$  and  $\mathcal{O}_4$  in the operator basis are taken into account for the final estimate of  $E_0$  which is obtained via the FLAG average (see Appendix D) [24]. According to Fig. 5.10, the final ground-state energy is found slightly above but within uncertainties in agreement with the  $B^*D$  threshold. For the first excited state, I renounce giving a final estimate

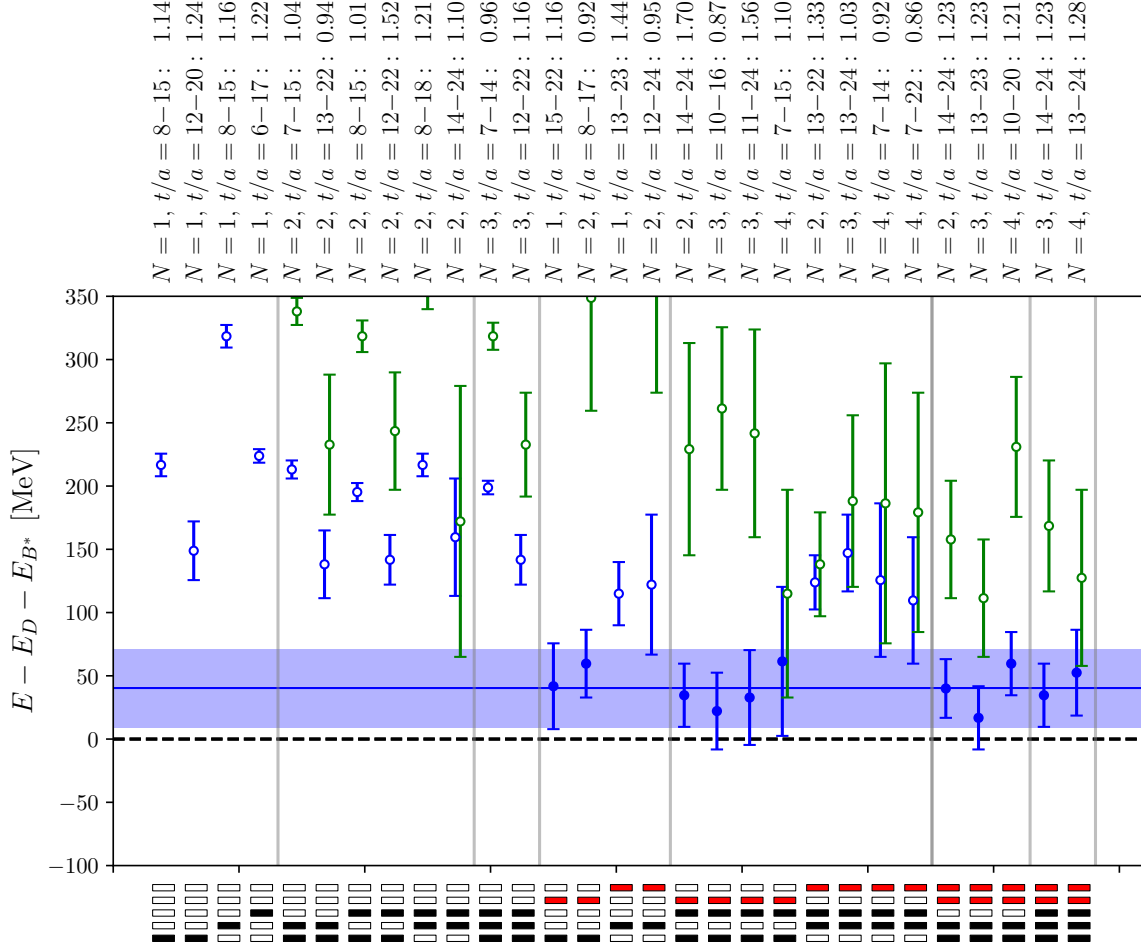


Figure 5.10.: Fit results for the two lowest energy levels  $\Delta E_0$  and  $\Delta E_1$  for the  $\bar{b}\bar{c}ud$  system with  $I(J^P) = 0(1^+)$  relative to the  $B^*D$  threshold obtained on ensemble C01. The notation is the same as for Fig. 5.2.

for the energy. Nevertheless, most fits have located  $E_1$  in the vicinity of the  $B^*D$  threshold which is approximately 100 MeV above the  $B^*D$  threshold [24]. The results for the other ensembles are similar and can be found in Appendix A of Ref. [24]. Consequently, the ground state in the  $\bar{b}\bar{c}ud$  system with  $J = 1$  seems to be a  $B^*D$  scattering state, while no evidence for a bound tetraquark state is observed.

The normalized overlap factors  $\tilde{Z}_j^n$ , obtained from a three-exponential fit to the full  $5 \times 3$  correlation matrix in the range  $14 \leq t/a \leq 20$  on ensemble F004, are shown in Fig. 5.11. We can see that  $|\tilde{Z}_4^0| \gg |\tilde{Z}_4^1|, |\tilde{Z}_4^2|$ , which indicates that the trial state  $\mathcal{O}_4^\dagger|\Omega\rangle$ , generated by the  $B^*D$  meson-meson scattering operator  $\mathcal{O}_4$ , has dominating overlap with the ground state  $|0\rangle$ , while it is nearly orthogonal to the other states [24]. This supports our interpretation of the ground state as a  $B^*D$  scattering state. Additionally, we find that  $|\tilde{Z}_5^1| \gg |\tilde{Z}_5^0|, |\tilde{Z}_5^2|$  which means that the trial state  $\mathcal{O}_5^\dagger|\Omega\rangle$  overlaps mainly

with the state  $|1\rangle$ . This coincides with the assumption that the first excitation is a  $BD^*$  scattering state.

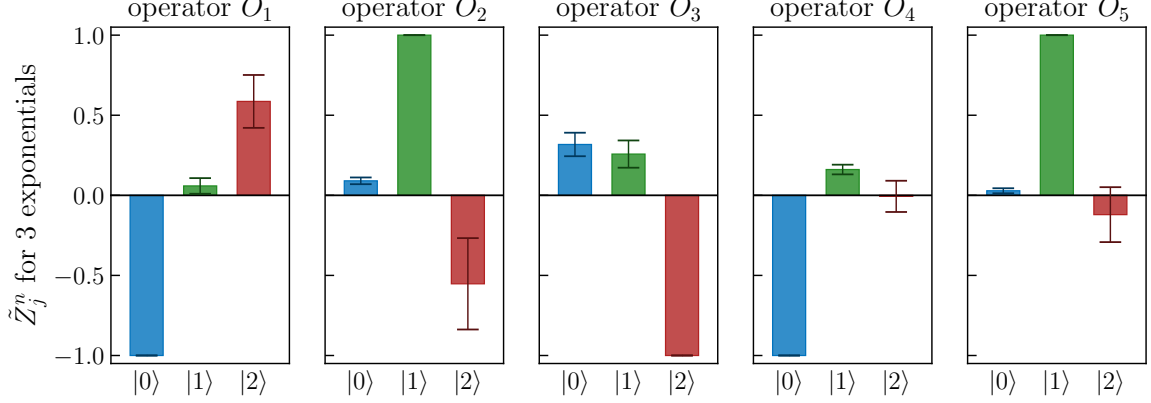


Figure 5.11.: Normalized overlap factors  $\tilde{Z}_j^n$  for the  $\bar{b}\bar{c}ud$  system with  $I(J^P) = 0(1^+)$  obtained via a three-exponential fit to the full  $5 \times 3$  correlation matrix in the range  $14 \leq t/a \leq 20$  on ensemble F004.

## 5.4 Final Results and Chiral Extrapolation

The final results for the ground-state energies relative to the lowest corresponding meson-meson threshold are listed in Table 5.8 for all four four-quark systems and for all five ensembles. Additionally, they are plotted as a function of  $m_\pi^2$  in Fig. 5.12. Note that for  $\bar{b}bus$  and  $\bar{b}\bar{c}ud$  with  $J = 0$  and  $J = 1$  I present the finite volume ground-state energy differences  $\Delta E_0$ , while for  $\bar{b}\bar{b}ud$  I show the infinite volume binding energy  $E_{\text{bind}}$ .

Ensemble	$\bar{b}\bar{b}ud$ $E_{\text{bind}}$ [MeV]	$\bar{b}bus$ $\Delta E_0$ [MeV]	$\bar{b}\bar{c}ud, J = 0$ $\Delta E_0$ [MeV]	$\bar{b}\bar{c}ud, J = 1$ $\Delta E_0$ [MeV]
C00078	-129(28)	-77(30)	-39(43)	-30(47)
C005	-123(34)	-76(22)	104(47)	79(35)
C01	-109(26)	-83(24)	43(29)	40(31)
F004	-122(25)	-92(15)	9(24)	21(40)
F006	-88(29)	-67(12)	101(29)	113(24)

Table 5.8.: Energies of the ground state relative to the lowest corresponding meson-meson threshold for all four four-quark systems and for all five ensembles. For  $\bar{b}\bar{b}ud$  the infinite volume binding energy  $E_{\text{bind}} = E_{\text{BS}} - E_B - E_{B^*}$  is presented where  $E_{\text{BS}}$  corresponds to the pole of the scattering amplitude as defined in Sec. 4.6. For the remaining three systems, the finite volume energies are listed, i.e.,  $\Delta E_0 = E_0 - E_B - E_{B_s^*}$  for  $\bar{b}bus$ ,  $\Delta E_0 = E_0 - E_B - E_D$  for  $\bar{b}\bar{c}ud$  with  $J = 0$ , and  $\Delta E_0 = E_0 - E_{B^*} - E_D$  for  $\bar{b}\bar{c}ud$  with  $J = 1$ .

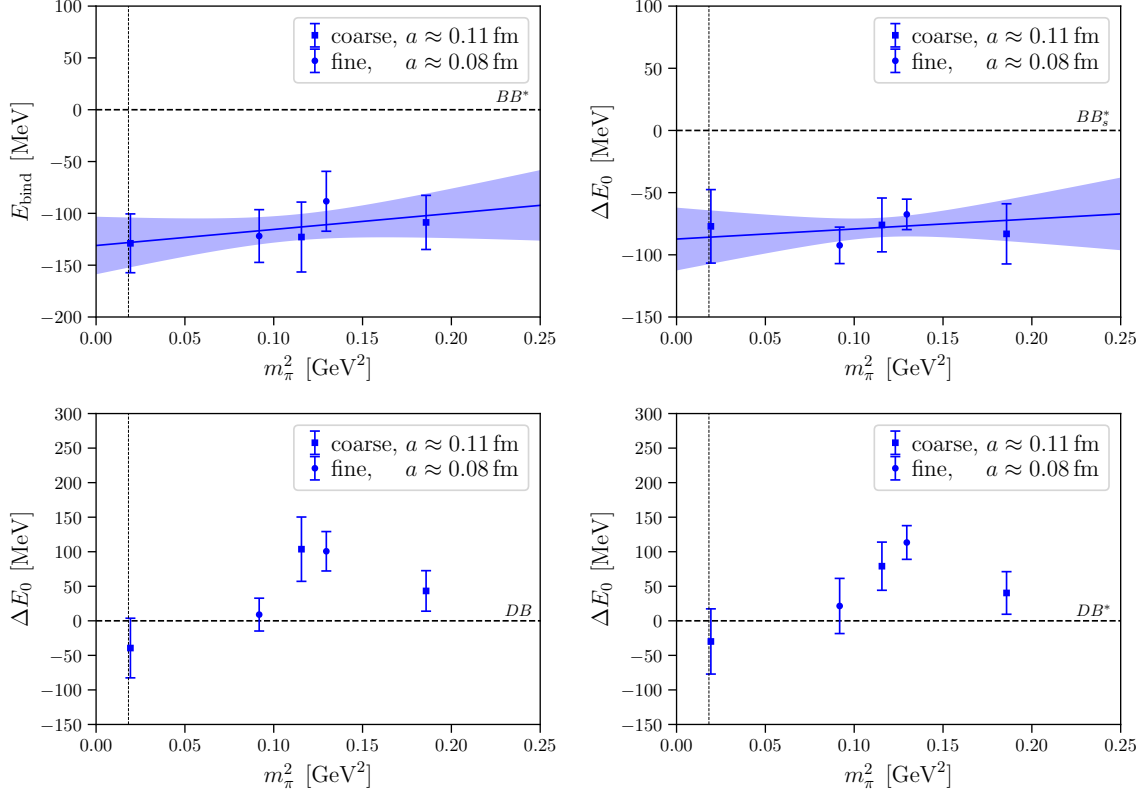


Figure 5.12.: Energies of the ground state relative to the lowest corresponding meson-meson threshold (indicated by the horizontal dashed lines) as a function of the squared pion mass  $m_\pi^2$  for the  $\bar{b}\bar{b}ud$  system (top left), the  $\bar{b}\bar{b}us$  system (top right), the  $\bar{b}\bar{c}ud$  system with  $I(J^P) = 0(0^+)$  (bottom left), and the  $\bar{b}\bar{c}ud$  system with  $I(J^P) = 0(1^+)$  (bottom right). For  $\bar{b}\bar{b}ud$  and  $\bar{b}\bar{b}us$  I also show the fit result of the chiral extrapolation according to Eq. (5.7) and Table 5.9.

As discussed in Sec. 5.3.1,  $E_{\text{bind}}$  is determined via a scattering analysis using the finite volume energy levels  $E_n$  and is found to be essentially identical to the finite volume ground-state energy  $\Delta E_0$ . Hereby, the effects due to the left-hand cut are neglected as stated at the end of Sec. 5.3.1.

The infinite volume binding energies for  $\bar{b}\bar{b}ud$  with  $I(J^P) = 0(1^+)$  are around 90 MeV to 130 MeV below the  $BB^*$  threshold indicating a hadronically stable four-quark state. In the case of  $\bar{b}\bar{b}us$  with  $J^P = 1^+$ , the finite volume ground-state energies are closer to the relevant threshold. Nevertheless, having ground-state energies of around 70 MeV to 100 MeV below the  $BB_s^*$  threshold, this indicates also for the  $\bar{b}\bar{b}us$  systems the existence of a bound four-quark state. In principle, it would be possible to extrapolate the results to the infinite volume in the same way as done for  $\bar{b}\bar{b}ud$ . However, this turns out to be technically more challenging [24]. For the case of  $\bar{b}\bar{b}us$  it would be necessary to consider the two scattering channels  $BB_s^*$  and  $B^*B_s$ , while the associated thresholds are separated only by a few MeV, making a coupled channel scattering

analysis indispensable. Additionally, we experienced in Sec. 5.3.2 that it is extremely difficult to reliably determine the energies of the excited states. However, we expect only small finite volume effects as the finite volume ground-state energy is significantly below the lowest meson-meson threshold. This assumption is also justified by the results for the  $\bar{b}bud$  sector, where the finite volume and infinite volume ground-state energies are essentially identical and discrepancies are much smaller than the statistical uncertainties. For those reasons, I refrain from performing a scattering analysis for the  $\bar{b}bus$  system in this setup and consider  $\Delta E_0$  as the binding energy of the  $\bar{b}bus$  system [24]. A successful treatment of finite volume effects will require the full consideration of scattering operators at the sink and the source which will be covered in Chapter 6. As the five ensembles used in this work differ in the pion mass  $m_\pi$ , ranging from 139 MeV to 431 MeV, we are able to extrapolate the binding energies to the physical point. Lattice discretization errors are expected to be of the order of a few MeV and thus no  $a$ -dependence is considered. I assume a quadratic pion-mass dependence, which corresponds to a linear dependence on the light quark masses  $m_{u;d}$ , according to

$$E_{\text{bind}}(m_\pi) = E_{\text{bind}}(m_{\pi,\text{phys}}) + c \left( m_\pi^2 - m_{\pi,\text{phys}}^2 \right), \quad (5.7)$$

where  $m_{\pi,\text{phys}} = 135$  MeV is the physical pion mass [24, 37]. The fit parameters  $E_{\text{bind}}(m_{\pi,\text{phys}})$  and  $c$  are determined by performing a  $\chi^2$ -minimizing fit using the ansatz in Eq. (5.7). The fit results as well as the  $\chi^2/\text{d.o.f.}$  of the corresponding fits are summarized in Table 5.9. In the last column, I give the mass of the bound tetraquark which is obtained by adding the experimental mass of the  $B$  and  $B^*$  mesons or the  $B$  and  $B_s^*$  mesons [87] to the binding energy  $E_{\text{bind}}$ . The resulting extrapolation is

	$E_{\text{bind}}(m_{\pi,\text{phys}})$ [MeV]	$c$ [ $10^{-4}/\text{MeV}^2$ ]	$\chi^2/\text{d.o.f.}$	$m_{\text{tetraquark}}(m_{\pi,\text{phys}})$ [MeV]
$\bar{b}bud$	-128(24)(10)	1.5(2.3)	0.27	10476(24)(10)
$\bar{b}bus$	-86(22)(10)	0.8(2.1)	0.81	10609(22)(10)

Table 5.9.: Fit results for the chiral extrapolation of the  $\bar{b}bud$  and  $\bar{b}bus$  systems to the physical pion mass  $m_\pi = 135$  MeV. The last column refers to the mass of the bound tetraquark obtained by adding the experimental meson masses [87] to  $E_{\text{bind}}$ . Statistical and systematic uncertainties are denoted in brackets.

also plotted together with the data points in Fig. 5.12. Since the  $\chi^2/\text{d.o.f.}$  is small for both fits, this indicates that the data points are successfully described by the fit function. Moreover, we observe that the slope parameter  $c$  is in both cases consistent with zero. Finally, the extrapolated binding energy  $E_{\text{bind}}(m_{\pi,\text{phys}})$  coincides well for both cases with the binding energy that has been determined on the ensemble C00078 with  $m_\pi = 139(1)$  MeV. This suggests that remaining systematic uncertainties due to the extrapolation in  $m_\pi$  are negligible [37].

Nevertheless, I expect systematic uncertainties which originate from lattice discretization errors and the NRQCD action. In Ref. [37] these errors were estimated to be

smaller than 10 MeV. They are denoted in Table 5.9 for  $E_{\text{bind}}$  and  $m_{\text{tetraquark}}$  in brackets right to the statistical uncertainties.

The finite volume ground-state energies that are obtained for the two  $\bar{b}\bar{c}ud$  systems are comparable with the corresponding lowest meson-meson thresholds. Consequently, I found no evidence for a hadronically stable tetraquark bound state in neither of the two channels. Note, however, that the existence of a shallow bound state close to the threshold or a resonance above the threshold might be possible [24].

Unfortunately, finite volume effects are expected to be large for states close to the threshold, but the determined spectrum for the two  $\bar{b}\bar{c}ud$  systems does not allow to quantify their actual size. For this reason, I do not perform a chiral extrapolation of the ground-state energy levels to the physical point as done for  $\bar{b}\bar{b}ud$  and  $\bar{b}\bar{b}us$ . Nevertheless, the final results for  $\Delta E_0$  obtained for both  $\bar{b}\bar{c}ud$  systems are shown in Fig. 5.12.

For a more precise study of the  $\bar{b}\bar{c}ud$  systems, it is necessary to include finite volume effects rigorously. This requires using a large basis of scattering operators to determine the low-lying finite volume energy spectrum and relate these energy levels to the infinite volume scattering amplitude using Lüscher's method. I perform such a more elaborated investigation of the  $\bar{b}\bar{c}ud$  four-quark systems in Chapter 7.





# 6

---

## COMPUTATION OF THE LOW-LYING ENERGY SPECTRUM FOR $\bar{b}\bar{b}ud$ AND $\bar{b}\bar{b}us$ TETRAQUARK STATES

---

So far, previous studies of the four-quark systems  $\bar{b}\bar{b}ud$  with  $I(J^P) = 0(1^+)$  and  $\bar{b}\bar{b}us$  with  $J^P = 1^+$  have relied either solely on local interpolating operators [35, 36, 38–40] or have used additional scattering operators only at the sink as in Refs. [24, 37] and in Chapter 5. There it was shown that this allows us to successfully extract the ground-state energy and to predict a bound tetraquark state for both the  $\bar{b}\bar{b}ud$  and  $\bar{b}\bar{b}us$  systems. However, higher excited states could not be resolved sufficiently precisely.

Since many tetraquark states are either bound states close to the threshold of strong decay or resonances in the spectrum of scattering states, their masses can only be reliably determined by considering the pole of the infinite volume scattering amplitude. As the scattering amplitude is related to the finite volume energy spectrum via Lüscher’s method, a large number of low-lying energy levels need to be resolved to parametrize the scattering amplitude successfully. This requires to fully include scattering operators when computing the correlation matrix.

In this chapter, I extend the investigations of the  $\bar{b}\bar{b}ud$  four-quark system with  $I(J^P) = 0(1^+)$  and the  $\bar{b}\bar{b}us$  four-quark system with  $J^P = 1^+$  by using scattering operators at the sink and at the source. This approach allows me to rigorously resolve also higher excited energy levels and to investigate potential finite volume effects in  $\bar{b}\bar{b}qq'$  systems. Moreover, it might also be beneficial for future studies of tetraquark systems which are candidates for shallow bound states or resonances. In Sec. 6.3, I present the low-lying finite volume energy spectra for the  $\bar{b}\bar{b}ud$  and  $\bar{b}\bar{b}us$  systems, focusing explicitly on the ground-state energies. Using the finite volume energy levels, I perform a scattering analysis applying Lüscher’s method in Sec. 6.4 to determine the infinite volume binding energies. Note that in this section I omit possible effects from left-hand cuts even though the utilized parametrization of the scattering amplitude exceeds the range of convergence that is defined by the one-particle left-hand cut branch point. In Sec. 6.5, I discuss the final results and extrapolate the binding energies to the physical pion mass. Before considering four-quark systems, I introduce the lattice setup in Sec. 6.1 and present the energies of the heavy-light pseudoscalar and vector  $B$  and  $B_s$  mesons in Sec. 6.2.

## 6.1 Lattice Setup

In the following, I introduce the gauge field configurations, present the fermion actions and the associated parameters that are used to compute the light, strange and bottom quark propagators and list the smearing parameters utilized for gauge field and quark field smearing.

### 6.1.1 Gauge Link Configurations

The calculations in this chapter are carried out using gauge link configurations generated by the MILC collaboration [186]. They use a one-loop Symanzik improved Lüscher-Weisz gauge action with perturbatively computed and tadpole improved coefficients [187] and the Highly Improved Staggered Quark (HISQ) action with 2+1+1 dynamical flavors to include the sea quarks [82]. I consider seven different ensembles which differ in the pion mass  $m_\pi$ , the lattice spacing  $a$  and the spatial volume. In particular, we have three ensembles with the same pion mass and lattice spacing but different spatial volumes. The details of all ensembles are listed in Table 6.1, while the lattice spacings have been determined in Ref. [186].

Ensemble	$N_s^3 \times N_t$	$a$ [fm]	$m_\pi^{(\text{sea})}$ [MeV]	$m_\pi^{(\text{val})}$ [MeV]	$N_{\text{conf}}$
a15m310	$16^3 \times 48$	0.1510(20)	306.9(5)	320.6(4.3)	11554
a12m310	$24^3 \times 64$	0.1207(11)	305.3(4)	310.2(2.8)	1053
a12m220S	$24^3 \times 64$	0.1202(12)	218.1(4)	225.0(2.3)	1020
a12m220	$32^3 \times 64$	0.1184(10)	216.9(2)	227.9(1.9)	1000
a12m220L	$40^3 \times 64$	0.1189(09)	217.0(2)	227.6(1.7)	1030
a09m310	$32^3 \times 96$	0.0888(08)	312.7(6)	313.0(2.8)	1166
a09m220	$48^3 \times 96$	0.0872(07)	220.3(2)	225.9(1.8)	657

Table 6.1.: List of gauge link ensembles [186] used in this chapter.  $N_s, N_t$ : number of lattice sites in spatial and temporal directions;  $a$ : lattice spacing;  $m_\pi^{(\text{sea})}$ : pion sea-quark mass;  $m_\pi^{(\text{val})}$ : pion valence-quark mass;  $N_{\text{conf}}$ : number of gauge field configurations.

### 6.1.2 Light and Strange Quark Propagators

I compute the light and strange valence quarks using the Wilson-clover action which I presented in Sec. 2.3.2. Staggered fermions which are used for the sea quarks provide some advantages like maintaining a remnant chiral symmetry or comparably low simulation costs. However, as a consequence of the staggered transformation in Eq. (2.43), which mixes space-time and Dirac indices, constructing interpolating operators with distinct spin and parity is complicated. This is not the case for Wilson-clover fermions, which are consequently the ideal choice for simulating the valence quarks in our study. The mixed action setup clover-on-HISQ utilized in this work follows the approach that

has also been successfully applied by the PNDME collaboration in Refs. [86, 188, 189]. There, they also ruled out the existence of exceptional configurations. I use the same parameters for the Wilson-clover action as the PNDME collaboration [86, 189] and summarize them in Table 6.2. A short discussion of benefits and problems of a mixed action setup has been presented in Sec. 2.3.5.

Ensemble	$am_l$	$am_s$	$c_{\text{sw}}$
a15m310	-0.0893	-0.021	1.05945
a12m310	-0.0695	-0.018718	1.05094
a12m220(S/L)	-0.075	-0.02118	1.05091
a09m310	-0.05138	-0.016075	1.04243
a09m220	-0.0554	-0.01761	1.04239

Table 6.2.: Parameters for the light and strange quarks used in the Wilson-clover action in Eq. (2.32). The parameter  $am_{l,s}$  is related to the so-called hopping parameter  $\kappa_{l,s}$  by  $2\kappa_{l,s} = 1/(am_{l,s} + 4)$  (e.g., see Ref. [50]). a12m220(S/L) stands for all three ensembles a12m220, a12m220S and a12m220L.

The light and strange quark propagators are computed using a multigrid (MG) solver according to the implementation discussed in Ref. [147] with three MG levels for all ensembles except for a15m310 where only two MG levels are used. On each level, I use 24 null vectors. The block sizes for each level are adjusted depending on the number of spatial and temporal lattice points for each ensemble.

### 6.1.3 Bottom Quark Propagators

I treat the bottom quarks in the framework of NRQCD as discussed in Sec. 2.4 using the same coefficients as the HPQCD collaboration [190, 191]. Tadpole improvement is hereby obtained in the same way as in Sec. 5.1.4, i.e., the gauge links are divided by the mean link  $u_{0L}$  in Landau gauge. The matching coefficients, however, differ from those which have been used for the calculations in Chapter 5. Here, all coefficients are set to their tree-level value  $c_i = 1$  besides the coefficients of the kinetic terms  $c_1, c_5$

Ensemble	$am_b$	$u_{0L}$	$c_1$	$c_5$	$c_6$
a15m310	3.42	0.8195	1.36	1.21	1.36
a12m310	2.66	0.834	1.31	1.16	1.31
a12m220(S/L)	2.62	0.8349	1.31	1.16	1.31
a09m310	1.91	0.8525	1.21	1.12	1.21
a09m220	1.90	0.8521	1.21	1.12	1.21

Table 6.3.: Parameters used in the NRQCD action in Eq. (2.76) for the bottom quarks.

and  $c_6$ . These are perturbatively determined as explained in Appendix B of Ref. [190]. I collect all parameters and the matching coefficients that deviate from their tree level values in Table 6.3. The coefficients for a09m220 are obtained by a linear interpolation in  $am_l$  between set 7 and set 8 of Ref. [191].

#### 6.1.4 Techniques to Compute Quark Propagators and Smearing of Quark Fields

In this chapter, I apply two different techniques to compute the quark propagators depending on the correlation matrix element that is computed. Point-to-all propagators as discussed in Sec. 4.4.1 are used for correlation matrix elements with local interpolating operators at the sink and the source. For each configuration, I employ 30 point sources at randomly chosen space-time positions for all ensembles except for the smallest one, a15m310. Here I only use 10 point sources. These propagators are also used for mesonic correlation functions. For correlation matrix elements with scattering interpolating operators at the sink and the source, I utilize stochastic timeslice-to-all propagators with spin and color dilution and additionally apply the one-end-trick (see Sec. 4.4.3). On all ensembles except for a15m310, I use stochastic sources at 4 equally distributed random timeslices with 5 different random seeds each. On ensemble a15m310, I also consider 5 different random seeds but only a single randomly chosen timeslice. For correlations between local and scattering operators, both techniques are applicable as the correlation matrix is hermitian. One can either use point-to-all propagators if the local operator is assigned to the source and the scattering operator to the sink or stochastic timeslice-to-all propagators if the scattering operator is assigned to the source and the local operator to the sink. As I obtained similar signal-to-noise ratios for both techniques, I apply both methods and average the results to increase the statistical precision. The explicit forms of the correlation matrix elements can be found in Appendix C.2

All quark fields appearing in the correlation matrix are smeared, regardless of the type of quark propagator chosen. I apply Gaussian smearing for all quark flavors. While I

Ensemble	Up and down quarks		Strange quarks		Bottom quarks	
	$N_{\text{Gauss}}$	$\kappa_{\text{Gauss}}$	$N_{\text{Gauss}}$	$\kappa_{\text{Gauss}}$	$N_{\text{Gauss}}$	$\sigma_{\text{Gauss}}$
very coarse	22	1.0	15	1.0	10	1.0
coarse	35	1.0	25	1.0	10	1.0
fine	70	1.0	50	1.0	10	1.0

Table 6.4.: Smearing parameters for the quark-fields used in the computation of the correlation functions. Gaussian smearing is carried out according to Eq. (4.78) for light and strange quarks and according to Eq. (4.77) for bottom quarks. The ensembles are cumulated corresponding to their lattice spacing, i.e., *very coarse* is equal to a15m310, *coarse* includes a12m310, a12m220S, a12m220, a12m220L, and *fine* covers a09m310 and a09m220.

use the Gaussian/Wuppertal prescription (see Ref. [160] and Sec. 4.5.2) for the light and strange quarks, the bottom quarks are smeared according to Eq. (4.77) as a consequence of the different numerical frameworks employed in this study. The smearing parameters are listed in Table 6.4. I illustrate the procedure to determine reasonable smearing parameters in Appendix E.1.

In order to reduce lattice artifacts and the probability that exceptional configurations appear as a consequence of the mixed action setup, I apply one sweep of HYP smearing with  $\alpha_1 = 0.75$ ,  $\alpha_2 = 0.6$  and  $\alpha_3 = 0.3$  (see [157] and Sec. 4.5.1.2) to the HISQ gauge links that are used in the light and strange quark smearing. Additionally, these gauge links are also spatially APE smeared (see [156] and Sec. 4.5.1.1) with  $N_{\text{APE}} = 50$  and  $\alpha_{\text{APE}} = 0.5$ . The bottom quark propagators are computed on unsmeared gauge links.

## 6.2 Energies and Kinetic Masses for Pseudoscalar and Vector $B$ and $B_s$ Mesons

The energies of the  $B$ ,  $B^*$ ,  $B_s$  and  $B_s^*$  mesons are computed via a correlated single-exponential fit to the two-point correlation function  $\langle \mathcal{O}_M(\mathbf{p}, t) \mathcal{O}_M^\dagger(\mathbf{p}, 0) \rangle$ , where  $\mathcal{O}_M$  is a meson interpolating operator according to Eqs. (4.15) to (4.18). I perform fits for various temporal separations with  $7 \leq t_{\text{min}}/a \leq 9$  and  $17 \leq t_{\text{max}}/a \leq 20$  and determine the final results for the meson energies via the FLAG average (see Appendix D) using the results obtained for all available fit ranges. In Fig. 6.1, I show the effective energies for zero momentum projection determined on ensemble a12m220L for all four mesons, while I collect the meson energies at rest for all ensembles in Table 6.5.

Note that the meson energies do not correspond to the physical masses but are shifted due to the use of NRQCD. As discussed in Sec. 5.2, these shifts cancel in energy differences with equal numbers of bottom quarks. Therefore, the relevant quantities

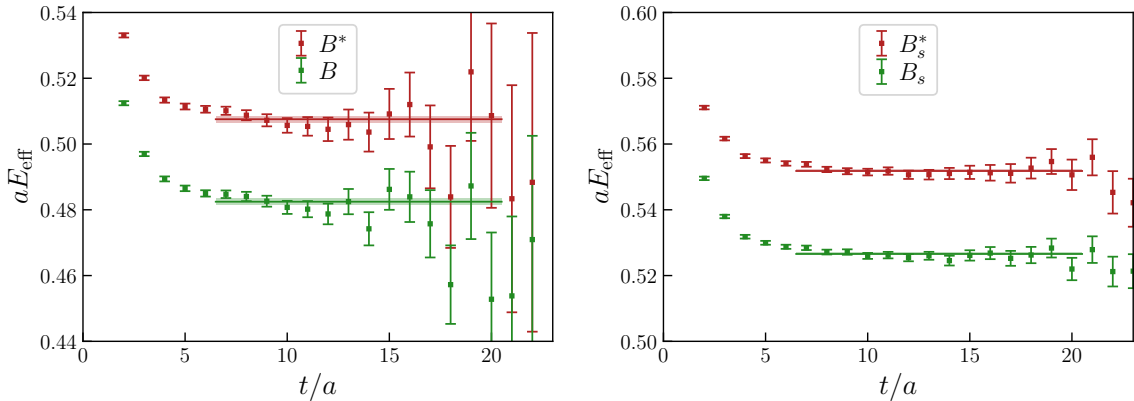


Figure 6.1.: Effective energies as defined in Eq. (4.6) at zero momentum for pseudoscalar and vector  $B$  and  $B_s$  mesons computed on ensemble a12m220L. The horizontal lines correspond to the final estimate of the mesons' energies that has been determined by various fits with  $7 \leq t_{\text{min}}/a \leq 9$  and  $17 \leq t_{\text{max}}/a \leq 20$ .

Ensemble	$aE_B(0)$	$aE_{B^*}(0)$	$aE_{B_s}(0)$	$aE_{B_s^*}(0)$
a15m310	0.56575(62)	0.59583(72)	0.61547(29)	0.64452(34)
a12m310	0.48902(88)	0.51561(99)	0.53050(43)	0.55641(51)
a12m220S	0.48269(113)	0.50820(126)	0.52653(44)	0.55215(50)
a12m220	0.48197(118)	0.50710(130)	0.52655(61)	0.55203(51)
a12m220L	0.48246(98)	0.50754(103)	0.52657(41)	0.55180(45)
a09m310	0.39766(53)	0.41713(59)	0.42922(29)	0.44894(33)
a09m220	0.38835(77)	0.40690(102)	0.42346(35)	0.44239(42)

 Table 6.5.: Energies of the pseudoscalar and vector  $B$  and  $B_s$  mesons at rest.

in this chapter are again the energy differences  $\Delta E_n = E_n - E_{M_1} - E_{M_2}$  where  $E_n$  is the  $n$ -th energy level of the four-quark state  $\bar{b}bqq'$  and  $M_1$  and  $M_2$  denote the mesons of the associated lowest two-meson threshold.

In order to perform the scattering analysis in Sec. 6.4, we require the momentum dependence of the mesons' energies. As discussed in Sec. 4.6.1, the antiheavy-light mesons with a  $\bar{b}$  quark treated in the framework of NRQCD obey the dispersion relation in Eq. (4.82). Using the interpolating operators given in Eqs. (4.15) to (4.18), I determine the meson energies  $E_M(\mathbf{p})$  up to the highest momentum  $\mathbf{p}^2 = 4(2\pi/L)^2$ . Afterwards, the dispersion relation in Eq. (4.82) is fitted to these energies, while  $E_{M,0}$  and  $m_{M,\text{kin}}$  are the free parameters of the fit. The results for the kinetic masses  $m_{M,\text{kin}}$  are listed in Table 6.6. The second parameter  $E_{M,0}$  can be used to examine if the parametrization indeed describes the data reasonably. In all cases, I have observed an excellent agreement of  $E_{M,0}$  with the meson energies at rest which are listed in Table 6.5. Since the ensembles a12m220S, a12m220 and a12m220L differ only in their

Ensemble	$am_{B,\text{kin}}$	$am_{B^*,\text{kin}}$	$am_{B_s,\text{kin}}$	$am_{B_s^*,\text{kin}}$
a15m310	4.015(47)	4.017(55)	4.100(24)	4.100(30)
a12m310	3.224(96)	3.238(108)	3.264(49)	3.266(57)
a12m220S	3.130(116)	3.115(127)	3.232(49)	3.223(55)
a12m220	3.167(208)	3.181(225)	3.216(107)	3.220(92)
a12m220L	3.121(252)	3.139(271)	3.208(112)	3.213(126)
a12m220co	3.121(84)	3.091(89)	3.233(37)	3.204(40)
a09m310	2.381(55)	2.382(60)	2.426(31)	2.427(35)
a09m220	2.342(161)	2.341(214)	2.397(79)	2.399(94)

 Table 6.6.: Kinetic masses for the pseudoscalar and vector  $B$  and  $B_s$  mesons determined by a  $\chi^2$ -minimizing fit.

spatial volume but have the same pion mass and lattice spacing, the energy levels determined on these three ensembles will be used in a single scattering analysis. For this reason, only a single kinetic mass is required for each meson. These kinetic masses are determined by a fit taking the meson energies  $E_M(\mathbf{p})$  from all three ensembles into account. I depict the momentum dependent meson energies together with the obtained dispersion relation in Fig. 6.2 for the  $B$  meson. The kinetic masses for all mesons are also listed in Table 6.6 labeled as  $a12m220co$ .

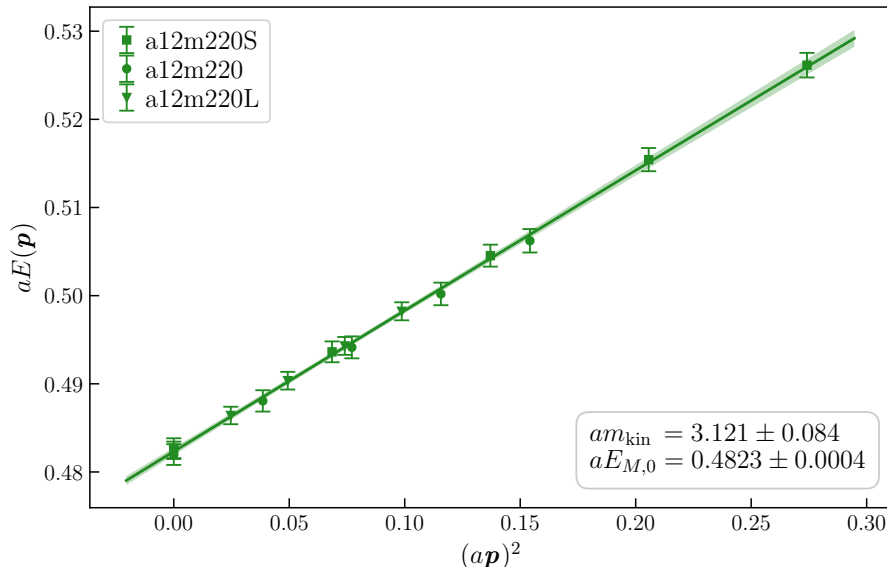


Figure 6.2.: Dispersion relation for the  $B$  meson based on the meson energies determined on the ensembles a12m220S, a12m220 and a12m220L. The momentum dependent energies  $aE(\mathbf{p})$  are determined for  $0 \leq \mathbf{p}^2 \leq 4(2\pi/L)^2$ .

### 6.3 Finite Volume $\bar{b}bqq'$ Energy Levels

The correlation matrices for the  $\bar{b}b\bar{u}d$  and  $\bar{b}b\bar{u}s$  four-quark systems are built of two-point correlation functions using the same interpolating operators as in Chapter 5, given by Eqs. (4.21) to (4.25) and Eqs. (4.26) to (4.32). However, now I compute the full correlation matrix, i.e., those correlation matrix elements with a scattering operator at the source are taken into account, too. Consequently, the resulting correlation matrices are square matrices of size  $5 \times 5$  for the case of  $\bar{b}b\bar{u}d$  and  $7 \times 7$  for the case of  $\bar{b}b\bar{u}s$ . This makes it possible to extract not only the ground-state energy level precisely but also higher excitations corresponding to meson-meson scattering states. Resolving the complete low-lying finite volume energy spectrum is an important preparatory step to be able to study finite volume effects in a rigorous way applying a scattering analysis using Lüscher's method.

The low-lying energy levels of the four-quark systems are determined by solving a generalized eigenvalue problem (GEVP, see Sec. 4.3.1) and fitting a single-exponential



ansatz as given in Eq. (4.46) to the resulting principal correlators  $\lambda_n(t, t_0)$  separately for each energy level  $n$ . The parameter  $t_0$  in the GEVP is chosen sufficiently large so that contributions from higher excitations are suppressed. I discuss the impact of  $t_0$  on the effective energies of the considered four-quark systems in Appendix E.2. In order to reduce systematic uncertainties due to the chosen fit range  $t_{\min} \leq t \leq t_{\max}$ , I perform several fits varying  $t_{\min}$  and  $t_{\max}$ . The final estimate for the energy of the  $n$ -th state is then obtained using the FLAG average including all fit results as discussed in Appendix D. I determine the associated statistical uncertainty via Jackknife resampling which means that separately for each Jackknife sample, I solve the GEVP and fit the principal correlators. For each reduced Jackknife sample, I compute then the FLAG average considering the results obtained for all fit ranges, while the weight-factor for a particular fit is governed by the associated statistical error computed via all Jackknife samples. Finally, the mean value and Jackknife error specify then the final estimate for the energy of the corresponding  $n$ -th energy level.

The eigenvector  $v_n(t)$  which can also be obtained from the GEVP contains certain information about the composition of the  $n$ -th eigenstate. The component  $v_n^j$  gives the contribution of the trial state  $\mathcal{O}_j^\dagger|\Omega\rangle$  to state  $|n\rangle$ ,

$$|n\rangle = \sum_j v_n^j \mathcal{O}_j^\dagger |\Omega\rangle. \quad (6.1)$$

Provided that the operator basis used contains all relevant structures to describe the low-lying energy spectrum of a specific channel, a large eigenvector component  $v_n^j$  indicates that the state  $|n\rangle$  has a large component of the quark structure that is described by operator  $\mathcal{O}_j$ . Finally, note that the eigenvector components  $v_n^j$  are related to the overlap factors  $Z_j^m$  that have been discussed in Sec. 5.3 according to

$$\sum_j Z_j^m v_n^j \approx \delta_{mn}, \quad (6.2)$$

where corrections are exponentially small [192].

### 6.3.1 Energy Spectrum for the Case of $\bar{b}\bar{b}ud$ with $I(J^P) = 0(1^+)$

I use the same operator basis to study the  $\bar{b}\bar{b}ud$  four-quark system with  $I(J^P) = 0(1^+)$  as in Sec. 5.3.1 consisting of the three local operators given in Eqs. (4.21) to (4.23) and the two scattering operators defined in Eqs. (4.24) and (4.25). In contrast to the previous investigation, the full squared  $5 \times 5$  correlation matrix is evaluated, so also correlation matrix elements with scattering operators at the source are computed.

In order to study the impact of the scattering operators on the low-lying energy spectrum, I extract the effective energies via a GEVP for the three lowest energy states (i) from the  $3 \times 3$  correlation matrix using only the local interpolating operators  $\mathcal{O}_1$ ,  $\mathcal{O}_2$  and  $\mathcal{O}_3$  and (ii) from the full  $5 \times 5$  correlation matrix using the scattering operators  $\mathcal{O}_4$  and  $\mathcal{O}_5$  in addition to the local interpolating operators. The corresponding effective energies determined on ensemble a12m220L are illustrated in Fig. 6.3. The



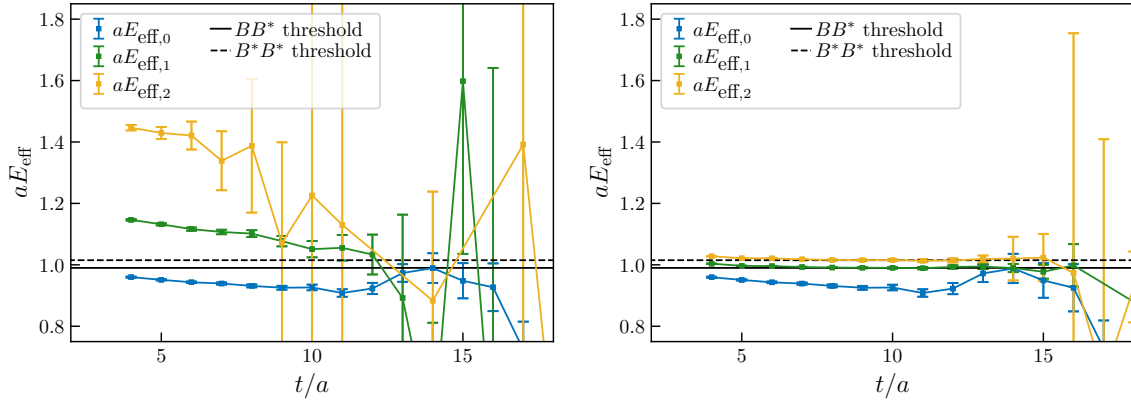


Figure 6.3.: Effective energies for the  $\bar{b}bq'q'$  four-quark system with  $I(J^P) = 0(1^+)$  for the  $3 \times 3$  matrix using only the local interpolating operators  $\mathcal{O}_1$ ,  $\mathcal{O}_2$  and  $\mathcal{O}_3$  (left) and for the  $5 \times 5$  matrix, using the local interpolating operators  $\mathcal{O}_1$ ,  $\mathcal{O}_2$  and  $\mathcal{O}_3$  as well as the scattering interpolating operators  $\mathcal{O}_4$  and  $\mathcal{O}_5$  (right) extracted from a GEVP on ensemble a12m220L.

ground-state energy level is found in both cases significantly below the  $BB^*$  threshold which agrees with the expectations based on the investigation in Sec. 5.3.1 and previous lattice QCD calculations [35–38]. Additionally, we expect that the first and second excited states coincide with  $BB^*$  and  $B^*B^*$  meson-meson scattering states and are consequently located close to the associated thresholds. However, we observe that the excited energy levels in the left plot of Fig. 6.3, where I only use local operators, have a large discrepancy to this expectation. But if the scattering operators  $\mathcal{O}_4$  and  $\mathcal{O}_5$  are included, we observe effective energies that are in accordance with the expectation, i.e., the effective energies of the first and second excited states coincide with the  $BB^*$  and  $B^*B^*$  thresholds as shown in the right plot of Fig. 6.3. This illustrates that scattering operators are essential to determine meson-meson scattering states and underlines their importance to reliably extract the low-lying energy spectrum. Note that these results also support the conclusions of Sec. 5.3.1 where I already pointed out the relevance of scattering operators to extract low-lying energy levels precisely. From now on, I will always consider the full  $5 \times 5$  correlation matrix, i.e., take all operators into account.

As discussed earlier, I perform correlated single-exponential fits to the principal correlators  $\lambda_n$ , which have been obtained by solving a GEVP, to extract the energies  $E_n$  of the associated states. The fit results for the three lowest energy levels relative to the  $BB^*$  threshold computed on ensemble a12m220L are presented in Fig. 6.4 for various fit ranges  $t_{\min} \leq t \leq t_{\max}$ . The lower boundary  $t_{\min}$  is chosen sufficiently large so that the effective energy has reached its plateau. The upper boundary  $t_{\max}$  should be chosen as large as possible before the signal is lost in noise. In practice, however, I experienced that the actual choice of  $t_{\max}$  has only mild effects on the fit results. For the temporal fit ranges, I use all possible combinations with  $8 \leq t_{\min}/a \leq 10$  and  $15 \leq t_{\max}/a \leq 19$ , while the fit range of a particular fit is shown at the top of each

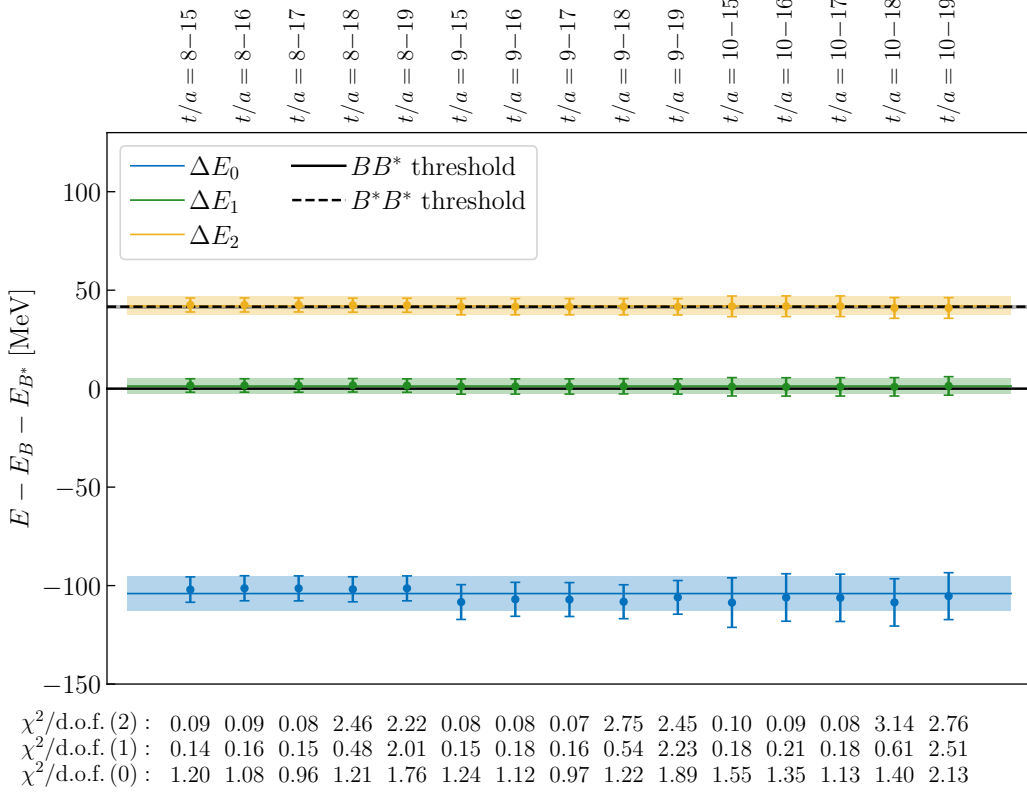


Figure 6.4.: Fit results for the three lowest energy levels for the  $\bar{b}\bar{b}ud$  system with  $I(J^P) = 0(1^+)$  relative to the  $BB^*$  threshold,  $\Delta E_n = E_n - E_B - E_{B^*}$  obtained on ensemble a12m220L. The horizontal black lines indicate the lowest two-meson thresholds  $BB^*$  (solid) and  $B^*B^*$  (dashed). Above each column, the temporal fit range is indicated, below the plot the value of  $\chi^2/\text{d.o.f.}(n)$  is shown. The colored horizontal lines with shaded error bands correspond to the final estimates for  $\Delta E_n$ .

column in Fig. 6.4. Below the plot, I depict the values of  $\chi^2/\text{d.o.f.}(n)$  for the single exponential fits of the  $n$ -th energy level. The horizontal lines with shaded bands represent my final estimates for the energy differences  $\Delta E_n$  obtained by a FLAG average (see Appendix D). Note that the energy differences  $\Delta E_n = E_n - E_B - E_{B^*}$  are first computed on each Jackknife sample independently, and only afterwards is the final result for  $\Delta E_n$  determined by calculating the mean and Jackknife error based on the Jackknife samples. This guarantees that presumably existing correlations between the meson energies and the energies of the  $\bar{b}\bar{b}ud$  levels are correctly incorporated in the statistical uncertainties.

We observe that the ground-state energy level is clearly below the  $BB^*$  threshold which is the lowest non-interacting meson-meson threshold in this channel. This indicates that the ground state is indeed a bound tetraquark state. The energy of the first excited state is slightly above but within uncertainties compatible with the  $BB^*$  threshold. This is in line with our expectation of the first excited state as a meson-

meson scattering state. Additionally, the energy of the second excited state is in good agreement with the  $B^*B^*$  threshold. Consequently, I interpret the second excited state as a  $B^*B^*$  scattering state. I repeat the same analysis for the remaining six ensembles and show the fit results for these ensembles in Appendix F. The final estimates for the finite volume energies relative to the  $BB^*$  threshold for the three lowest energy levels are collected in Table 6.7 and illustrated altogether in Fig. 6.5. According to

Ensemble	$\Delta E_0$ [MeV]	$\Delta E_1$ [MeV]	$\Delta E_2$ [MeV]
a15m310	-75.5(1.8)	2.7(2.2)	45.2(2.5)
a12m310	-70.1(4.2)	-1.8(3.8)	40.5(4.2)
a12m220S	-84.7(6.5)	1.9(5.3)	45.1(5.9)
a12m220	-83.1(5.2)	2.5(3.7)	45.2(3.9)
a12m220L	-104.0(6.8)	1.4(3.5)	42.1(3.7)
a09m310	-83.8(5.9)	-6.2(5.0)	44.1(6.2)
a09m220	-98.1(9.6)	-2.5(5.0)	37.1(5.5)

Table 6.7.: Finite volume energies of the three lowest energy levels for the  $\bar{b}bud$  system with  $I(J^P) = 0(1^+)$  on each ensemble in physical units relative to the  $BB^*$  threshold, i.e.,  $\Delta E_n = E_n - E_B - E_{B^*}$ .

Table 6.7, I find similar results for all ensembles with a ground-state energy about 70 MeV to 100 MeV below the  $BB^*$  threshold. Moreover, the first and second excited states agree in all cases with the non-interacting  $BB^*$  and  $B^*B^*$  threshold respectively. This is a strong indication for a bound tetraquark state. As the low-lying finite volume energy spectrum is now resolved precisely, these energy levels can be used as input for a scattering analysis in order to extract the  $\bar{b}bud$  binding energy in the infinite volume. This will be done in the subsequent section (see Sec. 6.4.1).

Note that I include only the two scattering operators  $\mathcal{O}_4$  and  $\mathcal{O}_5$  given in Eqs. (4.24) and (4.25) in the operator basis representing  $BB^*$  and  $B^*B^*$  scattering states with zero momentum projection for each meson. However, I do not consider scattering operators with so-called back-to-back momenta which means that the individual meson momenta are non-zero while the total momentum remains zero. Consequently, the associated scattering states are not resolved in the finite volume energy spectrum. Depending on the spatial volume of a particular ensemble, these states can have energies which are between the  $BB^*$  and the  $B^*B^*$  thresholds. I refrain from including these scattering operators and extracting the energies of the associated scattering states as they are not required to precisely determine the infinite volume ground-state energy for a potentially deeply bound state as in the case of  $\bar{b}bud$ , but would generate a large computational overhead.

The eigenvector components  $v_n^j$  that are obtained additionally to the principal correlators  $\lambda_n$  from solving a GEVP provide some information about the composition of the

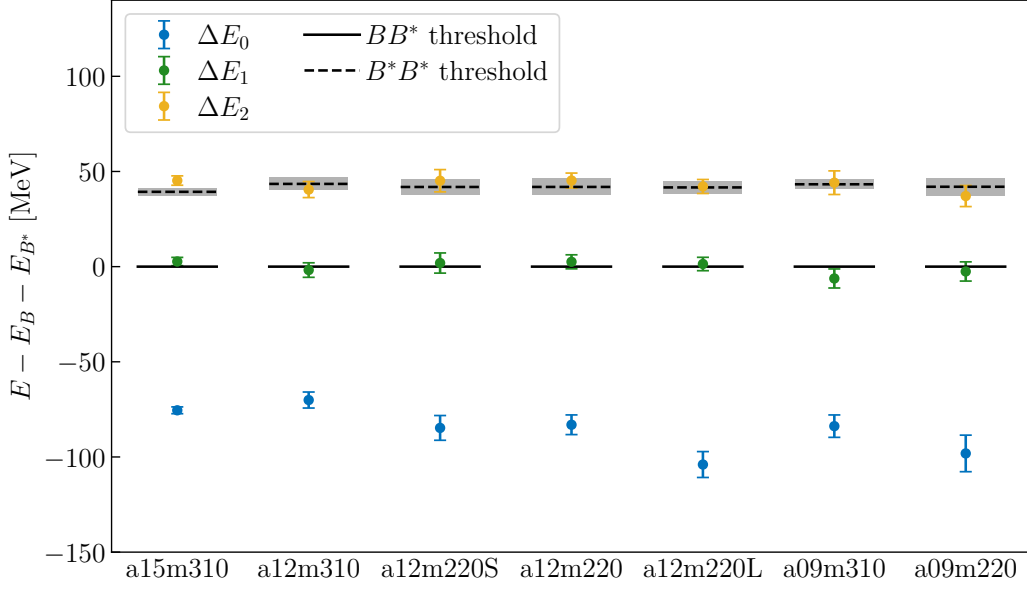


Figure 6.5.: Finite volume energies of the three lowest energy levels for the  $\bar{b}\bar{b}ud$  system with  $I(J^P) = 0(1^+)$  on each ensemble relative to the  $BB^*$  threshold,  $\Delta E_n = E_n - E_B - E_{B^*}$ . The black horizontal lines correspond to the  $BB^*$  (solid) and  $B^*B^*$  (dashed) thresholds.

low-lying states. This can be used to support the interpretation of the ground state as a bound four-quark state and of the first and second excited states as meson-meson scattering states. Additionally, the eigenvector component  $v_n^j$  represents the contribution of the trial state  $\mathcal{O}_j^\dagger|\Omega\rangle$  to the eigenstate  $|n\rangle$  and consequently allows us to draw conclusions about the quark structure of the tetraquark state. In Fig. 6.6, I depict the signed squared eigenvector components

$$\tilde{v}_n^j = \text{sign}(v_n^j)|v_n^j|^2, \quad (6.3)$$

which have been determined on ensemble a12m220L. They have been computed by solving a GEVP and afterwards fitting a constant to the  $t$ -dependent eigenvector components  $v_n^j$  using various fit ranges  $t_{\min} \leq t \leq t_{\max}$ , while for ensemble a12m220L I choose  $6 \leq t_{\min}/a \leq 9$  and  $12 \leq t_{\max}/a \leq 14$ . The final result for  $v_n^j$  is then obtained again as the FLAG average (see Appendix D) over all fit results. The number of the eigenstate above each plot is identical to the index  $n$ , while the numbers below each plot correspond to the indices  $j$  of the operators that are used to create the trial states  $\mathcal{O}_j^\dagger|\Omega\rangle$ .

We observe that the ground state is mainly composed of the trial states  $\mathcal{O}_j^\dagger|\Omega\rangle$  with  $j = 1, 2, 3$  generated by the local operators  $\mathcal{O}_1$ ,  $\mathcal{O}_2$  and  $\mathcal{O}_3$ . The eigenvector components  $\tilde{v}_0^4$  and  $\tilde{v}_0^5$  associated to the trial states generated by the scattering operators  $\mathcal{O}_4$  and  $\mathcal{O}_5$  are in contrast comparably small. This suggests that the ground state is mainly built of local four-quark structures which supports the interpretation of the ground state as a hadronically stable tetraquark. Considering the eigenvector components  $\tilde{v}_0^1$ ,

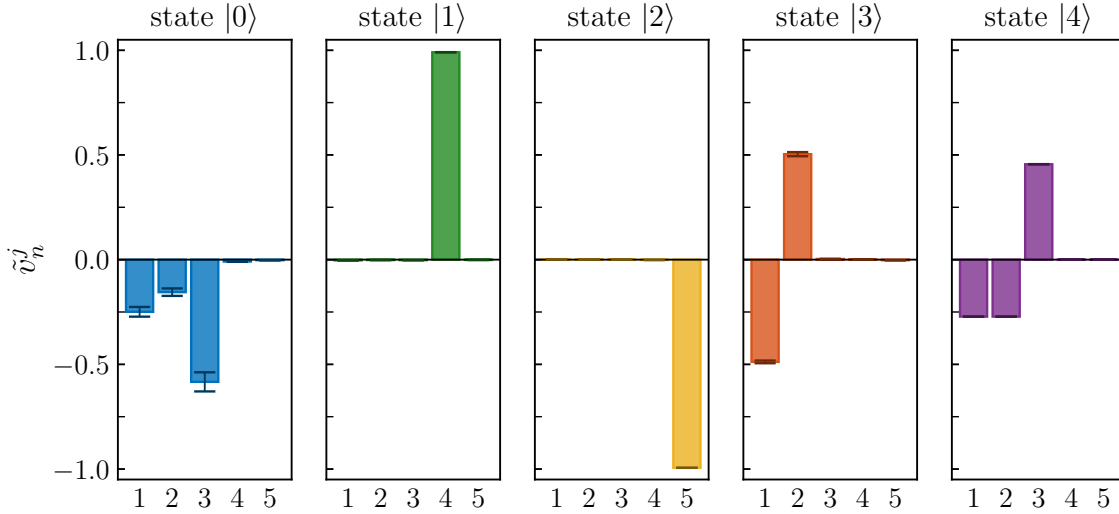


Figure 6.6.: Signed squared eigenvector components  $\tilde{v}_n^j$  for the  $\bar{b}bud$  system with  $I(J^P) = 0(1^+)$  obtained on ensemble a12m220L. The results are determined via constant fits to the  $t$ -dependent eigenvector components  $v_n^j$  in the range  $t_{\min} \leq t \leq t_{\max}$  with  $6 \leq t_{\min}/a \leq 9$  and  $12 \leq t_{\max}/a \leq 14$  followed by a FLAG average taking all fits into account.

$\tilde{v}_0^2$  and  $\tilde{v}_0^3$  associated to the trial states generated by the local operators  $\mathcal{O}_1$ ,  $\mathcal{O}_2$  and  $\mathcal{O}_3$  in more detail, we can infer the importance of the different structures for the  $\bar{b}bud$  ground state. We recognize that it has a dominating diquark-antidiquark component but also large meson-meson components. As the eigenvectors are normalized according to  $\sum_j (v_n^j)^2 = 1$ , we can directly extract the weight of the three local structures from Fig. 6.6 and find a  $BB^*$  component of 0.26(2), a  $B^*B^*$  component of 0.16(2) and a diquark-antidiquark component of 0.60(5). Consequently, the ratio of meson-meson to diquark-antidiquark structures for the  $\bar{b}bud$  tetraquark is approximately 40%/60% and indicates that both structures are present in the tetraquark state. This is in agreement with Refs. [136, 193] where also significant contributions of both structures have been identified. Note that in Refs. [136, 193] a slightly dominating meson-meson contribution has been found. However, the eigenvector decomposition allows qualitative statements rather than reliable quantitative conclusions regarding the composition of states since, for example, the quark field smearing can affect the actual eigenvectors. Consequently, my results support the assumption that both meson-meson and diquark-antidiquark structures are of similar importance for the formation of the bound  $\bar{b}bud$  tetraquark state. In addition, we observe that the  $BB^*$  and the  $B^*B^*$  components are of similar magnitude which agrees with the results obtained in Ref. [32].

The first excited state is almost completely governed by the trial state  $\mathcal{O}_4^\dagger|\Omega\rangle$ . As  $\mathcal{O}_4$  resembles a  $BB^*$  scattering structure, this confirms our interpretation of the first excited state as a  $BB^*$  scattering state. The same holds for the second excited state where  $\tilde{v}_2^5 \approx 1$  and  $\tilde{v}_2^k \approx 0$  for  $k \neq 5$ . Since  $\mathcal{O}_5$  resembles a  $B^*B^*$  structure, the second excited state can be identified as a  $B^*B^*$  scattering state.

### 6.3.2 Energy Spectrum for the Case of $\bar{b}\bar{b}us$ with $J^P = 1^+$

The operator basis that is used to study the  $\bar{b}\bar{b}us$  four-quark system with  $J^P = 1^+$  is the same as in Sec. 5.3.2, so I am using the four local interpolating operators given in Eqs. (4.26) to (4.29) and the three scattering interpolating operators in Eqs. (4.30) to (4.32). Note that I have refrained from including scattering operators with back-to-back momenta as discussed in Sec. 6.3.1 for the case of  $\bar{b}\bar{b}ud$ .

As in the previous section, I compute all possible correlation matrix elements and extract the low-lying energy levels by solving a GEVP and performing correlated single-exponential fits to the principal correlators  $\lambda_n$ . In Fig. 6.7, I show the effective energies for the four lowest energy eigenstates determined on ensemble a12m220L. The

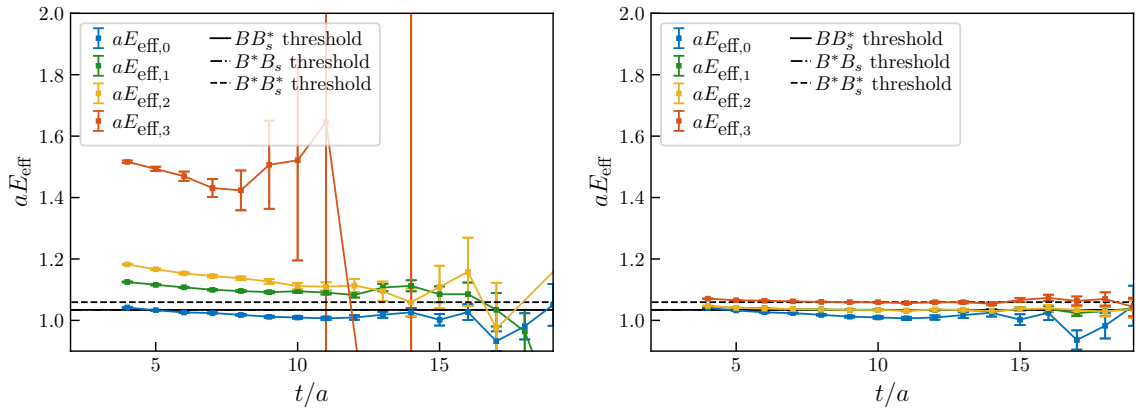


Figure 6.7.: Effective energies for the  $\bar{b}\bar{b}us$  four-quark system with  $J^P = 1^+$  for the  $4 \times 4$  matrix using only the local interpolating operators  $\mathcal{O}_1$ ,  $\mathcal{O}_2$ ,  $\mathcal{O}_3$  and  $\mathcal{O}_4$  (left) and for the  $7 \times 7$  matrix, with the local interpolating operators  $\mathcal{O}_1$ ,  $\mathcal{O}_2$ ,  $\mathcal{O}_3$  and  $\mathcal{O}_4$  and the scattering interpolating operators  $\mathcal{O}_5$ ,  $\mathcal{O}_6$  and  $\mathcal{O}_7$  (right) extracted from a GEVP on ensemble a12m220L.

effective energies in the left plot are extracted from a correlation matrix consisting only of the four local operators  $\mathcal{O}_1$  to  $\mathcal{O}_4$  while in the right plot the full correlation matrix composed of the local operators  $\mathcal{O}_1$  to  $\mathcal{O}_4$  as well as the scattering operators  $\mathcal{O}_5$  to  $\mathcal{O}_7$  is considered. Similar to the case of  $\bar{b}\bar{b}ud$ , we expect the ground-state energy level to be below the lowest non-interacting two-meson threshold. Additionally, the first three excited states should describe meson-meson scattering states associated to the three lowest meson-meson thresholds  $BB_s^*$ ,  $B^*B_s$  and  $B^*B_s^*$ . While the ground state is found in both plots of Fig. 6.7 well below the threshold of strong decay as expected, the effective energies of the excited states meet the expectations only in the right plot. This underlines again the importance of including scattering operators in the operator basis to reliably extract the low-lying energy levels as discussed in Secs. 5.3.2 and 6.3.1. For this reason, I consider from now on always the full  $7 \times 7$  correlation matrix.

In Fig. 6.8, I show the fit results for the four lowest energy levels that are determined by performing correlated single exponential fits for various  $t$ -ranges to the principal correlators, obtained by solving a GEVP, for ensemble a12m220L. Here, I consider all pos-

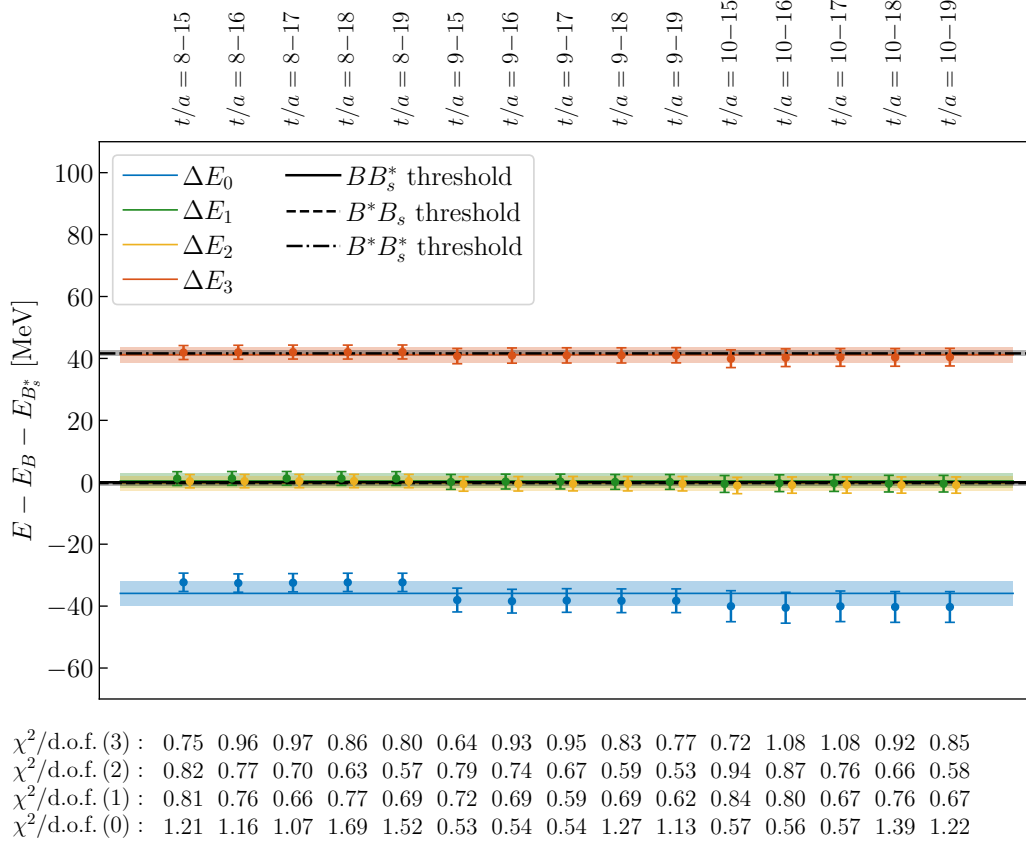


Figure 6.8.: Fit results for the four lowest energy levels for the  $\bar{b}\bar{b}us$  system with  $J^P = 1^+$  relative to the  $BB_s^*$  threshold,  $\Delta E_n = E_n - E_B - E_{B_s^*}$  obtained on ensemble a12m220L. The horizontal black lines indicate the lowest two-meson thresholds  $BB_s^*$  (solid),  $B^*B_s$  (dashed) and  $B^*B_s^*$  (dash-dot). Above each column, the temporal fit range is indicated, below the plot the value of  $\chi^2/\text{d.o.f.}(n)$  is shown. The colored horizontal lines with shaded error bands correspond to the final estimates for  $\Delta E_n$ .

sible temporal separations  $t_{\min} \leq t \leq t_{\max}$  with  $8 \leq t_{\min}/a \leq 10$  and  $15 \leq t_{\max}/a \leq 19$ . The horizontal lines with shaded error bands represent the final estimate for each energy level and are computed via the FLAG average (see Appendix D) taking all fit results into account.

The ground-state energy is found approximately 40 MeV below the  $BB_s^*$  threshold indicating a bound four-quark state. The first and second excited states are almost degenerate, and their energies are consistent with the  $BB_s^*$  and  $B^*B_s$  thresholds within uncertainties. Thus, these two excited states can be interpreted as  $BB_s^*$  and  $B^*B_s$  scattering states. The energy of the third excited state is found about 40 MeV above the  $BB_s^*$  threshold and is located close to the  $B^*B_s^*$  threshold. Consequently, the third excited state seems to be consistent with a  $B^*B_s^*$  scattering state. The same analysis has been repeated for the remaining six ensembles, while the associated fit results are

Ensemble	$\Delta E_0$ [MeV]	$\Delta E_1$ [MeV]	$\Delta E_2$ [MeV]	$\Delta E_3$ [MeV]
a15m310	-34.0(1.2)	2.4(1.4)	6.2(1.5)	41.2(1.7)
a12m310	-29.6(2.5)	-1.0(2.7)	0.7(2.4)	40.3(2.9)
a12m220S	-30.4(2.6)	4.2(3.0)	3.8(2.8)	44.5(3.2)
a12m220	-37.3(4.3)	-4.2(2.8)	-3.5(2.9)	36.6(3.2)
a12m220L	-35.8(3.2)	0.6(2.3)	-0.1(2.2)	41.4(2.3)
a09m310	-29.1(2.5)	-1.1(2.7)	-2.4(2.6)	41.2(3.2)
a09m220	-30.7(4.0)	-1.3(3.0)	-2.1(3.3)	40.5(3.3)

Table 6.8.: Finite volume energies of the four lowest energy levels for the  $\bar{b}\bar{b}us$  system with  $J^P = 1^+$  on each ensemble. The results are given in physical units relative to the  $BB_s^*$  threshold, i.e.,  $\Delta E_n = E_n - E_B - E_{B_s^*}$ .

collected in Appendix F. The final estimates for the four lowest finite volume energies represented by the horizontal lines in Figs. 6.8 and F.7 to F.12 are summarized in Table 6.8 and illustrated in Fig. 6.9. According to Table 6.8, we obtain similar results for all seven lattice ensembles: The ground-state energies are found about 30 MeV to 40 MeV below the  $BB_s^*$  threshold and are consistent with each other within uncertainties. The energies of the first, second and third excited states coincide with the

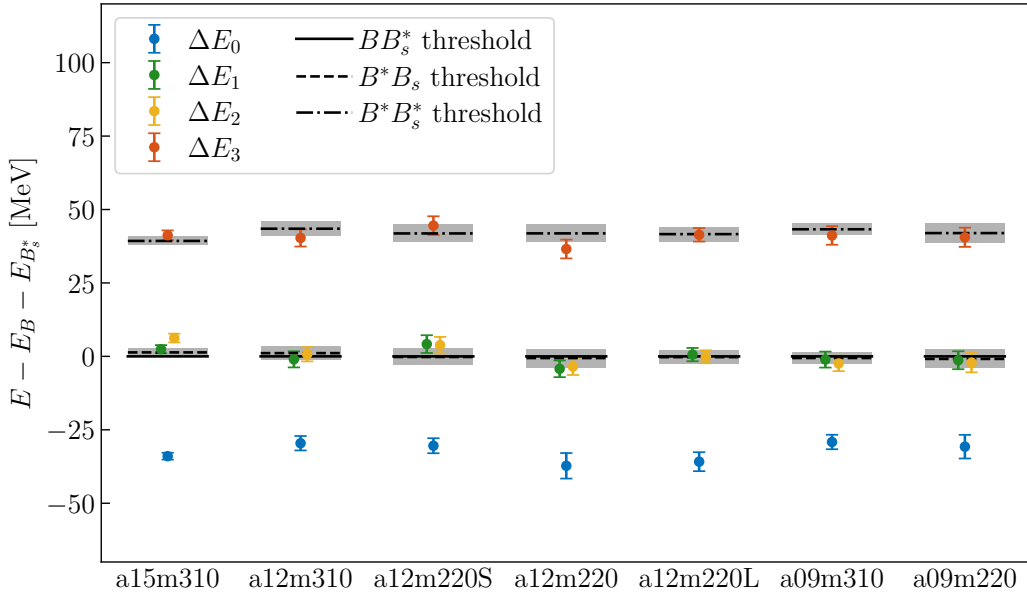


Figure 6.9.: Finite volume energies of the four lowest energy levels for the  $\bar{b}\bar{b}us$  system with  $J^P = 1^+$  on each ensemble relative to the  $BB_s^*$  threshold,  $\Delta E_n = E_n - E_B - E_{B_s^*}$ . The black horizontal lines correspond to the  $BB_s^*$  (solid),  $B^*B_s$  (dashed) and  $B^*B_s^*$  (dash-dot) thresholds.



$BB_s^*$ ,  $B^*B_s$  and  $B^*B_s^*$  thresholds and describe the associated two-meson scattering states. Consequently a strong indication for a bound  $\bar{b}bus$  tetraquark state is found. As the low-lying finite volume energy spectrum is precisely determined, these energy levels can be used as input for a scattering analysis. This allows us to investigate finite volume effects which might affect the ground-state energy and to determine the infinite volume binding energy, which is done in Sec. 6.4.2.

In Fig. 6.10, I present the signed squared eigenvector components  $\tilde{v}_n^j$  as defined in Eq. (6.3) for the  $\bar{b}bus$  system obtained on ensemble a12m220L. The  $\tilde{v}_n^j$  are determined by solving a GEVP and performing constant fits to the time-dependent eigenvector components  $v_n^j$  for various temporal separations  $t_{\min} \leq t \leq t_{\max}$  with  $5 \leq t_{\min}/a \leq 9$  and  $11 \leq t_{\max}/a \leq 14$ . The final estimate for the eigenvector components is then computed via the FLAG average taking all fit results into account. I start discussing

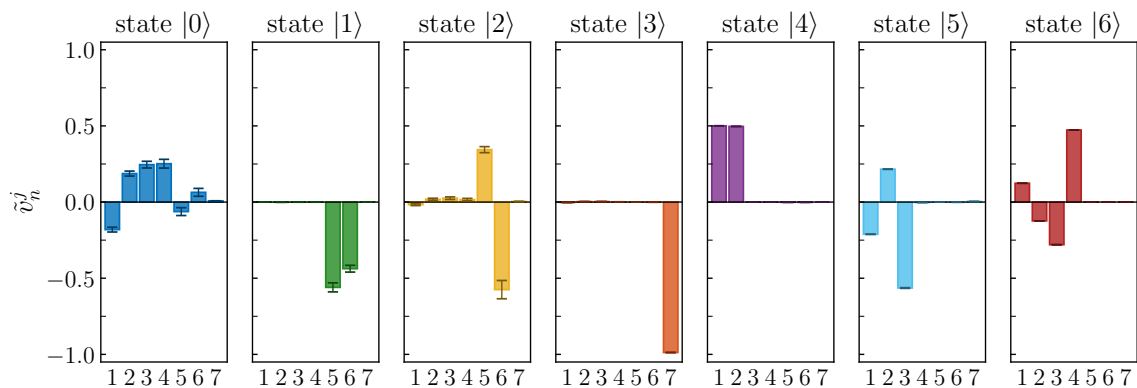


Figure 6.10.: Signed squared eigenvector components  $\tilde{v}_n^j$  for the  $\bar{b}bus$  system with  $J^P = 1^+$  obtained on ensemble a12m220L. The results are determined via constant fits to the  $t$ -dependent eigenvector components  $v_n^j$  in the range  $t_{\min} \leq t \leq t_{\max}$  with  $5 \leq t_{\min}/a \leq 9$  and  $11 \leq t_{\max}/a \leq 14$  followed by a FLAG average taking all fits into account.

the eigenvector components for the ground state  $|0\rangle$ . Here, we observe that  $|\tilde{v}_0^j| \gg |\tilde{v}_0^k|$  for  $j = 1, 2, 3, 4$  and  $k = 5, 6, 7$ . Consequently, the ground-state energy level  $|0\rangle$  is dominated by contributions of trial states generated by the local operators  $\mathcal{O}_1$  to  $\mathcal{O}_4$ . Meanwhile, the contributions of the trial states  $\mathcal{O}_k^\dagger|\Omega\rangle$  with  $k = 5, 6, 7$  generated by scattering operators are significantly smaller. This is a further indication that the  $\bar{b}bus$  ground state corresponds to a stable tetraquark. Moreover, in Fig. 6.10 we can recognize a diquark-antidiquark contribution to the ground state of about 25% while the meson-meson contribution is found to be approximately 75%. Thus, both structures are relevant to describe the ground state successfully even though the meson-meson contribution seems to be slightly dominating. This is in agreement with the results obtained in Sec. 5.3.2 and in Ref. [24], where I also found sizable meson-meson and diquark-antidiquark components, while the diquark-antidiquark contribution is somewhat smaller.

In comparison to the  $\bar{b}\bar{b}ud$  system discussed in Sec. 6.3.1 the ratio of meson-meson to diquark-antidiquark contributions is slightly larger for the case of  $\bar{b}\bar{b}us$ . Therefore, the diquark-antidiquark structure seems to be less important for the ground state in the  $\bar{b}\bar{b}us$  tetraquark compared to the  $\bar{b}\bar{b}ud$  ground state. This agrees with our findings in Ref. [193] where also a larger diquark-antidiquark contribution to the ground state has been found for  $\bar{b}\bar{b}ud$  than for  $\bar{b}\bar{b}us$ .

According to Fig. 6.10,  $\tilde{v}_0^1 \approx -\tilde{v}_0^2$ , so the local  $BB_s^*$  and  $B^*B_s$  components of the ground state are arranged antisymmetrically in the light flavors  $us$ . The same holds for the scattering  $BB_s^*$  and  $B^*B_s$  components, where we found  $\tilde{v}_0^5 \approx -\tilde{v}_0^6$ . Note that the operators  $\mathcal{O}_3$ ,  $\mathcal{O}_4$  and  $\mathcal{O}_7$  are already by construction antisymmetric in the light flavors (see Sec. 4.2.3), and so are the associated trial states. Consequently, the  $\bar{b}\bar{b}us$  ground state is completely antisymmetric in the light flavors  $us$  and seems to be the counterpart of the  $\bar{b}\bar{b}ud$  ground state with  $I(J^P) = 0(1^+)$  (see Sec. 6.3.1) which is also antisymmetric in its light flavors  $ud$ .

For the first and second excited states, we observe that  $|\tilde{v}_1^5|, |\tilde{v}_1^6| \gg |\tilde{v}_1^k|$  and  $|\tilde{v}_2^5|, |\tilde{v}_2^6| \gg |\tilde{v}_2^k|$  with  $k \neq 5, 6$ . Accordingly, these two states are mainly governed by the trial states of the operators  $\mathcal{O}_5$  and  $\mathcal{O}_6$ , corresponding to a  $BB_s^*$  and  $B^*B_s$  scattering state respectively, while contributions of all other structures are negligible. This supports our interpretation of the states  $|1\rangle$  and  $|2\rangle$  being meson-meson scattering states. However, we observe that they are not purely governed by a single trial state but are linear combinations of the trial states  $\mathcal{O}_5^\dagger|\Omega\rangle$  and  $\mathcal{O}_6^\dagger|\Omega\rangle$  with similar weight. For state  $|1\rangle$  we see that  $\tilde{v}_1^5 \approx \tilde{v}_1^6$ , so there is a scattering  $BB_s^*$  and  $B^*B_s$  component that is symmetric in the light flavors  $us$ , whereas  $\tilde{v}_2^5 \approx -\tilde{v}_2^6$  and subsequently state  $|2\rangle$  is antisymmetric in the light flavors. Therefore, state  $|2\rangle$  is the analogy of the first excited state in the  $\bar{b}\bar{b}ud$  spectrum with  $I = 0$ , while state  $|1\rangle$  corresponds to an isospin  $I = 1$  state with light flavors  $ud$ .

Since  $\tilde{v}_3^7 \approx 1$  and  $\tilde{v}_3^k \approx 0$  for  $k \neq 7$ , the third excited state is essentially identical to the trial state generated by  $\mathcal{O}_7$ , i.e.,  $|3\rangle \approx \mathcal{O}_7^\dagger|\Omega\rangle$ . As  $\mathcal{O}_7$  resembles a  $B^*B_s^*$  scattering structure, this supports the interpretation of the third excited state as a  $B^*B_s^*$  scattering state.  $\mathcal{O}_7$  is by construction antisymmetric in the light flavors, and so is state  $|3\rangle$ . Therefore, this energy level is the counterpart of the second excited state in the  $\bar{b}\bar{b}ud$  spectrum with  $I = 0$  discussed in Sec. 6.3.1.

In addition to that, also the remaining eigenstates are either symmetric (state  $|4\rangle$ ) or antisymmetric (states  $|5\rangle$  and  $|6\rangle$ ) in the light flavors  $us$ . This suggests that  $SU(3)$  flavor symmetry is approximately preserved for the  $\bar{b}\bar{b}us$  system in the finite volume. Similar results have been found in Sec. 5.3.2 and Ref. [24] where the ground state and the first two scattering states have also been identified to be either symmetric or antisymmetric in the light flavors  $us$ .

## 6.4 Scattering Analysis

The finite volume energy spectra of the four-quark states can be related to the infinite volume scattering amplitude  $T$  using Lüscher's formula. Since bound states appear as poles of the  $T$ -matrix on the real axis below the threshold of strong decay, this allows us to examine if the  $\bar{b}b\bar{u}d$  and  $\bar{b}b\bar{u}s$  ground states that have been found below the lowest two-meson thresholds in Sec. 6.3 are indeed bound states in the infinite volume. In this section, I follow the approach discussed in Sec. 4.6.2.2 which can be applied for single as well as coupled channel scattering analyses to determine the  $S$ -wave scattering amplitude. For both systems, I considered only the center-of-momentum frame where the relevant irrep is  $T_1^+$  of  $O_h$  and neglect contributions from higher partial waves.

Note that three of the seven ensembles that are used in this work (a12m220S, a12m220, a12m220L) have similar lattice spacings  $a \approx 0.12$  fm and pion masses  $m_\pi \approx 220$  MeV and differ only in their lattice volume  $V_S = L^3$  with  $L/a \in \{24, 32, 40\}$  (see Table 6.1). This allows us to use the energy levels extracted on these three ensembles in a single scattering analysis. Referring to the results of this combined analysis, the specifier *a12m220co* will be used. For the remaining four ensembles a15m310, a12m310, a09m220 and a09m310, I perform an independent scattering analysis for each ensemble.

Throughout this section, possible effects due to the left-hand cut are omitted even though I use  $T$ -matrix parametrizations whose ranges of convergence are limited by the left-hand cut branch point. I will estimate the position of this branch point and discuss its relevance with respect to this scattering analysis in Sec. 6.5.

### 6.4.1 Scattering Analysis for the Case of $\bar{b}b\bar{u}d$ with $I(J^P) = 0(1^+)$

For the case of  $\bar{b}b\bar{u}d$  with  $I(J^P) = 0(1^+)$ , the two lowest meson-meson thresholds are  $BB^*$  and  $B^*B^*$  which are separated by approximately 45 MeV [87]. Therefore, I expect that the coupling of the scattering amplitude to the  $B^*B^*$  channel is sufficiently suppressed and a single channel scattering analysis is adequate to determine the infinite volume ground-state energy. For this reason, I use only the ground-state energy level  $E_0$  and the energy level  $E_1$  associated to the first excited state (which has been identified as a  $BB^*$  scattering state) but not the energy  $E_2$  of the second excited state (which resembles a  $B^*B^*$  scattering state) in the following analysis. Another reason for omitting  $E_2$  is that, according to Sec. 6.3, I did not consider scattering operators with back-to-back momenta. The energies of the associated scattering states might be between the  $BB^*$  and the  $B^*B^*$  thresholds, and consequently energy levels below the  $B^*B^*$  threshold are potentially not resolved. Therefore, it would not be credible to include the second excited state and to perform a coupled channel scattering analysis. Following the approach discussed in Sec. 4.6.2.2, I perform a single channel scattering analysis to determine the infinite volume scattering amplitude. The  $T$ -matrix is parametrized according to Eqs. (4.91) and (4.92), so I apply the linear ansatz in  $s$  for

the inverse  $K$ -matrix,

$$[K^{-1}(s)]_{\text{single}}^{2\text{Par.}} = c^{(0)} + c^{(1)}s, \quad (6.4)$$

where  $c^{(0)}$  and  $c^{(1)}$  are the two free parameters. Additionally, I also utilize a constant  $K$ -matrix parametrization according to

$$[K^{-1}(s)]_{\text{single}}^{1\text{Par.}} = c^{(0)}, \quad (6.5)$$

which allows me to check the relevance of the term linear in  $s$ .

As stated above, the two lowest energy levels that are computed on each of the ensembles a12m220S, a12m220 and a12m220L are used in a single combined fit, thus increasing the number of data points for this fit. For the remaining four ensembles, the scattering analysis is performed separately using always the two lowest energy levels per ensemble. Consequently, I will end up with five infinite volume ground-state energy levels for different pion masses and lattice spacings.

For each scattering analysis, I use the finite volume energy levels  $E_0(L)$  and  $E_1(L)$  which have been determined in Sec. 6.3.1, the associated scattering momenta  $k_0(L)$  and  $k_1(L)$  which are governed via Eq. (4.84), and the kinetic masses of the  $B$  and  $B^*$  mesons given in Table 6.6 to determine the parameters  $c^{(0)}$  for the constant parametrization and  $c^{(0)}$  and  $c^{(1)}$  for the linear parametrization by minimizing the  $\chi^2$  function in Eq. (4.94) as described in Sec. 4.6.2.2. The results for the parameters  $c^{(j)}$  are listed in Table 6.9. Given knowledge of the optimal choice of the parameters, the infinite

Ensemble	$N_{\text{Par.}}$	$c^{(0)}$ [1]	$c^{(1)}$ [fm <sup>2</sup> ]	$ k_{\text{BS}} $ [MeV]	$E_{\text{bind}}$ [MeV]	$\chi^2/\text{d.o.f.}$
a15m310	1	-0.74(0.02)		628(8)	-75.4(1.8)	0.15
	2	-0.87(0.45)	-0.15(0.49)	628(8)	-75.4(1.8)	-
a12m310	1	-0.89(0.04)		605(26)	-69.6(4.2)	1.76
	2	0.36(1.05)	2.25(1.90)	607(26)	-70.1(4.2)	-
a12m220co	1	-1.02(0.04)		675(22)	-89.0(4.5)	1.41
	2	-0.67(0.46)	0.53(0.68)	675(22)	-88.9(4.5)	1.71
a09m310	1	-1.31(0.05)		661(40)	-83.0(5.9)	3.04
	2	-0.18(0.25)	3.17(0.69)	665(40)	-83.8(5.9)	-
a09m220	1	-1.43(0.08)		717(64)	-97.5(9.6)	0.57
	2	-0.12(0.42)	3.27(1.03)	719(64)	-98.1(9.6)	-

Table 6.9.: Fit results for the parameters  $c^{(0)}$  and  $c^{(1)}$  of a constant ( $N_{\text{Par.}} = 1$ ) and linear ( $N_{\text{Par.}} = 2$ )  $K^{-1}$ -matrix parametrization, scattering momentum  $|k_{\text{BS}}|$  and infinite volume binding energy  $E_{\text{bind}}$  for all ensembles obtained by a single channel scattering analysis for the  $\bar{b}\bar{b}ud$  system with  $I(J^P) = 0(1^+)$ . Note that for the fits with  $N_{\text{Par.}} = 2$  on a15m310, a12m310, a09m310 and a09m220 no value for  $\chi^2/\text{d.o.f.}$  is given, as the number of data points equals the number of fit parameters, but I verified that  $\chi^2 = 0$  for these cases.

volume ground-state energy is computed as the pole of the  $T$ -matrix in the complex energy plane. For all cases, the  $T$ -matrix pole is found at the real axis below the  $BB^*$  threshold. The associated binding energies  $E_{\text{bind}}$  and the binding momenta  $|k_{\text{BS}}|$  that are obtained by solving Eq. (4.89) for  $|k_{\text{BS}}|$  are also collected in Table 6.9. Note that the statistical uncertainties of the binding energies  $E_{\text{bind}}$  have been rescaled to take correlations between the meson energies and the  $\bar{b}b u d$  energy levels into account. The scaling factor has been determined from the ratio of the correlated and uncorrelated uncertainties for the finite volume energy differences  $\Delta E_0$ .

I show the low-lying finite volume energy levels computed on the ensembles a12m220S, a12m220 and a12m220L with spatial extents  $L/a = 24, 32, 40$  as gray points in Fig. 6.11. In the left plot, I additionally depict the non-interacting  $BB^*$  energies as blue solid lines and the non-interacting  $B^*B^*$  energies as green solid lines, while the associated two-meson thresholds are given by the horizontal lines at the bottom of each non-interacting spectrum. As already discussed, only the two lowest finite volume energy

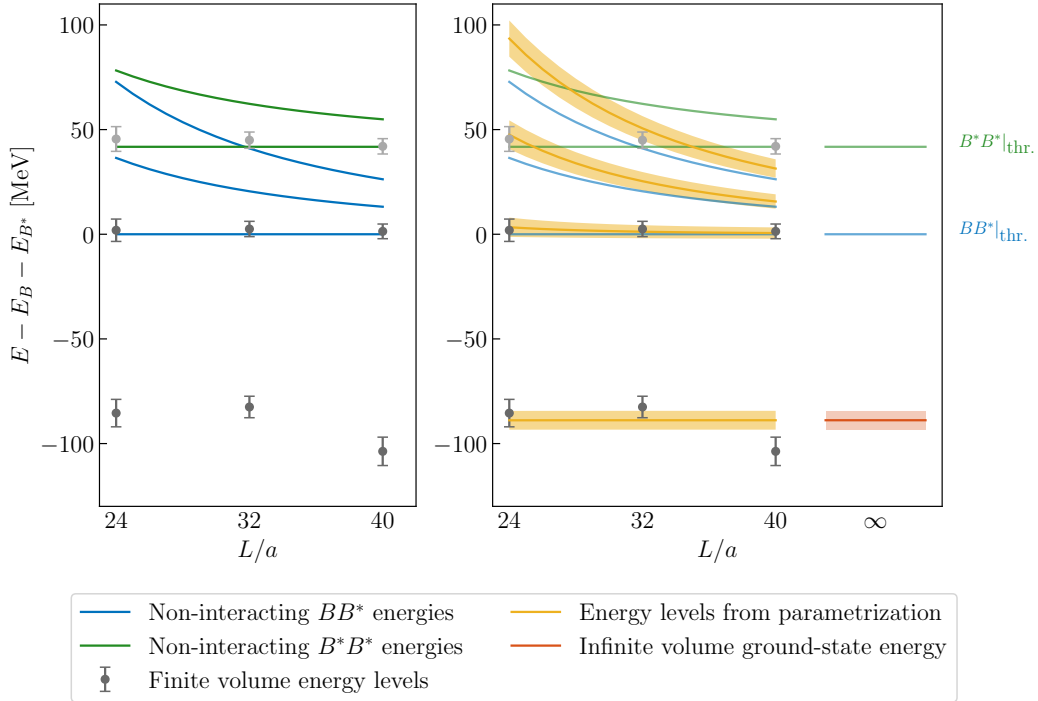


Figure 6.11.: Finite volume energy levels for the  $\bar{b}b u d$  four-quark system with  $I(J^P) = 0(1^+)$  computed on the ensembles a12m220S, a12m220 and a12m220L (dark gray points are used in the scattering analysis, while light gray points are excluded) and the non-interacting  $BB^*$  (in blue) and  $B^*B^*$  (in green) energies (left). Additionally, the energy levels calculated from Eq. (3.45) using the single channel  $K^{-1}$ -matrix parametrization in Eq. (6.4) are shown by yellow bands together with the infinite volume ground-state energy as a red horizontal line (right).

levels (illustrated by dark gray points in Fig. 6.11) are considered for the scattering analysis, while the energies of the second excited states depicted in light gray are excluded from the analysis. In the right plot of Fig. 6.11, the finite volume energy levels that are obtained from the quantization condition in Eq. (3.45) using the  $K^{-1}$ -matrix parametrization in Eq. (6.4) with  $c^{(0)}$  and  $c^{(1)}$  as defined in Table 6.9 are shown as yellow solid lines with shaded error bands. We observe that the two lowest yellow lines are in good agreement with the finite volume energy levels determined in the lattice calculation, indicating that the  $T$ -matrix parametrization is suitable to describe the finite volume energy spectrum. Moreover, the third and fourth energy levels obtained from the quantization condition can be associated to the non-interacting  $BB^*$  energy levels with back-to-back momenta  $\mathbf{p}^2 = (2\pi/L)^2$  and  $\mathbf{p}^2 = 2(2\pi/L)^2$ . Note that these energy levels slightly deviate from the non-interacting energies as a consequence of the finite lattice volume, while this effect increases for smaller volumes. Finally, the infinite volume ground-state energy corresponding to the pole position of the  $T$ -matrix in the complex energy plane is depicted by the red horizontal line, while the shaded band indicates the associated uncertainty.

Let us consider the fit results presented in Table 6.9 in more detail. We observe that both the constant parametrization (see Eq. (6.5)) and the linear parametrization (see Eq. (6.4)) of the inverse  $K$ -matrix are appropriate to reasonably describe the finite volume energy spectrum determined in the lattice calculation. For the ensembles a15m310, a12m310 and a12m220co, the fit results for the parameter  $c^{(0)}$  obtained by the constant and linear ansatz are consistent within uncertainties, while the results for  $c^{(1)}$  appearing in the linear parametrization are consistent with zero for the ensembles a15m310 and a12m220co. Accordingly, the infinite volume ground-state energies for those three ensembles that are obtained from the constant and linear  $K^{-1}$ -matrix parametrization are in excellent agreement. For the ensembles a09m310 and a09m220, we found different results for  $c^{(0)}$  depending on whether the linear term in  $s$  is considered in the  $K^{-1}$ -matrix parametrization or not. However, this is not surprising, since a constant ansatz is not suited to describe two energy levels (the ground-state energy level and the first excited state energy level) located below the lowest threshold as found for the ensembles a09m310 and a09m220 (see Fig. 6.5). Nevertheless, the infinite volume ground-state energies determined from the constant and linear  $K^{-1}$ -matrix parametrization are compatible within statistical uncertainties for both ensembles.

In the following, I use the infinite volume ground-state energies that are obtained via the linear  $K^{-1}$ -matrix parametrization as the final estimates for the infinite volume  $\bar{b}\bar{b}ud$  binding energies. Comparing these binding energies  $E_{\text{bind}}$  as listed in Table 6.9 with the finite volume energy differences  $\Delta E_0$  collected in Table 6.7, we observe that both energies are essentially identical. This supports the interpretation of the  $\bar{b}\bar{b}ud$  ground state as a stable tetraquark state.

As discussed at the beginning of this section, I neglect potential effects due to the coupling of the scattering amplitude to the  $B^*B^*$  channel. This assumption can be

justified by performing a coupled channel scattering analysis including also the second excited state  $E_2$  in the analysis. As  $BB^*$  scattering states with back-to-back momenta are not resolved, this is only feasible for ensemble a15m310 where the energy of the  $BB^*$  scattering state with  $\mathbf{p}^2 = (2\pi/L)^2$  is above the  $B^*B^*$  threshold as illustrated in the left plot of Fig. 6.12 with the same color code as for Fig. 6.11. I parametrize the inverse  $K$ -matrix in accordance with Eq. (4.93) as

$$[K^{-1}(s)]_{\text{coupled}}^{2\text{Par.}} = \begin{pmatrix} c_{00}^{(0)} & 0 \\ 0 & c_{11}^{(0)} \end{pmatrix}. \quad (6.6)$$

Such a constant parametrization can be motivated by the findings of the single channel analysis in the previous paragraph. The free parameters  $c_{00}^{(0)}$  and  $c_{11}^{(0)}$  are determined following the approach discussed in Sec. 4.6.2.2. I list the fit results for the parameters, the binding energy  $E_{\text{bind}}$ , the scattering momentum  $|k_{\text{BS}}|$  and  $\chi^2/\text{d.o.f.}$  in Table 6.10. In the right plot of Fig. 6.12, I show, in analogy to Fig. 6.11, the finite volume energy levels, obtained via the quantization condition in Eq. (3.45) using the constant parametrization of the inverse  $K$ -matrix, as yellow lines. As expected, these energy

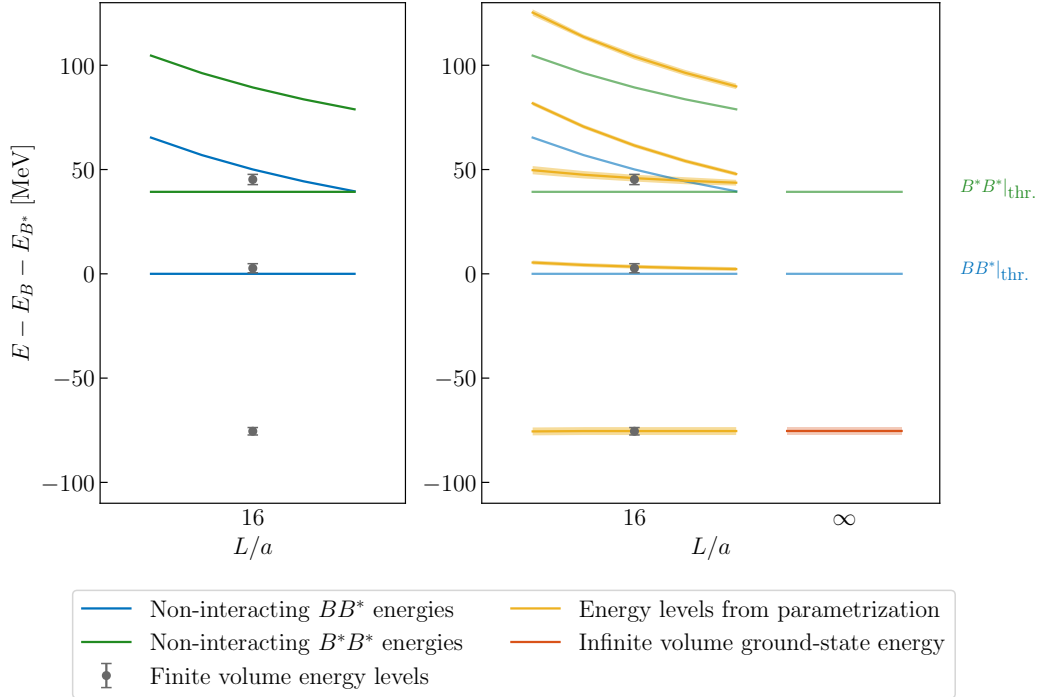


Figure 6.12.: Finite volume energy levels for the  $\bar{b}b\bar{u}d$  four-quark system computed on the ensemble a15m310 (dark gray points are used in the scattering analysis) and the non-interacting  $BB^*$  (in blue) and  $B^*B^*$  (in green) energies (left). Additionally, the energy levels calculated from Eq. (3.45) using the coupled channel  $K^{-1}$ -matrix parametrization in Eq. (6.6) are shown by yellow bands together with the infinite volume ground-state energy as a red horizontal line (right).



Ensemble	$N_{\text{Par.}}$	$c_{00}^{(0)}$ [1]	$c_{11}^{(0)}$ [1]	$ k_{\text{BS}} $ [MeV]	$E_{\text{bind}}$ [MeV]	$\chi^2/\text{d.o.f.}$
a15m310	2	-0.74(0.02)	-0.47(0.08)	628(9)	-75.3(1.9)	0.14

Table 6.10.: Fit results for the parameters  $c_{00}^{(0)}$  and  $c_{11}^{(0)}$  of the  $K^{-1}$ -matrix parametrization in Eq. (6.6), scattering momentum  $|k_{\text{BS}}|$  and infinite volume binding energy  $E_{\text{bind}}$  for ensemble a15m310 obtained from a coupled channel scattering analysis for the  $\bar{b}\bar{b}ud$  system with  $I(J^P) = 0(1^+)$ .

levels are in good agreement with the ground-state energy as well as with the energies of the first and second excited states. We can also observe, that the fourth and fifth energy levels can be associated to the  $BB^*$  and  $B^*B^*$  non-interacting energy levels with one momentum quantum,  $\mathbf{p}^2 = (2\pi/L)^2$ . Note that the upwards shift of the finite volume energies is caused by the relatively small spatial box size. The infinite volume ground-state energy is again shown as a red horizontal line with a shaded band indicating the associated uncertainty.

Comparing the binding energy computed in a coupled channel analysis with the binding energy from the single channel scattering analysis given in Table 6.9, we recognize that both energies are in full agreement. This supports the assumption that the  $B^*B^*$  channel can be neglected and couplings of the scattering amplitude to  $B^*B^*$  do not influence the  $\bar{b}\bar{b}ud$  ground state.

#### 6.4.2 Scattering Analysis for the Case of $\bar{b}\bar{b}us$ with $J^P = 1^+$

In the case of the  $\bar{b}\bar{b}us$  four-quark system with  $J^P = 1^+$ , the two lowest meson-meson thresholds  $BB_s^*$  and  $B^*B_s$  are separated by only 3 MeV while the next two-meson threshold  $B^*B_s^*$  is about 45 MeV above the  $BB_s^*$  threshold. For this reason, it is mandatory to perform a coupled channel scattering analysis including the two lowest meson-meson channels  $BB_s^*$  and  $B^*B_s$  while couplings to the  $B^*B_s^*$  threshold can be neglected similar to the case of  $\bar{b}\bar{b}ud$  as discussed in the previous section.

Note that a single channel scattering analysis is unfeasible for another reason. As I showed in Sec. 6.3.2, the first and second excited states have both approximately equal weighted contributions of the trial states generated by the operators  $\mathcal{O}_5$  and  $\mathcal{O}_6$  which resemble  $BB_s^*$  and  $B^*B_s$  scattering states. Consequently, the finite volume energy levels are not governed by a particular scattering state but appear as symmetric or antisymmetric  $BB_s^*$  and  $B^*B_s$  combinations in the light quark flavors. The physical states in the infinite volume, however, are supposed to be ordinary meson-meson states. Thus, in a single channel scattering analysis it would be unclear which finite volume energy level should be assigned to which meson-meson scattering channel.

Accordingly, I include the energy levels  $E_0$ ,  $E_1$  and  $E_2$  listed in Table 6.8 in the coupled channel scattering analysis, while the energy level  $E_3$  associated to the third excited state which resembles a  $B^*B_s^*$  scattering state is excluded. The scattering analysis is performed on the basis of the approach discussed in Sec. 4.6.2.2 and follows the same steps as illustrated in Sec. 6.4.1 for the  $\bar{b}\bar{b}ud$  system. I parametrize the inverse



$K$ -matrix as

$$[K^{-1}(s)]_{\text{coupled}}^{2\text{Par.}} = \begin{pmatrix} c_{00}^{(0)} & 0 \\ 0 & c_{11}^{(0)} \end{pmatrix}, \quad (6.7)$$

which is in accordance with the parametrization utilized for the coupled channel system in Sec. 6.4.1. The final fit results for the parameters  $c_{00}^{(0)}$  and  $c_{11}^{(0)}$  are collected together with the scattering momenta  $|k_{\text{BS}}|$  and the binding energies  $E_{\text{bind}}$  in Table 6.11 for all ensembles.

Ensemble	$c_{00}^{(0)}$	$c_{11}^{(0)}$	$ k_{\text{BS}} $ [MeV]	$E_{\text{bind}}$ [MeV]	$\chi^2/\text{d.o.f.}$
a15m310	-0.50(0.02)	-2.29(1.66)	421(12)	-33.5(1.2)	0.08
a12m310	-0.56(0.03)	0.64(0.99)	371(36)	-26.0(2.3)	4.09
a12m220co	-0.63(0.05)	-0.64(0.04)	413(34)	-32.7(2.6)	1.53
a09m310	-0.78(0.04)	7.75(52.80)	390(49)	-28.6(2.5)	4.20
a09m220	-0.81(0.07)	-0.66(9485.07)	400(78)	-29.9(3.9)	1.38

Table 6.11.: Fit results for the parameters  $c_{00}^{(0)}$  and  $c_{11}^{(0)}$  of the  $K^{-1}$ -matrix parametrization in Eq. (6.7), scattering momentum  $|k_{\text{BS}}|$  and infinite volume binding energy  $E_{\text{bind}}$  for all ensembles obtained by a coupled channel scattering analysis for the  $\bar{b}bus$  system with  $J^P = 1^+$ .

In Fig. 6.13, I depict the finite volume energy levels determined on the ensembles a12m220S, a12m220 and a12m220L as gray points, while energy levels presented in light gray are excluded from the analysis. Additionally, I show also the non-interacting two-meson energies for  $BB_s^*$  as violet solid lines, for  $B^*B_s$  as blue solid lines and for  $B^*B_s^*$  as green solid lines. The energy levels that are obtained via the quantization condition in Eq. (3.45) using the  $K^{-1}$ -matrix parametrization in Eq. (6.7) and the fit results for the parameters  $c_{00}^{(0)}$  and  $c_{11}^{(0)}$  are shown as yellow shaded bands in the right plot of Fig. 6.13. Note that we found two almost degenerate energy levels close to the non-interacting  $BB_s^*$  and  $B^*B_s$  energies. The first three energy levels coincide well with the energy levels obtained from the lattice calculation, thus supporting the assumption that the chosen parametrization is suitable to describe the data. The fourth and fifth energy levels can be associated to  $BB_s^*$  and  $B^*B_s$  scattering states with one quantum of back-to-back momentum,  $\mathbf{p}^2 = (2\pi/L)^2$ , and accordingly the sixth and seventh energy levels can be related to the scattering states with  $\mathbf{p}^2 = 2(2\pi/L)^2$ . Note that these energy levels are all slightly above the non-interacting energy levels as a consequence of the finite spatial lattice volume. Finally, I illustrate the infinite volume ground-state energy as a red horizontal line in the right plot of Fig. 6.13.

Considering the infinite volume binding energies  $E_{\text{bind}}$  shown in Fig. 6.13 for ensemble a12m220co and collected for all ensembles in Table 6.11, we recognize that they are compatible with the finite volume energy differences  $\Delta E_0$  listed in Table 6.8. This supports the interpretation that the  $\bar{b}bus$  ground state is a stable tetraquark. Note

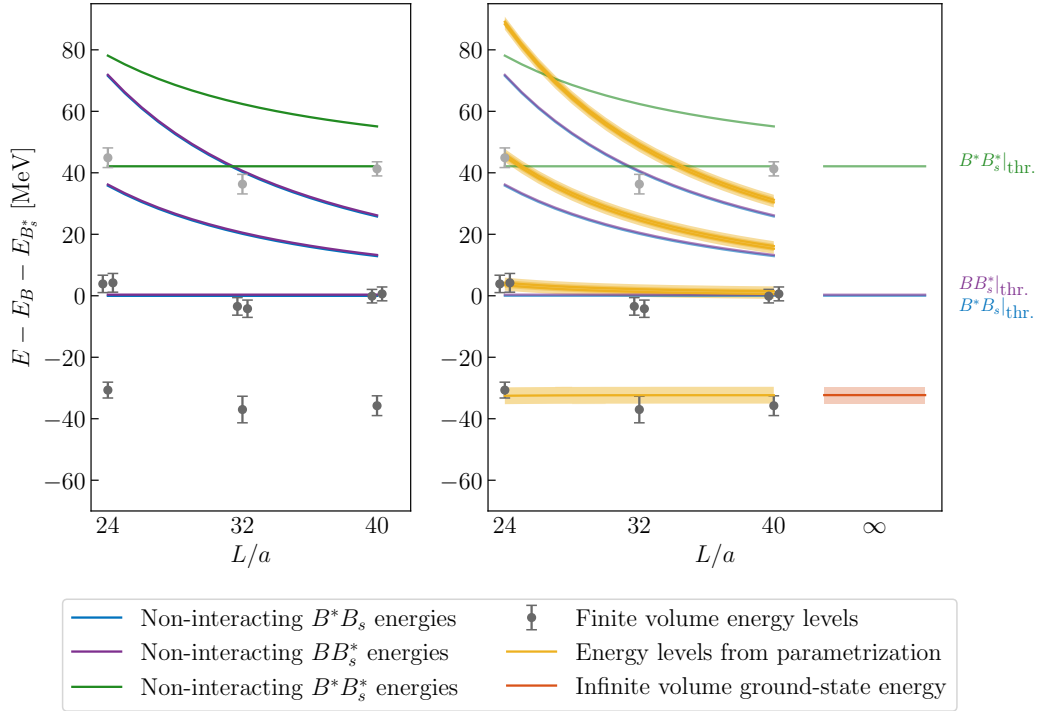


Figure 6.13.: Finite volume energy levels for the  $\bar{b}\bar{b}us$  four-quark system computed on the ensembles a12m220S, a12m220 and a12m220L (dark gray points are used in the scattering analysis, while light gray points are excluded) and the non-interacting  $B^*B_s$  (in blue),  $BB_s^*$  (in violet) and  $B^*B_s^*$  (in green) energies (left). Additionally, the energy levels calculated from Eq. (3.45) using the single channel  $K^{-1}$ -matrix parametrization in Eq. (6.7) are shown by yellow bands together with the infinite volume ground-state energy as a red horizontal line (right).

that the uncertainties of the binding energies  $E_{\text{bind}}$  in Table 6.11 are again rescaled appropriately to incorporate correlations of the meson energies and the  $\bar{b}\bar{b}us$  energy levels correctly.

## 6.5 Final Results and Investigation of Systematic Uncertainties

The infinite volume binding energies for the  $\bar{b}\bar{b}ud$  system with  $I(J^P) = 0(1^+)$  and the  $\bar{b}\bar{b}us$  system with  $J^P = 1^+$  that are listed in Tables 6.9 and 6.11 have been computed for various lattice spacings  $a \in \{0.09 \text{ fm}, 0.12 \text{ fm}, 0.15 \text{ fm}\}$  and unphysical pion masses  $m_\pi \in \{220 \text{ MeV}, 310 \text{ MeV}\}$ . Having a closer look on the results, we cannot observe an evident dependence of the binding energies on the lattice spacing  $a$ . Additionally, only the results for the  $\bar{b}\bar{b}ud$  system seem to depend mildly on the pion mass, while the binding energies in the  $\bar{b}\bar{b}us$  system seem to be rather independent of it.

In order to further investigate the binding energies' pion mass dependence and estimate

the final result at the physical point, I consider a chiral extrapolation which is quadratic in the pion mass, corresponding to a linear light quark mass dependence, according to

$$E_{\text{bind}}(m_\pi) = E_{\text{bind}}(m_{\pi,\text{phys}}) + c(m_\pi^2 - m_{\pi,\text{phys}}^2), \quad (6.8)$$

with  $m_{\pi,\text{phys}} = 135$  MeV the pion mass at the physical point. This is the same ansatz as utilized in Sec. 5.4. The two free parameters  $E_{\text{bind}}(m_{\pi,\text{phys}})$  and  $c$  in Eq. (6.8) are determined via a  $\chi^2$ -minimizing fit. I show the fit function for the  $\bar{b}\bar{b}ud$  system as well as for the  $\bar{b}\bar{b}us$  system together with the binding energies  $E_{\text{bind}}$  as a function of  $m_\pi^2$  in Fig. 6.14. The fit results and the values of  $\chi^2/\text{d.o.f.}$  are listed for both channels

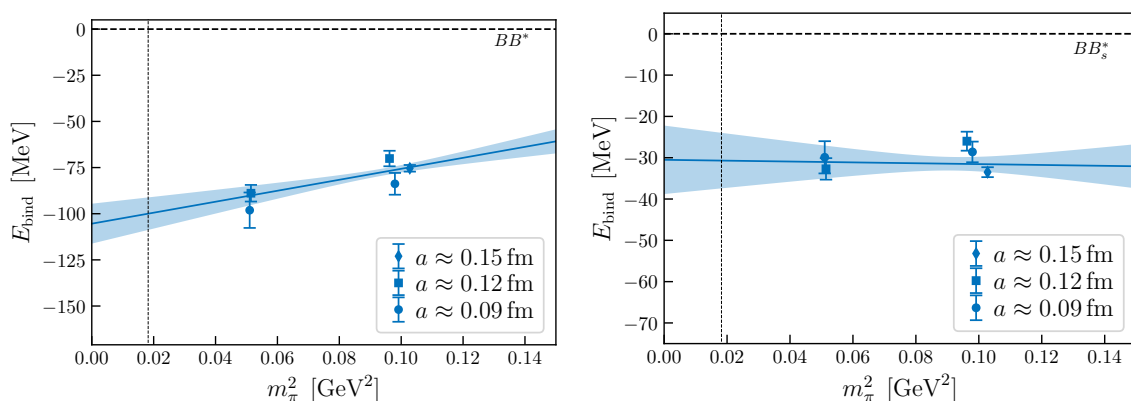


Figure 6.14.: Fits of the pion-mass dependence of the binding energies  $E_{\text{bind}}$  for the  $\bar{b}\bar{b}ud$  four-quark system with  $I(J^P) = 0(1^+)$  (left) and the  $\bar{b}\bar{b}us$  four-quark system with  $J^P = 1^+$  (right). The lowest meson-meson threshold for each channel is indicated by the horizontal dashed lines, while the vertical dashed line represents the physical pion mass.

in Table 6.12, while the statistical errors are rescaled by a factor of  $(\chi^2/\text{d.o.f.})^{1/2}$  if  $\chi^2/\text{d.o.f.} > 1$  to incorporate the fit's quality in the final result.

Moreover, in order to quantify possible discretization effects rigorously, I also study an additional  $a$ -dependence of the binding energies using an ansatz which adds a quadratic term in the lattice spacing  $a$  to Eq. (6.8),

$$E_{\text{bind}}(m_\pi, a) = E_{\text{bind}}(m_{\pi,\text{phys}}, a_{\text{cont}}) + c(m_\pi^2 - m_{\pi,\text{phys}}^2) + d a^2, \quad (6.9)$$

where  $d$  is the third free parameter and  $a_{\text{cont}} = 0$  the continuum lattice spacing. This allows us to partly remove potential discretization errors of  $\mathcal{O}(a^2)$ . Note that the gauge action as well as the HISQ action are already  $\mathcal{O}(a^2)$  improved, but using the mixed action setup with a Wilson-clover valence action, which is only  $\mathcal{O}(a)$  improved, might introduce additional uncertainties. These can be studied and if necessary removed by considering the  $a$ -dependent binding energy as given in Eq. (6.9). The free parameters in Eq. (6.9) are again determined via a  $\chi^2$ -minimizing fit, and the final results obtained by this chiral extrapolation with continuum limit can be found in Table 6.12. Fig. 6.15

displays the fit functions projected to the plane of constant lattice spacings  $a$  in the upper row and projected to the plane of constant pion masses  $m_\pi$  in the lower row for the  $\bar{b}\bar{b}ud$  and the  $\bar{b}\bar{b}us$  systems. The continuum binding energies at the physical pion mass  $E_{\text{bind}}(m_{\pi,\text{phys}}, a_{\text{cont}})$  are indicated in both projections by a black square. Comparing the final binding energies obtained from the chiral extrapolation with those governed by the chiral extrapolation with continuum limit, we observe that these binding energies are compatible within statistical uncertainties for both tetraquark states. Let us have a closer look on the fit results. In the case of  $\bar{b}\bar{b}ud$ , the binding energies show a mild dependence on the pion mass, while the energy decreases for decreasing pion mass, i.e.,  $c > 0$ . However, we do not find a significant  $a$ -dependence, as the fit parameter  $d$  is consistent with zero within statistical uncertainties. Interestingly, we observe the opposite behavior for the  $\bar{b}\bar{b}us$  system. Here, the binding energy is independent

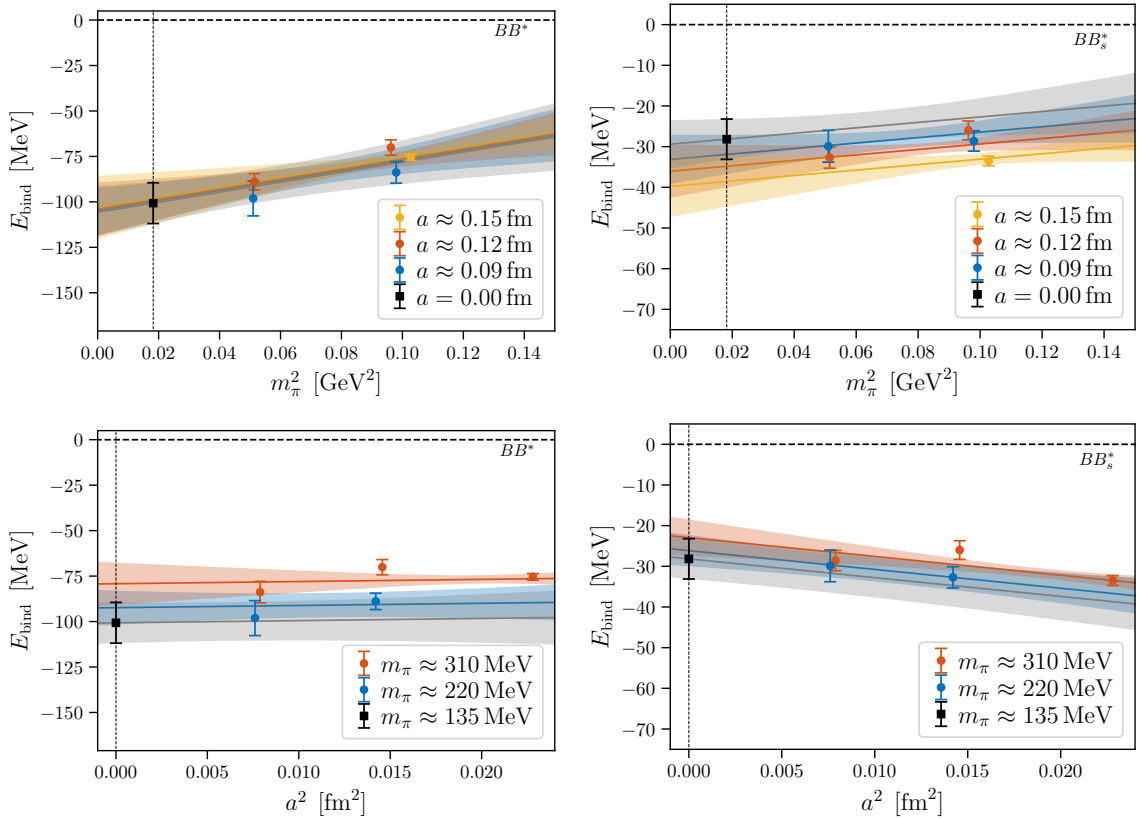


Figure 6.15.: Fits of the pion-mass and lattice spacing dependence of the binding energies  $E_{\text{bind}}$  for the  $\bar{b}\bar{b}ud$  four-quark system with  $I(J^P) = 0(1^+)$  (left) and the  $\bar{b}\bar{b}us$  four-quark system with  $J^P = 1^+$  (right). In the upper row, a projection to the plane of constant lattice spacings  $a$  is shown, in the lower row a projection to the plane of constant pion masses  $m_\pi$ . The lowest meson-meson threshold for each channel is indicated by the horizontal dashed lines, while the vertical dashed line represents either the physical pion mass or zero lattice spacing  $a$ . The black square indicates the final result for  $E_{\text{bind}}(m_{\pi,\text{phys}}, a_{\text{cont}})$ .

Chiral extrapolation				
	$E_{\text{bind}}(m_{\pi,\text{phys}})$ [MeV]	$c$ [ $10^{-4}/\text{MeV}$ ]	$\chi^2/\text{d.o.f.}$	
$\bar{b}bud$	-100(9)	3.0(1.1)	1.67	
$\bar{b}bus$	-31(7)	-0.10(88)	3.39	
Chiral extrapolation with continuum limit				
	$E_{\text{bind}}(m_{\pi,\text{phys}}, a_{\text{cont}})$ [MeV]	$c$ [ $10^{-4}/\text{MeV}$ ]	$d$ [ $10^2 \times \text{MeV}^3$ ]	$\chi^2/\text{d.o.f.}$
$\bar{b}bud$	-101(11)	2.8(1.7)	1.2(5.7)	2.44
$\bar{b}bus$	-28(5)	0.67(74)	-4.6(2.3)	1.72

Table 6.12.: Fit results for the chiral extrapolation and the chiral extrapolation with continuum limit of the binding energies  $E_{\text{bind}}$  for the  $\bar{b}bud$  system with  $I(J^P) = 0(1^+)$  and the  $\bar{b}bus$  system with  $J^P = 1^+$  to the physical pion mass  $m_{\pi} = 135$  MeV and to zero lattice spacing  $a = 0$ . The statistical uncertainties are rescaled by  $\max(1, (\chi^2/\text{d.o.f.})^{1/2})$  to incorporate the quality of the fit.

of the pion mass, i.e., the coefficient  $c$  is consistent with zero, while we discover a mild  $a$ -dependence that leads to a slightly lower binding energy when approaching the continuum limit. Nevertheless, lattice discretization effects for our setup are small, and in particular the mixed action setup does not seem to introduce additional major discretization errors. As the fits for the chiral extrapolation with continuum limit have reasonable quality, I conclude that remaining systematic uncertainties originating from unphysical pion masses and the lattice discretization are negligible.

Note that throughout the whole scattering analysis, I have omitted possible effects due to the left-hand cut which has been discussed in Sec. 4.6.3. In order to estimate the relevance of one-particle exchanges related to the left-hand cut, I first determine the location of the left-hand cut branch point for both channels. In the case of the  $\bar{b}bud$  system, the relevant interaction is one-pion exchange. Using Eq. (4.97) with  $\Delta m = m_{B^*} - m_B \simeq 45$  MeV and  $m_{\pi} \simeq 310$  MeV, we obtain

$$(k_{\text{lh}c}^{1\pi})^2 \approx \frac{1}{4}(\Delta m^2 - m_{\pi}^2) \approx -(153 \text{ MeV})^2. \quad (6.10)$$

Consequently, the branch point in the complex energy plane is located on the real axis below the  $BB^*$  threshold. Comparing  $k_{\text{lh}c}^{1\pi}$  with the  $\bar{b}bud$  binding momentum  $|k_{\text{BS}}| \sim 600$  MeV as given in Table 6.9, we recognize that the bound state pole is located below the branch point of the left-hand cut.

The situation is similar for the case of  $\bar{b}bus$  with a kaon being the exchange particle instead of a pion. The position  $k_{\text{lh}c}^{1\kappa}$  of the branch point is estimated in the same way, using  $\Delta m = m_{B_s^*} - m_B \simeq 136$  MeV and  $m_{\kappa} \simeq 498$  MeV, which yields

$$(k_{\text{lh}c}^{1\kappa})^2 \approx \frac{1}{4}(\Delta m^2 - m_{\kappa}^2) \approx -(240 \text{ MeV})^2. \quad (6.11)$$

As according to Table 6.11, the  $\bar{b}\bar{b}us$  binding momenta  $|k_{BS}|$  are of the order of 400 MeV, the bound state pole is again located below the left-hand cut branch point. Note that a second left-hand cut originating from the second scattering channel  $B^*B_s$  has a branch point which is shifted only by a few MeV compared to the case of  $BB_s^*$ .

Since the range of convergence of the utilized  $K^{-1}$ -matrix parametrizations is given by the location of the left-hand cut branch point, the bound state poles of the  $T$ -matrix are outside this region. Consequently, it is questionable how reliable the parametrization of the scattering amplitude is around the position of the bound state poles.

For this reason, I repeat the chiral extrapolation with continuum limit using the ansatz in Eq. (6.9) for the finite volume energy differences  $\Delta E_0$  given in Tables 6.7 and 6.8. I list the fit results in Table 6.13 and illustrate the fit functions in analogy to Fig. 6.15 as projections to the planes of constant pion mass  $m_\pi$  and constant lattice spacing  $a$  in Fig. 6.16. We recognize that the final results for the energies in Table 6.13 are within statistical uncertainties in agreement with the fit results in Table 6.12. Small deviations are mainly caused by the appearance of three energy levels instead of one for  $m_\pi \simeq 220$  MeV and  $a \simeq 0.12$  fm, leading to a different weight of the single energy levels in the extrapolation.

Chiral extrapolation with continuum limit				
	$\Delta E_0(m_{\pi,\text{phys}}, a_{\text{cont}})$ [MeV]	$c$ [ $10^{-4}/\text{MeV}$ ]	$d$ [ $10^{-4} \times \text{MeV}^3$ ]	$\chi^2/\text{d.o.f.}$
$\bar{b}\bar{b}ud$	-93(12)	2.1(1.5)	0.5(3.3)	2.54
$\bar{b}\bar{b}us$	-33(7)	-0.002(870)	0.01(1.74)	1.97

Table 6.13.: Fit results for the chiral extrapolation with continuum limit of the energy differences  $\Delta E_0$  for the  $\bar{b}\bar{b}ud$  system with  $I(J^P) = 0(1^+)$  and the  $\bar{b}\bar{b}us$  system with  $J^P = 1^+$  to the physical pion mass  $m_\pi = 135$  MeV and zero lattice spacing  $a = 0$ . The statistical uncertainties are rescaled by  $\max(1, (\chi^2/\text{d.o.f.})^{1/2})$  to incorporate the quality of the fit.

It might be possible that both tetraquarks are bound so deeply that finite volume effects and thus couplings of the scattering amplitude to the lowest two-meson threshold are small. Eventually, effects of one-particle exchange that give rise to the left-hand cut are then even smaller and can be neglected. Additionally, the tetraquark states in this chapter are not pure meson-meson molecules, as it has been assumed for studying the left-hand cut in  $DD^*$  scattering in Ref. [174], but are rather a combination of local meson-meson and diquark-antidiquark components (see the eigenvector decompositions in Secs. 6.3.1 and 6.3.2). This might be another argument that possible effects of the left-hand cut could be omitted. Note, however, that none of these two assumptions could be substantiated so far.

Likewise, it has not yet been conclusively clarified how to interpret the bound state poles beyond the range of convergence dictated by the left-hand cut branch point. One possible solution to describe such a pole rigorously might be using a different parametrization that is not affected by the mentioned range of convergence. The Padé

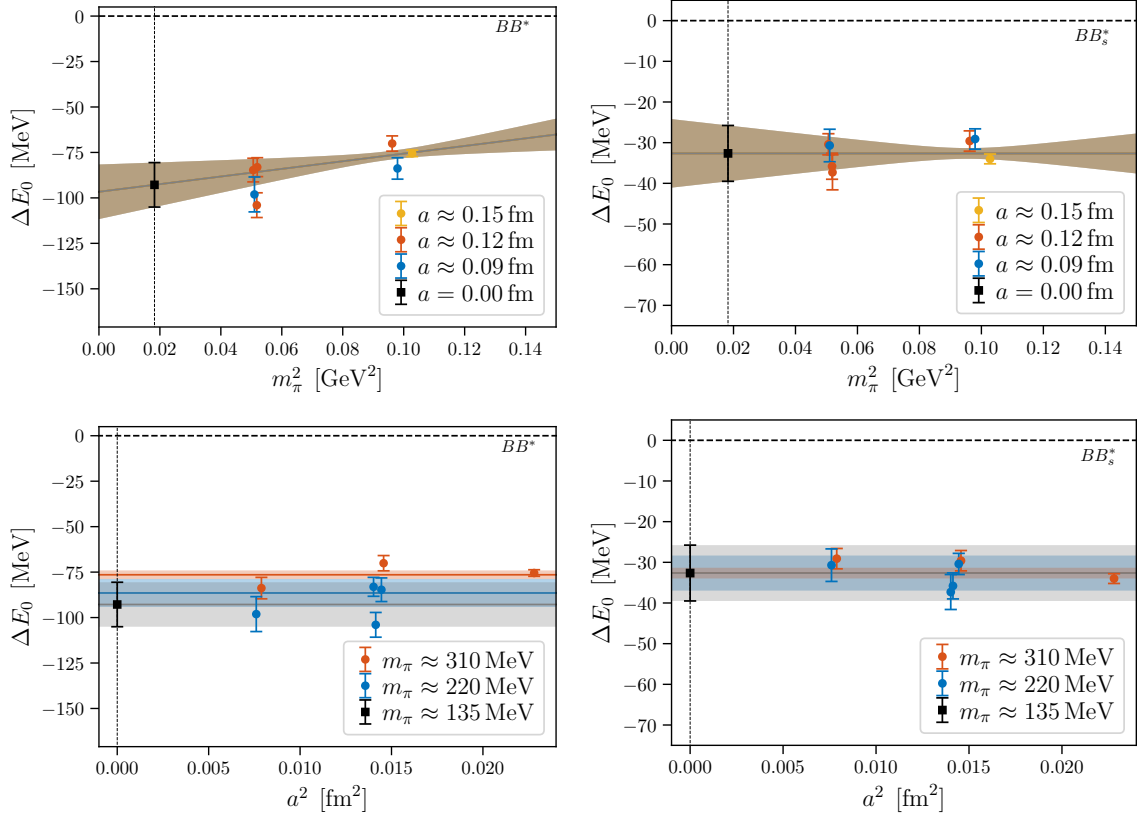


Figure 6.16.: Fits of the pion-mass and lattice spacing dependence of the energy differences  $\Delta E_0$  for the  $\bar{b}b\bar{u}d$  four-quark system with  $I(J^P) = 0(1^+)$  (left) and the  $\bar{b}b\bar{u}s$  four-quark system with  $J^P = 1^+$  (right). In the upper row, a projection to the plane of constant lattice spacings  $a$  is shown, in the lower row a projection to the plane of constant pion mass  $m_\pi$ . The lowest meson-meson threshold for each channel is indicated by the horizontal dashed lines, while the vertical dashed line represents either the physical pion mass or zero lattice spacing  $a$ . The black square indicates the final result for  $E_{\text{bind}}(m_{\pi,\text{phys}}, a_{\text{cont}})$ .

approximation might provide such a parametrization that could be applied also in the region of the bound state pole [175, 176, 194]. Nevertheless, it is still subject of ongoing research to investigate the effects of the left-hand cut and develop new techniques to rigorously incorporate the physics beyond the left-hand cut in the formalisms of scattering analyses.

In order to determine remaining systematic uncertainties, I follow the approach that has been applied in Ref. [37]. The Wilson-clover action that is used for the light and strange quarks introduces lattice discretization errors of order 1% for the fine lattices, around 1.5% for the coarse lattices and around 2% for the very coarse lattice. Using the QCD scale  $\Lambda_{\text{QCD}} \sim 300$  MeV, the associated discretization errors are expected to be of order 3 MeV to 6 MeV. This is in agreement with the quite small shift of the



final binding energies when considering the continuum limit in addition to a chiral extrapolation. Thus, this source of systematic errors is adequately covered. The major contribution to the systematic uncertainties, however, is introduced by the NRQCD action. Here, we need to distinguish between the heavy-light meson systems and the four-quark system. For the heavy-light mesons, the most significant systematic uncertainties for our choice of the NRQCD action and matching coefficients as presented in Sec. 6.1.3 are expected to be as follows:

- Four-quark operators are missing in the heavy quark action. They appear only at two-loop level in the QCD matching, i.e., at order  $\alpha_s^2$ , but according to Ref. [195] their effect can be up to 3 MeV.
- One-loop corrections of the operator  $-g/(2m_b)\boldsymbol{\sigma}\cdot\mathbf{B}$  are not included in the action, since the matching coefficient  $c_4$  is used at its tree level value. The associated uncertainties can be estimated as

$$\alpha_s\Lambda_{\text{QCD}}^2/m_b \approx 6 \text{ MeV}, \quad (6.12)$$

where I use  $\alpha_s \approx 0.3$  for the gauge coupling.

- I also use only tree-level values for the coefficients  $c_2$  and  $c_3$  associated to the operators of order  $(\Lambda_{\text{QCD}}^2/m_b^2)$ . The uncertainties that are governed by higher-order contributions to these coefficients are given by

$$\alpha_s\Lambda_{\text{QCD}}^3/m_b^2 \approx 0.4 \text{ MeV}. \quad (6.13)$$

As the matching coefficients  $c_1$ ,  $c_5$  and  $c_6$  are  $\mathcal{O}(\alpha_s)$  improved, systematic uncertainties arising from the related operators are negligible.

For the four-quark system, it is more sophisticated to identify the relevant sources of systematic errors as the power counting is more complicated due to the presence of two bottom quarks. A reasonable estimate for the systematic uncertainties can be obtained by replacing the QCD scale  $\Lambda_{\text{QCD}}$  by the binding momentum  $|k_{\text{BS}}|$  in the power counting [37]. This yields for the  $\bar{b}\bar{b}ud$  four-quark system a systematic uncertainty of around 25 MeV and for the  $\bar{b}\bar{b}us$  four-quark system of around 10 MeV. As I expect that the meson energies and the tetraquark energies are correlated, it is likely that the systematic uncertainties partly cancel when computing the binding energy as the difference  $E_{\text{bind}} = E_{\text{BS}} - E_{M_1} - E_{M_2}$  with  $M_1$  and  $M_2$  indicating the relevant mesons of the lowest threshold. Therefore, I estimate the final systematic uncertainty of the binding energies to be of the order of 25 MeV and 10 MeV for the case of  $\bar{b}\bar{b}ud$  and  $\bar{b}\bar{b}us$ , respectively.

For the final estimate of the tetraquark binding energies, I decide to consider the fit results  $E_{\text{bind}}(m_{\pi,\text{phys}}, a_{\text{cont}})$  that have been obtained from the chiral extrapolation with continuum limit based on the infinite volume binding energies. I assume here



that effects due to the left-hand cut can be omitted and the parametrization of the  $T$ -matrix yields reliable results despite the existence of the left-hand cut singularity. This might be reasonable for deeply bound tetraquarks but requires further validation in future research. The final results for the binding energies including the systematic uncertainties are given in Table 6.14. In the last column, I list the tetraquark masses  $m_{\text{tetraquark}}(m_{\pi,\text{phys}}, a_{\text{cont}})$  gained by adding the experimental  $B$  and  $B^*$  or  $B$  and  $B_s^*$  meson masses [87] to the binding energy.

	$E_{\text{bind}}(m_{\pi,\text{phys}}, a_{\text{cont}})$ [MeV]	$m_{\text{tetraquark}}(m_{\pi,\text{phys}}, a_{\text{cont}})$ [MeV]
$\bar{b}\bar{b}ud$	$-101(11)(25)$	$10503(11)(25)$
$\bar{b}\bar{b}us$	$-28(5)(10)$	$10660(5)(10)$

Table 6.14.: Final estimate for continuum binding energy at the physical pion mass  $m_{\pi} = 135$  MeV for the  $\bar{b}\bar{b}ud$  tetraquark with  $I(J^P) = 0(1^+)$  and the  $\bar{b}\bar{b}us$  tetraquark with  $J^P = 1^+$ . The last column refers to the mass of the bound tetraquark obtained by adding the experimental meson masses [87] to  $E_{\text{bind}}$ .



# 7

---

## INVESTIGATION OF $\bar{b}\bar{c}ud$ TETRAQUARK STATES IN $BD$ AND $B^*D$ SCATTERING

---

In this chapter, I will present an exploratory study of  $\bar{b}\bar{c}ud$  four-quark systems with the two possible quantum numbers  $I(J^P) = 0(0^+)$  and  $I(J^P) = 0(1^+)$ . In contrast to the  $\bar{b}bud$  four-quark system with  $I(J^P) = 0(1^+)$  and the  $\bar{b}bus$  four-quark system with  $J^P = 1^+$ , where stable tetraquark states have been consistently predicted in Chapters 5 and 6 as well as in various further lattice investigations [24, 35–40], the situation for  $\bar{b}\bar{c}ud$  four-quark systems is still inconclusive. In Chapter 5, I did not find evidence for deeply bound  $\bar{b}\bar{c}ud$  states, but likewise could not exclude the existence of a bound state close to the threshold or of a narrow resonance [24]. This is in agreement with the results of Ref. [42], where a previously predicted bound state has been revoked [41], but it contradicts the observations of Ref. [43]. Similar, also non-lattice approaches do not show a consistent picture. While in Refs. [196–207] the existence of a stable  $\bar{b}\bar{c}ud$  tetraquark is predicted, Refs. [27, 208–212] have not found evidence for a bound state.

A rigorous lattice investigation of the  $\bar{b}\bar{c}ud$  four-quark systems requires incorporating finite volume effects by performing a scattering analysis. Thus, I study the  $\bar{b}\bar{c}ud$  systems with  $I(J^P) = 0(0^+)$  and  $I(J^P) = 0(1^+)$  by calculating the  $BD$  and  $B^*D$   $S$ -wave scattering amplitudes using Lüscher’s method. A suitable setup for such computations has already been established in Chapter 6, where the low-lying energy levels that are essential for a scattering analysis have been determined for the  $\bar{b}bud$  and  $\bar{b}bus$  four-quark systems. Accordingly, I start in Sec. 7.1 with a brief overview of the lattice setup and discuss the implementation of the charm quarks in particular. In Sec. 7.2, I introduce the four-quark interpolating operators that are applied in this chapter. Especially, I focus on the construction of  $BD$  and  $B^*D$  scattering operators transforming according to the irreps of the relevant symmetry group for the center-of-momentum frame as well as for moving frames. This is followed by the computation of the  $D$  and  $D^*$  meson masses in Sec. 7.3, while the finite volume energy spectra for both  $\bar{b}\bar{c}ud$  systems are presented in Sec. 7.4. Finally, in Sec. 7.5 I perform a scattering analysis to determine the  $BD$  and  $B^*D$  scattering amplitudes whose poles can be associated to  $\bar{b}\bar{c}ud$  tetraquark states with  $J = 0$  and  $J = 1$ , respectively.

## 7.1 Lattice Setup and Tuning of the Charm Quark Mass

The calculations in this chapter use the same lattice setup as discussed in Sec. 6.1, i.e., I utilize the HISQ gauge-link configurations generated by the MILC collaboration [186]. For this exploratory study, I restrict myself to the two ensembles a12m220S and a12m220, which have the same pion mass ( $m_\pi \approx 220$  MeV) and lattice spacing ( $a \approx 0.12$  fm) and differ only in the spatial volume ( $L/a \in \{24, 32\}$ ). Details of these ensembles can be found in Table 6.1.

The light and bottom quark propagators are computed in exactly the same way as discussed in Secs. 6.1.2 and 6.1.3, i.e., I consider a Wilson-clover action for the light quarks, while the bottom quarks are treated in the framework of NRQCD. For the charm quarks, I use the Fermilab action in its simplest form as discussed in Sec. 2.5, i.e., the anisotropy  $\zeta$  is set to unity, and the clover coefficients are fixed to their tadpole improved tree-level value  $c_E = c_B = c_{\text{sw}}$ . The clover coefficient  $c_{\text{sw}}$  is identical to the coefficient used for the light quarks as listed in Table 6.2. Following the approach of Refs. [49, 106], I tune the hopping parameter  $\kappa_c$ , the only remaining free parameter, such that the spin-averaged kinetic  $D$  meson mass  $m_{D,\text{kin}}^{\text{spinav}} = (m_{D,\text{kin}} + 3m_{D^*,\text{kin}})/4$  matches its experimental value [87]. In accordance with Refs. [49, 106], I use the dispersion relation

$$E_{M_D}(\mathbf{p}) = M_1 + \frac{\mathbf{p}^2}{2M_2} - \frac{(\mathbf{p}^2)^2}{8M_4^3} \quad (7.1)$$

for the  $D$  and  $D^*$  mesons, where  $M_1$ ,  $M_2$  and  $M_4$  are free parameters with  $M_2$  corresponding to the kinetic mass.

In order to tune the charm quark mass appropriately, I use the interpolating operators in Eqs. (4.19) and (4.20) to compute the momentum-dependent  $D$  and  $D^*$  meson energies  $E_D(\mathbf{p})$  and  $E_{D^*}(\mathbf{p})$  with  $\mathbf{p}^2/(2\pi/L)^2 = 0, \dots, 4$  on ensemble a12m220S. The kinetic masses  $M_2$  for the  $D$  and  $D^*$  mesons are then determined by a  $\chi^2$ -minimizing fit of Eq. (7.1) to the energies  $E_D(\mathbf{p})$  and  $E_{D^*}(\mathbf{p})$ . Given knowledge of the kinetic masses, the spin-averaged kinetic  $D$  meson mass can be easily computed. This is repeated for several values of the charm hopping parameter  $\kappa_c$ . I depict the resulting spin-averaged kinetic  $D$  meson mass  $m_{D,\text{kin}}^{\text{spinav}}$  as a function of  $\kappa_c$  in the right plot of Fig. 7.1. Assuming a linear  $\kappa_c$ -dependence of  $m_{D,\text{kin}}^{\text{spinav}}$ , the final choice for the hopping parameter  $\kappa_c = 0.106756$  is obtained by interpolating to the physical spin-averaged kinetic  $D$  meson mass  $m_{D,\text{kin,phys}}^{\text{spinav}} = 1973.9$  MeV [87] indicated by the black horizontal line in this plot. In the left plot of Fig. 7.1, I show the  $D$  and  $D^*$  meson dispersion relation for the final choice of  $\kappa_c$ . In this case, the spin-averaged kinetic  $D$  meson mass is given by  $m_{D,\text{kin}}^{\text{spinav}} = 2031(57)$  MeV, which is slightly heavier than the physical spin-averaged kinetic mass but still in reasonable agreement.

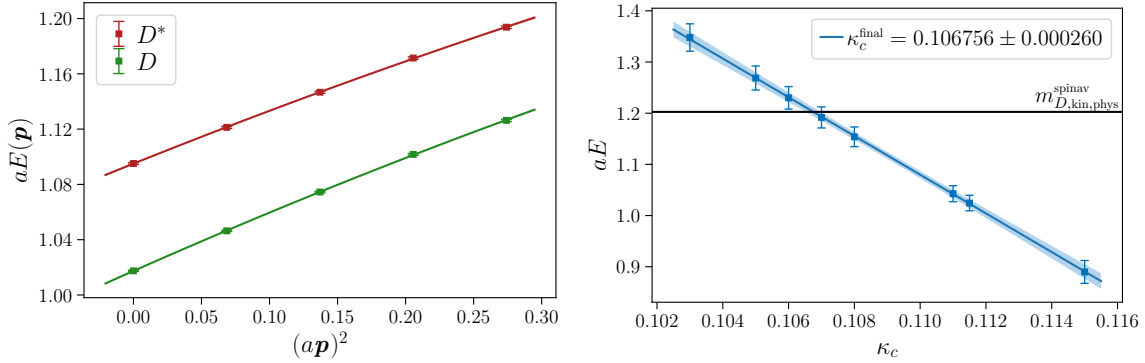


Figure 7.1.:  $D$  and  $D^*$  meson dispersion relation according to Eq. (7.1) for the final choice of the charm hopping parameter  $\kappa_c = 0.106756$  (left) and spin-averaged kinetic  $D$  meson mass  $m_{D,\text{kin}}^{\text{spinav}}$  in dependence of  $\kappa_c$  (right) computed on ensemble a12m220S. The black horizontal line in the right plot indicates the physical spin-averaged kinetic  $D$  meson mass in lattice units.

## 7.2 Interpolating Operators for $\bar{b}\bar{c}ud$ Four-Quark Systems

The interpolating operators that have been utilized in Chapter 5 to search for  $\bar{b}\bar{c}ud$  bound states with  $I(J^P) = 0(0^+)$  and  $I(J^P) = 0(1^+)$  have been discussed in detail in Secs. 4.2.3.3 and 4.2.3.4. However, in order to investigate  $\bar{b}\bar{c}ud$  four-quark states in  $S$ -wave  $BD$  and  $B^*D$  scattering, I slightly modify the utilized operator basis. I use the same local operators as given in Eqs. (4.33) and (4.34) and Eqs. (4.36) to (4.38) but add for both channels another local operator which resembles a local  $B^*D^*$  structure. Concerning the scattering operators, I consider only operators describing the meson-meson pair, which is associated to the lowest non-interacting two-meson threshold. In addition to the operator where the mesons' momenta are both projected to zero, I consider also operators where the individual meson momenta are non-zero. The highest meson momenta are hereby chosen such that the associated non-interacting two-meson energy is located in the vicinity of the second meson-meson threshold (either  $B^*D^*$  or  $BD^*$ ). In practice, this means that I consider up to six scattering operators.

Moreover, I intend to resolve the finite volume energy spectrum not only for the center-of-momentum frame but also for moving frames with non-zero total momentum  $\mathbf{P} = 2\pi\mathbf{d}/L$ . Here, I consider two moving frames with  $\mathbf{d} = (0, 0, 1)^T$  and  $\mathbf{d} = (1, 1, 0)^T$ . Consequently, I construct for each frame an appropriate set of interpolating operators based on the above mentioned guideline, while all operators must transform according to the relevant irrep of the symmetry group associated to the particular frame (see Sec. 4.2.1).

### 7.2.1 Symmetry Groups and Irreps

Apart from the center-of-momentum frame (CMF) with the symmetry group  $O_h$ , the relevant symmetry groups for the scattering of two mesons with different masses

are the group  $C_{4v}$  for the first moving frame (MF1) with total momentum  $\mathbf{P} = (2\pi/L)(0, 0, 1)^T$  and the group  $C_{2v}$  for the second moving frame (MF2) with total momentum  $\mathbf{P} = (2\pi/L)(1, 1, 0)^T$ . I list the relevant irreps that contain the continuum quantum numbers  $J^P = 0^+$  and  $J^P = 1^+$  in Table 7.1 together with the polynomials that transform according to the given irreps. A lattice interpolating operator for a state with distinct quantum numbers  $J^P$  must be constructed such that it transforms accordingly to a particular irrep that contains  $J^P$ , i.e., the operator transforms in the same way as the listed polynomials. Note that several spins  $J$  are subduced into the

$\mathbf{d}$	Symmetry group	$J^P = 0^+$		$J^P = 1^+$	
		Irrep $\Lambda$	Polynomial	Irrep $\Lambda$	Polynomial
$(0, 0, 0)$	$O_h$	$A_1^+$	1	$T_1^+$	$(R_x, R_y, R_z)$
$(0, 0, 1)$	$C_{4v}$	$A_1$	1, $z$	$A_2$	$i, R_z$
				$E$	$(x, y), (R_x, R_y)$
$(1, 1, 0)$	$C_{2v}$	$A_1$	1, $\tilde{x}$	$A_2$	$i, R_{\tilde{x}}$
				$B_1$	$z, R_{\tilde{y}}$
				$B_2$	$\tilde{y}, R_z$

Table 7.1.: Irreducible representations (irreps) of the symmetry groups  $O_h$ ,  $C_{4v}$  and  $C_{2v}$  that contain the quantum numbers  $J^P = 0^+$  and  $J^P = 1^+$ . Additionally, I also show polynomials that transform according to the given irrep, where  $R_j$  describes the rotation around the  $j$ -axis with  $j \in \{x, y, z\}$  and  $i$  represents the inversion. For  $C_{2v}$ , I denote the direction parallel to the boost by  $\tilde{x} \equiv x + y$  and the perpendicular direction by  $\tilde{y} \equiv x - y$ .

same irrep, so the energy spectrum that is computed within a specific irrep will be a mixture of different quantum numbers  $J^P$ . For the CMF, we observe according to Table 4.2 that the next quantum number that is contained in the  $A_1^+$  irrep is  $J^P = 4^+$  and in the  $T_1^+$  irrep is  $J^P = 3^+$ . As contributions of higher partial waves are suppressed, I do not expect that states with the associated quantum numbers contribute significantly and assume that the resolved energy spectra will describe exclusively  $J^P = 0^+$  and  $J^P = 1^+$  energy levels, respectively. For the moving frames, the situation is different. The lowest quantum numbers that are contained in the  $A_1$  irreps of  $C_{4v}$  and of  $C_{2v}$  are  $0^+$  and  $1^-$ , which means that contributions from states with  $J^P = 1^-$  to the energy spectrum are possible. For the irreps  $A_2$  of  $C_{4v}$  and  $C_{2v}$ , the situation is similar, as in addition to the quantum number  $J^P = 1^+$ , also  $J^P = 0^-$  is subduced into this irrep. The irreps  $E$  of  $C_{4v}$  as well as  $B_1$  and  $B_2$  of  $C_{2v}$  contain, additionally to  $J^P = 1^+$ , also the quantum numbers  $J^P = 1^-$  and  $J^P = 2^\pm$ . Consequently, for all irreps in moving frames we observe relevant contributions from higher partial waves, which might lead to mixing of states with different quantum numbers in the energy spectrum. Therefore, the energy spectra determined in moving frames must be treated with extreme care.

### 7.2.2 Interpolating Operators for $\bar{b}\bar{c}ud$ with $I(J^P) = 0(0^+)$

The interpolating operators for the  $\bar{b}\bar{c}ud$  system with  $I(J^P) = 0(0^+)$  are constructed in the  $A_1^+$  irrep for the CMF and in the irrep  $A_1$  for both moving frames. As discussed in Sec. 4.2.3.3, the lowest relevant two-meson threshold is given by  $BD$ , while the second threshold which is governed by  $B^*D^*$  is approximately 190 MeV above the  $BD$  threshold.

The local operators for the center-of-momentum frame and the moving frames differ only by their momentum projection to the total momentum  $\mathbf{P} = 2\pi\mathbf{d}/L$ . I use three local interpolating operators, two meson-meson operators and one diquark-antidiquark operator, which are given by

$$\mathcal{O}_1 = \frac{1}{\sqrt{V_S}} \sum_{\mathbf{x}} \bar{b}\gamma_5 u(\mathbf{x}) \bar{c}\gamma_5 d(\mathbf{x}) e^{i\mathbf{x}\mathbf{P}} - (d \leftrightarrow u), \quad (7.2)$$

$$\mathcal{O}_2 = \frac{1}{\sqrt{V_S}} \sum_{\mathbf{x}} \bar{b}\gamma_j u(\mathbf{x}) \bar{c}\gamma_j d(\mathbf{x}) e^{i\mathbf{x}\mathbf{P}} - (d \leftrightarrow u), \quad (7.3)$$

$$\mathcal{O}_3 = \frac{1}{\sqrt{V_S}} \sum_{\mathbf{x}} \bar{b}^a \gamma_5 \mathcal{C} \bar{c}^{b,T}(\mathbf{x}) u^{a,T} \mathcal{C} \gamma_5 d^b(\mathbf{x}) e^{i\mathbf{x}\mathbf{P}} - (d \leftrightarrow u), \quad (7.4)$$

where the total momentum  $\mathbf{P}$  is chosen according to the frame of interest as listed in Table 7.1. All operators transform as 1, which renders the correct transformation behavior for the relevant irreps.

Constructing the scattering operators, I take only operators resembling  $BD$  scattering states into account. In contrast to Sec. 4.2.3.3, I consider not only the operator where the meson momenta are projected to zero but also  $BD$  scattering operators where the individual meson momenta are non-zero. Using the short-term notations

$$B^+(\mathbf{q}_1) = \frac{1}{\sqrt{V_S}} \sum_{\mathbf{x}} \bar{b}\gamma_5 u e^{i\mathbf{p}_1 \mathbf{x}}, \quad D^-(\mathbf{q}_2) = \frac{1}{\sqrt{V_S}} \sum_{\mathbf{x}} \bar{c}\gamma_5 d e^{i\mathbf{p}_2 \mathbf{x}}, \quad (7.5)$$

where  $\mathbf{p}_1 = 2\pi\mathbf{q}_1/L$  and  $\mathbf{p}_2 = 2\pi\mathbf{q}_2/L$  are the individual meson momenta, a  $BD$  scattering operator in its most general form can be written as

$$\mathcal{O}_{BD \text{ scatt}}(\mathbf{q}_1, \mathbf{q}_2) = B^+(\mathbf{q}_1) D^-(\mathbf{q}_2) - (d \leftrightarrow u). \quad (7.6)$$

All scattering operators that are used in this work are constructed by adequately combining several terms of the general expression in Eq. (7.6) for specific values of the meson momenta  $\mathbf{p}_1$  and  $\mathbf{p}_2$ . The actual choice of  $\mathbf{p}_1$  and  $\mathbf{p}_2$  as well as the number of terms that appear depend on the total momentum  $\mathbf{P}$  of the moving frame and the irrep for which the operator is constructed. The fundamental principle is that several terms of the form of Eq. (7.6) with distinct meson momenta obeying  $\mathbf{p}_1 + \mathbf{p}_2 = \mathbf{P}$  are combined such that the resulting operator transforms according to the desired irrep  $\Lambda$  as defined in Eq. (4.9). To distinguish the operators for different frames, I introduce the upper index  $\Lambda(\mathbf{d}^2)$ , where  $\mathbf{d} = \mathbf{P}/(2\pi/L)$  specifies the total momentum and  $\Lambda$

denotes the considered irrep.

For the CMF with total momentum  $\mathbf{P} = (0, 0, 0)^T$ , the individual meson momenta must obey  $\mathbf{p} = 2\pi\mathbf{q}/L \equiv \mathbf{p}_1 = -\mathbf{p}_2$ . I consider four scattering operators for the CMF with  $\mathbf{q}^2 \leq 3$  which are constructed in such a way that they transform according to the  $A_1^+$  irrep of group  $O_h$ . The explicit interpolating operators expressed in terms of Eq. (7.5) are given by

$$\mathcal{O}_4^{A_1^+(0)} = B^+(0) D^-(0) - (d \leftrightarrow u), \quad (7.7)$$

$$\mathcal{O}_5^{A_1^+(0)} = \sum_{\mathbf{q}=\pm\mathbf{e}_{i=x,y,z}} B^+(\mathbf{q}) D^-(-\mathbf{q}) - (d \leftrightarrow u), \quad (7.8)$$

$$\mathcal{O}_6^{A_1^+(0)} = \sum_{\mathbf{q}=\pm\mathbf{e}_i \pm \mathbf{e}_j, i < j} B^+(\mathbf{q}) D^-(-\mathbf{q}) - (d \leftrightarrow u), \quad (7.9)$$

$$\mathcal{O}_7^{A_1^+(0)} = \sum_{\mathbf{q}=\pm\mathbf{e}_x \pm \mathbf{e}_y \pm \mathbf{e}_z} B^+(\mathbf{q}) D^-(-\mathbf{q}) - (d \leftrightarrow u), \quad (7.10)$$

where I use for  $\mathcal{O}_6^{A_1^+(0)}$   $i, j = x, y, z$  with the ‘‘ordering’’  $x < y < z$ .

For the first moving frame with total momentum  $\mathbf{P} = (2\pi/L)(0, 0, 1)^T$ , the scattering operators are constructed such that they transform according to the  $A_1$  irrep of the symmetry group  $C_{4v}$  (see Table 7.1). I consider six scattering operators which have the correct transformation behavior and whose meson momenta obey  $\mathbf{q}_i^2 \leq 3$ ,

$$\mathcal{O}_4^{A_1(1)} = B^+(0) D^-(\mathbf{e}_z) - (d \leftrightarrow u), \quad (7.11)$$

$$\mathcal{O}_5^{A_1(1)} = B^+(\mathbf{e}_z) D^-(0) - (d \leftrightarrow u), \quad (7.12)$$

$$\mathcal{O}_6^{A_1(1)} = \sum_{\mathbf{q}=\pm\mathbf{e}_{i=x,y}} B^+(\mathbf{q}) D^-(\mathbf{e}_z - \mathbf{q}) - (d \leftrightarrow u), \quad (7.13)$$

$$\mathcal{O}_7^{A_1(1)} = \sum_{\mathbf{q}=\pm\mathbf{e}_{i=x,y}} B^+(\mathbf{e}_z - \mathbf{q}) D^-(\mathbf{q}) - (d \leftrightarrow u), \quad (7.14)$$

$$\mathcal{O}_8^{A_1(1)} = \sum_{\mathbf{q}=\pm\mathbf{e}_x \pm \mathbf{e}_y} B^+(\mathbf{q}) D^-(\mathbf{e}_z - \mathbf{q}) - (d \leftrightarrow u), \quad (7.15)$$

$$\mathcal{O}_9^{A_1(1)} = \sum_{\mathbf{q}=\pm\mathbf{e}_x \pm \mathbf{e}_y} B^+(\mathbf{e}_z - \mathbf{q}) D^-(\mathbf{q}) - (d \leftrightarrow u). \quad (7.16)$$

I also use six scattering operators for the second moving frame whose total momentum is given by  $\mathbf{P} = (2\pi/L)(1, 1, 0)^T$ . The operators are constructed such that they



transform according to the  $A_1$  irrep of group  $C_{2v}$  and read

$$\mathcal{O}_4^{A_1(2)} = B^+(0) D^-(\mathbf{e}_x + \mathbf{e}_y) - (d \leftrightarrow u), \quad (7.17)$$

$$\mathcal{O}_5^{A_1(2)} = B^+(\mathbf{e}_x + \mathbf{e}_y) D^-(0) - (d \leftrightarrow u), \quad (7.18)$$

$$\mathcal{O}_6^{A_1(2)} = B^+(\mathbf{e}_x) D^-(\mathbf{e}_y) + B^+(\mathbf{e}_y) D^-(\mathbf{e}_x) - (d \leftrightarrow u), \quad (7.19)$$

$$\mathcal{O}_7^{A_1(2)} = \sum_{\mathbf{q}=\pm\mathbf{e}_z} B^+(\mathbf{e}_x + \mathbf{q}) D^-(\mathbf{e}_y - \mathbf{q}) + B^+(\mathbf{e}_y + \mathbf{q}) D^-(\mathbf{e}_x - \mathbf{q}) - (d \leftrightarrow u), \quad (7.20)$$

$$\mathcal{O}_8^{A_1(2)} = \sum_{\mathbf{q}=\pm\mathbf{e}_z} B^+(\mathbf{q}) D^-(\mathbf{e}_x + \mathbf{e}_y - \mathbf{q}) - (d \leftrightarrow u), \quad (7.21)$$

$$\mathcal{O}_9^{A_1(2)} = \sum_{\mathbf{q}=\pm\mathbf{e}_z} B^+(\mathbf{e}_x + \mathbf{e}_y - \mathbf{q}) D^-(\mathbf{q}) - (d \leftrightarrow u). \quad (7.22)$$

Just as in the case of the other two frames, I also take only operators with meson momenta  $\mathbf{q}_i^2 \leq 3$  into account.

### 7.2.3 Interpolating Operators for $\bar{b}\bar{c}ud$ with $I(J^P) = 0(1^+)$

For the  $\bar{b}\bar{c}ud$  system with  $I(J^P) = 0(1^+)$ , the interpolating operators for the CMF are constructed in the  $T_1^+$  irrep of group  $O_h$ . For the moving frames, we are in principle not restricted to a single irrep, as the quantum numbers  $J^P = 1^+$  are contained in the irreps  $A_2$  and  $E$  of  $C_{4v}$  for MF1 and in  $A_2$ ,  $B_1$  and  $B_2$  of  $C_{2v}$  for MF2. I decided to consider only the  $A_2$  irreps for both moving frames, while the other possible irreps are not used in this work.

Following the discussion in Sec. 7.2, I take four local interpolating operators into account, three meson-meson operators and one diquark-antidiquark operator which are given by

$$\mathcal{O}_1 = \frac{1}{\sqrt{V_S}} A_j \sum_{\mathbf{x}} \bar{b}\gamma_j u(\mathbf{x}, t) \bar{c}\gamma_5 d(\mathbf{x}, t) e^{i\mathbf{x}\mathbf{P}} - (d \leftrightarrow u), \quad (7.23)$$

$$\mathcal{O}_2 = \frac{1}{\sqrt{V_S}} A_j \sum_{\mathbf{x}} \bar{b}\gamma_5 u(\mathbf{x}, t) \bar{c}\gamma_j d(\mathbf{x}, t) e^{i\mathbf{x}\mathbf{P}} - (d \leftrightarrow u), \quad (7.24)$$

$$\mathcal{O}_3 = \frac{1}{\sqrt{V_S}} A_j \epsilon_{jkl} \sum_{\mathbf{x}} \bar{b}\gamma_k u(\mathbf{x}) \bar{c}\gamma_l d(\mathbf{x}) e^{i\mathbf{x}\mathbf{P}} - (d \leftrightarrow u), \quad (7.25)$$

$$\mathcal{O}_4 = \frac{1}{\sqrt{V_S}} A_j \sum_{\mathbf{x}} \bar{b}^a \gamma_j \mathcal{C} \bar{c}^{b,T}(\mathbf{x}, t) u^{a,T} \mathcal{C} \gamma_5 d^b(\mathbf{x}, t) e^{i\mathbf{x}\mathbf{P}} - (d \leftrightarrow u). \quad (7.26)$$

These operators can be applied for all frames and irreps by choosing the total momentum  $\mathbf{P} = 2\pi\mathbf{d}/L$  and the polarization  $\mathbf{A}$  appropriately according to

$$\begin{aligned} \text{CoM: } & T_1^+ \text{ of } O_h \quad \mathbf{d} = (0, 0, 0)^T, \quad \mathbf{A} = (1, 0, 0)^T \text{ or } (0, 1, 0)^T \text{ or } (0, 0, 1)^T, \\ \text{MF1: } & A_2 \text{ of } C_{4v} \quad \mathbf{d} = (0, 0, 1)^T, \quad \mathbf{A} = (0, 0, 1)^T, \\ \text{MF2: } & A_2 \text{ of } C_{2v} \quad \mathbf{d} = (1, 1, 0)^T, \quad \mathbf{A} = (1, 1, 0)^T. \end{aligned} \quad (7.27)$$

Hereby, the polarization  $\mathbf{A}$  determines the transformation behavior of the operators and is related to the polynomials in Table 7.1. If several polarization vectors  $\mathbf{A}$  lead to the same transformation behavior as, e.g., for  $T_1^+$  in Eq. (7.27), I average over all possible choices to increase the statistical precision.

The scattering operators are formulated similarly to those discussed for the  $I(J^P) = 0(0^+)$  channel in Sec. 7.2.2. Here, I consider exclusively  $B^*D$  scattering operators, while the individual meson momenta can be projected to zero or non-zero values. I use the abbreviations

$$B_j^{*+}(\mathbf{q}_1) = \frac{1}{\sqrt{V_S}} \sum_{\mathbf{x}} \bar{b}\gamma_j u e^{i\mathbf{p}_1\mathbf{x}}, \quad D^-(\mathbf{q}_2) = \frac{1}{\sqrt{V_S}} \sum_{\mathbf{x}} \bar{c}\gamma_5 d e^{i\mathbf{p}_2\mathbf{x}}. \quad (7.28)$$

with  $j = x, y, z$  to formulate a  $B^*D$  scattering operator in its most general form,

$$\mathcal{O}_{B^*D \text{ scatt}}(\mathbf{q}_1, \mathbf{q}_2) = B_j^{*+}(\mathbf{q}_1)D^-(\mathbf{q}_2) - (d \leftrightarrow u). \quad (7.29)$$

Note that  $B_j^{*+}$ , defined in Eq. (7.28), relies on the notation  $\gamma_x \equiv \gamma_1$ ,  $\gamma_y \equiv \gamma_2$  and  $\gamma_z \equiv \gamma_3$ , which allows a more consistent formulation of the scattering operators.

The final operators are again constructed by combining several terms of the expression in Eq. (7.29) with distinct momenta  $\mathbf{p}_1$  and  $\mathbf{p}_2$  such that they transform according to the desired irrep. Again, the operators are denoted by  $\Lambda(\mathbf{d}^2)$  to distinguish the different frames and irreps. However, one peculiarity needs to be taken into account for  $B^*D$  scattering in contrast to  $BD$  scattering. Since a vector meson, in this case the  $B^*$  meson, is involved in the scattering process, several partial waves can contribute to the continuum quantum numbers  $J^P = 1^+$  [171]. The reason for this is that the total spin  $J$  is governed by the tensor product of the mesons' total intrinsic spin  $S$  and the orbital angular momentum  $l$ . For pseudoscalar-vector scattering, like  $B^*D$  scattering, where the intrinsic spin is  $S = 1$ , the total spin  $J$  can take values  $J \in \{l - 1, l, l + 1\}$  for  $l \geq 1$  [171]. Accordingly, if we couple the intrinsic spin  $S = 1$  to the orbital angular momentum  $l$ , we observe that both  $S$ - and  $D$ -waves can contribute to the quantum numbers  $J^P = 1^+$  [171]. This gives rise to two degenerate energy levels in the case of non-interacting mesons. If interactions are turned on, these energy levels can be slightly split.

For this reason, I choose an appropriate set of scattering operators that allows me to describe also the degenerate energy levels. In practice this means that I use several operators with exactly the same momentum projection which differ either in their polarization or in the combination of terms given in Eq. (7.29). Consequently, the number of scattering operators included in the operator basis equals the number of non-interacting two-meson levels so that also the energy levels which are degenerate in the non-interacting case are correctly rendered.

For the CMF, where the individual meson momenta obey  $\mathbf{p} = 2\pi\mathbf{q}/L \equiv \mathbf{p}_1 = -\mathbf{p}_2$ , I consider four scattering operators in the  $T_1^+$  irrep whose individual meson momenta

obey  $\mathbf{q}^2 \leq 2$  and which are given by

$$\mathcal{O}_5^{T_1^+(0)} = B_k^{*+}(0) D^-(0) - (d \leftrightarrow u), \quad (7.30)$$

$$\mathcal{O}_6^{T_1^+(0)} = \sum_{\mathbf{q}=\pm\mathbf{e}_{i=x,y,z}} B_k^{*+}(\mathbf{q}) D^-(-\mathbf{q}) - (d \leftrightarrow u), \quad (7.31)$$

$$\mathcal{O}_7^{T_1^+(0)} = \sum_{\mathbf{q}=\pm\mathbf{e}_{i=x,y}} B_z^{*+}(\mathbf{q}) D^-(-\mathbf{q}) - 2 \sum_{\mathbf{q}'=\pm\mathbf{e}_z} B_z^{*+}(\mathbf{q}') D^-(-\mathbf{q}') - (d \leftrightarrow u), \quad (7.32)$$

$$\mathcal{O}_8^{T_1^+(0)} = \sum_{\mathbf{q}=\pm\mathbf{e}_i \pm \mathbf{e}_j, i < j} B_k^{*+}(\mathbf{q}) D^-(-\mathbf{q}) - (d \leftrightarrow u). \quad (7.33)$$

Note that for  $\mathcal{O}_8^{T_1^+(0)}$ , I use again  $i, j = x, y, z$  with the ‘‘ordering’’  $x < y < z$ . To increase the statistical precision, I average over all three polarizations  $k$  if possible.

For the first moving frame with  $\mathbf{P} = (2\pi/L)(0, 0, 1)^T$ , I use six different scattering operators constructed in the  $A_2$  irrep of group  $C_{4v}$  with individual meson momenta  $\mathbf{q}_i^2 \leq 2$ , according to

$$\mathcal{O}_5^{A_2(1)} = B_z^{*+}(0) D^-(\mathbf{e}_z) - (d \leftrightarrow u), \quad (7.34)$$

$$\mathcal{O}_6^{A_2(1)} = B_z^{*+}(\mathbf{e}_z) D^-(0) - (d \leftrightarrow u), \quad (7.35)$$

$$\mathcal{O}_7^{A_2(1)} = \sum_{\mathbf{q}=\pm\mathbf{e}_{i=x,y}} B_z^{*+}(\mathbf{q} + \mathbf{e}_z) D^-(-\mathbf{q}) - (d \leftrightarrow u), \quad (7.36)$$

$$\mathcal{O}_8^{A_2(1)} = \sum_{\mathbf{q}=\pm\mathbf{e}_{i=x,y}} B_z^{*+}(-\mathbf{q}) D^-(+\mathbf{e}_z + \mathbf{q}) - (d \leftrightarrow u), \quad (7.37)$$

$$\mathcal{O}_9^{A_2(1)} = \sum_{i=x,y} B_i^{*+}(-\mathbf{e}_i) D^-(\mathbf{e}_i + \mathbf{e}_z) - B_i^{*+}(\mathbf{e}_i) D^-(-\mathbf{e}_i + \mathbf{e}_z) - (d \leftrightarrow u), \quad (7.38)$$

$$\mathcal{O}_{10}^{A_2(1)} = \sum_{i=x,y} B_i^{*+}(-\mathbf{e}_i + \mathbf{e}_z) D^-(\mathbf{e}_i) - B_i^{*+}(\mathbf{e}_i + \mathbf{e}_z) D^-(-\mathbf{e}_i) - (d \leftrightarrow u). \quad (7.39)$$

Finally, for the second moving frame with  $\mathbf{P} = (2\pi/L)(1, 1, 0)^T$ , I consider four scattering operators with  $\mathbf{q}_i^2 \leq 2$  which transform according to the  $A_2$  irrep of  $C_{2v}$ . These operators are given by

$$\mathcal{O}_5^{A_2(2)} = B_x^{*+}(\mathbf{e}_x + \mathbf{e}_y) D^-(0) + B_y^{*+}(\mathbf{e}_x + \mathbf{e}_y) D^-(0) - (d \leftrightarrow u), \quad (7.40)$$

$$\mathcal{O}_6^{A_2(2)} = B_x^{*+}(0) D^-(\mathbf{e}_x + \mathbf{e}_y) + B_y^{*+}(0) D^-(\mathbf{e}_x + \mathbf{e}_y) - (d \leftrightarrow u), \quad (7.41)$$

$$\mathcal{O}_7^{A_2(2)} = B_x^{*+}(\mathbf{e}_y) D^-(\mathbf{e}_x) + B_y^{*+}(\mathbf{e}_x) D^-(\mathbf{e}_y) - (d \leftrightarrow u), \quad (7.42)$$

$$\mathcal{O}_8^{A_2(2)} = B_x^{*+}(\mathbf{e}_x) D^-(\mathbf{e}_y) + B_y^{*+}(\mathbf{e}_y) D^-(\mathbf{e}_x) - (d \leftrightarrow u). \quad (7.43)$$

### 7.2.4 Techniques to Compute Quark Propagators and Smearing of Quark Fields

In contrast to Sec. 6.1.4, I use point-to-all propagators to compute all correlation matrix elements containing at least one local interpolating operator, while I consider stochastic timeslice-to-all propagators only for those correlation matrix elements with scattering interpolating operators at the sink and the source. Remember that for correlations between local and scattering operators both techniques can in principle be applied thanks to the hermiticity of the correlation matrix. However, it turns out that it is beneficial to use only point-to-all propagators for those elements since using stochastic timeslice-to-all propagators is numerically more expensive at comparable signal-to-noise ratio.

For each configuration, I compute point-to-all propagators starting at 30 randomly distributed point sources. Applying stochastic timeslice-to-all propagators, I use stochastic sources at 4 equally distributed timeslices and consider 3 different random seeds for each timeslice.

All quark fields used in this calculation are Gaussian smeared as discussed in Sec. 6.1.4. The smearing parameters for the up, down and bottom quarks are the same as listed in Table 6.4. For the charm quarks, I use the Gaussian/Wuppertal prescription with the smearing parameters given in Table 7.2. The gauge links that are used in the charm quark smearing are HYP smeared, and additionally I applied spatial APE smearing, using the same parameters as employed in Sec. 6.1.4.

Ensemble	Charm quarks	
	$N_{\text{Gauss}}$	$\kappa_{\text{Gauss}}$
coarse	5	1.0

Table 7.2.: Smearing parameters for the charm quark-fields used in the computation of the correlation functions. Gaussian smearing is carried out according to Eq. (4.78). The ensembles are cumulated corresponding to their lattice spacing, while *coarse* includes a12m220S and a12m220.

## 7.3 Energies and Kinetic Masses for $D$ and $D^*$ Mesons

The  $D$  and  $D^*$  meson energies are determined analogously to the pseudoscalar and vector  $B$  and  $B_s$  meson energies in Sec. 6.2 via correlated single-exponential fits to the two-point correlation function computed from the interpolating operators in Eqs. (4.19) and (4.20). The final energies are calculated using the FLAG average for the results obtained for various temporal fit ranges with  $7 \leq t_{\text{min}}/a \leq 9$  and  $17 \leq t_{\text{max}}/a \leq 20$ . I depict the effective energies for zero momentum obtained on ensemble a12m220S for the  $D$  and  $D^*$  meson in the left plot of Fig. 7.2. The final results for the meson energies at rest for the ensembles a12m220S and a12m220 are listed in Table 7.3. Similarly to the case of the  $B$  and  $B_s$  mesons, whose energies do not coincide with their physical

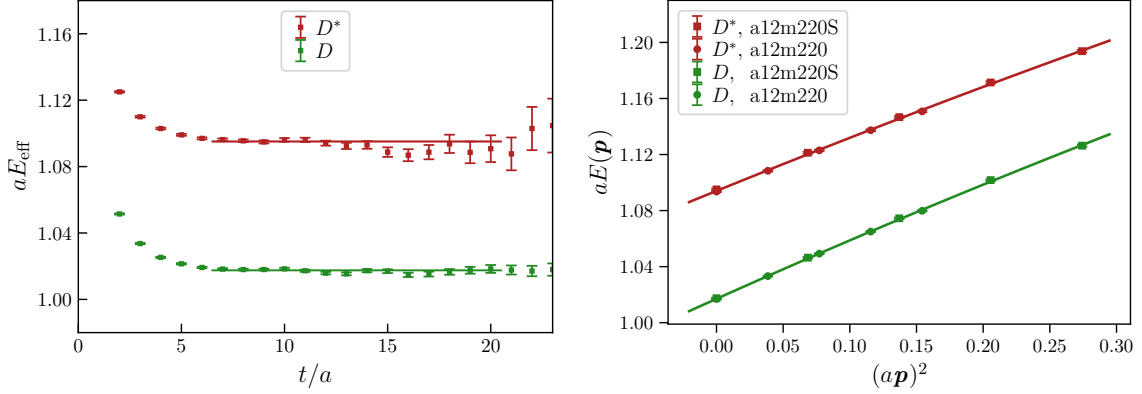


Figure 7.2.: Effective energies as defined in Eq. (4.6) for  $D$  and  $D^*$  mesons at zero momentum computed on ensemble a12m220S (left) and dispersion relation for the  $D$  and  $D^*$  mesons based on the momentum dependent meson energies  $aE(\mathbf{p})$  with  $0 \leq \mathbf{p}^2 \leq 4(2\pi/L)^2$  determined on the ensembles a12m220S and a12m220 (right). The horizontal lines in the left plot correspond to the final estimates of the mesons' energies that have been determined by various fits with  $7 \leq t_{\min}/a \leq 9$  and  $17 \leq t_{\max}/a \leq 20$ .

mass due to the use of NRQCD (see Sec. 6.2), the energy levels computed via the Fermilab action also suffer from an energy shift which cancels in energy differences with equal number of charm quarks. Consequently, for a scattering analysis we require the kinetic masses of the  $D$  and  $D^*$  mesons. They are determined by a fit of the dispersion relation, given in Eq. (7.1), to the momentum dependent meson energies  $E_D(\mathbf{p})$  and  $E_{D^*}(\mathbf{p})$ . The final results for the kinetic masses and  $M_4$  are given in Table 7.3.

Since the ensembles a12m220S and a12m220 differ only in their spatial volume and will be studied in a single scattering analysis, it is reasonable to determine a common value for each kinetic mass. This is done by a fit of the dispersion relation in Eq. (7.1) to the momentum dependent meson energies  $E(\mathbf{p})$  computed on both ensembles. The resulting dispersion relations are shown in the right plot of Fig. 7.2, while the kinetic masses and the parameters  $M_4$  that are obtained from these fits are summarized in

Ensemble	$aE_D(0)$	$aE_{D^*}(0)$	$am_{D,\text{kin}}$	$am_{D^*,\text{kin}}$	$aM_{4,D}$	$aM_{4,D^*}$
a12m220S	1.01746(47)	1.09512(67)	1.147(24)	1.267(39)	0.97(8)	1.01(12)
a12m220	1.01690(28)	1.09356(52)	1.156(25)	1.273(53)	0.93(13)	0.97(26)
a12m220co	1.01718(38)	1.09434(60)	1.172(14)	1.294(25)	1.09(9)	1.18(16)

Table 7.3.: Energies at rest, kinetic masses and parameters  $aM_4$  of the  $D$  and  $D^*$  mesons. The kinetic masses and the parameters  $aM_4$  are determined via a  $\chi^2$ -minimizing fit of the dispersion relation in Eq. (7.1) to the momentum dependent energies  $E_D(\mathbf{p})$  and  $E_{D^*}(\mathbf{p})$ .  $aE_D(0)$  and  $aE_{D^*}(0)$  on ensemble a12m220co are obtained by averaging the associated energies from the ensembles a12m220S and a12m220.

Table 7.3 using the ensemble specifier *a12m220co*. Note that for both mesons, the parameter  $M_1$  is found to be in excellent agreement with the energies at rest,  $aE_D(0)$  and  $aE_{D^*}(0)$ .

## 7.4 Finite Volume $\bar{b}\bar{c}ud$ Energy Levels

The correlation matrices for the  $\bar{b}\bar{c}ud$  four-quark systems with  $I(J^P) = 0(0^+)$  and  $I(J^P) = 0(1^+)$  are constructed via two-point correlation functions using the interpolating operators discussed in Sec. 7.2 for the three different frames with  $\mathbf{P}^2/(2\pi/L)^2 = 0, 1, 2$ . Consequently, the resulting correlation matrices have a size of  $7 \times 7$  for the CMF and  $9 \times 9$  for both moving frames in the case of  $\bar{b}\bar{c}ud$  with  $I(J^P) = 0(0^+)$  and a size of  $8 \times 8$  for the CMF,  $10 \times 10$  for MF1 and  $8 \times 8$  for MF2 in the case of  $\bar{b}\bar{c}ud$  with  $I(J^P) = 0(1^+)$ . The carefully selected operator bases, which contain additionally to several local operators also all relevant scattering operators with non-vanishing momenta (see Sec. 7.2), allow us to resolve the full low-lying energy spectrum precisely up to the second elastic meson-meson threshold for both four-quark systems. This is a crucial step which will enable us to perform a single channel scattering analysis using Lüscher's method to study the possible existence of  $\bar{b}\bar{c}ud$  tetraquark states located close to or above the lowest two-meson threshold.

In order to compute the energy spectrum, I follow the approach that I introduced in Sec. 6.3, which means that I solve a GEVP (see Sec. 4.3.1) and extract the energy levels  $E_n$  by fitting a single-exponential function to the principal correlators  $\lambda_n(t, t_0)$ . As discussed in Sec. 6.3, the temporal fit range is varied, and the results for all fit ranges are taken into account via a weighted average according to Appendix D. The statistical uncertainties are again determined via Jackknife resampling. This is done by using the previously described method for each reduced Jackknife sample, while the weight factor for a particular fit range relies on the statistical error obtained for the corresponding fit range using all Jackknife samples. In the end, the mean value and the associated Jackknife error specify the final estimate for each energy level.

### 7.4.1 Energy Spectrum for the Case of $\bar{b}\bar{c}ud$ with $I(J^P) = 0(0^+)$

To study the  $\bar{b}\bar{c}ud$  four-quark system with  $I(J^P) = 0(0^+)$ , I use the operator basis defined in Sec. 7.2, which consists of the three local interpolating operators in Eqs. (7.2) to (7.4) and the scattering operators defined according to Eqs. (7.7) to (7.20) for the three different total momenta that are considered. I extract the low-lying energy spectrum for the CMF as well as for both moving frames by evaluating the full squared correlation matrix. In Fig. 7.3, I show the effective energies  $aE_{\text{eff},n}$  according to Eq. (4.47) for the five lowest energy eigenstates that have been determined by solving a GEVP for the  $7 \times 7$  correlation matrix in the CMF on ensemble a12m220S. We observe that the effective energies for all five eigenstates are either below or in the vicinity of the  $B^*D^*$  threshold which represents the second relevant scattering channel. Moreover, the ground-state energy level is found to be slightly below the  $BD$  threshold.

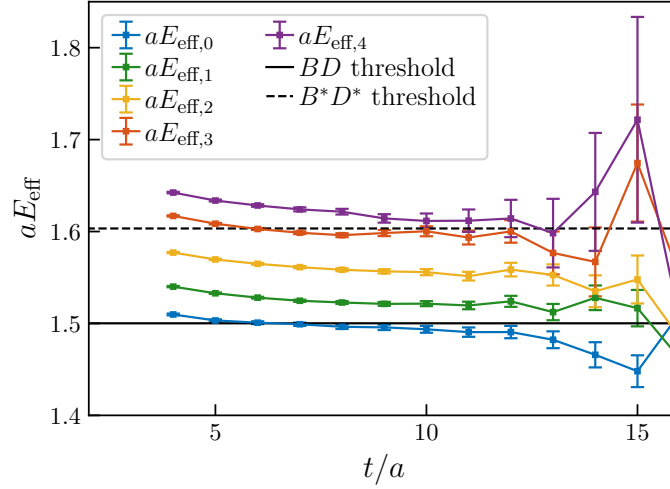


Figure 7.3.: Effective energies of the five lowest energy eigenstates for the  $\bar{b}\bar{c}ud$  four-quark system with  $I(J^P) = 0(0^+)$  obtained by solving a GEVP for the  $7 \times 7$  correlation matrix of the CMF on ensemble a12m220S.

Following the approach described in Sec. 7.4, the final estimates for the energy levels are determined by single-exponential fits of the form of Eq. (4.46) to the principal correlators  $\lambda_n(t, t_0)$  in the temporal range  $t_{\min} \leq t \leq t_{\max}$ . I utilize all possible fit range combinations with  $8 \leq t_{\min}/a \leq 10$  and  $15 \leq t_{\max}/a \leq 19$  for all irreps and for both ensembles. The final results for the lowest finite volume energy levels determined on the ensembles a12m220S (with  $L/a = 24$ ) and a12m220 (with  $L/a = 32$ ) are illustrated as gray points in Fig. 7.4 for all three frames. Above each plot, the corresponding irrep is denoted together with the total momentum of the frame using the abbreviation  $\mathbf{P} = 2\pi/L (d_1, d_2, d_3)^T \equiv [d_1, d_2, d_3]$ . Note that all energies  $\Delta E_{\text{cm},n}$  are given in the center-of-momentum frame relative to the  $BD$  threshold, i.e., the energy levels determined for moving frames are shifted back to the center-of-momentum frame according to Eq. (3.8). The solid blue lines in Fig. 7.4 show the relevant non-interacting  $BD$  energies for each irrep given by

$$E_{BD}^{\text{ni}} = E_B(\mathbf{p}_1) + E_D(\mathbf{p}_2), \quad (7.44)$$

where  $E_B(\mathbf{p}_1)$  is governed by Eq. (4.82) and  $E_D(\mathbf{p}_2)$  by Eq. (7.1) while the utilized parameters can be found in Tables 6.6 and 7.3. The blue and green horizontal dashed lines correspond to the  $BD$  and  $B^*D^*$  threshold, respectively, with  $B^*D^*$  being the second possible scattering channel.

We observe that the energy levels  $\Delta E_{\text{cm},n}$  are shifted with respect to the non-interacting  $BD$  energies which indicates the presence of non-trivial interactions. In particular, we found for all irreps an additional energy level compared to the number expected from counting the non-interacting  $BD$  energy levels in the same energy region. This could be a hint for a  $\bar{b}\bar{c}ud$  tetraquark state which might be either a bound state slightly

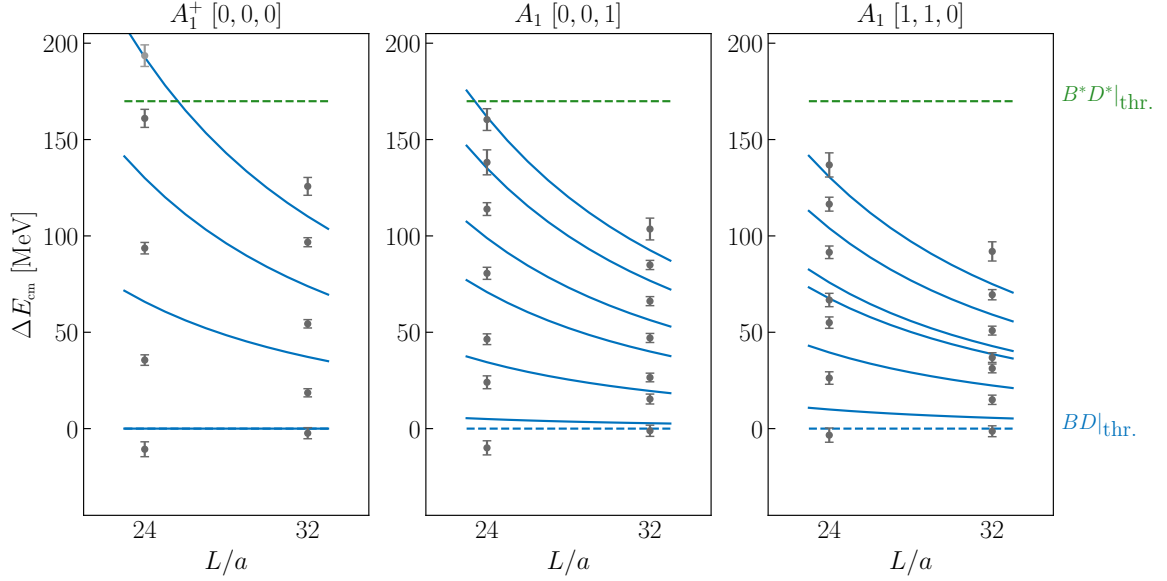


Figure 7.4.: Center-of-momentum energies  $\Delta E_{\text{cm},n}$  relative to the  $BD$  threshold for the  $\bar{b}\bar{c}ud$  four-quark system with  $I(J^P) = 0(0^+)$  in several finite volume irreps for the ensembles a12m220S ( $L/a = 24$ ) and a12m220 ( $L/a = 32$ ). Above each plot, I denote the irrep and the total momentum using the abbreviation  $\mathbf{P} = 2\pi/L (d_1, d_2, d_3)^T \equiv [d_1, d_2, d_3]$ . The solid blue lines represent the non-interaction  $BD$  energies, while the blue and green dashed lines correspond to the  $BD$  and  $B^*D^*$  threshold, respectively. Energy levels depicted in light gray are excluded from the subsequent scattering analysis.

below or a resonance above the  $BD$  threshold. Note that the shifted energy levels contain information about the  $BD$  scattering amplitude. Consequently, utilizing the determined energy spectra as input for a scattering analysis using Lüscher's method will allow us to calculate the infinite volume scattering amplitude and to draw conclusions about a possibly existing hadronic state. Such an analysis will be carried out in Sec. 7.5.1.

#### 7.4.2 Energy Spectrum for the Case of $\bar{b}\bar{c}ud$ with $I(J^P) = 0(1^+)$

The operator bases that are utilized to study the  $\bar{b}\bar{c}ud$  four-quark system with  $I(J^P) = 0(1^+)$  consist of the four local operators given in Eqs. (7.23) to (7.26), which are projected to the correct irrep according to Eq. (7.27), and the associated scattering operators for the particular irrep displayed in Eqs. (7.30) to (7.43). In Fig. 7.5, I show the five lowest effective energies  $aE_{\text{eff},n}$  as defined in Eq. (4.47) which have been obtained by solving a GEVP for the  $8 \times 8$  correlation matrix of the CMF for ensemble a12m220S. The relevant two-meson thresholds  $B^*D$  and  $BD^*$  are depicted by horizontal black lines. We observe that the effective energies are well separated and the four lowest energies are located below or around the  $BD^*$  threshold, resembling the second possible scattering channel, while the ground-state energy level seems to



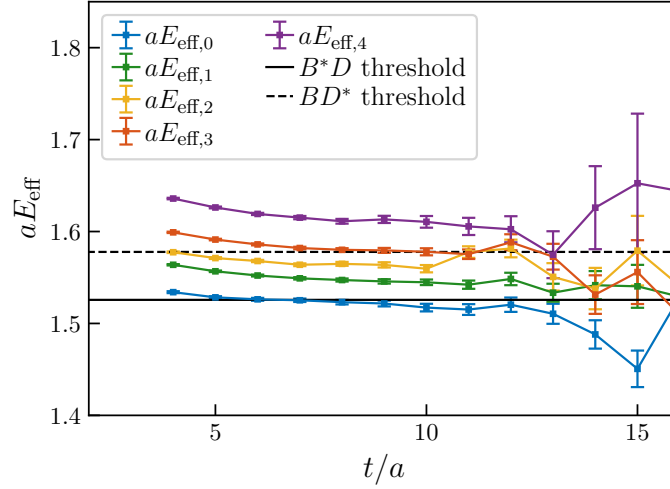


Figure 7.5.: Effective energies of the five lowest energy eigenstates for the  $\bar{b}\bar{c}ud$  four-quark system with  $I(J^P) = 0(1^+)$  obtained by solving a GEVP for the  $8 \times 8$  correlation matrix of the CMF on ensemble a12m220S.

be slightly below the  $B^*D$  threshold.

The final estimates for the energies  $E_n$  are obtained following the approach discussed in Sec. 7.4, i.e., the principal correlators, extracted from the GEVP, are fitted by a single-exponential according to Eq. (4.46) for various temporal ranges  $t_{\min} \leq t \leq t_{\max}$ . In this case, I choose  $9 \leq t_{\min}/a \leq 11$  and  $15 \leq t_{\max}/a \leq 19$  and exploit all possible combinations of  $t_{\min}$  and  $t_{\max}$ . This is repeated for both moving frames on ensemble a12m220S as well as for all frames on ensemble a12m220. I show the final results obtained in the  $T_1^+$  irrep of  $O_h$  for the CMF, in the  $A_2$  irrep of  $C_{4v}$  for MF1 and in the  $A_2$  irrep of  $C_{2v}$  for MF2 for both lattice volumes  $L/a = 24$  (ensemble a12m220S) and  $L/a = 32$  (ensemble a12m220) in Fig. 7.6 as gray points. Note that these energies correspond to the center-of-momentum energies  $\Delta E_{\text{cm},n}$  governed by Eq. (3.8) relative to the  $B^*D$  threshold, i.e., the energies obtained in the moving frames are transformed back to the CMF. Only those energy levels that are depicted in dark gray will be considered in the scattering analysis in Sec. 7.5.2, while light gray points will be excluded from the analysis. Above each plot, I indicate the considered irrep as well as the total momentum in the short notation  $\mathbf{P} = 2\pi/L(d_1, d_2, d_3)^T \equiv [d_1, d_2, d_3]$ . Similarly to Sec. 7.4.1, the solid blue lines represent the relevant non-interacting  $B^*D$  energies for each irrep according to

$$E_{B^*D}^{\text{ni}} = E_{B^*}(\mathbf{p}_1) + E_D(\mathbf{p}_2) \quad (7.45)$$

with  $E_{B^*}(\mathbf{p}_1)$  given by Eq. (4.82) and  $E_D(\mathbf{p}_2)$  by Eq. (7.1), while the  $B^*D$  threshold is indicated by the blue horizontal dashed line. Finally, the green horizontal dashed line corresponds to the  $BD^*$  threshold. As discussed in Sec. 7.2.3, some of the non-interacting energy levels are degenerate since both  $S$ - and  $D$ -waves contribute to the

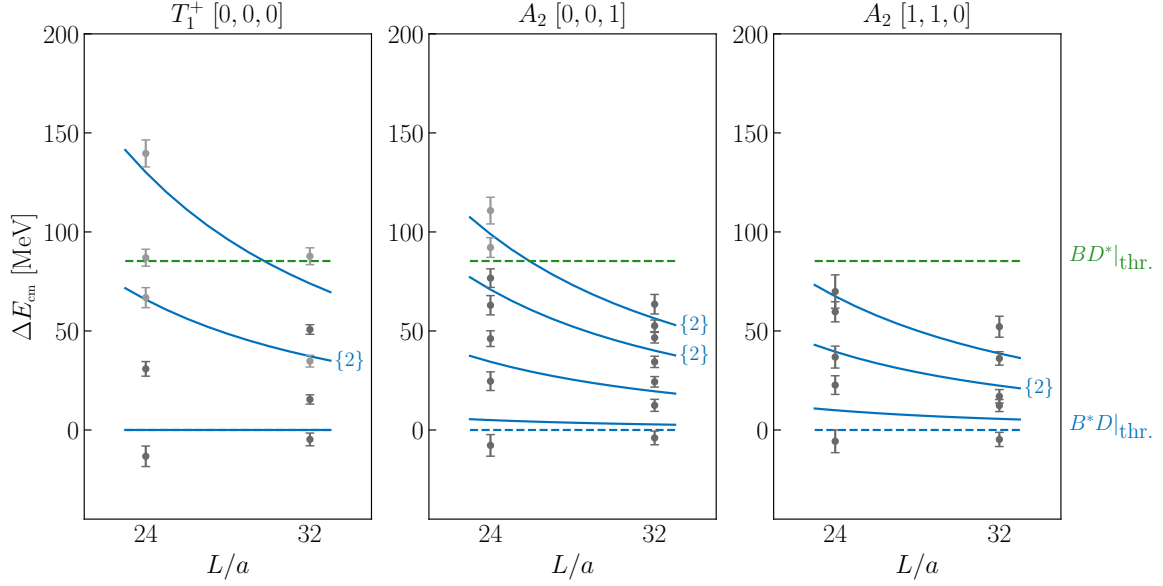


Figure 7.6.: Center-of-momentum energies  $\Delta E_{\text{cm},n}$  relative to the  $B^*D$  threshold for the  $\bar{b}\bar{c}ud$  four-quark system with  $I(J^P) = 0(1^+)$  in several finite volume irreps for the ensembles a12m220S ( $L/a = 24$ ) and a12m220 ( $L/a = 32$ ). Above each plot, I denote the irrep and the total momentum using the abbreviation  $\mathbf{P} = 2\pi/L (d_1, d_2, d_3)^T \equiv [d_1, d_2, d_3]$ . The solid blue lines represent the non-interaction  $B^*D$  energies, while the blue and green dashed lines correspond to the  $B^*D$  and  $BD^*$  threshold, respectively. Energy levels depicted in light gray are excluded from the subsequent scattering analysis.

quantum numbers  $J^P = 1^+$  for pseudoscalar-vector scattering. I indicate these degenerate non-interacting energy levels by  $\{2\}$  in Fig. 7.6.

We observe for all irreps and both spatial volumes that the finite volume energies are shifted with respect to the non-interacting  $B^*D$  energies. Moreover, we find one additional energy level compared to the number of non-interacting two-meson energies in the same energy region. These findings are indications for non-trivial interactions. Note that the degenerate non-interacting  $B^*D$  energies are correctly rendered by our operator basis giving rise to two energy levels in the finite volume spectrum for each degenerate non-interacting two-meson level. In the case of the CMF, we clearly recognize that one of the two energy levels is consistent with the non-interacting energy level, while the other one is slightly shifted. Assuming that the unshifted energy level resembles a  $D$ -wave state, we can conclude that non-trivial interactions do not appear for  $l = 2$ . For moving frames, however, the picture is less clear. Here, we cannot clearly identify a particular finite volume energy level that exactly matches this degenerate non-interacting  $B^*D$  energy, but observe instead several energy levels that are close to the non-interacting meson-meson level.

In order to further investigate the non-trivial interactions that have been deduced from the shifted energies in the finite volume energy spectrum, a reasonable approach is to

determine the infinite volume  $B^*D$  scattering amplitude based on the finite volume energy levels using Lüscher's formula as it will be done in Sec. 7.5.2. This allows us to study if a hadronic state like a shallow bound state or a resonance exists in the  $\bar{b}\bar{c}ud$  channel with  $I(J^P) = 0(1^+)$ .

## 7.5 Scattering Analysis

The finite volume energy spectra for the  $\bar{b}\bar{c}ud$  four-quark systems with  $I(J^P) = 0(0^+)$  and  $I(J^P) = 0(1^+)$  that have been studied in Sec. 7.4 show evidence for non-trivial interactions. However, the ground-state energy level is located close to the threshold of strong decay in both cases, and accordingly no deeply bound states could be predicted. Thus, the interactions might render a shallow bound state close to the threshold or a resonance in the spectrum of scattering states. In both cases, finite volume effects play a crucial role, which makes it mandatory to study the  $\bar{b}\bar{c}ud$  four-quark systems in a scattering analysis, while I consider  $BD$  scattering for  $J = 0$  and  $B^*D$  scattering in the case of  $J = 1$ . This is done by exploiting Lüscher's method to parametrize the infinite volume scattering amplitude based on the finite volume energy levels. Here, I follow the approach discussed in Sec. 4.6.2.1, i.e., I compute the  $S$ -wave phase shift  $\delta_0(k_n)$  for each finite volume energy level using the quantization condition in Eq. (3.35). Note that the  $M$ -matrix is simplified as a consequence of the discrete lattice symmetries as discussed in Sec. 3.2. The actual form of the  $M$ -matrix depends on the present irrep, while all simplified  $M$ -matrices which are relevant in this section can be found in Eqs. (3.42) and (B.14) to (B.17). If the phase shifts are computed, they will be used to parametrize the scattering amplitude  $T$  defined by Eq. (3.36). For the two systems of interest, where I expect an  $S$ -wave state in the vicinity or above the threshold of strong decay, a reasonable parametrization is given by the effective range expansion (ERE) which has been introduced in Sec. 4.6.2.1. It turned out, however, that an ERE which is linear in  $k^2$  is not sufficient to describe the data, but a quadratic term in  $k^2$  is required to render the phase shift adequately. Consequently, the ERE with a quadratic term in  $k^2$ , which is utilized in this section to parametrize the phase shift, is given by

$$k \cot(\delta_0(k)) = \frac{1}{a_0} + \frac{1}{2}r_0k^2 + b_0k^4 + \mathcal{O}(k^6), \quad (7.46)$$

where  $a_0$  and  $r_0$  are the well-known  $S$ -wave scattering length and effective range and  $b_0$  is a shape parameter. In order to determine the three free parameters  $a_0$ ,  $r_0$  and  $b_0$ , I perform a  $\chi^2$ -minimizing fit of Eq. (7.46) to the phase shifts  $\delta_0(k_n)$  that have been determined for the finite volume energy levels  $E_{n,\text{cm}}$ . In principle, all energy levels that have been computed on the two ensembles a12m220S and a12m220 in all three irreps can be used to parametrize the phase shift. In practice, however, only the levels that are indicated by dark gray points in Figs. 7.4 and 7.6 are included in the scattering analyses, while energy levels indicated by light gray points are excluded. The majority of these excluded energy levels are above or in agreement with the second meson-meson threshold, and thus couplings to this scattering channel are likely and

might affect such an energy level. If you wanted to include those levels, a coupled channel scattering analysis would be required. Note that for the case of  $\bar{b}\bar{c}ud$  with  $I(J^P) = 0(1^+)$  I also exclude the energy levels which can be assigned to  $D$ -wave levels. I will focus on this in more detail in Sec. 7.5.2.

As discussed in Sec. 4.2.1, each lattice irrep  $\Lambda$  contains an infinite number of continuum spins  $J$ . In Sec. 7.2.1, I have studied which quantum numbers  $J^P$  are subduced to the particular irreps that are used to investigate the  $\bar{b}\bar{c}ud$  four-quark systems with  $I(J^P) = 0(0^+)$  and  $I(J^P) = 0(1^+)$ . In the center-of-momentum frame, where I consider the  $A_1^+$  and  $T_1^+$  irreps, we observe that besides the  $S$ -wave, no partial-wave contributions with  $l \leq 2$  appear. Since higher partial waves are suppressed, I assume that all other partial-wave contributions are negligible and the resolved energy spectrum describes exclusively  $J^P = 0^+$  and  $J^P = 1^+$ , respectively. For the moving frames, however, higher partial-wave contributions can be relevant in all irreps. According to Sec. 7.2.1, the  $A_1$  irreps of  $C_{4v}$  and  $C_{2v}$ , that are used to investigate the  $\bar{b}\bar{c}ud$  system with  $J^P = 0^+$ , contain the quantum numbers  $J^P = 1^-$  in addition to  $J^P = 0^+$ . Consequently, the energy spectrum might be a mixture of  $S$ - and  $P$ -wave states. The situation is similar for the  $A_2$  irreps of  $C_{4v}$  and  $C_{2v}$ , which is taken into account to study the  $\bar{b}\bar{c}ud$  system with quantum numbers  $J^P = 1^+$ . Here, also  $J^P = 0^-$  is subduced to the same irreps, and accordingly we might experience  $P$ -wave admixtures in this case, too.

In order to minimize the contributions of higher partial waves, I first perform the scattering analyses relying only on the finite volume energy levels that have been determined in the CMF. This guarantees that I am studying  $S$ -wave scattering exclusively. In a second step, I also include the energy levels obtained from moving frames and repeat the scattering analysis. Even though I cannot exclude that  $P$ -wave contributions are present, this might be a first step to estimate the effect of  $P$ -wave admixtures to the scattering amplitude.

If the phase shift and therefore the scattering amplitude  $T$  are reasonably parametrized, I search for poles of the  $T$ -matrix in the complex energy plane. As it is unclear if a shallow bound state or a resonance exists in the case of the  $\bar{b}\bar{c}ud$  four-quark systems, I study the scattering amplitude in the full complex plane and not only, as done in Chapter 6, on the real axis where bound states appear.

### 7.5.1 Scattering Analysis for the Case of $\bar{b}\bar{c}ud$ with $I(J^P) = 0(0^+)$

The  $\bar{b}\bar{c}ud$  four-quark system with  $I(J^P) = 0(0^+)$  is studied in this chapter in  $BD$  scattering. The second possible scattering channel corresponds to  $B^*D^*$  and is located approximately 190 MeV above the  $BD$  threshold. Thus couplings of the scattering amplitude to  $B^*D^*$  are negligible, and a single channel scattering analysis is sufficient. According to Fig. 7.4, all finite volume energy levels except for  $E_{4,\text{cm}}$  in the CMF on ensemble a12m220S are found to be below the  $B^*D^*$  threshold and can consequently be taken into account for the scattering analysis. As already stated, these levels are indicated by dark gray points, while the data points in light gray are excluded from

the analysis.

In order to compute the phase shift  $\delta_0(k_n)$  for each finite volume energy level, I exploit Lüscher's quantization condition in Eq. (3.35). For the CMF, where the relevant symmetry group is  $O_h$ , the  $M$ -matrix is block diagonal and given by Eq. (3.42). Accordingly, the  $S$ -wave phase shift is governed by

$$\mathbf{P} = \frac{2\pi}{L}(0, 0, 0)^T, \quad A_1^+ \text{ of } O_h : \quad \cot(\delta_0(k)) = \omega_{00}, \quad (7.47)$$

where  $\omega_{lm}$  is defined in Eq. (3.29). As discussed in Sec. 7.2.1, only the quantum numbers  $J^P = 0^+, 4^+, \dots$  are subduced to the  $A_1^+$  irrep. Accordingly, higher partial waves are negligible, and the obtained phase shift is expected to render  $S$ -wave scattering exclusively. For the moving frames, the situation is different, as the  $A_1$  irreps of  $C_{4v}$  and  $C_{2v}$  both contain the quantum numbers  $J^P = 0^+, 1^-, 2^+, \dots$ , and consequently higher partial-wave states appear in the same irrep. This is also reflected by the shape of the  $M$ -matrices as shown in Eqs. (B.16) and (B.18), since the matrix is in both cases not fully diagonal. In fact, the determinant condition for the remaining  $2 \times 2$  block, associated to the  $A_1$  irrep, mixes  $S$ - and  $P$ -wave phase shifts. As  $\delta_0$  appears solely in this equation, it is challenging to determine the  $S$ -wave phase shift reliably. In Ref. [116], several possible strategies to extract the  $S$ -wave phase shift from the two-dimensional determinant condition in the  $A_1$  irrep have been discussed. However, in the absence of data that allow us to determine the phase shift  $\delta_1$  explicitly, it is not possible to utilize any of the proposed approaches. Therefore, I assume that the  $P$ -wave phase shift is negligible in the considered energy region, i.e.,  $\delta_1(k) \approx 0$ . Let me emphasize that this assumption has not been verified and further work needs to be done to support or refute it. Neglecting  $P$ -wave contributions, the phase shift formulas reduce to

$$\mathbf{P} = \frac{2\pi}{L}(0, 0, 1)^T, \quad A_1 \text{ of } C_{4v} : \quad \cot(\delta_0(k)) = \omega_{00}, \quad (7.48)$$

$$\mathbf{P} = \frac{2\pi}{L}(1, 1, 0)^T, \quad A_1 \text{ of } C_{2v} : \quad \cot(\delta_0(k)) = \omega_{00}. \quad (7.49)$$

In this section, I utilize Eqs. (7.48) and (7.49) to determine the phase shifts  $\delta_0$  for the moving frames.

Since the phase shifts extracted for the moving frames might be unreliable, as mentioned above, I consider only the energy levels obtained in the CMF for the main analysis. The phase shifts  $\delta_0(k_n)$  are computed via Eq. (7.47) for the scattering momenta  $k_n$  that are related to the finite volume energy levels  $E_{n,\text{cm}}$  by Eq. (3.15). Based on these phase shifts and scattering momenta, I perform a combined  $\chi^2$ -minimizing fit taking into account the 9 energy levels computed in the CMF on ensembles a12m220S and a12m220. As a fit function, I use the quadratic ERE parametrization of  $k \cot(\delta_0(k))$  as defined in Eq. (7.46). In Fig. 7.7, I present  $k_n \cot(\delta_0(k_n))$ , obtained via Eq. (7.47), for the finite volume scattering momenta  $k_n$  in the CMF as blue circles and squares. The

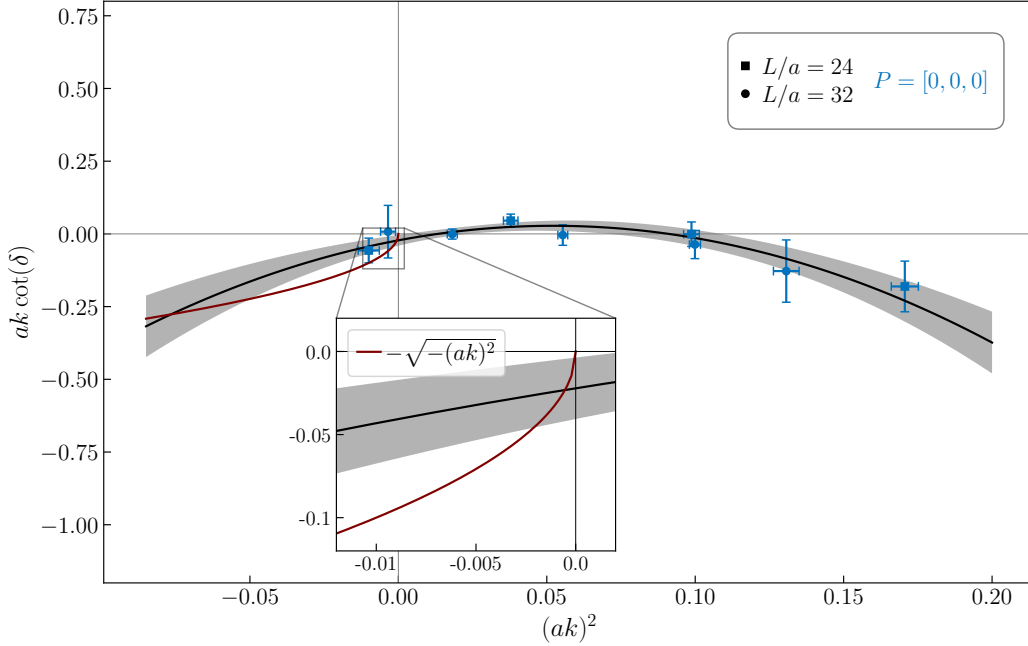


Figure 7.7.: Plot of  $ak \cot(\delta_0(k))$  as a function of the squared scattering momentum  $k^2$  in lattice units for  $BD$  scattering. The blue data points correspond to the phase shifts obtained for the finite volume energy levels on the ensembles a12m220S (squares) and a12m220 (circles) in the CMF. The black curve with shaded error band represents a quadratic ERE fit as defined in Eq. (7.46) to the data. I also depict  $-\sqrt{-(ak)^2}$  as a brown line.

shaded black line corresponds to the quadratic ERE parametrization of  $k \cot(\delta_0(k))$ . As we can see, the final fit describes the data excellently, which is also reflected by the value of  $\chi^2/\text{d.o.f.} = 0.48$ . Note that the data obviously do not behave linearly in  $k^2$ , which is the reason why an “ordinary” ERE is not suited to parametrize the phase shift. The final results for the  $S$ -wave scattering length  $a_0$ , the  $S$ -wave effective range  $r_0$  and the shape parameter  $b_0$  can be found in Table 7.4.

Having parametrized the phase shift and thus also the scattering amplitude according to Eq. (3.36), I search for poles of the  $T$ -matrix in the complex energy plane. In Fig. 7.8, I show the absolute value of the  $S$ -wave scattering amplitude  $|T^{(0)}(s)|$  as a function of the complex center-of-momentum energy  $\sqrt{s}$ . Accordingly, we observe four  $T$ -matrix poles: The first is located on the real axis below the threshold, the second is in the vicinity of the threshold with zero imaginary part, and the third and fourth appear above the threshold with the same real part, one with positive and one with negative imaginary energy. Let us first consider the two poles on the real axis which seem to be candidates for bound states at first sight. Since bound states correspond to poles of the scattering amplitude with purely imaginary scattering momentum  $k$  and  $\text{Im}(k) > 0$ , the bound state momentum is governed by the intersection point of  $-\sqrt{-k^2}$  with the parametrization of  $k \cot(\delta_0(k))$ . In Fig. 7.7, I show  $-\sqrt{-k^2}$  as a brown curve, and we can identify both intersection points. However, according to

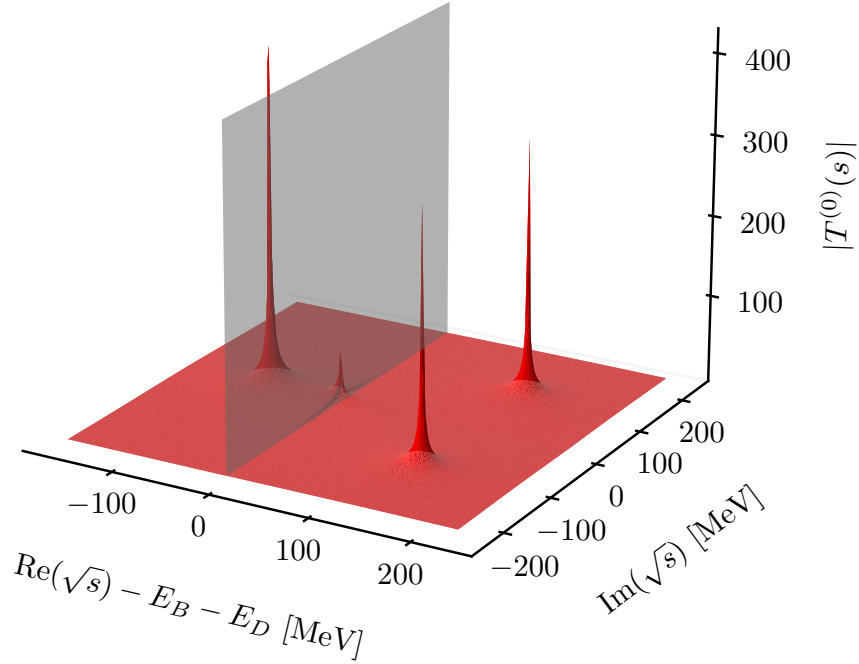


Figure 7.8.:  $S$ -wave scattering amplitude  $|T^{(0)}(s)|$  for  $BD$  scattering in the plane of complex energies. The  $BD$  threshold is depicted by the gray plane. The deeper pole below the threshold is unphysical as discussed in the text, while the other pole corresponds probably to the threshold scattering state. Above the threshold, a resonance pole appears off the real axis in the second Riemann sheet, while a shoulder is found in the first Riemann sheet at positive imaginary energy.

Eq. (6) of Ref. [213], for a bound state pole the slope of  $k \cot(\delta_0(k))$  must be smaller than the slope of  $-\sqrt{-k^2}$ . This is not the case for the pole well below the threshold, which is therefore identified as an unphysical pole. The second pole passes the consistency check, but is located almost directly at the threshold and consequently corresponds probably to the threshold scattering state but not a bound tetraquark. The remaining two poles, however, indicate the existence of a  $\bar{b}cud$  tetraquark resonance. One of the poles is located off the real axis with negative imaginary part in the second Riemann sheet as expected for a resonance. The other pole, which is located at the same real energy but has the opposite imaginary energy, corresponds to its shoulder appearing in the first Riemann sheet. Hence, I determine the resonance parameters from the first of the two poles and list the resonance energy  $E_{\text{res}} = \text{Re}(\sqrt{s}) - E_B - E_D$  and the decay width  $\Gamma = -2 \text{Im}(\sqrt{s})$  in Table 7.4. Note that the exact position of a  $T$ -matrix pole in  $S$ -wave scattering might depend on the actual parametrization as it has been observed in Ref. [214]. Hence, it will be necessary to investigate different parametrizations in the future to estimate possible systematic uncertainties concerning the  $T$ -matrix pole position.



Ensemble	$1/a_0$ [fm $^{-1}$ ]	$r_0$ [fm]	$b_0$ [fm $^3$ ]	$E_{\text{res}}$ [MeV]	$\Gamma$ [MeV]
a12m220co	-0.19(16)	0.46(16)	-0.031(8)	138(13)	229(35)

Table 7.4.: Fit results for the inverse scattering length  $1/a_0$ , the effective range  $r_0$  and the shape parameter  $b_0$  of the quadratic ERE parametrization in Eq. (7.46) based on the CMF finite volume energy levels for  $BD$  scattering. I also list the parameters for the potential tetraquark resonance corresponding to a pole of the associated scattering amplitude  $T$ .

As already mentioned at the beginning of this paragraph, I repeat the same analysis taking into account also the energy levels that have been obtained in the moving frames. Accordingly, I parametrize the phase shift based on these discrete energy levels using the quadratic ERE parametrization. In Fig. 7.9, I show the resulting fit function together with  $k_n \cot(\delta_0(k_n))$  for the discrete scattering momenta  $k_n$ . The fit parameters are listed in Table 7.5. First, we notice that the data points are reasonably described by the quadratic ERE which is supported by  $\chi^2/\text{d.o.f.} = 1.20$  for the final fit. Second, we observe that the fit results for the parameters are consistent with those listed in Table 7.4. This is encouraging, as it might be an indication that only small

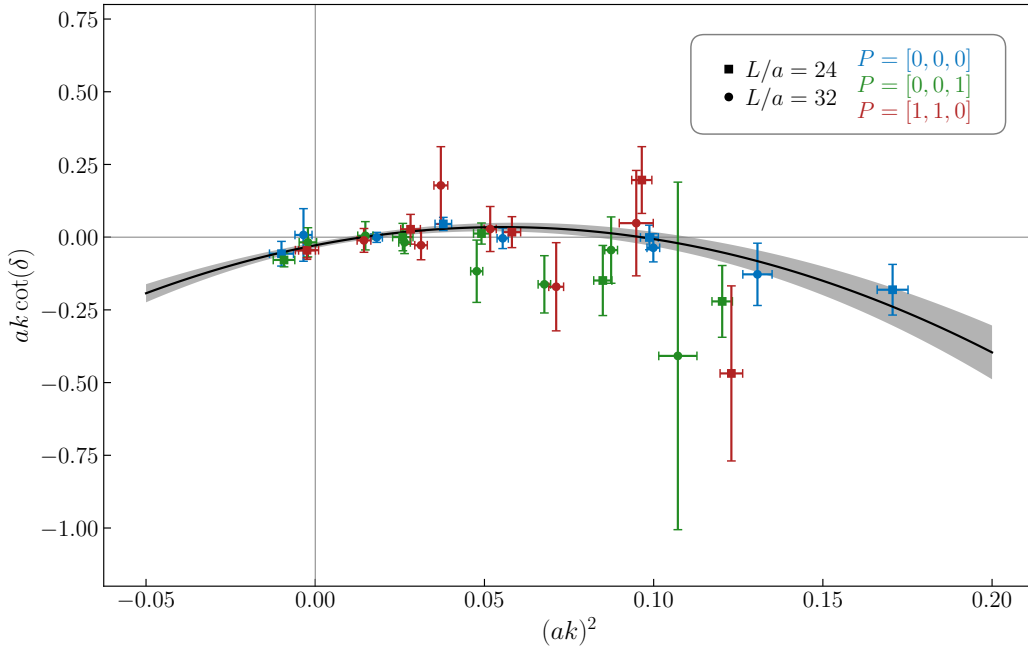


Figure 7.9.: Plot of  $ak \cot(\delta_0(k))$  as a function of the squared scattering momentum  $k^2$  in lattice units for  $BD$  scattering. The blue, green and red data points correspond to the phase shifts obtained for the finite volume energy levels on the ensembles a12m220S (squares) and a12m220 (circles) in the CMF (blue), the MF1 (green) and the MF2 (red). The black curve with shaded error band represents a quadratic ERE fit to the data as defined in Eq. (7.46).



$P$ -wave contributions appear in the considered energy region. Using the quadratic ERE parametrization with the final choice of the free parameters in Table 7.5, I also determine the poles of the scattering amplitude in the complex energy plane. Again, I detect a pole above the threshold and off the real axis which could be assigned to a tetraquark resonance. The associated resonance energy and the decay width are listed in Table 7.5, and both are in excellent agreement with the resonance parameters found for the case where only the CMF energy levels are considered.

Ensemble	$1/a_0$ [fm $^{-1}$ ]	$r_0$ [fm]	$b_0$ [fm $^3$ ]	$E_{\text{res}}$ [MeV]	$\Gamma$ [MeV]
a12m220co	-0.23(8)	0.54(9)	-0.035(6)	137(15)	211(17)

Table 7.5.: Fit results for the inverse scattering length  $1/a_0$ , the effective range  $r_0$  and the shape parameter  $b_0$  of the quadratic ERE parametrization in Eq. (7.46) based on the finite volume energy levels from the CMF and moving frames for  $BD$  scattering. I also list the parameters for the potential tetraquark resonance corresponding to a pole of the associated scattering amplitude  $T$ .

To sum up, I discover a possible candidate for a broad  $\bar{b}\bar{c}ud$  resonance with quantum numbers  $I(J^P) = 0(0^+)$  that is located about 140 MeV above the  $BD$  threshold and has a width of around 230 MeV. Note that this energy is well below the  $B^*D^*$  threshold. Consequently, I assume that a single channel scattering analysis is sufficient to describe this potential tetraquark resonance, and couplings of the scattering amplitude to the  $B^*D^*$  channel are indeed negligible.

I will end with a short discussion of the left-hand cut (see Sec. 4.6.3) for  $BD$  scattering. Here, one-pion exchange needs to be considered. Using  $m_\pi \simeq 220$  MeV and  $\Delta m = m_B - m_D \simeq 3409$  MeV, we find the left-hand cut branch point according to Eq. (4.97) at

$$(k_{\text{hlc}}^{1\pi})^2 \approx \frac{1}{4}(\Delta m^2 - m_\pi^2) \approx (1700 \text{ MeV})^2. \quad (7.50)$$

In contrast, the resonance pole is located at  $k_{\text{res}} \sim (675 - 250i)$  MeV. Consequently, the left-hand cut does not affect the energy region that is considered to study  $BD$  scattering, and the branch point does not limit decisively the radius of convergence of the ERE.

### 7.5.2 Scattering Analysis for the Case of $\bar{b}\bar{c}ud$ with $I(J^P) = 0(1^+)$

In this section, I investigate the  $\bar{b}\bar{c}ud$  four-quark system with  $I(J^P) = 0(1^+)$  in  $B^*D$  scattering. Here, the second possible scattering channel is  $BD^*$  which is about 100 MeV above the  $B^*D$  threshold. Accordingly, I neglect possible couplings of the scattering amplitude to the  $BD^*$  channel and consider a single channel scattering process exclusively. Since the energy difference between the first and second two-meson threshold is smaller compared to the case of  $J = 0$  discussed in the previous section, fewer finite volume energy levels appear in the energy region that can be considered for the

single channel analysis. In Fig. 7.6, I depict those finite volume energy levels that are included in the analysis in dark gray, while all light gray points are excluded from the analysis. Most of them are located either above or close to the  $BD^*$  threshold, and thus coupling to this channel might be substantial. Additionally, I also exclude two data points below the threshold for the case of the CMF. As discussed in Secs. 7.2.3 and 7.4.2, both  $S$ - and  $D$ -waves contribute to the quantum numbers  $J^P = 1^+$  leading to degenerate non-interacting meson-meson energy levels which are slightly split in the interacting case. In Fig. 7.6, I have identified one of these energy levels being identical to the non-interacting energy level for the case of CMF, and I have assumed that it resembles a  $D$ -wave state. Accordingly, the  $D$ -wave scattering amplitude  $T^{(2)}$  is consistent with zero, and the mixing of  $l = 2$  and  $l = 0$  for  $J = 1$  is negligible. Since I intend to describe only the  $S$ -wave scattering amplitude, I exclude the two finite volume energy levels that are assigned to  $D$ -wave states from the analysis. For the moving frames, it was not possible to clearly identify such energy levels in the same way. Hence, I refrain from excluding any additional energy levels in this case.

Following the same approach as utilized in Sec. 7.5.1, I compute the phase shifts  $\delta_0(k_n)$  for each finite volume energy level  $E_n$  using the quantization condition in Eq. (3.35) with the  $M$ -matrices defined in Eqs. (3.42), (B.16) and (B.17). As for the CMF only the quantum numbers  $J^P = 1^+, 3^+, 4^+, \dots$  appear in the  $T_1^+$  irrep of  $O_h$  according to Sec. 4.2.1, I conclude that contributions of higher partial waves can be neglected, and the quantization condition reduces to

$$\mathbf{P} = \frac{2\pi}{L}(0, 0, 0)^T, \quad T_1^+ \text{ of } O_h : \quad \cot(\delta_0(k)) = \omega_{00}. \quad (7.51)$$

For the moving frames, however, the situation is similar to the case of  $J = 0$  in Sec. 7.5.1. The  $A_2$  irreps of  $C_{4v}$  and  $C_{2v}$  both contain the quantum numbers  $J^P = 0^-, 1^+, 2^-, \dots$ , and therefore also higher partial waves appear in these irreps. Note that the  $A_2$  irrep of  $C_{4v}$  transforms like  $i$  or  $R_z$  and the  $A_2$  irrep of  $C_{2v}$  like  $i$  or  $R_{\hat{x}}$ , as can be seen in Table 7.1. Hence, the mixing of  $S$ - and  $P$ -waves in the  $A_2$  irrep is again expressed by the  $2 \times 2$  blocks of the  $M$ -matrices in Eqs. (B.16) and (B.18). Following the discussion in Sec. 7.5.1, I assume that the  $P$ -wave phase shift is approximately zero in the relevant energy region, i.e.,  $\delta_1(k) \approx 0$ , and I consider the resulting reduced phase shift equations given by

$$\mathbf{P} = \frac{2\pi}{L}(0, 0, 1)^T, \quad A_2 \text{ of } C_{4v} : \quad \cot(\delta_0(k)) = \omega_{00} + 2\omega_{20}, \quad (7.52)$$

$$\mathbf{P} = \frac{2\pi}{L}(1, 1, 0)^T, \quad A_2 \text{ of } C_{2v} : \quad \cot(\delta_0(k)) = \omega_{00} - \omega_{20} - i\sqrt{6}\omega_{22}. \quad (7.53)$$

Since  $P$ -wave contributions in the moving frames might be substantial, only the finite volume energy levels obtained in the CMF are considered for the main analysis. Here we can reliably neglect contributions from higher excited waves. Using Eq. (7.51), I compute the phase shifts  $\delta_0(k_n)$  for the scattering momenta  $k_n$  that are associated to

the five energy levels in the CMF depicted in dark gray in Fig. 7.6. Taking into account the results obtained on both ensembles, I perform a  $\chi^2$ -minimizing fit of  $k \cot(\delta_0(k))$  using the quadratic ERE parametrization in Eq. (7.46) as the fit function. In Fig. 7.10, I depict  $k_n \cot(\delta_0(k_n))$  for the finite volume scattering momenta  $k_n$  as blue circles and squares as well as the quadratic ERE fit function as a black shaded band. Additionally, I also show  $-\sqrt{-k^2}$  as a brown curve. The final fit results for the  $S$ -wave scattering

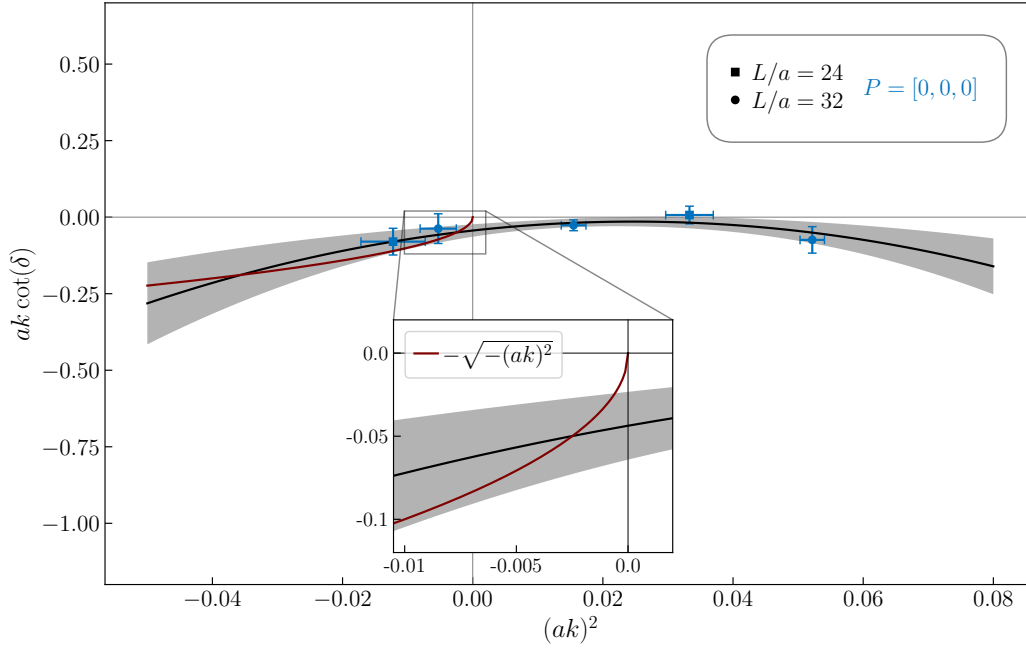


Figure 7.10.: Plot of  $ak \cot(\delta_0(k))$  as a function of the squared scattering momentum  $k^2$  in lattice units for  $B^*D$  scattering. The blue data points correspond to the phase shifts obtained for the finite volume energy levels on the ensembles a12m220S (squares) and a12m220 (circles) in the CMF. The black curve with shaded error band represents a quadratic ERE fit as defined in Eq. (7.46) to the data. I also depict  $-\sqrt{-(ak)^2}$  as a brown line.

length  $a_0$ , the  $S$ -wave effective range  $r_0$  and the shape parameter  $b_0$  are listed in Table 7.6. We observe that the quadratic ERE parametrization excellently describes the data, which is supported by the value of  $\chi^2/\text{d.o.f.} = 0.84$ .

In the next step, I use the final parametrization of  $k \cot(\delta_0(k))$  to search for poles of the  $T$ -matrix in the complex energy plane. I display  $|T^{(0)}(s)|$  as a function of the complex center-of-momentum energy  $\sqrt{s}$  in Fig. 7.11. We can observe a qualitatively similar picture as for the case of  $J = 0$  in Fig. 7.8. Again, I detect two poles at the real axis which are below the  $B^*D$  threshold. The lower one, however, does not fulfill the consistency condition given in Eq. (6) of Ref. [213] as it is clearly visible in Fig. 7.10 and corresponds thus to an unphysical pole. The second pole is again almost consistent with the threshold and can presumably be interpreted as the threshold state. Finally, we observe a pair of poles above the threshold, one with positive and one with negative imaginary part. I identify the pole with negative imaginary part, which is located on

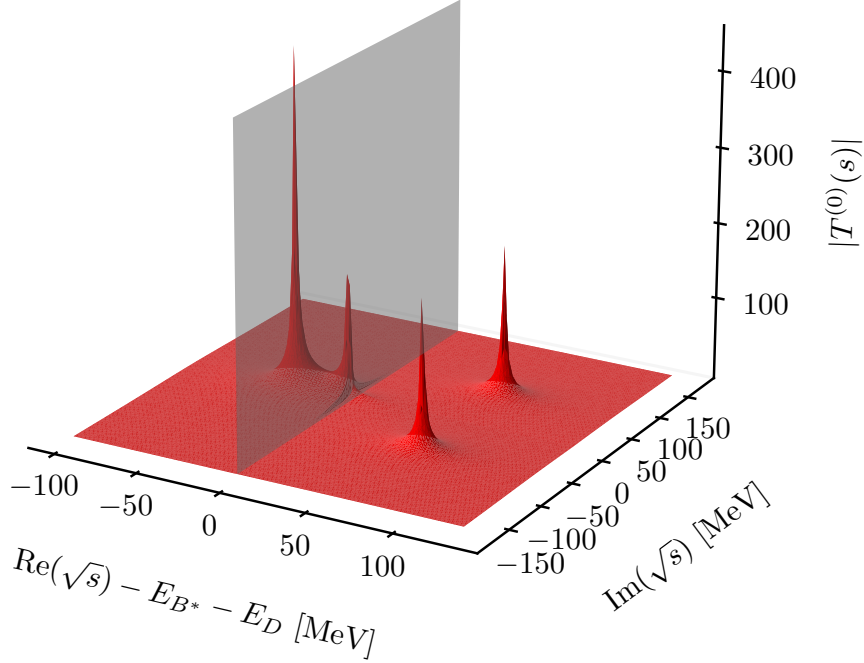


Figure 7.11.:  $S$ -wave scattering amplitude  $|T^{(0)}(s)|$  for  $B^*D$  scattering in the plane of complex energies. The  $BD$  threshold is depicted by the gray plane. The deeper pole below the threshold is unphysical as discussed in the text, while the other pole corresponds probably to the threshold scattering state. Above the threshold, a resonance pole appears off the real axis in the second Riemann sheet, while a shoulder is found in the first Riemann sheet at positive imaginary energy.

the second Riemann sheet, as a resonance pole, while the other pole corresponds to its shoulder in the first Riemann sheet. The associated resonance energy  $E_{\text{res}}$  and the decay width  $\Gamma$  are collected in Table 7.6. As already stated in Sec. 7.5.1, the pole position might be strongly varying with the actual choice of the phase shift parametrization [214]. In order to study possible systematic uncertainties originating from the parametrization, it is essential to investigate also other fit functions than the quadratic ERE parametrization in future work.

Ensemble	$1/a_0$ [ $\text{fm}^{-1}$ ]	$r_0$ [fm]	$b_0$ [ $\text{fm}^3$ ]	$E_{\text{res}}$ [MeV]	$\Gamma$ [MeV]
a12m220co	-0.37(17)	0.56(30)	-0.081(41)	67(24)	131(32)

Table 7.6.: Fit results for the inverse scattering length  $1/a_0$ , the effective range  $r_0$  and the shape parameter  $b_0$  of the quadratic ERE parametrization in Eq. (7.46) based on the CMF finite volume energy levels for  $B^*D$  scattering. I also list the parameters for the potential tetraquark resonance corresponding to a pole of the associated scattering amplitude  $T$ .

Finally, I repeat the same analysis including the finite volume energy levels that have been obtained in the moving frames. In Fig. 7.12, I show the associated results for  $k_n \cot(\delta_0(k_n))$  as a function of the squared finite volume scattering momenta  $k_n^2$  as blue, green and red circles and squares. Additionally, I depict the fit of these data points using a quadratic ERE parametrization as a black line with shaded error band and list the fit results in Table 7.7. There, I also present the resonance parameters corresponding to the pole of the associated scattering amplitude in the second Riemann sheet of the complex plane. Even though the fit parameters as well as the resonance energy and decay width agree fairly well with the results obtained in Table 7.6, we see that the final fit in Fig. 7.12 does not describe the data very well, corresponding also to a rather bad value of  $\chi^2/\text{d.o.f.} = 3.65$ . However, this is not completely surprising, as we know that additional  $D$ -wave contributions appear for  $J^P = 1^+$ . In contrast to the CMF, the associated energy levels could not be clearly identified and thus are still present in the energy spectrum. Having a closer look at Fig. 7.12, it is conspicuous that for each ensemble and moving frame exactly one data point lies below the fit function. Interestingly, we recognize that these data points correspond to the third energy levels in the case of MF1 and to the fourth energy levels in the case of MF2. Excluding these energy levels from the fit would result in a significantly improved fit quality

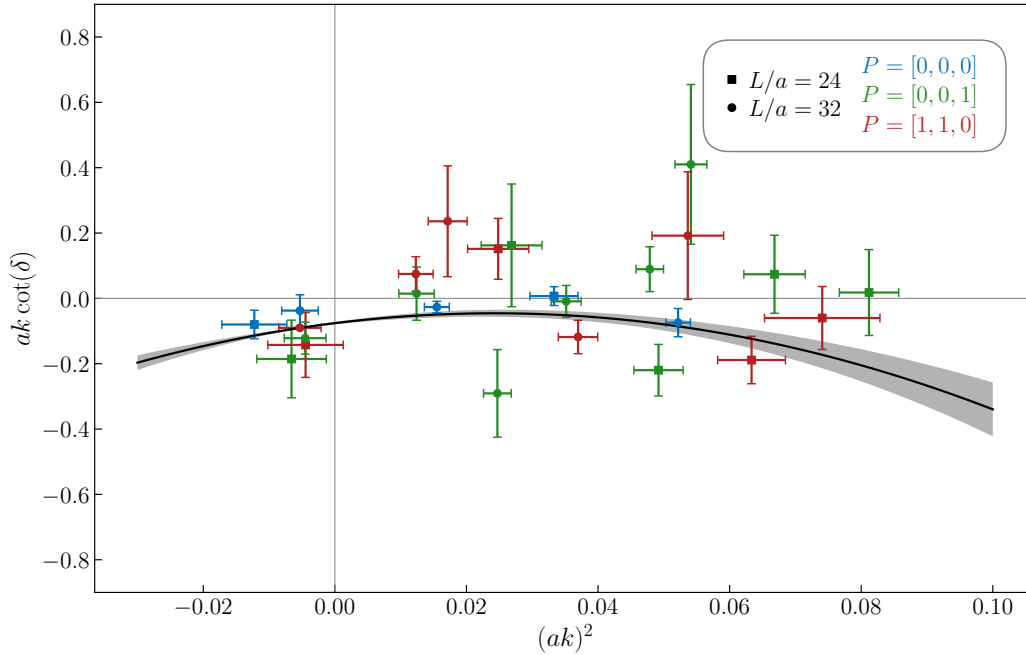


Figure 7.12.: Plot of  $ak \cot(\delta_0(k))$  as a function of the squared scattering momentum  $k^2$  in lattice units for  $B^*D$  scattering. The blue, green and red data points correspond to the phase shifts obtained for the finite volume energy levels on the ensembles a12m220S (squares) and a12m220 (circles) in the CMF (blue), the MF1 (green) and the MF2 (red). The black curve with shaded error band represents a quadratic ERE fit as defined in Eq. (7.46) to the data.

Ensemble	$1/a_0$ [fm $^{-1}$ ]	$r_0$ [fm]	$b_0$ [fm $^3$ ]	$E_{\text{res}}$ [MeV]	$\Gamma$ [MeV]
a12m220co	-0.63(3)	0.59(12)	-0.087(20)	62(12)	133(14)

Table 7.7.: Fit results for the inverse scattering length  $1/a_0$ , the effective range  $r_0$  and the shape parameter  $b_0$  of the quadratic ERE parametrization in Eq. (7.46) based on the finite volume energy levels from the CMF and moving frames for  $B^*D$  scattering. I also list the parameters for the potential tetraquark resonance corresponding to a pole of the associated scattering amplitude  $T$ .

( $\chi^2/\text{d.o.f.} = 1.45$ ). According to Fig. 7.6, however, there is no substantial reason to exclude these data points, i.e., they do not seem to be associated to a degenerate non-interacting energy level. Thus I refrain from continuing an analysis excluding those energy levels. Nevertheless, we can conclude that still more work needs to be done to consider also moving frames in the analysis of  $B^*D$  scattering. Especially a rigorous treatment of  $P$ - and  $D$ -wave contributions is essential to reliably include the energy levels obtained in the  $A_2$  irreps of  $C_{4v}$  and  $C_{2v}$  in the parametrization of the phase shift.

Relying on the poles detected in the CMF, I found evidence for a broad  $\bar{b}\bar{c}ud$  resonance in the  $I(J^P) = 0(1^+)$  channel with a resonance energy of around 70 MeV above the  $B^*D$  threshold and a width of approximately 130 MeV. Note that this potential tetraquark state is located well below the  $BD^*$  threshold so I assume that contributions of the second scattering channel can be indeed omitted.

At the end of this section, I briefly discuss possible effects of the left-hand cut. As in the previous section, the closest branch point appears due to one-pion exchange. Considering Eq. (4.97) with  $m_\pi \simeq 220$  MeV and  $\Delta m = m_{B^*} - m_D \simeq 3454$  MeV, we find the left-hand cut branch point at

$$(k_{\text{lhc}}^{1\pi})^2 \approx \frac{1}{4}(\Delta m^2 - m_\pi^2) \approx (1725 \text{ MeV})^2. \quad (7.54)$$

Note that the resonance pole is located at  $k_{\text{res}} \sim (475 - 200i)$  MeV. Consequently, the left-hand cut branch point associated to one-pion exchange does not affect the  $B^*D$  scattering, and the quadratic ERE can be applied without concerns regarding its range of convergence.

# 8

---

## INVESTIGATION OF THE $\bar{b}\bar{b}ud$ RESONANCE CANDIDATE WITH $I(J^P) = 0(1^-)$ IN $BB$ SCATTERING

---

In this chapter, I will study the  $\bar{b}\bar{b}ud$  four-quark system with quantum numbers  $I(J^P) = 0(1^-)$  which is a potential candidate for a tetraquark resonance in  $P$ -wave  $BB$  scattering. In a previous work, which relies on lattice QCD potentials and the Born-Oppenheimer approximation, the existence of such a tetraquark resonance has been predicted with a resonance energy of  $E_{\text{res}} \approx 17 \text{ MeV}$  and a decay width of  $\Gamma \approx 100 \text{ MeV}$  [33]. However, a refined Born-Oppenheimer investigation based on the same approach but including heavy quark spin effects did not find any indication for a tetraquark resonance in this channel [34]. These results naturally rely on certain approximations like the assumption of static heavy  $b$  quarks and cannot compete with full lattice QCD results. So far, however, there exists no full lattice QCD study of the  $\bar{b}\bar{b}ud$  four-quark system in the  $I(J^P) = 0(1^-)$  channel. A rigorous investigation is quite challenging, as a large number of  $BB$  scattering states must be resolved, while the energy spectrum is quite dense and the second scattering channel  $BB^*$  is separated by only 45 MeV from the  $BB$  threshold. Therefore, I will first discuss the feasibility of such a lattice study and then illustrate an early stage lattice QCD calculation searching for a possibly existing  $\bar{b}\bar{b}ud$  resonance with  $I(J^P) = 0(1^-)$  in  $P$ -wave  $BB$  scattering.

In Sec. 8.1, I begin with a preparatory investigation based on the Born-Oppenheimer approximation. Using phase shifts that have been computed in this setup, I mimic the input from a lattice QCD calculation and check if these data allow a reliable parametrization of the scattering amplitude. In the following sections, I present an exploratory lattice study of  $BB$  scattering, starting with a short introduction of the lattice setup in Sec. 8.2. The interpolating operators that are applied to compute the two-point correlation functions are discussed in Sec. 8.3, while I present the finite volume energy spectrum in Sec. 8.4. Finally, I discuss the strategy to perform a scattering analysis in Sec. 8.5.



## 8.1 Preparatory Investigation of $BB$ Scattering Based on the Born-Oppenheimer Approach

Simple  $P$ -wave resonances like the  $\rho$  meson are characterized by a phase shift  $\delta_1(s)$  which exhibits a sharp rise from  $\approx 0$  to  $\approx \pi$  in the energy region around the resonance mass (e.g., see Refs. [167, 173, 215, 216] for phase shifts of the  $\rho$  meson). Such a pronounced behavior makes it easy to identify a resonance and facilitates the parametrization of the phase shift in lattice calculations. This phase shift parametrization allows then to determine the pole of the scattering amplitude in the second Riemann sheet, while the real and imaginary part of the pole position correspond to the energy and decay width of the resonance.

In the Born-Oppenheimer investigation of the  $\bar{b}b\bar{u}d$  resonance with  $I(J^P) = 0(1^-)$  carried out in Ref. [33], we have not observed such a sharp rise of the phase shift to  $\approx \pi$  but only a gradual increase to  $\approx \pi/4$ . This complicates the determination of the resonance parameters based on the real-valued phase shift. However, in the Born-Oppenheimer approach we are not restricted to real and discrete energies. Hence, in Ref. [33] the scattering amplitude  $T^{(1)}(s)$ , given by Eq. (3.36), has been computed directly for complex energies  $\sqrt{s}$ , which made it easy to identify the resonance pole. If we now want to carry out a full QCD calculation for the  $\bar{b}b\bar{u}d$  system, two questions will arise. First, is it feasible to parametrize the phase shift appropriately relying only on the finite number of discrete real energy levels from a lattice QCD calculation? And second, is it possible to correctly determine the pole of the scattering amplitude based on this phase shift showing no sharp rise?

In this section, I will use phase shifts  $\delta_1(s)$  that are computed for a finite number of real energies  $E$  via a Born-Oppenheimer calculation using the same setup as described in Ref. [33]. These energies and phase shifts mimic the results which could have been obtained from a lattice QCD calculation by computing the finite volume energy levels and extracting the associated phase shifts using Lüscher's method (see Chapter 3). Using these data, I will perform a preparatory study to examine if the available phase shifts are sufficient to parametrize the scattering amplitude. Additionally, I will check if the analytic continuation of this scattering amplitude to the complex energy plane yields the same  $T$ -matrix pole position as found in Ref. [33], where the  $T$ -matrix has been directly computed as a function of the complex energy.

### 8.1.1 Parametrization of the Scattering Phase Shift

In order to extract an analytic expression for the scattering amplitude, we require a reasonable parametrization that appropriately describes the phase shift  $\delta_1(s)$  in dependence of the center-of-momentum energy  $\sqrt{s}$ . As discussed in Sec. 4.6.2.1, the Breit-Wigner parametrization given in Eq. (4.90) is well-suited to describe  $P$ -wave scattering. Note that the Breit-Wigner function corresponds to a parametrization of  $k^3 \cot(\delta_1(k))/\sqrt{s}$  that is linear in  $s$ ,

$$\frac{k^3}{\sqrt{s}} \cot(\delta_1(s)) = \frac{6\pi}{g^2}(m_R^2 - s) \equiv a - bs. \quad (8.1)$$



## 8.1. Preparatory Investigation of $BB$ Scattering Based on Born-Oppenheimer Setup

Here, the scattering momentum  $k$  is again related to the center-of-momentum energy  $\sqrt{s}$  according to Eq. (3.15), and the free parameters of the Breit-Wigner function are the resonance mass  $m_R$  and the coupling  $g$ . A second parametrization that is suitable to describe resonances is quadratic in the squared center-of-momentum energy  $s$  and is consequently given by

$$\frac{k^3}{\sqrt{s}} \cot(\delta_1(s)) = a + bs + cs^2. \quad (8.2)$$

I will consider both parametrizations to describe the energy dependence of the phase shift in the following paragraph.

### 8.1.2 T-Matrix Pole Based on Born-Oppenheimer Data

The Born-Oppenheimer approximation allows us to compute the phase shift  $\delta_1(s)$  for arbitrary energies  $E$ . The resulting  $P$ -wave phase shift for  $BB$  scattering that has been computed in a Born-Oppenheimer setup is depicted in Fig. 8.1 as a blue solid line. Here, the dashed vertical line represents the  $BB^*$  threshold while the  $BB$  threshold is located at  $\Delta E = 0$ . I select now 10 energies which are arbitrarily distributed between the  $BB$  threshold and the  $BB^*$  threshold. These energies and the associated phase shifts represent the input data for my parametrization of the phase shift and consequently mimic the results from a lattice QCD calculation. In Fig. 8.1, I indicate these data points  $(\Delta E_n, \delta_1(s_n))$  by red dots. Note that I only consider the energy region below the  $BB^*$  threshold, since only energy levels in this region can be used for a single channel scattering analysis using Lüscher's method. If you would like to take also higher energies into account, a coupled channel analysis would be required.

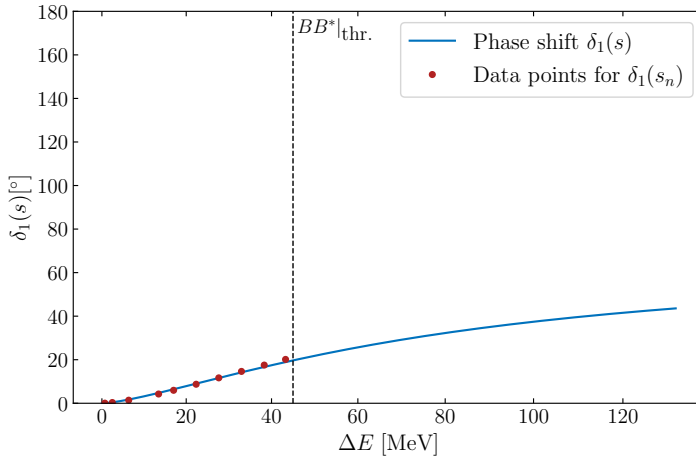


Figure 8.1.:  $P$ -wave  $BB$  scattering phase shift  $\delta_1(s)$  obtained from a Born-Oppenheimer calculation as done in Ref. [33]. The red points indicate the selected data points. Energies are given relative to the  $BB$  threshold, i.e.,  $\Delta E = \sqrt{s} - 2m_B$ .

In the next step, I parametrize the phase shift by fitting a Breit-Wigner function according to Eq. (8.1) as well as a quadratic function as given in Eq. (8.2) to the 10 data points  $(\Delta E_n, \delta_1(s_n))$ . In Fig. 8.2, I show  $k_n^3 \cot(\delta_1(s_n))/\sqrt{s_n}$  for the discrete energy levels  $\Delta E_n$  obtained from the Born-Oppenheimer calculation as blue points together with the final fit results as black shaded bands. In the left plot, the Breit-Wigner fit is presented, and in the right plot I depict the resulting quadratic parametrization. Note that I have introduced a small arbitrarily chosen statistical uncertainty for all values of  $k_n^3 \cot(\delta_1(s_n))/\sqrt{s_n}$  to make the Born-Oppenheimer data more realistic with regard to lattice QCD results. This uncertainty is set to  $200 \text{ MeV}^2$  for all data points, which corresponds to a relative error of  $\sim 1\%$ .

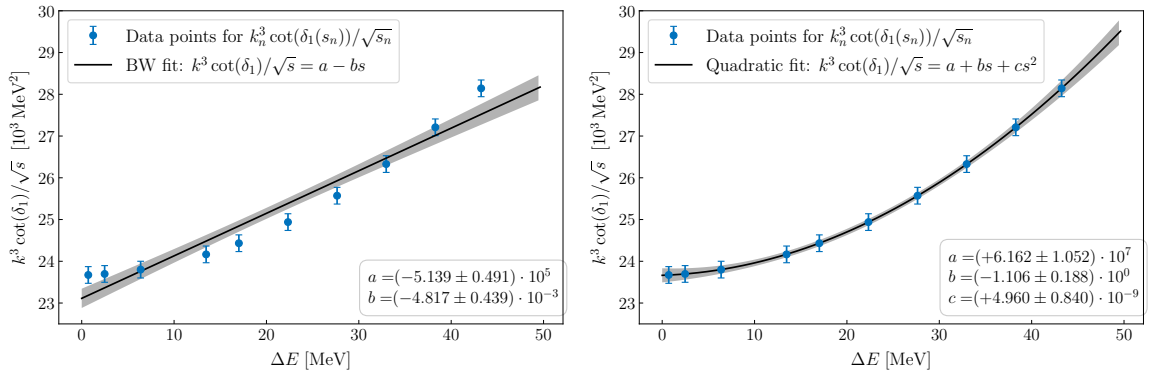


Figure 8.2.: Plot of  $k^3 \cot(\delta_1(s))/\sqrt{s}$  as a function of the energy difference  $\Delta E = \sqrt{s} - 2m_B$  for  $BB$  scattering. The blue data points correspond to the phase shifts obtained by a Born-Oppenheimer computation. The black curve with shaded error band represents a Breit-Wigner fit according to Eq. (8.1) (left) and a quadratic fit according to Eq. (8.2) (right).

Obviously, the quadratic function describes the data almost perfectly, which is reflected by a value of  $\chi^2/\text{d.o.f.} = 0.00$ . In contrast, the Breit-Wigner parametrization matches the data rather badly, corresponding to  $\chi^2/\text{d.o.f.} = 4.36$ . However, this is not surprising as the Breit-Wigner function characterizes a narrow resonance with a sharp rising phase shift. As visible in Fig. 8.1, this is not the case for the  $\bar{b}b\bar{u}d$  resonance in the  $I(J^P) = 0(1^-)$  channel, and thus an additional term which is quadratic in  $s$  is required to adequately render the data.

In the final step, I utilize both parametrizations to determine the pole of the scattering amplitude in the complex energy plane. Given knowledge of the pole position  $\sqrt{s_{\text{Pole}}}$ , the resonance energy is identified as  $E_{\text{res}} = \text{Re}(\sqrt{s_{\text{Pole}}}) - 2m_B$ , and the decay width is given by  $\Gamma = -2\text{Im}(\sqrt{s_{\text{Pole}}})$ . The results are listed for both parametrizations in Table 8.1 together with the resonance parameters that have been obtained in Ref. [33] by computing directly the  $T$ -matrix pole for complex energies. Note that the statistical uncertainties are determined on the basis of the arbitrarily chosen errors of  $k_n^3 \cot(\delta_1(s_n))/\sqrt{s_n}$ , and therefore they should only be considered as a rough estimate of the order of magnitude.

With regard to Table 8.1, we observe excellent agreement of the resonance parameters

	Born-Oppenheimer result from Ref. [33]	Breit-Wigner fit	Quadratic fit
$E_{\text{res}}$ [MeV]	$17_{-4}^{+4}$	26(1)	19(1)
$\Gamma$ [MeV]	$112_{-103}^{+90}$	155(2)	118(1)

Table 8.1.: Resonance energy  $E_{\text{res}}$  and decay width  $\Gamma$  extracted from the pole of the scattering amplitude  $T$  obtained in the Born-Oppenheimer calculation in Ref. [33] or computed via a Breit-Wigner or a quadratic parametrization of  $k^3 \cot(\delta_1)/\sqrt{s}$ .

determined via the quadratic parametrization of  $k^3 \cot(\delta_1)/\sqrt{s}$  with those obtained directly from the Born-Oppenheimer computation. Moreover, also the parametrization based on the Breit-Wigner fit, which describes the data only in a mediocre way, yields a  $T$ -matrix pole which is comparable to the Born-Oppenheimer result. Consequently, it should be feasible to successfully parametrize the phase shift based on precisely computed finite volume energy levels, obtained in a full lattice QCD calculation, and determine afterwards the pole of the scattering amplitude.

In practice, however, this is still a challenging task, as a large number of finite volume energy levels need to be computed extremely precisely. Since the spectrum of  $BB$  scattering states is quite dense, already small statistical fluctuations of the energies will lead to rather strongly fluctuating values of  $k_n^3 \cot(\delta_1(s_n))/\sqrt{s_n}$ . Thus, the statistical uncertainties for  $k_n^3 \cot(\delta_1(s_n))/\sqrt{s_n}$  are expected to be larger than those shown in Fig. 8.2. Another difficulty is the rather small energy region that can be considered for single channel scattering, which severely restricts the number of accessible energy levels. Nevertheless, I will focus on an exploratory lattice investigation of  $BB$  scattering in the following paragraphs.

## 8.2 Lattice Setup

For the lattice calculation that will be carried out in the subsequent sections, I will use the same setup as discussed in Sec. 6.1, i.e., I use the HISQ-MILC gauge link configurations with a one-loop Symanzik improved Lüscher-Weisz gauge action [186]. As in Chapter 7, I consider only the two ensembles a12m220S and a12m220, which have similar pion mass ( $m_\pi \approx 220$  MeV) and lattice spacing ( $a \approx 0.12$  fm) and differ only in their spatial lattice volume. More details about the ensembles can be found in Table 6.1.

For the light quarks, I use the Wilson-clover action as discussed in Sec. 6.1.2 with the bare quark mass and the clover coefficient given in Table 6.2. The bottom quarks are treated in the framework of NRQCD, and the actual choice of the matching parameters is the same as discussed in Sec. 6.1.3.

### 8.3 Interpolating Operators for the $\bar{b}\bar{b}ud$ Four-Quark System with $I(J^P) = 0(1^-)$

For this exploratory study of the  $\bar{b}\bar{b}ud$  system with  $I(J^P) = 0(1^-)$ , I consider only scattering interpolating operators and do not take local operators into account. A similar approach has been successfully applied in Ref. [47] for  $S$ -wave  $DD^*$  scattering. The scattering operators that are utilized in this chapter resemble  $BB$  scattering states with orbital angular momentum  $l = 1$  and different meson momenta  $\mathbf{p}_i = 2\pi\mathbf{q}_i/L$ , while the maximum momentum is governed by  $\mathbf{q}_i^2 \leq 3$ . As in the previous chapter, I consider not only the center-of-momentum frame but also two moving frames with  $\mathbf{P}/(2\pi/L) = (0, 0, 1)^T$  (MF1) and  $\mathbf{P}/(2\pi/L) = (1, 1, 0)^T$  (MF2). Consequently, I construct a basis of appropriate scattering interpolating operators for each frame, while each operator is designed such that it transforms according to the irrep  $\Lambda$  of the relevant symmetry group containing the quantum numbers  $J^P = 1^-$ . In the case of the CMF, the relevant symmetry group is still  $O_h$ , and the quantum numbers  $J^P = 1^-$  are subduced to the  $T_1^-$  irrep. For the moving frames, the symmetry groups differ from those that have been used in Chapter 7, since we study now the scattering process of two mesons with equal masses. The relevant symmetry groups are hence given by  $D_{4h}$  for  $\mathbf{P}/(2\pi/L) = (0, 0, 1)^T$  and  $D_{2h}$  for  $\mathbf{P}/(2\pi/L) = (1, 1, 0)^T$  (see Sec. 3.2). The associated irreps that contain the quantum numbers  $J^P = 1^-$  are listed in Table 8.2 together with the polynomials that transform according to these irreps. For the subsequent calculations, I decide to consider the  $A_2^-$  irrep of group  $D_{4h}$  for MF1 and the irrep  $B_3^-$  of group  $D_{2h}$  for MF2.

In order to construct the scattering operators, I use (in analogy to Sec. 7.2.2) the notation

$$B^+(\mathbf{q}_1) = \frac{1}{\sqrt{V_S}} \sum_{\mathbf{x}} \bar{b}\gamma_5 u e^{i\mathbf{p}_1\mathbf{x}}, \quad B^0(\mathbf{q}_2) = \frac{1}{\sqrt{V_S}} \sum_{\mathbf{x}} \bar{b}\gamma_5 d e^{i\mathbf{p}_2\mathbf{x}}, \quad (8.3)$$

$\mathbf{d}$	Symmetry group	$J^P = 1^-$	
		Irreps	Polynomial
$(0, 0, 0)^T$	$O_h$	$T_1^-$	$(x, y, z)$
$(0, 0, 1)^T$	$D_{4h}$	$A_2^-$	$z$
		$E^-$	$(x, y)$
$(1, 1, 0)^T$	$D_{2h}$	$B_1^-$	$\tilde{x}$
		$B_2^-$	$\tilde{y}$
		$B_3^-$	$z$

Table 8.2.: Irreducible representations (irreps) of the symmetry groups  $O_h$ ,  $D_{4h}$  and  $D_{2h}$  that contain the quantum numbers  $J^P = 1^-$ . Additionally, I also show polynomials that transform according to the given irrep. For  $D_{2h}$ , I denote the direction parallel to the boost by  $\tilde{x} \equiv x + y$  and the perpendicular direction by  $\tilde{y} \equiv x - y$ .

where  $\mathbf{p}_1 = 2\pi\mathbf{q}_1/L$  and  $\mathbf{p}_2 = 2\pi\mathbf{q}_2/L$  are the individual meson momenta. A general  $BB$  scattering operator is then given by

$$\mathcal{O}_{BB \text{ scatt}}(\mathbf{q}_1, \mathbf{q}_2) = B^+(\mathbf{q}_1) B^0(\mathbf{q}_2) - (d \leftrightarrow u). \quad (8.4)$$

The final scattering operators for a particular irrep  $\Lambda$  are constructed by combining several terms of the general expression in Eq. (8.4) with distinct meson momenta such that the resulting operators have the desired transformation behavior. For the center-of-momentum frame, where the individual meson momenta obey  $\mathbf{p}_1 = -\mathbf{p}_2$ , I use three different operators with  $\mathbf{q}_i^2 = 1, 2, 3$ , given by

$$\mathcal{O}_1^{T_1^- (0)} = B^+(\mathbf{e}_z) B^0(-\mathbf{e}_z) - B^+(-\mathbf{e}_z) B^0(\mathbf{e}_z) - (d \leftrightarrow u), \quad (8.5)$$

$$\mathcal{O}_2^{T_1^- (0)} = \sum_{\mathbf{q}=\pm\mathbf{e}_{i=x,y}} B^+(\mathbf{e}_z + \mathbf{q}) B^0(-\mathbf{e}_z - \mathbf{q}) - B^+(-\mathbf{e}_z + \mathbf{q}) B^0(\mathbf{e}_z - \mathbf{q}) - (d \leftrightarrow u), \quad (8.6)$$

$$\mathcal{O}_3^{T_1^- (0)} = \sum_{\mathbf{q}=\pm\mathbf{e}_x \pm \mathbf{e}_y} B^+(\mathbf{e}_z + \mathbf{q}) B^0(-\mathbf{e}_z - \mathbf{q}) - B^+(-\mathbf{e}_z + \mathbf{q}) B^0(\mathbf{e}_z - \mathbf{q}) - (d \leftrightarrow u). \quad (8.7)$$

Note that no operator with  $\mathbf{q}_i^2 = 0$  exists for the irrep  $T_1^-$ .

For the first moving frame with  $\mathbf{P}/(2\pi/L) = (0, 0, 1)^T$ , the three scattering operators that are utilized in this chapter are

$$\mathcal{O}_1^{A_2^- (1)} = B^+(\mathbf{e}_z) B^0(0) - B^+(0) B^0(\mathbf{e}_z) - (d \leftrightarrow u), \quad (8.8)$$

$$\mathcal{O}_2^{A_2^- (1)} = \sum_{\mathbf{q}=\pm\mathbf{e}_{i=x,y}} B^+(\mathbf{e}_z + \mathbf{q}) B^0(-\mathbf{q}) - B^+(\mathbf{q}) B^0(\mathbf{e}_z - \mathbf{q}) - (d \leftrightarrow u), \quad (8.9)$$

$$\mathcal{O}_3^{A_2^- (1)} = \sum_{\mathbf{q}=\pm\mathbf{e}_x \pm \mathbf{e}_y} B^+(\mathbf{e}_z + \mathbf{q}) B^0(-\mathbf{q}) - B^+(\mathbf{q}) B^0(\mathbf{e}_z - \mathbf{q}) - (d \leftrightarrow u). \quad (8.10)$$

As already discussed, these operators are constructed such that they transform according to the  $A_2^-$  irrep of group  $D_{4h}$ .

Finally, I use two scattering operators for the second moving frame with  $\mathbf{P}/(2\pi/L) = (1, 1, 0)^T$ . These operators are constructed in the  $B_3^-$  irrep of  $D_{2h}$  and are given by

$$\mathcal{O}_1^{B_3^- (2)} = B^+(\mathbf{e}_x + \mathbf{e}_y) B^0(0) - B^+(0) B^0(\mathbf{e}_x + \mathbf{e}_y) - (d \leftrightarrow u), \quad (8.11)$$

$$\mathcal{O}_2^{B_3^- (2)} = \sum_{\mathbf{q}=\pm\mathbf{e}_z} B^+(\mathbf{e}_x + \mathbf{e}_y + \mathbf{q}) B^0(-\mathbf{q}) - B^+(\mathbf{q}) B^0(\mathbf{e}_x + \mathbf{e}_y - \mathbf{q}) - (d \leftrightarrow u). \quad (8.12)$$

Using these operators, the correlation matrix is determined independently for each

frame. The associated two-point correlation functions are computed using stochastic timeslice-to-all propagators with spin and color dilution and exploiting the one-end-trick. On each configuration, I use stochastic timeslice sources at 4 equally distributed random timeslices with 3 different random seeds for each timeslice.

All quark fields that appear in the operators in Eqs. (8.5) to (8.12) are Gaussian smeared to improve the overlap with the low-lying energy spectrum as discussed in Sec. 6.1.4. The smearing parameters that are used for the up, down and bottom quarks are the same as listed in Table 6.4. For the light quark smearing I use HYP and APE smeared gauge links as presented in Sec. 6.1.4, while the gauge links used in the smearing of the bottom quarks are unsmearred.

#### 8.4 Finite Volume Energy Levels for $\bar{b}bud$ with $I(J^P) = 0(1^-)$

The finite volume energy spectrum for the  $\bar{b}bud$  system with  $I(J^P) = 0(1^-)$  is determined following the same approach as discussed in Sec. 6.3. Using the scattering operators given in Eqs. (8.5) to (8.12), I compute the associated two-point correlation functions and determine the correlation matrices for all three frames. For the CMF, the correlation matrix has a size of  $3 \times 3$ , for the first moving frame with  $\mathbf{P}/(2\pi/L) = (0, 0, 1)^T$  a size of  $3 \times 3$  and for the second moving frame with  $\mathbf{P}/(2\pi/L) = (1, 1, 0)^T$  a size of  $2 \times 2$ . The finite volume energy levels are extracted by solving a GEVP and performing single-exponential fits to the obtained principal correlators  $\lambda_n(t, t_0)$  according to Eq. (4.46). As pointed out in Sec. 6.3, various temporal fit ranges are taken into account, and the final result is determined via a weighted average over all fit ranges using the FLAG method (see Appendix D). Additionally, statistical uncertainties are estimated by Jackknife resampling.

As in the previous chapters, the extracted energies do not correspond to the actual physical masses but are shifted due to the use of the NRQCD action (see Sec. 6.2). However, this shift cancels in energy differences with equal number of bottom quarks. Thus, I consider again only the energy differences to the  $BB$  threshold. The energies of the pseudoscalar and vector  $B$  mesons as well as their kinetic masses, which would be needed for a scattering analysis, have already been determined in Sec. 6.2. The actual values can be found in Tables 6.5 and 6.6.

The finite volume energy levels that have been computed on the ensembles a12m220S and a12m220 are shown in Fig. 8.3 as gray points for the CMF as well as for both moving frames. Above each plot I list the associated irrep and the total momentum of the frame in the short notation  $\mathbf{P} = 2\pi/L(d_1, d_2, d_3)^T = [d_1, d_2, d_3]$ . The energy differences  $\Delta E_{\text{cm},n}$  relative to the  $BB$  threshold are given in the center-of-momentum frame, which means that the energies that are computed in a moving frame are shifted back to the CMF according to Eq. (3.8). The solid blue lines in Fig. 8.3 indicate the relevant non-interacting  $BB$  energies according to

$$E_{BB}^{\text{ni}} = E_B(\mathbf{p}_1) + E_B(\mathbf{p}_2), \quad (8.13)$$

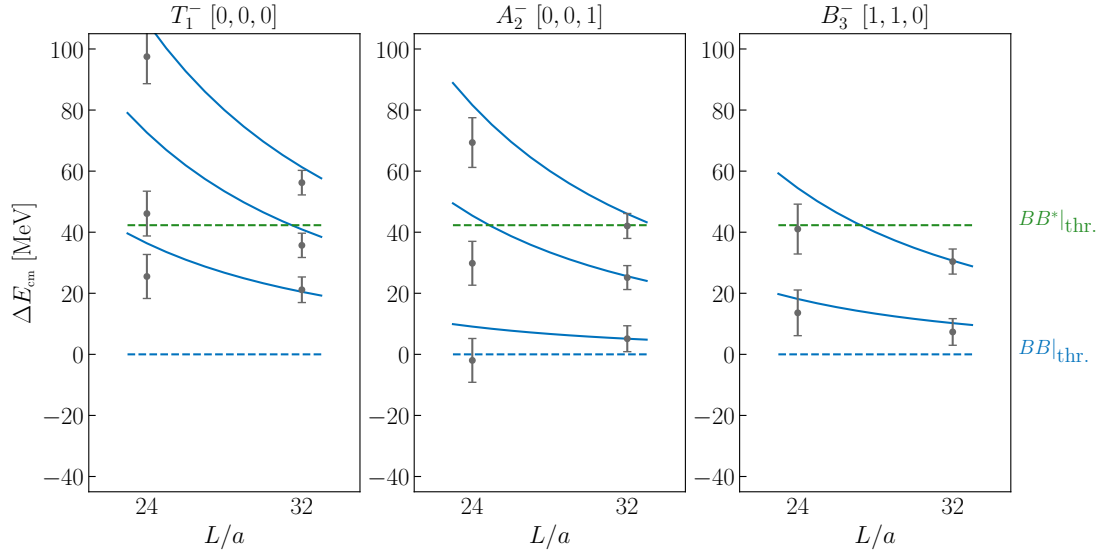


Figure 8.3.: Center-of-momentum energies  $\Delta E_{\text{cm},n}$  relative to the  $BB$  threshold for the  $\bar{b}\bar{b}ud$  four-quark system with  $I(J^P) = 0(1^-)$  in several finite volume irreps for the ensembles a12m220S ( $L/a = 24$ ) and a12m220 ( $L/a = 32$ ). Above each plot, I denote the irrep and the total momentum using the abbreviation  $\mathbf{P} = 2\pi/L (d_1, d_2, d_3)^T \equiv [d_1, d_2, d_3]$ . The solid blue lines represent the non-interaction  $BB$  energies, while the blue and green dashed lines correspond to the  $BB$  and  $BB^*$  threshold, respectively.

where  $E_B(\mathbf{p})$  is governed by Eq. (4.82). The blue and green horizontal dashed lines represent the  $BB$  and  $BB^*$  threshold, respectively. Note that only energy levels  $\Delta E_{n,\text{cm}}$  that are located well below the  $BB^*$  threshold are suited as input for a single channel scattering analysis. For energy levels above the  $BB^*$  threshold, couplings to this channel might be significant, and a coupled channel scattering analysis would be required to incorporate also these levels in the analysis.

We observe in Fig. 8.3 that for each ensemble and irrep only one or two energy levels are located below the  $BB^*$  threshold. This is a consequence of the rather small energy difference between the  $BB$  and  $BB^*$  thresholds. Consequently, the total number of energy levels that could be used in a single channel scattering analysis is quite small even if both ensembles and all three irreps are taken into account. Additionally, most of the energy levels below the  $BB^*$  threshold are consistent with the associated non-interacting energy levels. Only the lowest energy level obtained on the ensemble a12m220S seems to be slightly shifted with respect to the non-interacting  $BB$  spectrum. Therefore, I have not found a clear evidence for non-trivial interactions which would be represented by a considerably shifted energy spectrum. However, I cannot exclude with certainty the presence of such non-trivial interactions either, since there are too few levels per ensemble and irrep and too large statistical uncertainties. Consequently, it is unclear if energy shifts originate from non-trivial interactions or appear only due to statistical fluctuations. For this reason, I refrain from performing



a scattering analysis relying on the finite volume energies  $E_{n,\text{cm}}$  in Fig. 8.3. These results would not allow us to make reliable statements about the possible existence of a  $P$ -wave tetraquark resonance in  $BB$  scattering. Nevertheless, I will present the essential steps for a single channel scattering analysis in the following section.

### 8.5 Strategy for Performing a Scattering Analysis for the $\bar{b}bud$ channel with $I(J^P) = 0(1^-)$

Finite volume energy levels like those extracted in the previous section render information about the infinite volume scattering amplitude. Following the approach presented in Sec. 4.6.2.1, one can compute the phase shifts  $\delta_1(s_n)$  for each lattice energy level  $E_n$  and determine a reasonable parametrization for  $\cot(\delta_1)$ . As discussed in Sec. 4.6.2.1 and Sec. 8.1.1, the Breit-Wigner function according to Eq. (8.1) provides a suitable description of  $P$ -wave resonances and is therefore appropriate to parametrize  $k^3 \cot(\delta_1)/\sqrt{s}$  for the present system. Additionally, also a quadratic parametrization as given in Eq. (8.2) is a reasonable choice.

The phase shift  $\delta_1(s_n)$  for each energy level  $E_n$  is obtained from the quantization condition in Eq. (3.35) using the explicit form of the  $M$ -matrix given in Eqs. (3.42), (B.14) and (B.15) for the relevant symmetry group. Let us have a short look on the mixing of different quantum numbers for the irreps of interest. According to Table 4.2, the  $T_1^-$  irrep of  $O_h$  contains the quantum numbers  $J^P = 1^-, 3^-, 4^-, \dots$ , so additionally to the  $P$ -wave states only states with  $l \geq 3$  appear. The situation is similar for the irrep  $A_2^-$  of  $D_{4h}$  which also contains  $J^P = 1^-, 3^-, 4^-, \dots$  (see Table 4.4). For the last moving frame, the quantum numbers  $J^P = 1^-, 2^-, 3^-, \dots$  are subduced to the irrep  $B_3^-$  of  $D_{2h}$ . Note, however, that again no  $D$ -wave  $BB$  states can appear in this irrep since such a state would have the wrong parity. In particular, we find for all three frames no mixing of  $S$ - and  $P$ -waves. This is also reflected by the block-diagonal form of the  $M$ -matrices in Eqs. (3.42), (B.14) and (B.15). As contributions from higher partial waves are suppressed, I neglect all contributions with  $l \geq 2$ . For the center-of-momentum frame where the symmetry group is  $O_h$ , the quantization condition for the  $T_1^-$  irrep can be derived from Eq. (3.42) and is given by Eq. (3.44),

$$\mathbf{P} = \frac{2\pi}{L}(0, 0, 0)^T, \quad T_1^- \text{ of } O_h : \quad \cot(\delta_1(s)) = \omega_{00}, \quad (8.14)$$

where  $\omega_{lm}$  is defined in Eq. (3.29). For the moving frame with  $\mathbf{P}/(2\pi/L) = (0, 0, 1)^T$ , I consider the  $A_2^-$  irrep of group  $D_{4h}$  which transforms according to Table 8.2 like  $z$ . Relying on the  $M$ -matrix for the group  $D_{4h}$  in Eq. (B.14), the associated quantization condition is governed by

$$\mathbf{P} = \frac{2\pi}{L}(0, 0, 1)^T, \quad A_2^- \text{ of } D_{4h} : \quad \cot(\delta_1(s)) = \omega_{00} + 2\omega_{20}. \quad (8.15)$$

Finally, for the moving frame with  $\mathbf{P}/(2\pi/L) = (1, 1, 0)^T$ , the relevant symmetry group is  $D_{2h}$  with the reduced  $M$ -matrix given in Eq. (B.15). Here, I consider the



irrep  $B_3^-$  which transforms according to Table 8.2 like  $z$ . Consequently, it follows that the quantization condition is given by

$$\mathbf{P} = \frac{2\pi}{L}(1, 1, 0)^T, \quad B_3^- \text{ of } D_{2h} : \quad \cot(\delta_1(s)) = \omega_{00} + 2\omega_{20}. \quad (8.16)$$

Finally, if the phase shifts were computed, one would proceed in a similar manner to Sec. 7.5, and  $k^3 \cot(\delta_1)/\sqrt{s}$  would be parametrized using the Breit-Wigner or the quadratic function. Using this parametrization, one would search for poles of the scattering amplitude  $T^{(1)}$  given by Eq. (3.36) in the complex energy plane. As already stated at the end of Sec. 8.4, I refrain from performing a scattering analysis, as the finite volume energy levels are not sufficiently precise for such an analysis. Here, further work needs to be done to provide an energy spectrum that enables us to perform a rigorous scattering analysis and makes it possible to draw reliable conclusions about the potentially existing  $\bar{b}b\bar{u}d$  tetraquark resonance in the  $I(J^P) = 0(1^-)$  channel. Using the same gauge link configurations, a possible approach to improving the energy spectrum might be to include also local interpolating operators. Additionally, one could also think about performing a coupled channel scattering analysis with  $BB^*$  as the second scattering channel. This would enlarge the relevant energy region and increase the number of accessible energy levels significantly. Of course this would require further  $BB$  scattering operators with higher meson momenta and additionally  $BB^*$  scattering operators with back-to-back momenta.

Let me conclude with a short discussion of the left-hand cut for this system. The left-hand cut branch point for one-pion exchange is found according to Eq. (4.97) at

$$(k_{\text{lhc}}^{1\pi})^2 \approx \frac{1}{4}(\Delta m^2 - m_\pi^2) \approx -(110 \text{ MeV})^2, \quad (8.17)$$

where I use  $\Delta m = m_B - m_B = 0 \text{ MeV}$  and  $m_\pi \simeq 220 \text{ MeV}$ . Accordingly, the branch point is located in the complex energy plane on the real axis at about 3 MeV below the  $BB$  threshold. Hence, for a rigorous analysis of  $P$ -wave  $BB$  scattering also the effects of the left-hand cut originating from one-pion exchange must be taken into account.



# 9

---

## CONCLUSIONS

---

In this thesis, I investigated several four-quark systems  $\bar{Q}\bar{Q}'qq'$  with at least one heavy anti-bottom quark using lattice QCD. In particular, I searched for the existence of hadronically stable states in the  $\bar{b}\bar{b}ud$  system with  $I(J^P) = 0(1^+)$ , the  $\bar{b}\bar{b}us$  system with  $J^P = 1^+$  and the  $\bar{b}\bar{c}ud$  systems with  $I(J^P) = 0(0^+)$  and  $I(J^P) = 0(1^+)$ . For all systems, I performed lattice QCD calculations using two different lattice setups to compute the low-lying energy spectrum. Expanding on previous studies on heavy-light tetraquarks, where only local operators were considered [35, 36, 38–43], I additionally included scattering operators. In the first lattice setup, I employed scattering operators only at the sink, while in the second setup scattering operators were considered at the sink and the source. Moreover, using the latter setup, I searched for a  $P$ -wave resonance in  $BB$  scattering, corresponding to a  $\bar{b}\bar{b}ud$  tetraquark with  $I(J^P) = 0(1^-)$ . Throughout this work I treated the bottom quarks in the framework of NRQCD.

Since most tetraquarks are either resonances above or bound states close to the threshold of strong decay, finite volume effects usually play a crucial role. Therefore, one major objective of this work has been to perform a Lüscher analysis [22] for each four-quark system to study potential finite volume effects in the relevant meson-meson scattering processes. This allows me to determine the infinite volume binding energies for stable tetraquarks or even the mass and decay width of tetraquark resonances.

Before discussing the findings of this thesis in detail, let me start with a brief overview of the results obtained for the doubly-heavy tetraquark systems under investigation:

- For the  $\bar{b}\bar{b}ud$  four-quark system with  $I(J^P) = 0(1^+)$ , I found a deeply bound tetraquark state. The energy of the ground state, calculated in Chapter 6, agrees with the result found in a previous work of our collaboration in Refs. [37, 92], which was summarized in Chapter 5.
- Similar results were obtained for the  $\bar{b}\bar{b}us$  system with  $J^P = 1^+$  for which also a stable tetraquark was predicted, being slightly less bound than the  $\bar{b}\bar{b}ud$  tetraquark (see Chapters 5 and 6).
- For the  $\bar{b}\bar{c}ud$  four-quark systems with  $(J^P) = 0(0^+)$  and  $(J^P) = 0(1^+)$ , I did not find evidence for a deeply bound state (see Chapter 5), but a scattering analysis, carried out in Chapter 7, indicates the existence of a broad tetraquark resonance for both channels.

- In the case of the  $\bar{b}\bar{b}ud$  four-quark system with  $I(J^P) = 0(1^-)$ , neither could the existence of a narrow resonance been confirmed, nor could it be excluded with certainty (see Chapter 8).

The results on the  $\bar{b}\bar{b}ud$  four-quark system with  $I(J^P) = 0(1^+)$  and the  $\bar{b}\bar{b}us$  four-quark system with  $J^P = 1^+$  revealed that scattering operators are mandatory to reliably resolve the ground-state energy level and higher excitations. However, only if scattering operators were included at the sink and the source I was able to precisely extract the complete low-lying energy spectrum.

In the case of  $\bar{b}\bar{b}ud$ , the finite volume ground-state energy has been found in both studies well below the threshold of strong decay. Performing a Lüscher analysis afterwards for both setups, the infinite volume binding energies were determined. However, they have been found to be essentially identical to the finite volume ground-state energies, which might be an indication that couplings of the ground state to the  $BB^*$  threshold are weak and thus finite volume effects are small. After carrying out a chiral extrapolation in both studies and additionally considering the continuum limit in Chapter 6, the final binding energies were found to be  $-128(24)(10)$  MeV (see Chapter 5) and  $-101(11)(25)$  MeV (see Chapter 6). Obviously, both results are consistent within uncertainties and confirm the existence of a hadronically stable  $\bar{b}\bar{b}ud$  tetraquark.

In Fig. 9.1, I compare the  $\bar{b}\bar{b}ud$  binding energies presented in this thesis with the results previously obtained in other calculations. Further lattice QCD studies using NRQCD for the heavy  $\bar{b}$  quarks [35, 36, 38–40] are colored in blue, while results that are based on lattice QCD potentials and the Born-Oppenheimer approximation [28, 29, 32] are indicated in red. Finally, I also depict the results obtained from quark models, effective field theories or QCD sum rules [25, 27, 196, 198, 205–209, 212, 217–230] in green. We observe that the results of this work are consistent with most of the previous lattice QCD calculations which utilized only local operators. A potential source for the deviation from the results of Ref. [35] might be that they used ratios of correlation functions to determine the ground-state energy with the consequence that the plateau for the effective energies is approached from below. This method can be problematic as for a dense spectrum (like in the case of  $BB^*$ ) fake plateaus can appear for small temporal separations [231]. In Ref. [38], where also a significantly lower binding energy was found, the light quark mass was tuned differently for local meson-meson and diquark-antidiquark operators which could be the reason for the discrepancy with regard to our results.

The calculations based on static  $\bar{b}\bar{b}$  potentials yield significantly smaller binding energies compared to full lattice QCD computations. This might be caused by the approximations of the Born-Oppenheimer approach where, for instance, contributions of  $1/m_b$  to the potential were neglected. Finally, the non-lattice binding energies vary widely between  $\sim 20$  MeV to  $\sim 400$  MeV below the  $BB^*$  threshold, but all results agree qualitatively that a bound tetraquark state exists.

For the  $\bar{b}\bar{b}us$  system, I also found in both setups a finite volume ground-state energy below the threshold of strong decay. Studying finite volume effects in this channel is,

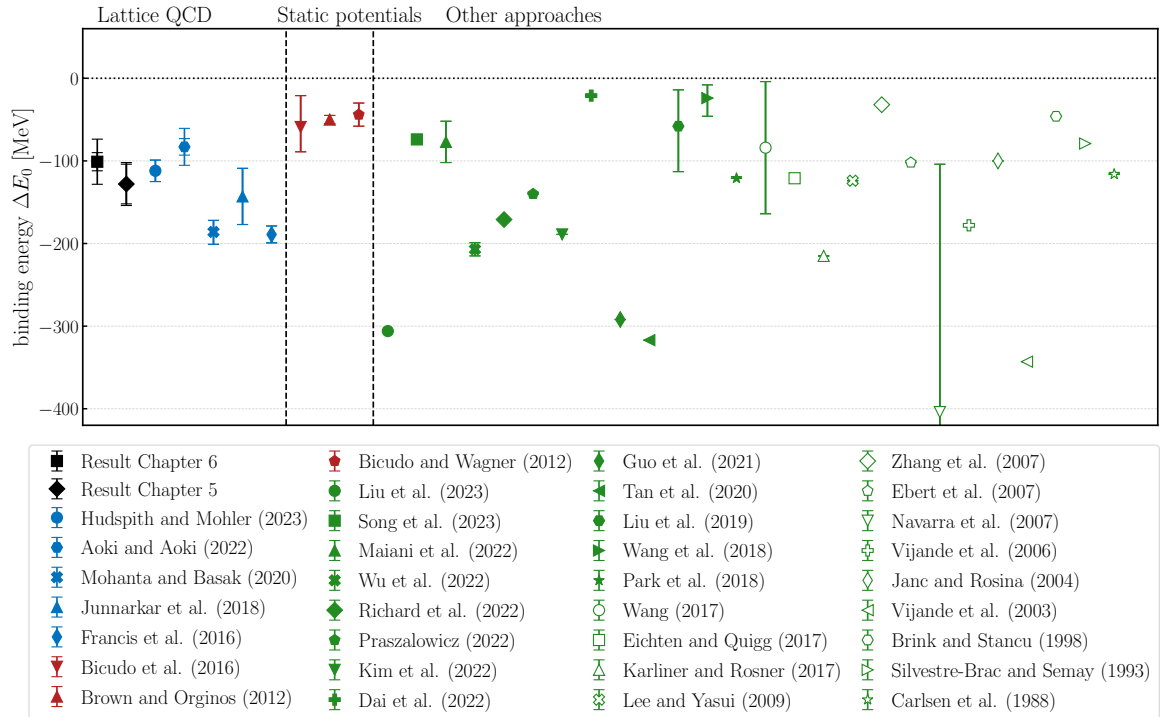


Figure 9.1.: Comparison of the results for the binding energies of the  $\bar{b}b\bar{d}$  tetraquark with  $I(J^P) = 0(1^+)$ . Black: results presented in this work, *Result Chapter 5* refers to our publication Ref. [37]; blue: previous lattice QCD calculations using NRQCD [35, 36, 38–40]; red: lattice QCD potentials and the Born-Oppenheimer approximation [28, 29, 32]; green: quark models, effective field theories or QCD sum rules [25, 27, 196, 198, 205–209, 212, 217–230].

however, more challenging and requires a coupled channel scattering analysis, as the two lowest meson-meson thresholds are barely separated. It turned out that this is only feasible if scattering operators are fully included. Otherwise excited states, which are crucial for a scattering analysis, cannot be sufficiently resolved. Accordingly, in Chapter 5, a scattering analysis was not possible. Therefore I relied exclusively on the finite volume ground-state energies and extrapolated them to the physical pion mass, yielding a binding energy of  $-86(22)(10)$  MeV. In Chapter 6, where the relevant low-lying energy spectrum could be resolved, I performed a coupled channel Lüscher analysis to calculate the infinite volume binding energies but found them to be essentially identical to the finite volume ground-state energies. Carrying out afterwards a chiral extrapolation and considering the continuum limit, the final binding energy of  $-28(5)(10)$  MeV was determined.

In Fig. 9.2, I depict both  $\bar{b}b\bar{u}s$  binding energies together with results from previous lattice QCD calculations [35, 36, 40] and non-lattice approaches like quark models, phenomenological considerations, or QCD sum rules [27, 196, 200, 205, 208–212, 217, 223, 224, 227, 228, 232–234]. While the binding energy obtained in Chapter 5, labeled with a black diamond, agrees well with the results of Refs. [35, 36], we observe that these

three energies deviate from the results obtained in Chapter 6 and Ref. [40]. Nevertheless, all lattice QCD results agree about the existence of a stable  $\bar{b}b\bar{u}s$  tetraquark with a binding energy of around  $\sim 30$  MeV to  $\sim 80$  MeV below the threshold of strong decay. This coincides with the vast majority of non-lattice calculations, predicting also a bound state, although the associated results for the binding energies vary again widely.

Even though this work provides a significant improvement compared to previous studies by including scattering operators, some open questions remain. The discrepancies of the binding energies for the  $\bar{b}b\bar{u}d$  and in particular the  $\bar{b}b\bar{u}s$  system found in my studies could not be fully resolved. They might be rooted in the different tuning of the matching coefficients in the NRQCD action. Therefore, it would be desirable to study the dependence of the binding energy on the matching coefficients in more detail. Furthermore, the presence of a left-hand cut branch point in the relevant energy region of both systems, which was omitted in my investigations, challenges the reliability of the scattering analysis. Possible approaches to deal with this issue might be to use a parametrization like the Padé approximation [175, 176, 194], which can be considered beyond the range of convergence, or to study the systems in a three-particle scattering

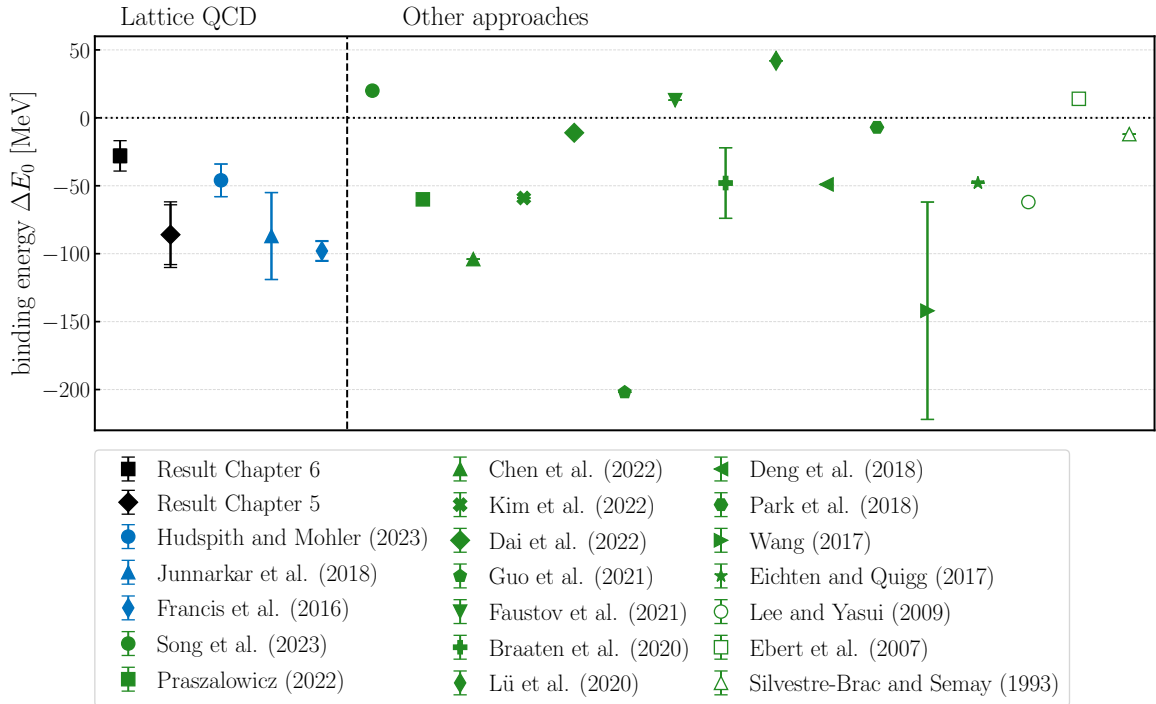


Figure 9.2.: Comparison of the results for the binding energies of the  $\bar{b}b\bar{u}s$  tetraquark with  $J^P = 1^+$ . Black: results obtained in this work, *Result Chapter 5* refers to our publication Ref. [24]; blue: previous lattice QCD calculations using NRQCD [35, 36, 40]; green: quark models, effective field theories or QCD sum rules [27, 196, 200, 205, 208–212, 217, 223, 224, 227, 228, 232–234].

---

process [235–237]. However, in order to rigorously implement the one-particle exchange, which gives rise to the left-hand cut branch point, new theoretical formalisms need to be developed [177, 178].

The  $\bar{b}\bar{c}ud$  systems with  $I(J^P) = 0(0^+)$  and  $I(J^P) = 0(1^+)$  were studied in Chapters 5 and 7. In Chapter 5, where I utilized local operators and scattering operators at the sink, I neither found evidence for a stable tetraquark, nor could I exclude the existence of a shallow bound state or a resonance. Thus, I investigated both  $\bar{b}\bar{c}ud$  channels in Chapter 7 considering  $BD$  and  $B^*D$  scattering, respectively. While similar local operators were utilized, the number of scattering operators was enlarged by including several  $BD$  or  $B^*D$  operators with non-zero momenta, which allows us to resolve a large spectrum of energy levels. To increase the number of finite volume energies even further, I also considered moving frames, but excluded them from the main analysis due to potential admixtures of higher partial waves. Even though the ground-state energy levels are located again in the vicinity of the threshold of strong decay, an additional energy level compared to the number of non-interacting two-meson energies was found in the finite volume  $\bar{b}\bar{c}ud$  energy spectra, indicating non-trivial interactions. Performing a single channel Lüscher analysis, I found for both systems a  $T$ -matrix pole in the second Riemann sheet, which indicates the existence of a broad  $\bar{b}\bar{c}ud$  tetraquark resonance.

The results of both studies are consistent, showing a ground-state energy level close to the threshold. This excludes the existence of a deeply bound state. Additionally, the results in Chapter 5 do not allow conclusions to be drawn about the existence of a shallow bound state or a resonance, since excited energy levels could not be resolved due to the lack of a suitable and fully included set of scattering operators. Thus, the observation of the potential resonance in Chapter 7 does not contradict the results of Chapter 5. Moreover, my findings also agree with the results of Ref. [42], where no evidence for a deeply bound four-quark state was found either. In contrast to that, in Ref. [43] a  $\bar{b}\bar{c}ud$  bound state with  $I(J^P) = 0(1^+)$  was predicted about 20 MeV to 40 MeV below the  $B^*D$  threshold. Note, however, that this computation was carried out at quite large pion masses of around 500 MeV and finite volume effects were not taken into account then. The potentially large impact of finite volume effects in the  $\bar{b}\bar{c}ud$  sector was experienced in Refs. [41, 42], where a  $\bar{b}\bar{c}ud$  bound state first had been predicted for a rather small spatial volume [41] but was revoked later when larger volumes were taken into account [42]. Note that also non-lattice approaches do not show a conclusive picture about the existence of a hadronically stable  $\bar{b}\bar{c}ud$  state, as some studies predict a bound state [196–207] while others rule it out [27, 208–212].

The observation of non-trivial interactions in Chapter 7, indicating the existence of a resonance, might help to clarify the still inconclusive picture for the  $\bar{b}\bar{c}ud$  systems: A ground-state energy level, found slightly below the threshold of strong decay, does not necessarily have to be a bound state, but can also be explained by a shifted energy spectrum, originating from non-trivial interactions and indicating the presence of a resonance. Consequently, for a reliable statement about the nature of the ground state,

it is crucial to rigorously study finite volume effects in the  $\bar{b}\bar{c}ud$  systems by performing a scattering analysis, as done in this work. This emphasizes also the importance of a well-suited operator basis that allows a precise determination of the low-lying finite volume energy spectrum.

For future investigations, it is advisable to focus on a more sophisticated scattering analysis. In particular, a rigorous consideration of moving frames is desirable, as this will provide additional finite volume energy levels for the parametrization of the scattering amplitude. However, this requires considering also relevant contributions of higher partial waves complicating the scattering formalism. In addition, further parametrizations of the scattering amplitude should be taken into account to investigate whether the resonance pole is independent of the actual parametrization. Moreover, neither have the results been extrapolated to the physical pion mass, nor have lattice discretization effects been studied. Even though I do not expect that the qualitative result, i.e., the detection of a resonance pole, will change drastically, the actual pole position might vary slightly due to the previously mentioned aspects.

Finally, in Chapter 8 I studied the  $\bar{b}\bar{b}ud$  four-quark system with  $I(J^P) = 0(1^-)$ , which is, according to Ref. [33], a potential candidate for a tetraquark resonance. In a preparatory investigation I considered a small number of discrete energy levels and associated phase shifts obtained from a Born-Oppenheimer calculation, which mimics the finite volume energy spectrum from a full lattice QCD computation. Based on these data, I concluded that in principle it should be possible to successfully parametrize the phase shift of the potentially existing  $P$ -wave  $\bar{b}\bar{b}ud$  resonance. In an early stage lattice QCD study of  $P$ -wave  $BB$  scattering, however, I have not found evidence for non-trivial interactions in this channel. This could be an indication that the resonance does not exist for physical bottom quark masses as already stated in Ref. [34]. Nevertheless, I could not exclude either with certainty the existence of a narrow resonance based on the lattice data. For a better understanding of this channel, further rigorous lattice QCD studies are needed. In particular, local operators should be considered to obtain a larger operator basis. Furthermore, it might be beneficial to study this system in coupled  $BB$  and  $BB^*$  scattering. This would enlarge the accessible energy region, so that the number of finite volume energy levels increases significantly. Moreover, also potential couplings to the  $BB^*$  channel, which have been neglected so far in the single channel scattering analysis, would be incorporated. Note that additionally the left-hand cut is relevant for this system. This makes a rigorous implementation of one-pion exchange indispensable for reliable statements about the existence or non-existence of a  $\bar{b}\bar{b}ud$  resonance with  $I(J^P) = 0(1^-)$ .

To summarize, I experienced that lattice QCD provides an excellent framework to study tetraquarks. Especially antiheavy-antiheavy four-quark systems in the bottom sector, which are promising candidates for strong-interaction stable states, are well accessible with current lattice QCD techniques. Hereby, Lüscher's method is of particular importance since it provides a matured tool that allows the examination of



---

finite volume effects appearing due to the finite spatial size of the lattice, and it even enables us to study resonances based on the discrete spectrum of finite volume energy states. Relying on these techniques, I have successfully predicted hadronically stable tetraquark states in the  $\bar{b}\bar{b}ud$  and  $\bar{b}\bar{b}us$  sector and pointed out the possible existence of broad tetraquark resonances for  $\bar{b}\bar{c}ud$  four-quark systems. These results may serve as valuable input for future experimental search for tetraquarks in the doubly-heavy sector. The encouraging observation of the doubly charmed tetraquark  $T_{cc}$  by the LHCb collaboration [20, 21] reveals the unabated experimental efforts to discover further exotic hadrons. Accordingly, theoretical predictions like those made in this thesis can help nascent experimental searches for tetraquark states in the bottom-bottom and bottom-charm sectors [238].



# Appendix A

---

## CONVENTIONS

---

- I use natural units, i.e.,  $\hbar = c = 1$ .
- Throughout this work I use bold italic symbols  $\mathbf{x} = (x_1, x_2, x_3)$  to express three-dimensional vectors. Four-dimensional space-time vectors are given by  $x = (\mathbf{x}, t)$ .
- I use Greek and Latin letters as indices, while Greek indices  $\mu, \nu, \dots$  run from  $0, \dots, 3$  and Latin indices  $i, j, \dots$  run from  $1, \dots, 3$ .
- Einsteins sum convention is applied, i.e., if an index appears twice, it is summed over all allowed values, unless otherwise stated.
- All lattice calculations are carried out in Euclidean space.

- The Euclidean gamma matrices that are used in this work are defined as

$$\gamma_0 = \begin{pmatrix} \sigma_0 & 0 \\ 0 & -\sigma_0 \end{pmatrix}, \quad \gamma_j = \begin{pmatrix} 0 & -i\sigma_j \\ i\sigma_j & 0 \end{pmatrix}, \quad \gamma_5 = \gamma_0\gamma_1\gamma_2\gamma_3 \begin{pmatrix} 0 & \sigma_0 \\ \sigma_0 & 0 \end{pmatrix}, \quad (\text{A.1})$$

where  $\sigma_j$  are the Pauli matrices and I defined  $\sigma_0 = \mathbb{1}_{2 \times 2}$  for convenience.

- For calculations in Minkowski space, I use the gamma matrices

$$\hat{\gamma}_0 = \begin{pmatrix} \sigma_0 & 0 \\ 0 & -\sigma_0 \end{pmatrix}, \quad \hat{\gamma}_j = \begin{pmatrix} 0 & \sigma_j \\ -\sigma_j & 0 \end{pmatrix}, \quad \hat{\gamma}_5 = i\hat{\gamma}_0\hat{\gamma}_1\hat{\gamma}_2\hat{\gamma}_3 \begin{pmatrix} 0 & \sigma_0 \\ \sigma_0 & 0 \end{pmatrix}, \quad (\text{A.2})$$

which are indicated by a hat to distinguish them from the Euclidean gamma matrices.

- In order to compute derivatives on the lattice, I use the following expressions:

$$\begin{aligned} \nabla_\mu \psi(x) &= \frac{1}{2a} \left( U_\mu(x) \psi(x + \hat{\mu}) - U_{-\mu} \psi(x - \hat{\mu}) \right), \\ \nabla_\mu^{(2)} \psi(x) &= \frac{1}{a^2} \left( U_\mu(x) \psi(x + \hat{\mu}) - 2\psi(x) + U_{-\mu} \psi(x - \hat{\mu}) \right), \\ \Delta^{(2)} \psi(x) &= \frac{1}{a^2} \sum_{j=1}^3 \left( U_j(x) \psi(x + \hat{j}) - 2\psi(x) + U_{-j} \psi(x - \hat{j}) \right). \end{aligned} \quad (\text{A.3})$$

All derivatives are symmetrized using a combination of forward and backward derivatives. Note that these are unimproved versions of the derivatives whose discretization errors are of order  $\mathcal{O}(a^2)$ . This is sufficiently precise for most applications and used in this work if not otherwise stated.

# Appendix B

---

## GROUP THEORETICAL BACKGROUND OF SYMMETRY CONSIDERATIONS

---

### B.1 Basics of Representation Theory

In this section, I give a brief summary of group theoretical methods necessary to incorporate the discrete symmetries of the lattice in our theory. For a more elaborated treatment of the group theoretical backgrounds, I refer to Refs. [118, 239]. In the subsequent paragraph, I will illustrate some basic quantities originating from group theory by the example of the group  $\mathbb{G} = C_{3v}$ . This is the symmetry group of an equilateral triangle if all transformations that lead out of the triangle plane are neglected. This group has only six elements  $\hat{R}$ : the identity  $I$ , the two rotations by  $2/3\pi$  ( $C_3$ ) and  $4/3\pi$  ( $C_3^2$ ) around the  $z$ -axis and the reflections at the planes which are spanned by the  $z$ -axis and the three angle bisectors ( $\sigma_v^{(1)}, \sigma_v^{(2)}, \sigma_v^{(3)}$ ). In short, the group elements can be written as  $\mathbb{G} = C_{3v} : \hat{R} \in \{I, C_3, C_3^2, \sigma_v^{(1)}, \sigma_v^{(2)}, \sigma_v^{(3)}\}$ . It can easily be shown that these elements fulfill the group axioms. The total number of elements in a group  $\mathbb{G}$  is called order  $g$ . Obviously, the order of  $C_{3v}$  is  $g = 6$ .

Two elements  $\hat{R}, \hat{S} \in \mathbb{G}$  are called conjugated to each other if there exists an element  $\hat{X} \in \mathbb{G}$ , so that

$$\hat{X}^{-1} \hat{R} \hat{X} = \hat{S}, \quad (\text{B.1})$$

with  $\hat{X} \neq \hat{R}$ . The set of all elements  $R^{(i)}$  and  $S^{(i)}$  that are conjugated to each other form a class  $\mathbb{K}_i$  according to

$$\hat{X}^{-1} \hat{R}^{(i)} \hat{X} = \hat{S}^{(i)}, \quad \hat{X} \in \mathbb{G}, \quad \hat{R}^{(i)}, \hat{S}^{(i)} \in \mathbb{K}_i. \quad (\text{B.2})$$

The number of elements in a class is labeled by  $g_i$  while the sum over all  $g_i$  is equal to  $g$  [239]. Note that  $g_i$  is also a divisor of  $g$ . In the case of the group  $C_{3v}$  one finds three classes,

$$\begin{aligned} \mathbb{K}_1 &= \{E\}, & g_1 &= 1, \\ \mathbb{K}_2 &= \{C_3, C_3^2\}, & g_2 &= 2, \\ \mathbb{K}_3 &= \{\sigma_v^{(1)}, \sigma_v^{(2)}, \sigma_v^{(3)}\}, & g_3 &= 3. \end{aligned} \quad (\text{B.3})$$

We call  $\Gamma$  the representation of a group  $\mathbb{G}$  if it projects the group  $\mathbb{G}$  onto a matrix group  $\Gamma$ . Each element  $\hat{R} \in \mathbb{G}$  is represented by a square matrix  $\Gamma(\hat{R})$  while the product of two elements  $\hat{R}, \hat{S} \in \mathbb{G}$  is given by the matrix product  $\Gamma(\hat{R})\Gamma(\hat{S})$ . A representation  $\Gamma(\hat{R})$  is called reducible if there exists a transformation  $\Gamma'(\hat{R}) = M^{-1}\Gamma(\hat{R})M$  so that for each  $\hat{R} \in \mathbb{G}$ ,  $\Gamma'(\hat{R})$  is block-diagonal according to

$$\Gamma'(\hat{R}) = \begin{pmatrix} \Gamma^{(\Lambda_1)}(\hat{R}) & 0 & 0 & \dots \\ 0 & \Gamma^{(\Lambda_2)}(\hat{R}) & 0 & \\ 0 & 0 & \Gamma^{(\Lambda_3)}(\hat{R}) & \\ \vdots & & & \ddots \end{pmatrix}. \quad (\text{B.4})$$

If the  $\Gamma^{(\Lambda)}(\hat{R})$  are not anymore reducible, they are called irreducible representations, which are simply named as  $\Lambda \equiv \Gamma^{(\Lambda)}$ , and  $\Gamma$  can be expressed as

$$\Gamma = \sum_{\Lambda} a_{\Lambda} \Lambda, \quad (\text{B.5})$$

where  $a_{\Lambda}$  is the multiplicity of  $\Lambda$  and specifies how often the associated irreducible representation appears in  $\Gamma$ . The number of irreducible representation  $n_{\text{IR}}$  is according to the 1. Burnside theorem equal to the number of classes  $n_{\text{K}}$  [239]. The 2. Burnside theorem [239] determines the dimensions of the irreps  $d_{\Lambda}$  according to

$$\sum_{\Lambda} d_{\Lambda}^2 = g. \quad (\text{B.6})$$

Consequently, for the case of  $C_{3v}$  there exist three irreps,  $\Lambda \in \{A_1, A_2, E\}$  while one ( $E$ ) is two-dimensional.

In addition to that, we define the character  $\chi(\hat{R})$  of an element  $\hat{R}$  as the trace over the representation  $\Gamma(\hat{R})$ ,

$$\chi(\hat{R}) = \text{Tr}[\Gamma(\hat{R})]. \quad (\text{B.7})$$

All elements of the same class have the same character, so we can write  $\chi(\mathbb{K}_i)$  instead of  $\chi(\hat{R})$ . In a character table, all characters  $\chi^{(\Lambda)}(\mathbb{K}_i)$  for the irrep  $\Lambda$  are collected for all classes  $\mathbb{K}_i$ . These tables are available in literature (e.g., see Ref. [239]). The reduction of an arbitrary representation  $\Gamma$  to the irreps is governed by the reduction formula [239]

$$a_{\Lambda} = \frac{1}{g} \cdot \sum_{i=1}^{n_{\text{K}}} g_i \cdot \chi^{(\Lambda)}(\mathbb{K}_i) \cdot \chi(\mathbb{K}_i), \quad (\text{B.8})$$

which allows us to determine the prefactors  $a_{\Lambda}$  that appear in Eq. (B.5). Here,  $\chi(\mathbb{K}_i)$  can be determined from the representation of  $\Gamma$  via Eq. (B.7),  $\chi^{(\Lambda)}(\mathbb{K}_i)$  can be taken from a character table, and  $g_i$  is the number of elements in the class  $\mathbb{K}_i$ .

## B.2 Decomposition of the Rotational Group into Irreducible Representations

As a consequence of the discretized space-time lattice, the continuous rotational symmetry is reduced to the symmetry of the group  $\mathbb{G}$  which contains all transformations that leave the mesh  $P_{\mathbf{d}}$  in Eq. (3.10) invariant. From this follows that the representations  $\Gamma^{(l)}$  of the orthogonal group  $O(3)$  are decomposed into the irreducible representations of the group  $\mathbb{G}$  as discussed in Sec. 3.2. Here, I will carry out the decomposition into the irreps for the group  $O_h$  in detail, while I will also summarize the results for the groups  $D_{4h}$ ,  $D_{2h}$ ,  $C_{4v}$  and  $C_{2v}$ . Note that the representations  $\Gamma^{(l)}$  describe the transformation behavior of two spin-less particles (with same parity) with orbital angular momentum  $l$ , i.e., the total spin  $J$  equals the orbital angular momentum  $l$ . The associated parity counterpart with same spin can be easily obtained by considering the opposite transformation behavior with respect to inversions.

In order to determine the decomposition into the irreps, I first consider the transformation behavior of the spherical harmonics  $Y_{lm}$  under transformations  $\hat{R} \in \mathbb{G}$  and determine the associated representation matrix  $\Gamma^{(l)}(\hat{R})$ . The spherical harmonics  $Y_{lm}$  are listed in Table B.1 for  $l \leq 2$  in Cartesian coordinates. Afterwards, the characters

$Y_{lm}(x, y, z)$	$l = 0$	$l = 1$	$l = 2$
$m = -2$			$\sqrt{\frac{15}{32\pi}}(x - iy)^2$
$m = -1$		$\sqrt{\frac{3}{8\pi}}(x - iy)$	$\sqrt{\frac{15}{8\pi}}z(x - iy)$
$m = 0$	$\sqrt{\frac{1}{4\pi}}$	$\sqrt{\frac{3}{4\pi}}z$	$\sqrt{\frac{5}{16\pi}}(3z^2 - 1)$
$m = 1$		$-\sqrt{\frac{3}{8\pi}}(x + iy)$	$-\sqrt{\frac{15}{8\pi}}z(x + iy)$
$m = 2$			$\sqrt{\frac{15}{32\pi}}(x + iy)^2$

Table B.1.: Spherical harmonics  $Y_{lm}(x, y, z)$  for  $l = 0, 1, 2$  in Cartesian coordinates.

$\chi(\mathbb{K}_i)$  are computed for each class according to Eq. (B.7). Finally, the decomposition into the irreps is determined using Eq. (B.8) and the character table given in Table B.2.

To obtain the decomposition of  $\Gamma^{(0)}$ , we consider the transformation behavior of  $Y_{00}(x, y, z)$  with respect to  $\hat{R} \in \mathbb{G}$ . Obviously,  $Y_{00}$  is invariant with respect to all transformations, i.e.,  $\Gamma^{(0)}(\hat{R}) = 1$  and consequently  $\chi(\hat{R}) = 1$  for all  $\hat{R}$ . Applying Eq. (B.8), we find that  $a_{A_1^+} = 1$  and  $a_{\Lambda} = 0$  for all other irreps. Therefore, we obtain the decomposition into irreps as  $\Gamma^{(0)} = A_1^+$ .

To obtain the irreps for  $\Gamma^{(1)}$ , one requires the transformation behavior of  $Y_{1m}(x, y, z)$  with respect to  $\hat{R} \in \mathbb{G}$ . For each class of transformations  $\mathbb{K}_i$ , I have investigated one specific transformation  $\hat{R} \in \mathbb{K}_i$  and have determined the associated character  $\chi(\hat{R})$ . As all elements of one class have the same character, this is sufficient to determine the irreps. In Table B.3, I list the transformation behavior of  $Y_{1m}(x, y, z)$  as well as the representations  $\Gamma(\hat{R})$  and the characters  $\chi(\hat{R})$ . Using the characters listed in Ta-

$O_h$	$I$	$6C_4$	$3C_4^2 = 3C_2$	$8C_3'$	$6C_2''$	$i$	$3\sigma_h$	$6\sigma_d$	$8S_6$	$6S_4$
$A_1^+$	1	1	1	1	1	1	1	1	1	1
$A_2^+$	1	-1	1	1	-1	1	1	-1	1	-1
$A_1^-$	1	1	1	1	1	-1	-1	-1	-1	-1
$A_2^-$	1	-1	1	1	-1	-1	-1	1	-1	1
$E^+$	2	0	2	-1	0	2	2	0	-1	0
$E^-$	2	0	2	-1	0	-2	-2	0	1	0
$T_1^+$	3	1	-1	0	-1	3	-1	-1	0	1
$T_2^+$	3	-1	-1	0	1	3	-1	1	0	-1
$T_1^-$	3	1	-1	0	-1	-3	1	1	0	-1
$T_2^-$	3	-1	-1	0	1	-3	1	-1	0	1

 Table B.2.: Character table for  $O_h$ .

ble B.3 and the character table given in Table B.2, the prefactors  $a_\Lambda$  are according to Eq. (B.8) found as  $a_{T_1^-} = 1$  and  $a_\Lambda = 0$  for all others. The same approach can be repeated for higher  $l$  and finally yields

$$\begin{aligned}
 \Gamma^{(0)} &= A_1^+, \\
 \Gamma^{(1)} &= T_1^-, \\
 \Gamma^{(2)} &= E^+ \oplus T_2^+, \\
 \Gamma^{(3)} &= T_1^- \oplus T_2^- \oplus A_2^-, \\
 \Gamma^{(4)} &= A_1^+ \oplus T_1^+ \oplus T_2^+ \oplus E^+.
 \end{aligned} \tag{B.9}$$

Repeating the procedure for the symmetry groups  $\mathbb{G} \in \{D_{4h}, D_{2h}, C_{4v}, C_{2v}\}$  while using the associated symmetry transformations  $\hat{R} \in \mathbb{G}$ , the resulting decomposition of  $\Gamma^{(l)}$  up to  $l = 4$  is given by:

$D_{4h}$  :

$$\begin{aligned}
 \Gamma^{(0)} &= A_1^+, \\
 \Gamma^{(1)} &= A_2^- \oplus E^-, \\
 \Gamma^{(2)} &= A_1^+ \oplus B_1^+ \oplus B_2^+ \oplus E^+, \\
 \Gamma^{(3)} &= A_2^- \oplus B_1^- \oplus B_2^- \oplus 2E^-, \\
 \Gamma^{(4)} &= 2A_1^+ \oplus A_2^+ \oplus B_1^+ \oplus B_2^+ \oplus 2E^+.
 \end{aligned} \tag{B.10}$$



$D_{2h}$  :

$$\begin{aligned}
 \Gamma^{(0)} &= A^+, \\
 \Gamma^{(1)} &= B_1^- \oplus B_2^- \oplus B_3^-, \\
 \Gamma^{(2)} &= 2A^+ \oplus B_1^+ \oplus B_2^+ \oplus B_3^+, \\
 \Gamma^{(3)} &= A^- \oplus 2B_1^- \oplus 2B_2^- \oplus 2B_3^-, \\
 \Gamma^{(4)} &= 3A^+ \oplus 2B_1^+ \oplus 2B_2^+ \oplus 2B_3^+.
 \end{aligned} \tag{B.11}$$

$C_{4v}$  :

$$\begin{aligned}
 \Gamma^{(0)} &= A_1, \\
 \Gamma^{(1)} &= A_1 \oplus E, \\
 \Gamma^{(2)} &= A_1 \oplus B_1 \oplus B_2 \oplus E, \\
 \Gamma^{(3)} &= A_1 \oplus B_1 \oplus B_2 \oplus 2E, \\
 \Gamma^{(4)} &= 2A_1 \oplus A_2 \oplus B_1 \oplus B_2 \oplus 2E.
 \end{aligned} \tag{B.12}$$

$C_{2v}$  :

$$\begin{aligned}
 \Gamma^{(0)} &= A_1, \\
 \Gamma^{(1)} &= A_1 \oplus B_1 \oplus B_2, \\
 \Gamma^{(2)} &= 2A_1 \oplus A_2 \oplus B_1 \oplus B_2, \\
 \Gamma^{(3)} &= 2A_1 \oplus A_2 \oplus 2B_1 \oplus 2B_2, \\
 \Gamma^{(4)} &= 3A_1 \oplus 2A_2 \oplus 2B_1 \oplus 2B_2.
 \end{aligned} \tag{B.13}$$

If the parity is inverted, the associated decomposition for  $O_h$ ,  $D_{4h}$  and  $D_{2h}$  is obtained by replacing  $+$  with  $-$  and vice versa for all irreps. For  $C_{4v}$  and  $C_{2v}$ , the parity counterparts are obtained by interchanging the irreps  $A_1$  and  $A_2$ .

### B.3 Simplification of $M$ -Matrix due to Group Symmetries

The  $M$ -matrix given in Eq. (3.28) can be simplified by considering the transformation behavior of the zeta function  $\mathcal{Z}_{lm}(s; q^2)$  as stated in Eq. (3.40) with respect to the present symmetry group. In the following, I briefly mention the relevant symmetry properties and specify the resulting simplified  $M$ -matrices for the four symmetry groups  $D_{4h}$ ,  $D_{2h}$ ,  $C_{4v}$  and  $C_{2v}$ .

#### B.3.1 Group $D_{4h}$

For the tetragonal group  $D_{4h}$ , we observe that all  $\mathcal{Z}_{lm}(s; q^2)$  with odd  $l$  vanish since inversion is an element of the symmetry group. Additionally, also  $\mathcal{Z}_{2\pm 1}(s; q^2)$  and  $\mathcal{Z}_{2\pm 2}(s; q^2)$  are found to vanish due to the symmetry transformations  $C_2$  and  $C_4$ .

Consequently, the  $M$ -matrix is simplified to

$$M = \mathcal{M}_{lm,l'm'}^d = \begin{matrix} & 00 & 10 & 11 & 1-1 \\ \begin{matrix} 00 \\ 10 \\ 11 \\ 1-1 \end{matrix} & \begin{pmatrix} w_{00} & 0 & 0 & 0 \\ 0 & w_{00} + 2w_{20} & 0 & 0 \\ 0 & 0 & w_{00} - w_{20} & 0 \\ 0 & 0 & 0 & w_{00} - w_{20} \end{pmatrix} \end{matrix}. \quad (\text{B.14})$$

### B.3.2 Group $D_{2h}$

The symmetry group  $D_{2h}$  also contains inversion and the rotational transformation  $C_2$ , which is why  $\mathcal{Z}_{lm}(s; q^2)$  for odd  $l$  and  $\mathcal{Z}_{2\pm 1}(s; q^2)$  vanish. Apart from that, no other simplifications are possible, and the final form of the  $M$ -matrix is given by

$$M = \mathcal{M}_{lm,l'm'}^d = \begin{matrix} & 00 & 10 & 11 & 1-1 \\ \begin{matrix} 00 \\ 10 \\ 11 \\ 1-1 \end{matrix} & \begin{pmatrix} w_{00} & 0 & 0 & 0 \\ 0 & w_{00} + 2w_{20} & 0 & 0 \\ 0 & 0 & w_{00} - w_{20} & -\sqrt{6}w_{2-2} \\ 0 & 0 & -\sqrt{6}w_{22} & w_{00} - w_{20} \end{pmatrix} \end{matrix}. \quad (\text{B.15})$$

### B.3.3 Group $C_{4v}$

Since inversion is no element of the group  $C_{4v}$ , we observe also terms with odd  $l$  in the associated  $M$ -matrix. However, as  $C_2$  and  $C_4$  are elements of  $C_{4v}$ , the terms  $\mathcal{Z}_{1\pm 1}(s; q^2)$ ,  $\mathcal{Z}_{2\pm 1}(s; q^2)$  and  $\mathcal{Z}_{2\pm 2}(s; q^2)$  vanish, which yields

$$M = \mathcal{M}_{lm,l'm'}^d = \begin{matrix} & 00 & 10 & 11 & 1-1 \\ \begin{matrix} 00 \\ 10 \\ 11 \\ 1-1 \end{matrix} & \begin{pmatrix} w_{00} & i\sqrt{3}w_{10} & 0 & 0 \\ -i\sqrt{3}w_{10} & w_{00} + 2w_{20} & 0 & 0 \\ 0 & 0 & w_{00} - w_{20} & 0 \\ 0 & 0 & 0 & w_{00} - w_{20} \end{pmatrix} \end{matrix}. \quad (\text{B.16})$$

### B.3.4 Group $C_{2v}$

For the group  $C_{2v}$ , the reflection at the plane perpendicular to the  $z$ -axis leads to the fact that  $\mathcal{Z}_{10}(s; q^2)$  and  $\mathcal{Z}_{2\pm 1}(s; q^2)$  vanish. Consequently, we obtain for the  $M$ -matrix

$$M = \mathcal{M}_{lm,l'm'}^d = \begin{matrix} & 00 & 10 & 11 & 1-1 \\ \begin{matrix} 00 \\ 10 \\ 11 \\ 1-1 \end{matrix} & \begin{pmatrix} w_{00} & 0 & i\sqrt{3}w_{11} & i\sqrt{3}w_{1-1} \\ 0 & w_{00} + 2w_{20} & 0 & 0 \\ i\sqrt{3}w_{1-1} & 0 & w_{00} - w_{20} & -\sqrt{6}w_{2-2} \\ i\sqrt{3}w_{11} & 0 & -\sqrt{6}w_{22} & w_{00} - w_{20} \end{pmatrix} \end{matrix}. \quad (\text{B.17})$$

Note that this matrix can be further block-diagonalized if one performs a basis transformation governed by  $\mathbf{u}_1 = 1/\sqrt{2}(-iY_{11} + Y_{1-1}) \propto (x - y)$  and  $\mathbf{u}_2 = 1/\sqrt{2}(Y_{11} - iY_{1-1}) \propto (x + y)$ . These new basis vectors coincide with the symmetry axes of  $C_{2v}$  which are

---

B.3. Simplification of  $M$ -Matrix due to Group Symmetries

parallel ( $\propto (x + y)$ ) and perpendicular ( $\propto (x - y)$ ) to the direction of the Lorentz boost. The block-diagonalized  $M$ -matrix is then given by

$$M^B = \begin{matrix} Y_{00} \\ Y_{10} \\ \frac{-iY_{11}+Y_{1-1}}{\sqrt{s}} \\ \frac{Y_{11}-iY_{1-1}}{\sqrt{2}} \end{matrix} \begin{pmatrix} Y_{00} & Y_{10} & \frac{-iY_{11}+Y_{1-1}}{\sqrt{s}} & \frac{Y_{11}-iY_{1-1}}{\sqrt{2}} \\ w_{00} & 0 & 0 & i\sqrt{6}w_{11} \\ 0 & w_{00} + 2w_{20} & 0 & 0 \\ 0 & 0 & w_{00} - w_{20} + i\sqrt{6}w_{22} & 0 \\ -\sqrt{6}w_{11} & 0 & 0 & w_{00} - w_{20} - i\sqrt{6}w_{22} \end{pmatrix}. \quad (\text{B.18})$$

Appendix B. Group Theoretical Background of Symmetry Considerations

$\mathbb{K}_i$	Trafo $\hat{R}$	$Y_{10}$	$Y_{1\pm 1}$	$\Gamma^{(1)}(\hat{R})$	$\chi(\hat{R})$
$I$	$(x, y, z)$ $\rightarrow (x, y, z)$	$Y_{10}$	$Y_{1\pm 1}$	$\begin{pmatrix} 1 & 0 & 0 \\ 0 & 1 & 0 \\ 0 & 0 & 1 \end{pmatrix}$	3
$C_4$	$(x, y, z)$ $\rightarrow$ $(y, -x, z)$	$Y_{10}$	$\mp i Y_{1\pm 1}$	$\begin{pmatrix} 1 & 0 & 0 \\ 0 & -i & 0 \\ 0 & 0 & +i \end{pmatrix}$	1
$C_2$	$(x, y, z)$ $\rightarrow$ $(-x, -y, z)$	$Y_{10}$	$-Y_{1\pm 1}$	$\begin{pmatrix} 1 & 0 & 0 \\ 0 & -1 & 0 \\ 0 & 0 & -1 \end{pmatrix}$	-1
$C'_3$	$(x, y, z)$ $\rightarrow$ $(-y, -z, x)$	$\frac{1}{\sqrt{2}}(Y_{1-1} - Y_{11})$	$\mp \frac{i}{2}(Y_{1-1} + Y_{11})$ $+\frac{i}{\sqrt{2}}Y_{10}$	$\begin{pmatrix} 0 & \frac{1}{\sqrt{2}} & -\frac{1}{\sqrt{2}} \\ \frac{i}{\sqrt{2}} & -\frac{i}{2} & -\frac{i}{2} \\ \frac{i}{\sqrt{2}} & \frac{i}{2} & \frac{i}{2} \end{pmatrix}$	0
$C''_2$	$(x, y, z)$ $\rightarrow$ $(-x, z, y)$	$\frac{i}{\sqrt{2}}(Y_{1-1} + Y_{11})$	$\pm \frac{1}{2}(Y_{1-1} - Y_{11})$ $-\frac{i}{\sqrt{2}}Y_{10}$	$\begin{pmatrix} 0 & \frac{i}{\sqrt{2}} & \frac{i}{\sqrt{2}} \\ -\frac{i}{\sqrt{2}} & -\frac{1}{2} & \frac{1}{2} \\ -\frac{i}{\sqrt{2}} & \frac{1}{2} & -\frac{1}{2} \end{pmatrix}$	-1
$i$	$(x, y, z)$ $\rightarrow$ $(-x, -y, -z)$	$-Y_{10}$	$-Y_{1\pm 1}$	$\begin{pmatrix} -1 & 0 & 0 \\ 0 & -1 & 0 \\ 0 & 0 & -1 \end{pmatrix}$	-3
$\sigma_h$	$(x, y, z)$ $\rightarrow$ $(x, y, -z)$	$-Y_{10}$	$Y_{1\pm 1}$	$\begin{pmatrix} -1 & 0 & 0 \\ 0 & 1 & 0 \\ 0 & 0 & 1 \end{pmatrix}$	1
$\sigma_d$	$(x, y, z)$ $\rightarrow (x, z, y)$	$\frac{i}{\sqrt{2}}(Y_{1-1} + Y_{11})$	$\mp \frac{1}{2}(Y_{1-1} - Y_{11})$ $-\frac{i}{\sqrt{2}}Y_{10}$	$\begin{pmatrix} 0 & \frac{i}{\sqrt{2}} & \frac{i}{\sqrt{2}} \\ -\frac{i}{\sqrt{2}} & \frac{1}{2} & -\frac{1}{2} \\ -\frac{i}{\sqrt{2}} & -\frac{1}{2} & \frac{1}{2} \end{pmatrix}$	1
$S_6$	$(x, y, z)$ $\rightarrow$ $(z, -x, y)$	$\frac{i}{\sqrt{2}}(Y_{1-1} + Y_{11})$	$\frac{i}{2}(Y_{1-1} - Y_{11})$ $\mp \frac{1}{\sqrt{2}}Y_{10}$	$\begin{pmatrix} 0 & \frac{i}{\sqrt{2}} & \frac{i}{\sqrt{2}} \\ -\frac{1}{\sqrt{2}} & -\frac{i}{2} & \frac{i}{2} \\ \frac{1}{\sqrt{2}} & -\frac{i}{2} & \frac{i}{2} \end{pmatrix}$	0
$S_4$	$(x, y, z)$ $\rightarrow$ $(y, -x, z)$	$-Y_{10}$	$\mp i Y_{1\pm 1}$	$\begin{pmatrix} -1 & 0 & 0 \\ 0 & -i & 0 \\ 0 & 0 & +i \end{pmatrix}$	-1

Table B.3.: Transformation behavior of  $Y_{1m}$  under the transformations  $\hat{R} \in O_h$ , representations  $\Gamma^{(1)}(\hat{R})$  and characters  $\chi^{(1)}(\hat{R})$  for one element of each class  $\mathbb{K}_i$  of group  $O_h$ .

# Appendix C

## CORRELATION FUNCTIONS FOR FOUR-QUARK OPERATORS

The two-point correlation functions for four-quark systems are computed analogously to the correlation function for a meson as discussed in Sec. 4.2.2. The only difference is that each operator contains four instead of two quark fields, which adds additional terms in the correlation functions. In order to compute the full correlation matrix, a large number of correlation functions, equaling the number of interpolating operators squared, is required. However, it is not necessary to derive the final contracted expression for each element independently but one can combine the derivation of several elements which are similar in their structure. In this section, I will illustrate how to calculate an analytic expression for the correlation matrix elements for the case of  $\bar{b}bud$ . This can be easily transferred to the cases of  $\bar{b}bus$  and  $\bar{b}cud$ .

The correlation matrix elements  $C_{jk}$  can be classified in two ways: In the first case, I distinguish whether a local or a scattering operator is at the sink and at the source

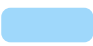






$C_{11}$	$C_{12}$	$C_{13}$	$C_{14}$	$C_{15}$	$C_{11}$	$C_{12}$	$C_{13}$	$C_{14}$	$C_{15}$				
$C_{21}$	$C_{22}$	$C_{23}$	$C_{24}$	$C_{25}$	$C_{21}$	$C_{22}$	$C_{23}$	$C_{24}$	$C_{25}$				
$C_{31}$	$C_{32}$	$C_{33}$	$C_{34}$	$C_{35}$	$C_{31}$	$C_{32}$	$C_{33}$	$C_{34}$	$C_{35}$				
$C_{41}$	$C_{42}$	$C_{43}$	$C_{44}$	$C_{45}$	$C_{41}$	$C_{42}$	$C_{43}$	$C_{44}$	$C_{45}$				
$C_{51}$	$C_{52}$	$C_{53}$	$C_{54}$	$C_{55}$	$C_{51}$	$C_{52}$	$C_{53}$	$C_{54}$	$C_{55}$				
	meson-meson operator at sink meson-meson operator at source		diquark-antidiquark operator at sink meson-meson operator at source		meson-meson operator at sink diquark-antidiquark operator at source		local operator at sink local operator at source		scattering operator at sink local operator at source		local operator at sink scattering operator at source		scattering operator at sink scattering operator at source

Table C.1.: Classification of correlation matrix elements for the case of  $\bar{b}bud$ . Distinguishing between meson-meson and diquark-antidiquark operator at sink and source (left) and distinguishing between local and scattering operator at sink and source (right).

yielding four different classifications as illustrated in the right part of Table C.1. This distinction is useful to decide which method is used to compute the quark propagators for a specific correlation matrix element. I will cover this more detailed in Appendix C.2. The second classification distinguishes whether a meson-meson or a diquark-antidiquark operator is at the source and at the sink as shown in the left part of Table C.1. This is the required classification to simplify the derivation of the analytic expression for the correlation matrix elements.

## C.1 Derivation of Correlation Matrix Elements

Relying on the distinction between meson-meson and diquark-antidiquark operators, I distinguish four different types of correlation matrix elements. For each type of correlation functions, I derive in the following a generic analytic expression that allows us to compute all matrix elements that are assigned to this type.

### C.1.1 Type I Correlation Matrix Elements

The first type corresponds to the correlation function  $\langle \mathcal{O}_i(t) \mathcal{O}_j^\dagger(0) \rangle$  where  $\mathcal{O}_i$  and  $\mathcal{O}_j$  are meson-meson operators, i.e.,  $i, j \in \{1, 2, 4, 5\}$ . The associated operator can be written in a generic form as

$$\mathcal{O}_i(t) = \frac{1}{V_S} \sum_{\mathbf{x}, \mathbf{y}} \bar{b} \Gamma_1^{(i)} u(\mathbf{x}, t) \bar{b} \Gamma_2^{(i)} d(\mathbf{y}, t) - \bar{b} \Gamma_1^{(i)} d(\mathbf{x}, t) \bar{b} \Gamma_2^{(i)} u(\mathbf{y}, t), \quad (\text{C.1})$$

where the Gamma matrices can be read of from Eqs. (4.21) to (4.25). A differentiation between local and non-local operators can be easily done after the calculation as the local operators are obtained formally by replacing the spatial sum over  $\mathbf{y}$  by a volume factor  $\sqrt{V_S}$  and identifying  $\mathbf{y} = \mathbf{x}$ . For the Gamma matrices of the daggered operator  $\mathcal{O}_j^\dagger$  I will use the abbreviation  $\Gamma^{(j)'} = \gamma_0 \Gamma^{(j)\dagger} \gamma_0$ . Note that I omit expectation values over the gauge fields throughout this chapter, as these are incorporated by averaging over different gauge field configurations. Consequently, the type I correlation matrix elements are found to be

$$\begin{aligned} C_I(t) &= \left\langle \mathcal{O}_i(t) \mathcal{O}_j^\dagger(0) \right\rangle \\ &= \frac{1}{V_S^2} \sum_{\mathbf{x}, \mathbf{y}, \mathbf{z}, \mathbf{u}} \left\langle \left[ \bar{b} \Gamma_1^{(i)} u(\mathbf{x}, t) \bar{b} \Gamma_2^{(i)} d(\mathbf{y}, t) - \bar{b} \Gamma_1^{(i)} d(\mathbf{x}, t) \bar{b} \Gamma_2^{(i)} u(\mathbf{y}, t) \right] \right. \\ &\quad \left. \times \left[ \bar{u} \Gamma_1^{(j)'} b(\mathbf{z}, 0) \bar{d} \Gamma_2^{(j)'} b(\mathbf{u}, 0) - \bar{d} \Gamma_1^{(j)'} b(\mathbf{z}, 0) \bar{u} \Gamma_2^{(j)'} b(\mathbf{u}, 0) \right] \right\rangle_F. \end{aligned} \quad (\text{C.2})$$

For the sake of brevity, I omit space-time arguments from now on, as they are directly related to color indices according to

$$(\mathbf{x}, t) \leftrightarrow a, \quad (\mathbf{y}, t) \leftrightarrow b, \quad (\mathbf{z}, 0) \leftrightarrow a', \quad (\mathbf{u}, 0) \leftrightarrow b'. \quad (\text{C.3})$$

Introducing index notation, we obtain

$$\begin{aligned}
 &= \frac{1}{V_S^2} \sum_{x,y,z,u} \Gamma_{1AB}^{(i)} \Gamma_{2CD}^{(i)} \Gamma_{1A'B'}^{(j)'} \Gamma_{2C'D'}^{(j)'} \\
 &\quad \times \left\langle \bar{b}_A^a u_B^a \bar{b}_C^b d_D^b \bar{u}_{A'}^{a'} b_{B'}^{a'} \bar{d}_{C'}^{b'} b_{D'}^{b'} - \bar{b}_A^a u_B^a \bar{b}_C^b d_D^b \bar{d}_{A'}^{a'} b_{B'}^{a'} \bar{u}_{C'}^{b'} b_{D'}^{b'} \right. \\
 &\quad \left. - \bar{b}_A^a d_B^a \bar{b}_C^b u_D^b \bar{u}_{A'}^{a'} b_{B'}^{a'} \bar{d}_{C'}^{b'} b_{D'}^{b'} + \bar{b}_A^a d_B^a \bar{b}_C^b u_D^b \bar{d}_{A'}^{a'} b_{B'}^{a'} \bar{u}_{C'}^{b'} b_{D'}^{b'} \right\rangle_F, \tag{C.4}
 \end{aligned}$$

which can be contracted using Wick's theorem in Eq. (2.20), yielding

$$\begin{aligned}
 &= \frac{1}{V_S^2} \sum_{x,y,z,u} \Gamma_{1AB}^{(i)} \Gamma_{2CD}^{(i)} \Gamma_{1A'B'}^{(j)'} \Gamma_{2C'D'}^{(j)'} \left( B_{D'A}^{b'a} B_{B'C}^{a'b} - B_{B'A}^{a'a} B_{D'C}^{b'b} \right) \\
 &\quad \times \left( -U_{BA'}^{aa'} D_{DC'}^{bb'} - U_{BC'}^{ab'} D_{DA'}^{ba'} - U_{DA'}^{ba'} D_{BC'}^{ab'} - U_{DC'}^{bb'} D_{BA'}^{aa'} \right). \tag{C.5}
 \end{aligned}$$

Since I do not distinguish between  $u$  and  $d$  quarks in my lattice computations, i.e., full SU(2) isospin symmetry is assumed, I identify  $D = U$  and obtain

$$\begin{aligned}
 &= \frac{2}{V_S^2} \sum_{x,y,z,u} \Gamma_{1AB}^{(i)} \Gamma_{2CD}^{(i)} \Gamma_{1A'B'}^{(j)'} \Gamma_{2C'D'}^{(j)'} \\
 &\quad \times \left( B_{D'A}^{b'a} B_{B'C}^{a'b} - B_{B'A}^{a'a} B_{D'C}^{b'b} \right) \left( -U_{BA'}^{aa'} U_{DC'}^{bb'} - U_{BC'}^{ab'} U_{DA'}^{ba'} \right). \tag{C.6}
 \end{aligned}$$

This can be rewritten in terms of traces by exploiting the structure of color and Dirac indices. Reestablishing also space-time arguments and using  $\gamma_5$ -hermiticity, the correlation matrix element of type I reads

$$\begin{aligned}
 &= \frac{2}{V_S^2} \sum_{x,y,z,u} \text{Tr} \left[ U(x; u) \Gamma_2^{(j)'} \gamma_5 B^\dagger(y; u) \gamma_5 \Gamma_2^{(i)} U(y; z) \Gamma_1^{(j)'} \gamma_5 B^\dagger(x; z) \gamma_5 \Gamma_1^{(i)} \right] \\
 &\quad + \text{Tr} \left[ U(x; z) \Gamma_1^{(j)'} \gamma_5 B^\dagger(x; z) \gamma_5 \Gamma_1^{(i)} \right] \text{Tr} \left[ U(y; u) \Gamma_2^{(j)'} \gamma_5 B^\dagger(y; u) \gamma_5 \Gamma_2^{(i)} \right] \\
 &\quad - \text{Tr} \left[ U(x; u) \Gamma_2^{(j)'} \gamma_5 B^\dagger(x; u) \gamma_5 \Gamma_1^{(i)} \right] \text{Tr} \left[ U(y; z) \Gamma_1^{(j)'} \gamma_5 B^\dagger(y; z) \gamma_5 \Gamma_2^{(i)} \right] \\
 &\quad - \text{Tr} \left[ U(x; z) \Gamma_1^{(j)'} \gamma_5 B^\dagger(y; z) \gamma_5 \Gamma_2^{(i)} U(y; u) \Gamma_2^{(j)'} \gamma_5 B^\dagger(x; u) \gamma_5 \Gamma_1^{(i)} \right]. \tag{C.7}
 \end{aligned}$$

### C.1.2 Type II Correlation Matrix Elements

The second type of correlation functions covers matrix elements with a meson-meson operator at the source and the diquark-antidiquark operator in Eq. (4.23) at the sink. Using the generic meson-meson operator as defined in Eq. (C.1), the correlation function is given as

$$\begin{aligned}
 C_{\text{II}}(t) &= \left\langle \mathcal{O}_2(t) \mathcal{O}_j^\dagger(0) \right\rangle \\
 &= \frac{2}{V_S^{3/2}} \sum_{x,z,u} \left\langle \left[ \bar{b}^a \Gamma_1^{(2)} \bar{b}^{b,T}(\mathbf{x}) u^{a,T} \Gamma_2^{(2)} d^b(\mathbf{x}) \right] \right. \\
 &\quad \left. \times \left[ \bar{u} \Gamma_1^{(j)'} b(\mathbf{z}, 0) \bar{d} \Gamma_2^{(j)'} b(\mathbf{u}, 0) - \bar{d} \Gamma_1^{(j)'} b(\mathbf{z}, 0) \bar{u} \Gamma_2^{(j)'} b(\mathbf{u}, 0) \right] \right\rangle_F. \tag{C.8}
 \end{aligned}$$

Note that I use  $\Gamma_1^{(2)} = \gamma_j \mathcal{C}$  and  $\Gamma_2^{(2)} = \mathcal{C} \gamma_5$  for the sake of briefness and will omit the  $T$  indicating a transposed quark field. Additionally, I employ that the second term in  $\mathcal{O}_2$  is equal to the first, which can be seen by interchanging both the light and heavy quark fields, renaming the indices and using the relations  $\Gamma_{1AB}^{(2)} = \Gamma_{1BA}^{(2)}$  and  $\Gamma_{2AB}^{(2)} = -\Gamma_{2BA}^{(2)}$ . Finally, as the diquark-antidiquark operator is always a local operator, no spatial sum over  $\mathbf{y}$  appears. The correlation function is written as

$$\begin{aligned}
 &= \frac{2}{V_S^{3/2}} \sum_{x,z,u} \Gamma_{1AB}^{(2)} \Gamma_{2CD}^{(2)} \Gamma_{1A'B'}^{(j)'} \Gamma_{2C'D'}^{(j)'} \\
 &\quad \times \left\langle \bar{b}_A^a \bar{b}_B^b u_C^a d_D^b \bar{u}_{A'}^{a'} b_{B'}^{a'} \bar{d}_{C'}^{b'} b_{D'}^{b'} - \bar{b}_A^a \bar{b}_B^b u_C^a d_D^b \bar{d}_{A'}^{a'} b_{B'}^{a'} \bar{u}_{C'}^{b'} b_{D'}^{b'} \right\rangle_F \\
 &= \frac{2}{V_S^{3/2}} \sum_{x,z,u} \Gamma_{1AB}^{(2)} \Gamma_{2CD}^{(2)} \Gamma_{1A'B'}^{(j)'} \Gamma_{2C'D'}^{(j)'} \\
 &\quad \times \left( B_{D'A}^{b'a} B_{B'B}^{a'b} - B_{B'A}^{a'a} B_{D'B}^{b'b} \right) \left( U_{CA'}^{aa'} U_{DC'}^{bb'} + U_{CC'}^{ab'} U_{DA'}^{ba'} \right). \tag{C.9}
 \end{aligned}$$

This can be further simplified considering the second half of the expression given by

$$\Gamma_{1AB}^{(2)} \Gamma_{2CD}^{(2)} \Gamma_{1A'B'}^{(j)'} \Gamma_{2C'D'}^{(j)'} \left( B_{D'A}^{b'a} B_{B'B}^{a'b} - B_{B'A}^{a'a} B_{D'B}^{b'b} \right) U_{CC'}^{ab'} U_{DA'}^{ba'}. \tag{C.10}$$

Interchanging the color indices  $a \leftrightarrow b$  as well as the Dirac indices  $A \leftrightarrow B$  and  $C \leftrightarrow D$  we obtain

$$\begin{aligned}
 &\Gamma_{1BA}^{(2)} \Gamma_{2DC}^{(2)} \Gamma_{1A'B'}^{(j)'} \Gamma_{2C'D'}^{(j)'} \left( B_{D'B}^{b'b} B_{B'A}^{a'a} - B_{B'B}^{a'b} B_{D'A}^{b'a} \right) U_{DC'}^{bb'} U_{CA'}^{aa'} \\
 &= -\Gamma_{1AB}^{(2)} \Gamma_{2CD}^{(2)} \Gamma_{1A'B'}^{(j)'} \Gamma_{2C'D'}^{(j)'} \left( B_{D'B}^{b'b} B_{B'A}^{a'a} - B_{B'B}^{a'b} B_{D'A}^{b'a} \right) U_{DC'}^{bb'} U_{CA'}^{aa'}, \tag{C.11}
 \end{aligned}$$

which is identical to the first half of of the expression. Consequently, using once again  $\Gamma_{1AB}^{(2)} = \Gamma_{1BA}^{(2)}$  and  $\Gamma_{2AB}^{(2)} = -\Gamma_{2BA}^{(2)}$  and reestablishing space-time arguments, we write

$$\begin{aligned}
 &= \frac{4}{V_S^{3/2}} \sum_{x,z,u} \Gamma_{1AB}^{(2)} \Gamma_{2CD}^{(2)} \Gamma_{1A'B'}^{(j)'} \Gamma_{2C'D'}^{(j)'} \\
 &\quad \times \left( B_{D'A}^{b'a} B_{B'B}^{a'b} - B_{B'A}^{a'a} B_{D'B}^{b'b} \right) U_{CA'}^{aa'} U_{DC'}^{bb'} \\
 &= \frac{4}{V_S^{3/2}} \sum_{x,z,u} \left[ U(x; z) \Gamma_1^{(j)'} \gamma_5 B^\dagger(x; z) \gamma_5 \Gamma_1^{(2)} \right]_{CA}^{ab} \left[ \Gamma_2^{(2)} U(x; u) \Gamma_2^{(j)'} \gamma_5 B^\dagger(x; u) \gamma_5 \right]_{CA}^{ba} \\
 &\quad - \left[ U(x; z) \Gamma_1^{(j)'} \gamma_5 B^\dagger(x; z) \gamma_5 \Gamma_1^{(2)} \right]_{CB}^{aa} \left[ \Gamma_2^{(2)} U(x; u) \Gamma_2^{(j)'} \gamma_5 B^\dagger(x; u) \gamma_5 \right]_{CB}^{bb}, \tag{C.12}
 \end{aligned}$$

### C.1.3 Type III Correlation Matrix Elements

The third type of correlation matrix elements involves the diquark-antidiquark operator in Eq. (4.23) at the source and a meson-meson-operator according to Eq. (C.1) at the sink. The proceeding is quite similar to the case of type II correlation matrix



elements and yields for the correlation function

$$\begin{aligned}
 C_{\text{III}}(t) &= \left\langle \mathcal{O}_i(t) \mathcal{O}_2^\dagger(0) \right\rangle \\
 &= \frac{2}{V_S^{3/2}} \sum_{\mathbf{x}, \mathbf{y}, \mathbf{z}} \left\langle \left[ \bar{b} \Gamma_1^{(i)} u(\mathbf{x}, t) \bar{b} \Gamma_2^{(i)} d(\mathbf{y}, t) - \bar{b} \Gamma_1^{(i)} d(\mathbf{x}, t) \bar{b} \Gamma_2^{(i)} u(\mathbf{y}, t) \right] \right. \\
 &\quad \left. \times \bar{d}^{a'} \Gamma_2^{(2)'} \bar{u}^{b', T}(\mathbf{z}, 0) b^{a', T} \Gamma_1^{(2)'} b^{b'}(\mathbf{z}, 0) \right\rangle_F \\
 &= \frac{2}{V_S^{3/2}} \sum_{\mathbf{x}, \mathbf{y}, \mathbf{z}} \Gamma_{1AB}^{(i)} \Gamma_{2CD}^{(i)} \Gamma_{1C'D'}^{(2)'} \Gamma_{2A'B'}^{(2)'} \\
 &\quad \times \left\langle \bar{b}_A^a u_B^a \bar{b}_C^b d_D^b \bar{d}_{A'}^{a'} \bar{u}_{B'}^{b'} b_{C'}^{a'} b_{D'}^{b'} - \bar{b}_A^a d_B^a \bar{b}_C^b u_D^b \bar{d}_{A'}^{a'} \bar{u}_{B'}^{b'} b_{C'}^{a'} b_{D'}^{b'} \right\rangle_F \\
 &= \frac{2}{V_S^{3/2}} \sum_{\mathbf{x}, \mathbf{y}, \mathbf{z}} \Gamma_{1AB}^{(i)} \Gamma_{2CD}^{(i)} \Gamma_{1C'D'}^{(2)'} \Gamma_{2A'B'}^{(2)'} \\
 &\quad \times \left( B_{D'A}^{b'a} B_{C'C}^{a'b} - B_{C'A}^{a'a} B_{D'C}^{b'b} \right) \left( -U_{BB'}^{ab'} U_{DA'}^{ba'} - U_{DB'}^{bb'} U_{BA'}^{aa'} \right) \\
 &= -\frac{4}{V_S^{3/2}} \sum_{\mathbf{x}, \mathbf{y}, \mathbf{u}} \Gamma_{1AB}^{(i)} \Gamma_{2CD}^{(i)} \Gamma_{1C'D'}^{(2)'} \Gamma_{2A'B'}^{(2)'} \\
 &\quad \times \left( B_{D'A}^{b'a} B_{C'C}^{a'b} - B_{C'A}^{a'a} B_{D'C}^{b'b} \right) U_{BB'}^{ab'} U_{DA'}^{ba'} \\
 &= \frac{4}{V_S^{3/2}} \sum_{\mathbf{x}, \mathbf{y}, \mathbf{z}} \left[ \Gamma_1^{(2)'} \gamma_5 B^\dagger(x; z) \gamma_5 \Gamma_1^{(i)} U(x; z) \right]_{CB}^{bb} \left[ \gamma_5 B^\dagger(y; z) \gamma_5 \Gamma_2^{(i)} U(y; z) \Gamma_2^{(2)'} \right]_{CB}^{aa} \\
 &\quad - \left[ \Gamma_1^{(2)'} \gamma_5 B^\dagger(x; z) \gamma_5 \Gamma_1^{(i)} U(x; z) \right]_{DB}^{ab} \left[ \gamma_5 B^\dagger(y; z) \gamma_5 \Gamma_2^{(i)} U(y; z) \Gamma_2^{(2)'} \right]_{DB}^{ba}.
 \end{aligned} \tag{C.14}$$

#### C.1.4 Type IV Correlation Matrix Elements

Finally, I consider the correlation matrix element with a diquark-antidiquark operator both at sink and source. Here, the correlation function is

$$\begin{aligned}
 C_{\text{IV}}(t) &= \left\langle \mathcal{O}_2(t) \mathcal{O}_2^\dagger(0) \right\rangle \\
 &= \frac{4}{V_S} \sum_{\mathbf{x}, \mathbf{z}} \left\langle \left[ \bar{b}^a \Gamma_1^{(2)} \bar{b}^{b, T}(\mathbf{x}) u^{a, T} \Gamma_2^{(2)} d^b(\mathbf{x}) \right] \left[ \bar{d}^{a'} \Gamma_2^{(2)'} \bar{u}^{b', T}(\mathbf{z}, 0) b^{a', T} \Gamma_1^{(2)'} b^{b'}(\mathbf{z}, 0) \right] \right\rangle_F \\
 &= \frac{4}{V_S} \sum_{\mathbf{x}, \mathbf{z}} \Gamma_{1AB}^{(2)} \Gamma_{2CD}^{(2)} \Gamma_{1C'D'}^{(2)'} \Gamma_{2A'B'}^{(2)'} \left\langle \bar{b}_A^a \bar{b}_B^b u_C^a d_D^b \bar{d}_{A'}^{a'} \bar{u}_{B'}^{b'} b_{C'}^{a'} b_{D'}^{b'} \right\rangle_F \\
 &= \frac{4}{V_S} \sum_{\mathbf{x}, \mathbf{z}} \Gamma_{1AB}^{(2)} \Gamma_{2CD}^{(2)} \Gamma_{1C'D'}^{(2)'} \Gamma_{2A'B'}^{(2)'} \left( B_{D'A}^{b'a} B_{C'B}^{a'b} - B_{C'A}^{a'a} B_{D'B}^{b'b} \right) U_{CB'}^{ab'} U_{DA'}^{ba'} \\
 &= \frac{4}{V_S} \sum_{\mathbf{x}, \mathbf{z}} \left[ \Gamma_1^{(2)'} \gamma_5 B^\dagger(x; z) \gamma_5 \Gamma_1^{(2)} \right]_{C'B}^{b'a} \left[ U(x; z) \right]_{CB'}^{ab'} \left[ \Gamma_2^{(2)} D(x; z) \Gamma_2^{(2)'} \right]_{C'B'}^{ba'} \left[ \gamma_5 B(x; z) \gamma_5 \right]_{C'B}^{a'b} \\
 &\quad - \left[ \Gamma_1^{(2)'} \gamma_5 B^\dagger(x; z) \gamma_5 \Gamma_1^{(2)} \right]_{D'B}^{a'a} \left[ U(x; z) \right]_{CB'}^{ab'} \left[ \Gamma_2^{(2)} D(x; z) \Gamma_2^{(2)'} \right]_{C'B'}^{ba'} \left[ \gamma_5 B(x; z) \gamma_5 \right]_{D'B}^{b'b}.
 \end{aligned} \tag{C.15}$$

## C.2 Quark Propagator Types for Correlation Matrix Elements

Here, I will show which type of quark propagator is used for numerically computing each correlation matrix element. In contrast to the previous section where I distinguish between meson-meson and diquark-antidiquark operators, an appropriate classification for this case are local and scattering operators as illustrated in the right part of Table C.1. As the type I correlation matrix elements cover all four different combinations of local and scattering operators at sink and source, I will use the correlation function in Eq. (C.7) to depict which quark propagator is used for which correlation matrix element. The four different correlation functions are labeled as  $C_{\alpha\beta} = \langle \mathcal{O}_\alpha(t) \mathcal{O}_\beta^\dagger(0) \rangle$  with  $\alpha, \beta \in \{l, s\}$  where  $l$  indicates a local and  $s$  a scattering operator.

Correlation functions with a local operator at the source, i.e.,  $C_{ll}$  and  $C_{sl}$  utilize point-to-all propagators. Expressing the solutions  $\phi_A^{(f)a}(x)[b, B, y]$  in a matrix-like shape

$$\phi_A^{(f)a}(x)[b, B, y] = F_{AB}^{ab}(x; y), \quad (\text{C.16})$$

we can stick to the representation of the correlation function in matrix form but keep in mind that each column of  $F(x; y)$  corresponds to one solution  $\phi^{(f)}(x)$ . For the correlation matrix element  $C_{ll}$ , this results in

$$\begin{aligned} C_{ll}(t) = & 2 \sum_x \text{Tr} \left[ U(x; z) \Gamma_2^{(j)'} \gamma_5 B^\dagger(x; z) \gamma_5 \Gamma_2^{(i)} U(x; z) \Gamma_1^{(j)'} \gamma_5 B^\dagger(x; z) \gamma_5 \Gamma_1^{(i)} \right] \\ & + \text{Tr} \left[ U(x; z) \Gamma_1^{(j)'} \gamma_5 B^\dagger(x; z) \gamma_5 \Gamma_1^{(i)} \right] \text{Tr} \left[ U(x; z) \Gamma_2^{(j)'} \gamma_5 B^\dagger(x; z) \gamma_5 \Gamma_2^{(i)} \right] \\ & - \text{Tr} \left[ U(x; z) \Gamma_2^{(j)'} \gamma_5 B^\dagger(x; z) \gamma_5 \Gamma_1^{(i)} \right] \text{Tr} \left[ U(x; z) \Gamma_1^{(j)'} \gamma_5 B^\dagger(x; z) \gamma_5 \Gamma_2^{(i)} \right] \\ & - \text{Tr} \left[ U(x; z) \Gamma_1^{(j)'} \gamma_5 B^\dagger(x; z) \gamma_5 \Gamma_2^{(i)} U(x; z) \Gamma_2^{(j)'} \gamma_5 B^\dagger(x; z) \gamma_5 \Gamma_1^{(i)} \right] \end{aligned} \quad (\text{C.17})$$

where the sum over  $z$  is replaced by a volume factor  $V_S$  due to the use of point-to-all propagators. Similarly, for  $C_{sl}$  one obtains

$$\begin{aligned} C_{sl}(t) = & \frac{2}{\sqrt{V_S}} \sum_{x, y} \text{Tr} \left[ U(x; z) \Gamma_2^{(j)'} \gamma_5 B^\dagger(y; z) \gamma_5 \Gamma_2^{(i)} U(y; z) \Gamma_1^{(j)'} \gamma_5 B^\dagger(x; z) \gamma_5 \Gamma_1^{(i)} \right] \\ & + \text{Tr} \left[ U(x; z) \Gamma_1^{(j)'} \gamma_5 B^\dagger(x; z) \gamma_5 \Gamma_1^{(i)} \right] \text{Tr} \left[ U(y; z) \Gamma_2^{(j)'} \gamma_5 B^\dagger(y; z) \gamma_5 \Gamma_2^{(i)} \right] \\ & - \text{Tr} \left[ U(x; z) \Gamma_2^{(j)'} \gamma_5 B^\dagger(x; z) \gamma_5 \Gamma_1^{(i)} \right] \text{Tr} \left[ U(y; z) \Gamma_1^{(j)'} \gamma_5 B^\dagger(y; z) \gamma_5 \Gamma_2^{(i)} \right] \\ & - \text{Tr} \left[ U(x; z) \Gamma_1^{(j)'} \gamma_5 B^\dagger(y; z) \gamma_5 \Gamma_2^{(i)} U(y; z) \Gamma_2^{(j)'} \gamma_5 B^\dagger(x; z) \gamma_5 \Gamma_1^{(i)} \right]. \end{aligned} \quad (\text{C.18})$$

For the remaining two correlation matrix elements  $C_{ls}$  and  $C_{ss}$ , which have a scattering operator at the source, I apply stochastic timeslice-to-all propagators using the one-end-trick and spin and color dilution. In analogy to the case of point-to-all propagators,

I write the solutions  $\phi^{(f)b}_B(y)[t_0, C, c, r]$  in a matrix-like shape as

$$\phi^{(f)a}_A(x)[t_0, B, b, r] = \mathcal{F}_{AB}^{ab}(x)[t_0, r], \quad (\text{C.19})$$

which allows us again to keep the matrix structure of the correlation function. Using this, we end up with

$$\begin{aligned} C_{ls} = & \frac{2}{V_S^{3/2}} \frac{1}{N_R(N_R - 1)} \sum_{\mathbf{x}} \sum_{\substack{r, \tilde{r} \\ r \neq \tilde{r}}} \\ & \text{Tr} \left[ \mathcal{U}(x)[t_0, r] \Gamma_2^{(j)'} \gamma_5 \mathcal{B}^\dagger(x)[t_0, r] \gamma_5 \Gamma_2^{(i)} \mathcal{U}(x)[t_0, \tilde{r}] \Gamma_1^{(j)'} \gamma_5 \mathcal{B}^\dagger(x)[t_0, \tilde{r}] \gamma_5 \Gamma_1^{(i)} \right] \\ & + \text{Tr} \left[ \mathcal{U}(x)[t_0, r] \Gamma_1^{(j)'} \gamma_5 \mathcal{B}^\dagger(x)[t_0, r] \gamma_5 \Gamma_1^{(i)} \right] \text{Tr} \left[ \mathcal{U}(x)[t_0, \tilde{r}] \Gamma_2^{(j)'} \gamma_5 \mathcal{B}^\dagger(x)[t_0, \tilde{r}] \gamma_5 \Gamma_2^{(i)} \right] \\ & - \text{Tr} \left[ \mathcal{U}(x)[t_0, r] \Gamma_2^{(j)'} \gamma_5 \mathcal{B}^\dagger(x)[t_0, r] \gamma_5 \Gamma_1^{(i)} \right] \text{Tr} \left[ \mathcal{U}(x)[t_0, \tilde{r}] \Gamma_1^{(j)'} \gamma_5 \mathcal{B}^\dagger(x)[t_0, \tilde{r}] \gamma_5 \Gamma_2^{(i)} \right] \\ & - \text{Tr} \left[ \mathcal{U}(x)[t_0, r] \Gamma_1^{(j)'} \gamma_5 \mathcal{B}^\dagger(x)[t_0, r] \gamma_5 \Gamma_2^{(i)} \mathcal{U}(x)[t_0, \tilde{r}] \Gamma_2^{(j)'} \gamma_5 \mathcal{B}^\dagger(x)[t_0, \tilde{r}] \gamma_5 \Gamma_1^{(i)} \right] \end{aligned} \quad (\text{C.20})$$

and

$$\begin{aligned} C_{ss} = & \frac{2}{V_S^2} \frac{1}{N_R(N_R - 1)} \sum_{\mathbf{x}, \mathbf{y}} \sum_{\substack{r, \tilde{r} \\ r \neq \tilde{r}}} \\ & \text{Tr} \left[ \mathcal{U}(x)[t_0, r] \Gamma_2^{(j)'} \gamma_5 \mathcal{B}^\dagger(y)[t_0, r] \gamma_5 \Gamma_2^{(i)} \mathcal{U}(y)[t_0, \tilde{r}] \Gamma_1^{(j)'} \gamma_5 \mathcal{B}^\dagger(x)[t_0, \tilde{r}] \gamma_5 \Gamma_1^{(i)} \right] \\ & + \text{Tr} \left[ \mathcal{U}(x)[t_0, r] \Gamma_1^{(j)'} \gamma_5 \mathcal{B}^\dagger(x)[t_0, r] \gamma_5 \Gamma_1^{(i)} \right] \text{Tr} \left[ \mathcal{U}(y)[t_0, \tilde{r}] \Gamma_2^{(j)'} \gamma_5 \mathcal{B}^\dagger(y)[t_0, \tilde{r}] \gamma_5 \Gamma_2^{(i)} \right] \\ & - \text{Tr} \left[ \mathcal{U}(x)[t_0, r] \Gamma_2^{(j)'} \gamma_5 \mathcal{B}^\dagger(x)[t_0, r] \gamma_5 \Gamma_1^{(i)} \right] \text{Tr} \left[ \mathcal{U}(y)[t_0, \tilde{r}] \Gamma_1^{(j)'} \gamma_5 \mathcal{B}^\dagger(y)[t_0, \tilde{r}] \gamma_5 \Gamma_2^{(i)} \right] \\ & - \text{Tr} \left[ \mathcal{U}(x)[t_0, r] \Gamma_1^{(j)'} \gamma_5 \mathcal{B}^\dagger(y)[t_0, r] \gamma_5 \Gamma_2^{(i)} \mathcal{U}(y)[t_0, \tilde{r}] \Gamma_2^{(j)'} \gamma_5 \mathcal{B}^\dagger(x)[t_0, \tilde{r}] \gamma_5 \Gamma_1^{(i)} \right]. \end{aligned} \quad (\text{C.21})$$

Note that for stochastic propagators employing the one-end trick, two different random sources must be considered. To increase the statistical precision, I average over all possible combinations with  $r \neq \tilde{r}$ .



# Appendix D

---

## METHOD TO COMPUTE THE WEIGHTED AVERAGE INCLUDING STATISTICAL UNCERTAINTIES

---

The ground-state energies and their statistical uncertainties are computed either via multi-exponential matrix fits considering different sub-matrices and temporal fit ranges or by single exponential fits to the principal correlators for various fit ranges. Based on these fits, the final estimates for the ground-state energies and the associated uncertainties are obtained by a weighted average following the approach of the FLAG collaboration that has been presented in Section 2.3.1 of the 2019 FLAG review [185]. To recapitulate this approach, I label the result of the  $j$ -th fit as

$$E_0^{(j)} \pm \Delta E_0^{(j)}, \quad (\text{D.1})$$

where  $E_0^{(j)}$  is the mean value of the ground-state energy and  $\Delta E_0^{(j)}$  the associated statistical uncertainty. The final estimate for the ground-state energy is determined by a weighted average

$$\bar{E}_0 = \sum_j \omega^{(j)} E_0^{(j)}, \quad (\text{D.2})$$

where the weights are given by

$$\omega^{(j)} = \frac{1/(\Delta E_0^{(j)})^2}{\sum_j 1/(S^{(j)} \Delta E_0^{(j)})^2}, \quad (\text{D.3})$$

with  $S^{(j)} = \max(1, (\chi_j^2/\text{d.o.f.})^{(j)})^{1/2}$ . Consequently, this approach is identical to a weighted, uncorrelated  $\chi^2$ -minimizing fit of a constant to the results given by Eq. (D.1), where fit results with a bad value of  $\chi^2/\text{d.o.f.}$  are further suppressed by the factor  $S^{(j)}$ . As all fits are based on the same gauge link configurations and two-point functions, the resulting energies are expected to be highly correlated. In a conservative approach, I assume that the data are fully correlated, and the corresponding uncertainty of the ground-state energy is then obtained as

$$\Delta \bar{E}_0 = \left( \sum_{j,k} \omega^{(j)} \omega^{(k)} \sigma^{(j)} \sigma^{(k)} \right)^{1/2}, \quad (\text{D.4})$$

where  $\sigma^{(j)} = S^{(j)} \Delta E_0^{(j)}$ .



# Appendix E

## TUNING OF PARAMETERS FOR THE MILC-HISQ SETUP

### E.1 Determination of Smearing Parameters for Fermion Fields

The smearing parameters for the Gaussian/Wuppertal smearing of the light and strange quark fields that are given in Table 6.4 are tuned such that (i) the effective energy plateaus for the ground-state energy of the  $\bar{b}b\bar{u}d$  or  $\bar{b}b\bar{u}s$  four-quark system are reached at sufficiently small values of  $t/a$  while at the same time the signal-to-noise ratio stays relatively small and (ii) the radius of the smeared quark field has a reasonable physical size.

In the first step, I solved the GEVP for the  $\bar{b}b\bar{u}d$  system on a subset of ensemble a09m310 (50 configurations) for various combinations of  $\kappa_{\text{Gauss}}$  and  $N_{\text{Gauss}}$  used for the light quark smearing. In Fig. E.1 I depict the effective energies for the ground state as well as the associated relative errors for some selected combinations of  $\kappa_{\text{Gauss}}$  and  $N_{\text{Gauss}}$ . We observe that stronger smearing, i.e., increasing  $\kappa_{\text{Gauss}}$  and/or  $N_{\text{Gauss}}$  lowers the effective energy at small values of  $t/a$  and the plateau is reached earlier (see left plot in Fig. E.1). However, a drawback of strongly smeared quark fields is that the signal-to-noise ratio becomes worse and fluctuations are much stronger espe-

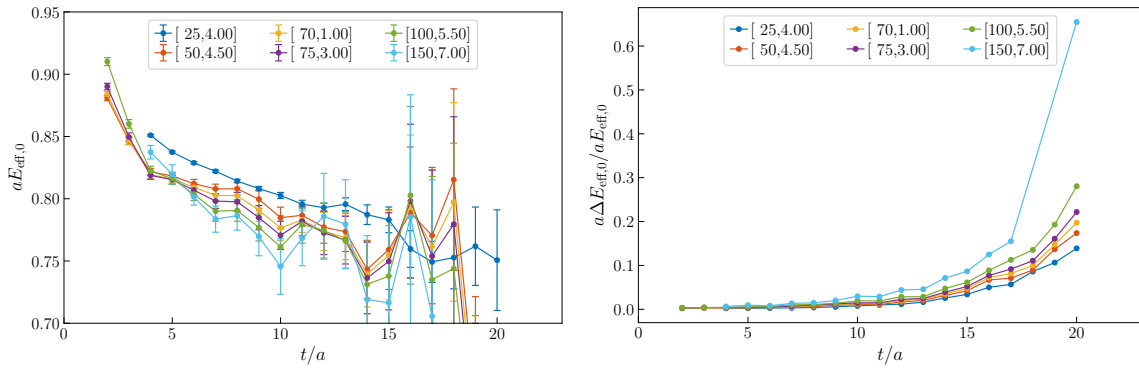


Figure E.1.: Effective energy  $aE_{\text{eff},0}$  for the  $\bar{b}b\bar{u}d$  ground state (left) and the associated relative error  $a\Delta E_{\text{eff},0}/aE_{\text{eff},0}$  (right) on a subset of 50 configurations of ensemble a09m310 for various combinations of the smearing parameters  $[N_{\text{Gauss}}, \kappa_{\text{Gauss}}]$ .

cially for large temporal separations as can be seen in the right plot in Fig. E.1. As a reasonable compromise to obtain stable plateaus for small values of  $t/a$  and keep the signal-to-noise ratio acceptable in the meantime, I chose  $\kappa_{\text{Gauss}} = 1.0$  and  $N_{\text{Gauss}} = 70$ . Note that according to Fig. 1 in Ref. [161], choosing  $\kappa_{\text{Gauss}} \gtrsim 1$  hardly increases the radius of the smeared quark field and thus it is not recommendable to use large values of  $\kappa_{\text{Gauss}}$ . For this reason, I keep  $\kappa_{\text{Gauss}} = 1.0$  fixed for all ensembles and quark flavors and vary only the number of smearing steps  $N_{\text{Gauss}}$  to adjust the smearing width. Following the definition in Ref. [240], I computed the root mean square (r.m.s.) radius of a smeared point source for  $\kappa_{\text{Gauss}} = 1.0$  and various values of  $N_{\text{Gauss}}$ , which is illustrated in Fig. E.2. The black dashed lines indicate the chosen smearing parameters with  $N_{\text{Gauss}} = 70$  for the smearing of the light quarks, yielding  $r_{\text{r.m.s.}} \simeq 0.61$  fm.

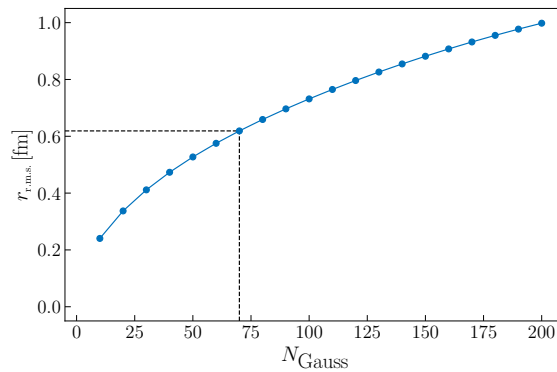


Figure E.2.: Root mean square (r.m.s.) radius for  $\kappa_{\text{Gauss}} = 1.0$  in dependence of the number of Gaussian/Wuppertal smearing steps  $N_{\text{Gauss}}$ . The black dashed lines indicate the choice of  $N_{\text{Gauss}}$  for the light quarks.

The same approach is repeated to determine the smearing parameters for the strange quark fields by considering the ground-state energy of the  $\bar{b}b\bar{u}s$  four-quark system for various values of  $N_{\text{Gauss}}$  as shown in Fig. E.3. While keeping  $\kappa_{\text{Gauss}} = 1.0$ , I chose  $N_{\text{Gauss}} = 50$ , which yields a stable plateau and an adequate signal-to-noise ratio at the same time. As the strange quark is heavier than the up and down quarks, it is more localized, which is also represented by the corresponding smaller r.m.s. radius of  $r_{\text{r.m.s.}} \simeq 0.53$  fm.

The smearing parameters for the ensembles with different lattice spacing  $a$  are chosen such that the smearing width is kept approximately constant. According to Eq. (4.80), the number of Gaussian smearing steps  $N_2$  applied for quark fields of flavor  $f$  on an ensemble with lattice spacing  $a_2$  can be estimated as

$$N_2 \simeq N_1 \left( \frac{a_1}{a_2} \right)^2, \quad (\text{E.1})$$

where  $a_1$  is the lattice spacing of ensemble a09m310 and  $N_1$  the number of Gaussian smearing steps applied for quark fields of the same flavor  $f$  on ensemble a09m310.



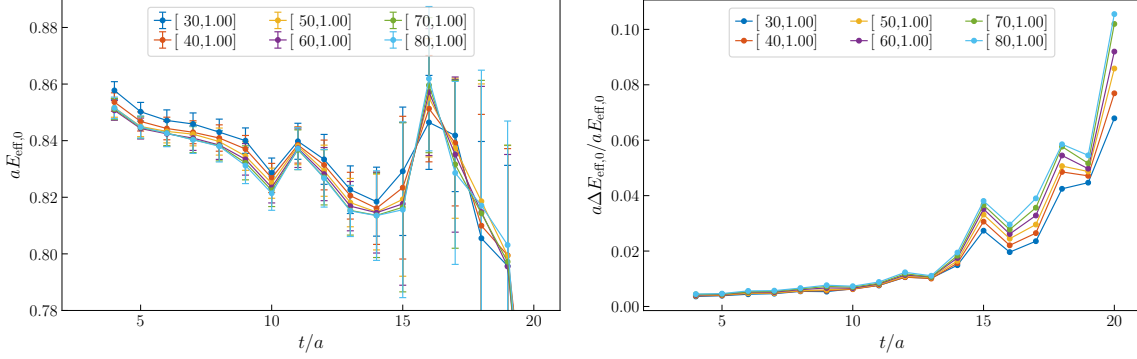


Figure E.3.: Effective energy  $aE_{\text{eff},0}$  for the  $\bar{b}b\bar{u}s$  ground state (left) and the associated relative error  $a\Delta E_{\text{eff},0}/aE_{\text{eff},0}$  (right) on a subset of 50 configurations of ensemble a09m310 for various combinations of the smearing parameters  $[N_{\text{Gauss}}, \kappa_{\text{Gauss}}]$  used in the light quark smearing.

Note that this is only valid as long as we keep  $\kappa_{\text{Gauss}}$  constant, which is the case in our smearing approach.

## E.2 Determination of GEVP Normalization $t_0$

The parameter  $t_0$  which appears in the GEVP in Eq. (4.45) should be chosen sufficiently large to minimize contributions of higher excited states to a specific eigenstate. Meanwhile, larger values of  $t_0$  lead to a worse signal-to-noise ratio. For this reason, a suitable choice of  $t_0$  is mandatory to extract energy levels precisely. In order to determine a reasonable value of  $t_0$ , I solved the GEVP for the  $\bar{b}b\bar{u}d$  and the  $\bar{b}b\bar{u}s$  four-quark system on each ensemble for various values of  $t_0$ . In Figs. E.4 and E.5, I depict the associated effective energies obtained on the three ensembles a15m310, a12m220L and a09m310 by solving GEVPs for  $2 \leq t_0/a \leq 6$ . The final value of  $t_0$  is chosen as large as necessary and as small as possible to ensure that the effective energies are independent of  $t_0$  for all eigenstates. The final values of  $t_0$  are collected in Table E.1. It is reasonable to choose  $t_0/a$  depending on the lattice spacing  $a$ , which leads to similar values of  $t_0$  in physical units. Accordingly, for ensembles with the same lattice spacing, the same value of  $t_0$  is used for each four-quark system. While

	$t_0/a$ for $\bar{b}b\bar{u}d$	$t_0/a$ for $\bar{b}b\bar{u}s$
very coarse	2	2
coarse	3	3
fine	4	6

Table E.1.: Parameter  $t_0/a$  used in the GEVP in Eq. (4.45) for the cases of  $\bar{b}b\bar{u}d$  and  $\bar{b}b\bar{u}s$  four-quark systems for the very coarse lattice (a15m310), the coarse lattices (a12m310, a12m220S, a12m220L) and the fine lattices (a09m310, a09m220).

for the very coarse and coarse lattices, I also use the same choice of  $t_0$  for the cases of  $\bar{b}b u d$  and  $\bar{b}b u s$ , for the fine lattices, a larger  $t_0$  is required for the case of  $\bar{b}b u s$  to obtain sufficiently stable effective energies (see the upper right plot in Fig. E.4 and the upper right plot in Fig. E.5).

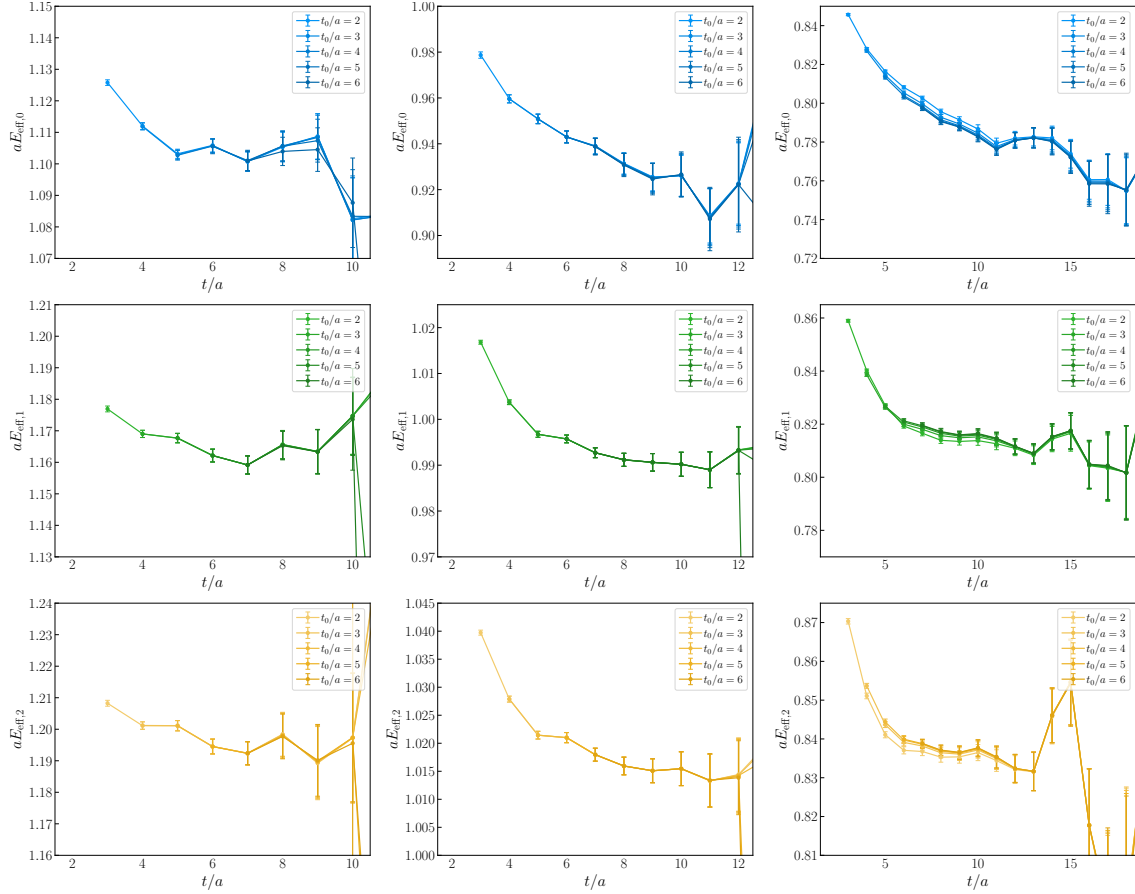


Figure E.4.: Effective energies for the three lowest  $\bar{b}b u d$  eigenstates extracted from GEVPs with  $2 \leq t_0/a \leq 6$ . The effective energy plots in the  $n$ -th row belong to the  $n$ -th energy eigenstate. The first column shows the results for the a15m310 ensemble, the second column for the a12m220L ensemble and the third column for the a09m310 ensemble.

## E.2. Determination of GEVP Normalization $t_0$

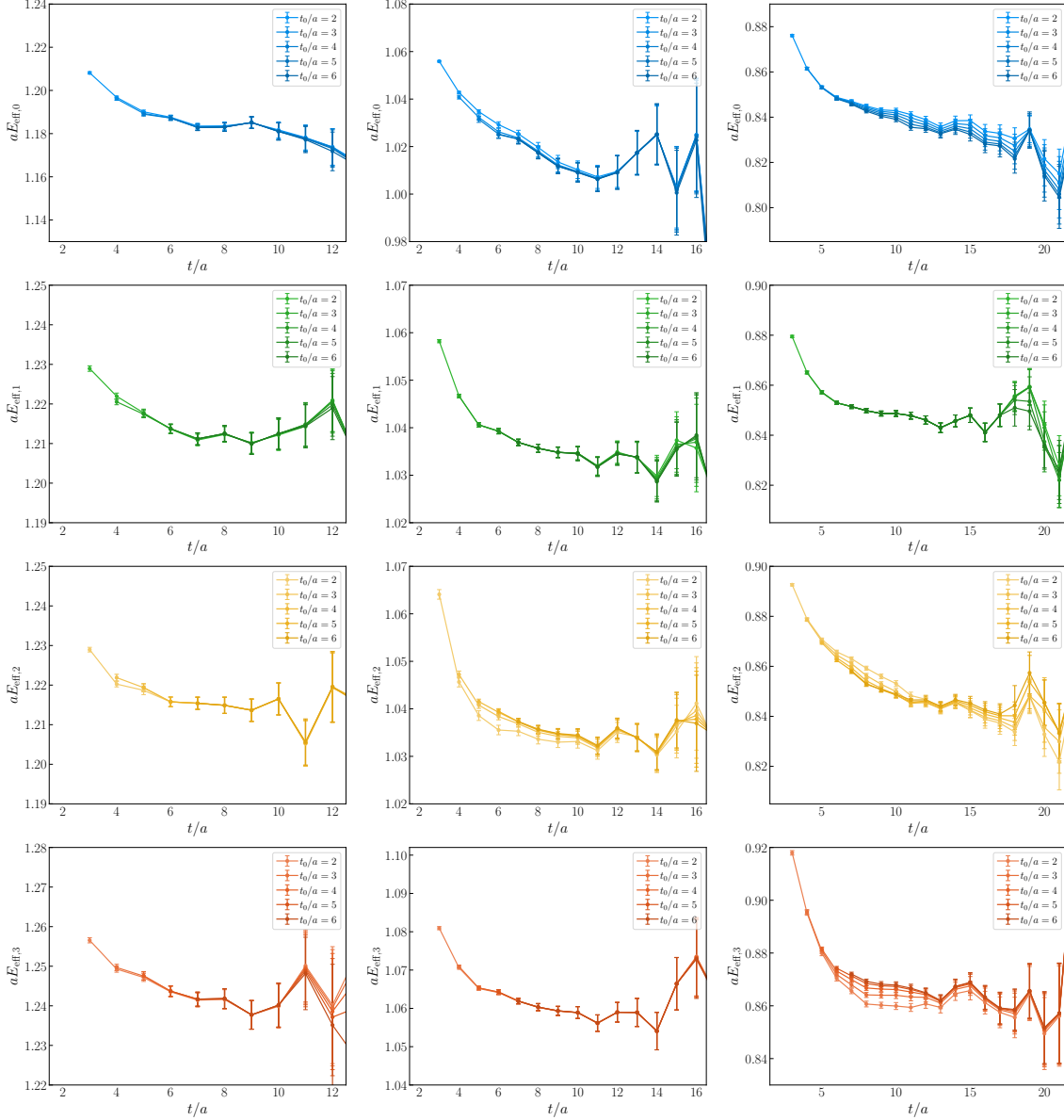


Figure E.5.: Effective energies for the four lowest  $\bar{b}b$  eigenstates extracted from GEVPs with  $2 \leq t_0/a \leq 6$ . The effective energy plots in the  $n$ -th row belong to the  $n$ -th energy eigenstate. The first column shows the results for the a15m310 ensemble, the second column for the a12m220L ensemble and the third column for the a09m310 ensemble.



# Appendix F

## PLOTS OF SINGLE-EXPONENTIAL FITS TO DETERMINE THE ENERGY LEVELS FOR THE HISQ-ENSEMBLES

In this appendix, I show the results for the lowest energy levels obtained from single-exponential fits to the principal correlators that have been determined by solving a GEVP for the ensembles a15m310, a12m310, a12m220S, a12m220, a09m310 and a09m220. The plots for the  $\bar{b}b\bar{u}d$  system with  $I(J^P) = 0(1^+)$  are collected in Figs. F.1 to F.6, while the plots for the  $\bar{b}b\bar{u}s$  system can be found in Figs. F.7 to F.12. These figures use the same style as Figs. 6.4 and 6.8, where the lowest energy levels obtained on ensemble a12m220L are depicted and which are discussed in detail in Sec. 6.3.

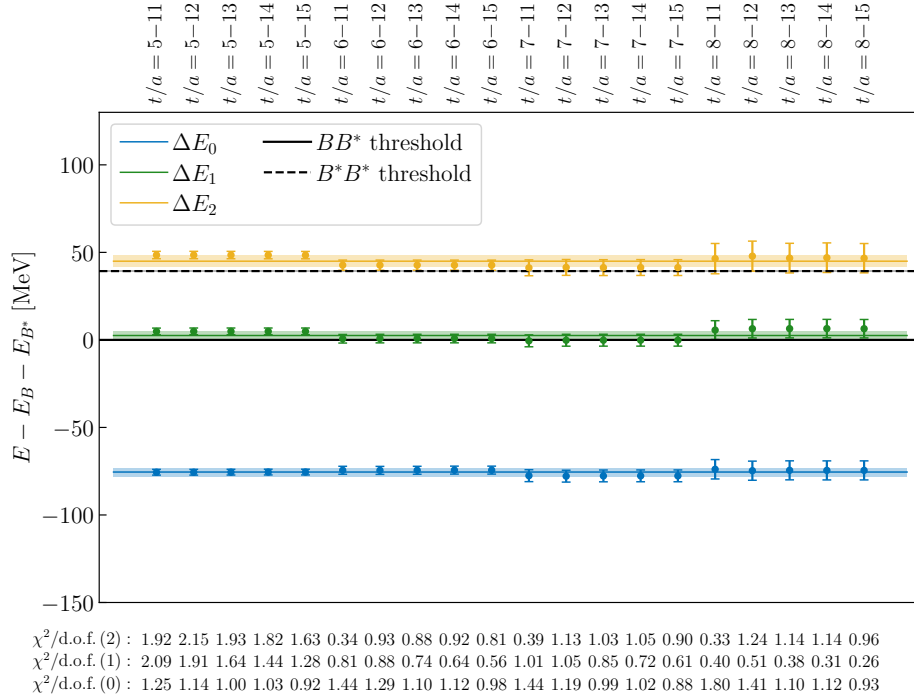


Figure F.1.: Fit results for the three lowest energy levels for the  $\bar{b}b\bar{u}d$  system with  $I(J^P) = 0(1^+)$  relative to the  $BB^*$  threshold,  $\Delta E_n = E_n - E_B - E_{B^*}$ , obtained on ensemble a15m310.

Appendix F. Plots of Single-Exponential Fits to Determine the Energy Levels for the HISQ-Ensembles

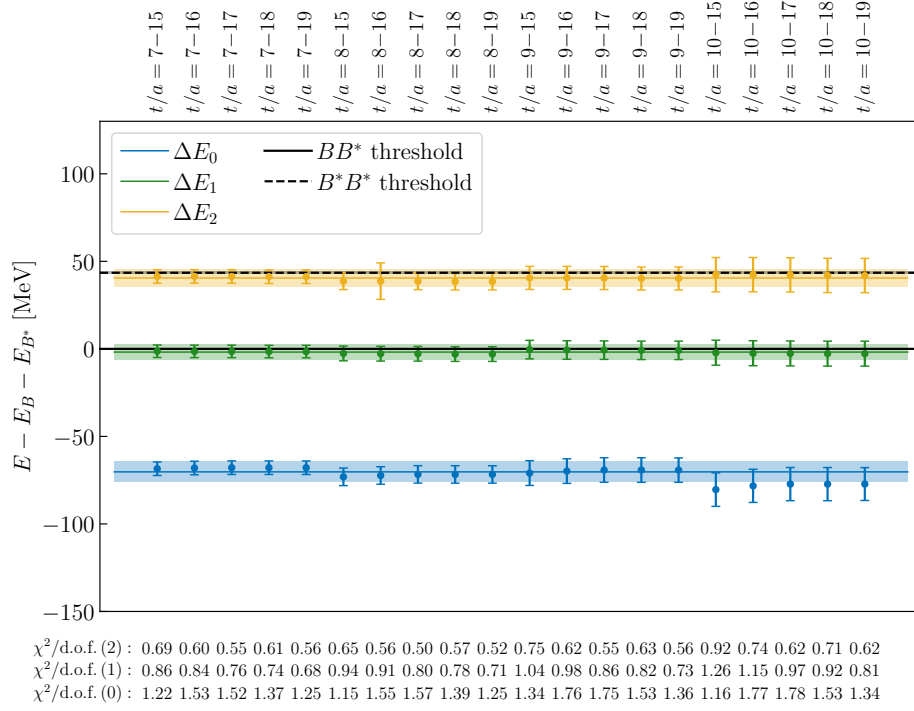


Figure F.2.: Fit results for the three lowest energy levels for the  $\bar{b}b u d$  system with  $I(J^P) = 0(1^+)$  relative to the  $BB^*$  threshold,  $\Delta E_n = E_n - E_B - E_{B^*}$ , obtained on ensemble a12m310.

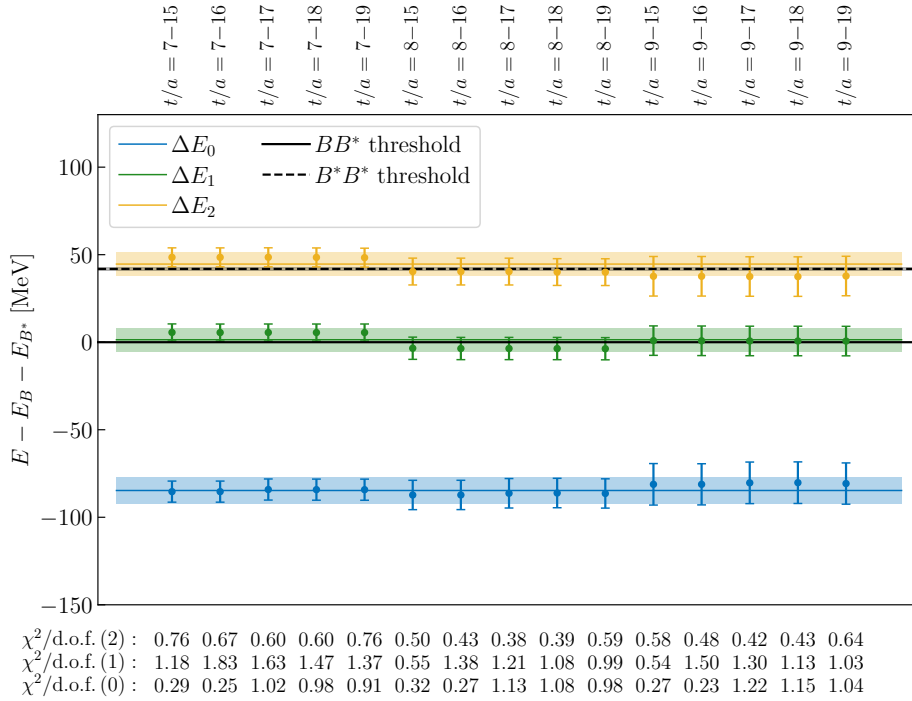


Figure F.3.: Fit results for the three lowest energy levels for the  $\bar{b}b u d$  system with  $I(J^P) = 0(1^+)$  relative to the  $BB^*$  threshold,  $\Delta E_n = E_n - E_B - E_{B^*}$ , obtained on ensemble a12m220S.

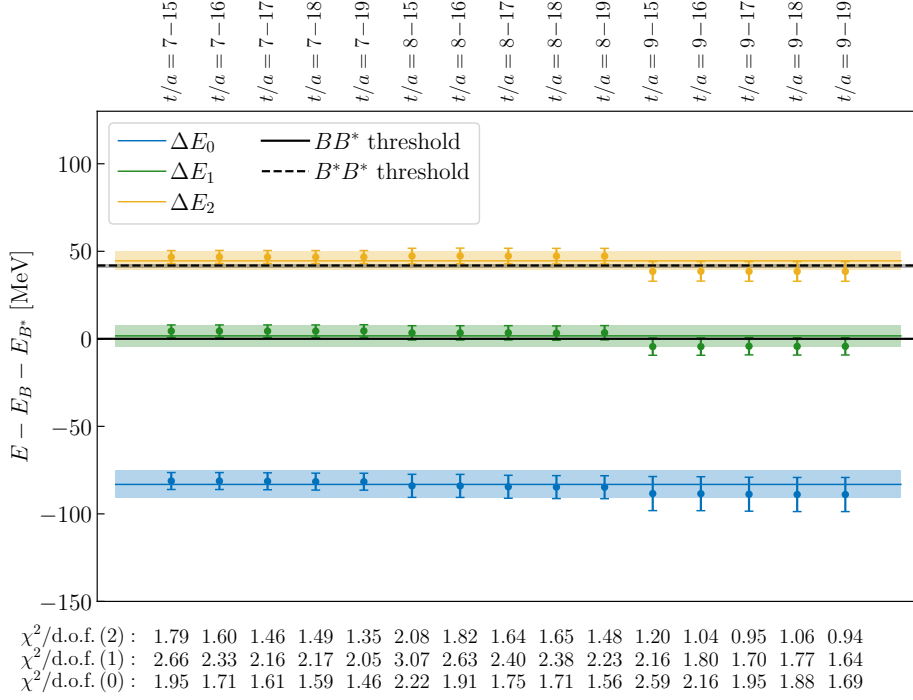


Figure F.4.: Fit results for the three lowest energy levels for the  $\bar{b}b u d$  system with  $I(J^P) = 0(1^+)$  relative to the  $BB^*$  threshold,  $\Delta E_n = E_n - E_B - E_{B^*}$ , obtained on ensemble a12m220.

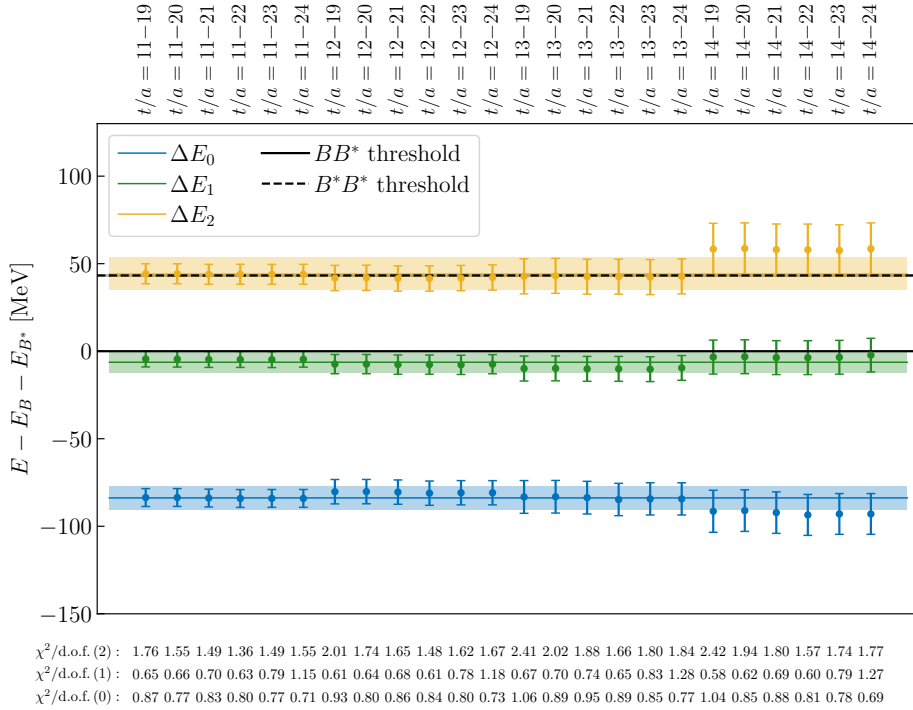


Figure F.5.: Fit results for the three lowest energy levels for the  $\bar{b}b u d$  system with  $I(J^P) = 0(1^+)$  relative to the  $BB^*$  threshold,  $\Delta E_n = E_n - E_B - E_{B^*}$ , obtained on ensemble a09m310.

Appendix F. Plots of Single-Exponential Fits to Determine the Energy Levels for the HISQ-Ensembles

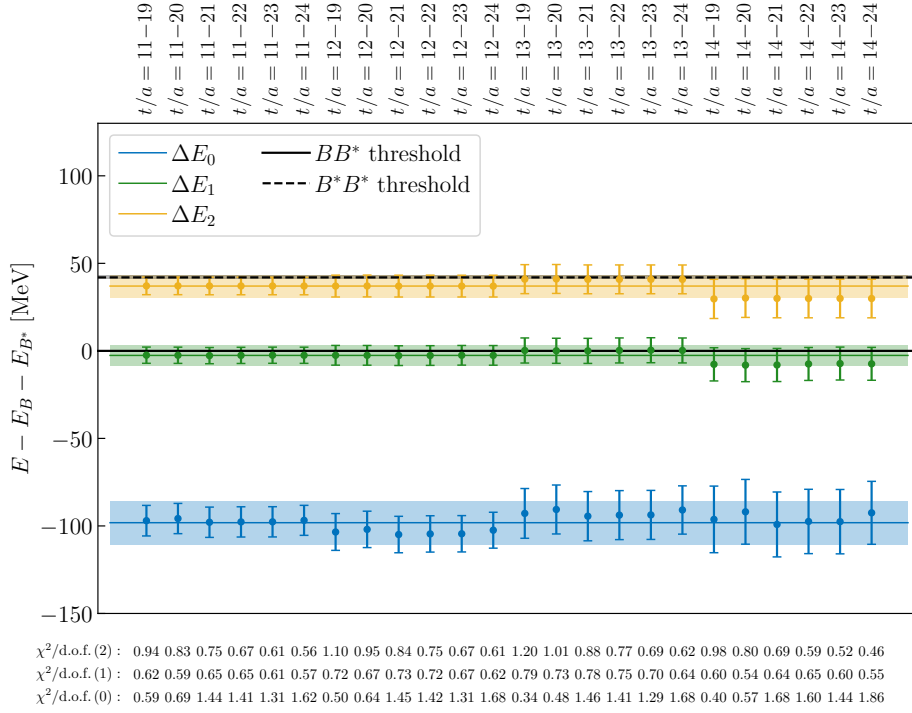


Figure F.6.: Fit results for the three lowest energy levels for the  $\bar{b}b u d$  system with  $I(J^P) = 0(1^+)$  relative to the  $BB^*$  threshold,  $\Delta E_n = E_n - E_B - E_{B^*}$ , obtained on ensemble a09m220.

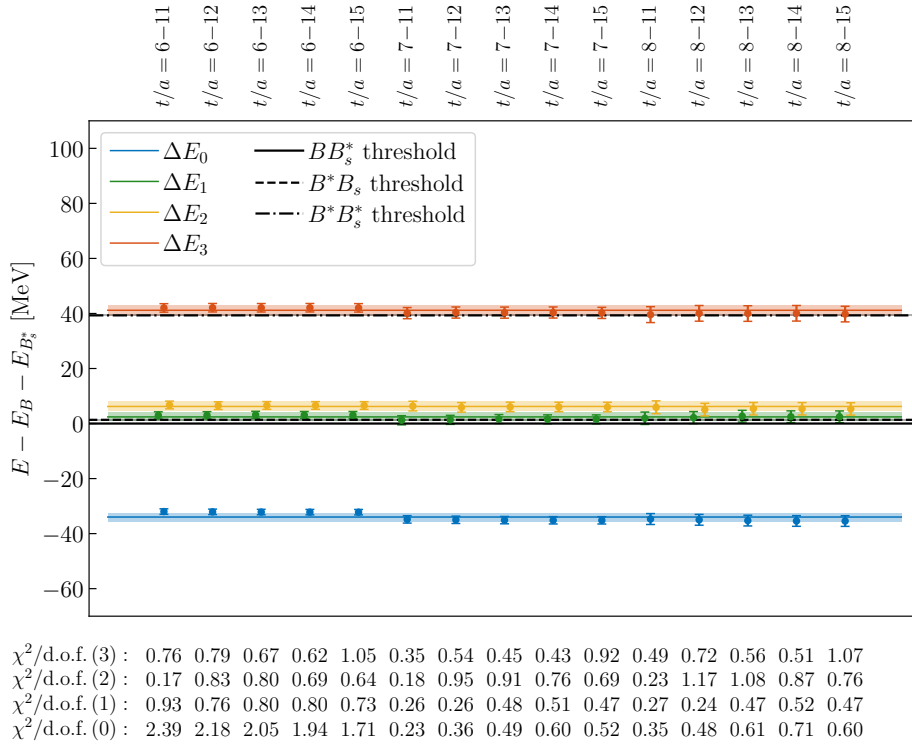


Figure F.7.: Fit results for the four lowest energy levels for the  $\bar{b}b u s$  system with  $J^P = 1^+$  relative to the  $BB_s^*$  threshold,  $\Delta E_n = E_n - E_B - E_{B_s^*}$ , obtained on ensemble a15m310.



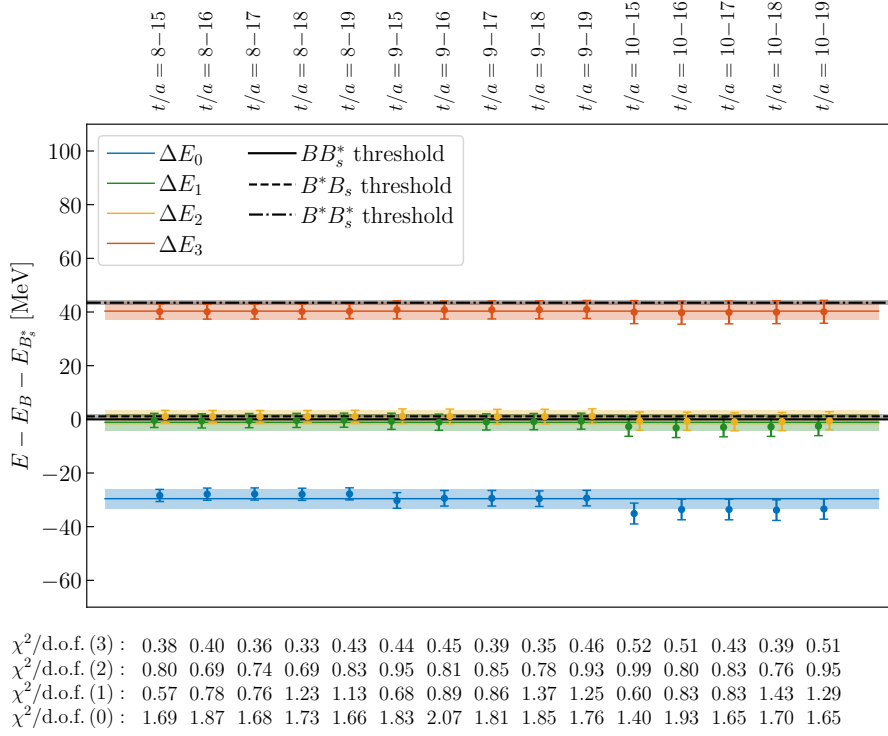


Figure F.8.: Fit results for the four lowest energy levels for the  $\bar{b}b\bar{u}s$  system with  $J^P = 1^+$  relative to the  $BB_s^*$  threshold,  $\Delta E_n = E_n - E_B - E_{B_s^*}$ , obtained on ensemble a12m310.

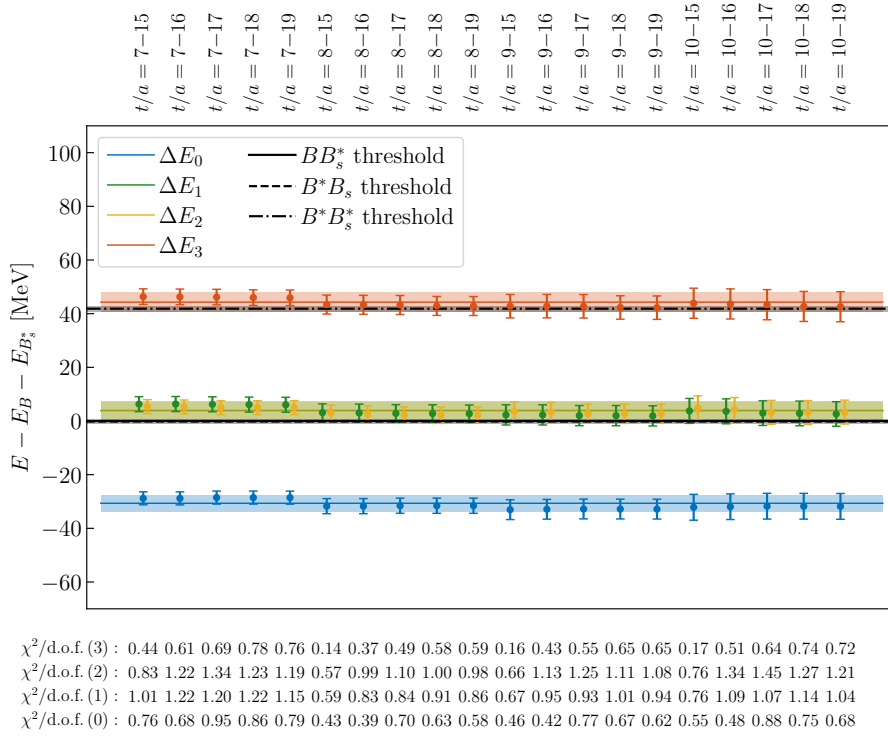


Figure F.9.: Fit results for the four lowest energy levels for the  $\bar{b}b\bar{u}s$  system with  $J^P = 1^+$  relative to the  $BB_s^*$  threshold,  $\Delta E_n = E_n - E_B - E_{B_s^*}$ , obtained on ensemble a12m220S.

Appendix F. Plots of Single-Exponential Fits to Determine the Energy Levels for the HISQ-Ensembles

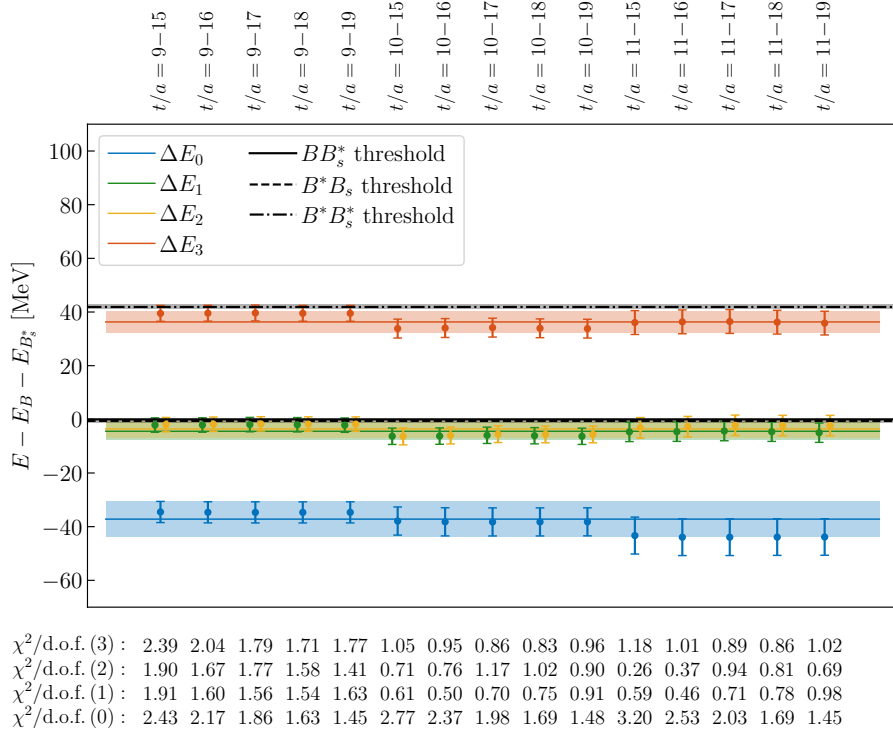


Figure F.10.: Fit results for the four lowest energy levels for the  $\bar{b}b$  system with  $J^P = 1^+$  relative to the  $BB_s^*$  threshold,  $\Delta E_n = E_n - E_B - E_{B_s^*}$ , obtained on ensemble a12m220.

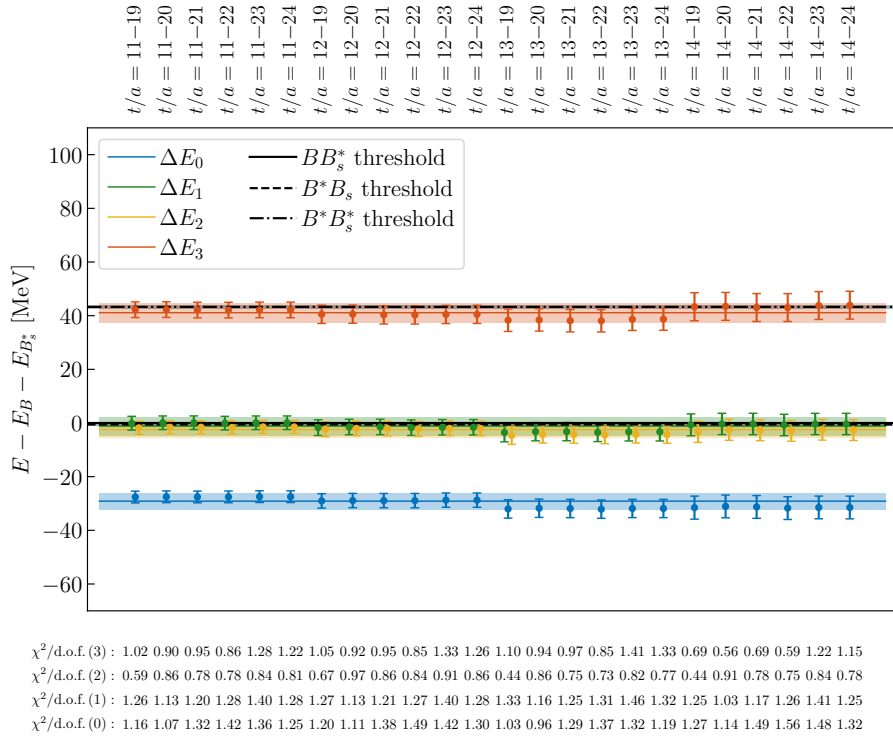


Figure F.11.: Fit results for the four lowest energy levels for the  $\bar{b}b$  system with  $J^P = 1^+$  relative to the  $BB_s^*$  threshold,  $\Delta E_n = E_n - E_B - E_{B_s^*}$ , obtained on ensemble a09m310.

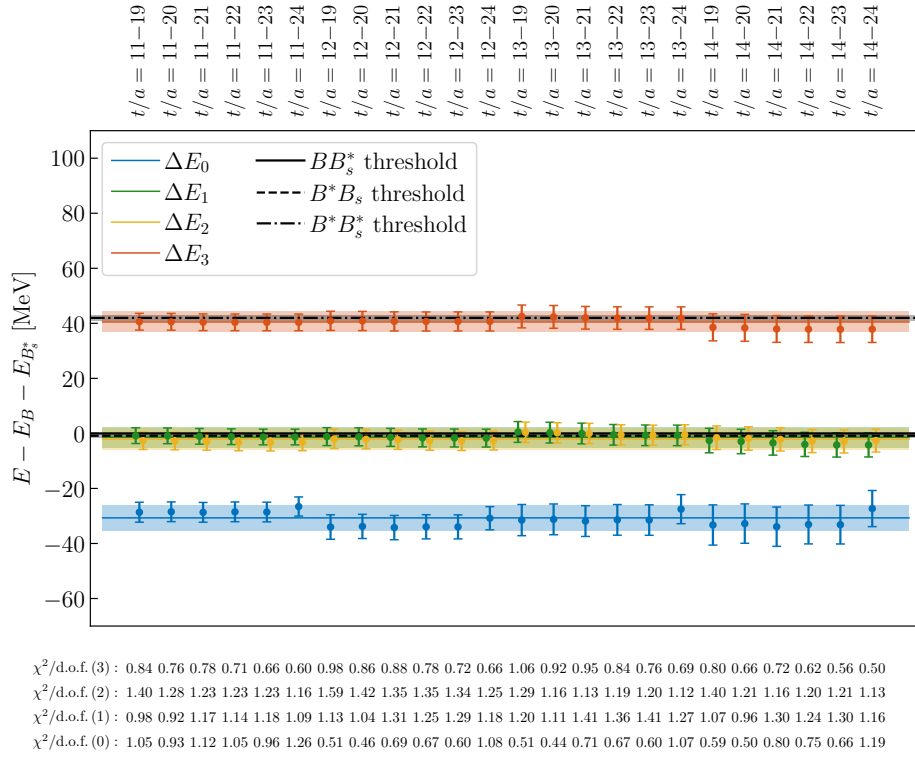


Figure F.12.: Fit results for the four lowest energy levels for the  $\bar{b}b us$  system with  $J^P = 1^+$  relative to the  $BB_s^*$  threshold,  $\Delta E_n = E_n - E_B - E_{B_s^*}$ , obtained on ensemble a09m220.



---

## BIBLIOGRAPHY

---

- [1] K. G. Wilson, “Confinement of Quarks,” *Phys. Rev. D* **10** (1974) 2445–2459.
- [2] M. Gell-Mann, “A Schematic Model of Baryons and Mesons,” *Phys. Lett.* **8** (1964) 214–215.
- [3] G. Zweig, *An  $SU(3)$  model for strong interaction symmetry and its breaking. Version 2*, pp. 22–101. 2, 1964.
- [4] Belle Collaboration, Z. Q. Liu *et al.*, “Study of  $e^+e^- \rightarrow \pi^+\pi^- J/\psi$  and Observation of a Charged Charmoniumlike State at Belle,” *Phys. Rev. Lett.* **110** (2013) 252002, [arXiv:1304.0121 \[hep-ex\]](#). [Erratum: *Phys. Rev. Lett.* 111, 019901 (2013)].
- [5] BESIII Collaboration, M. Ablikim *et al.*, “Observation of a Charged Charmoniumlike Structure in  $e^+e^- \rightarrow \pi^+\pi^- J/\psi$  at  $\sqrt{s}=4.26$  GeV,” *Phys. Rev. Lett.* **110** (2013) 252001, [arXiv:1303.5949 \[hep-ex\]](#).
- [6] Belle Collaboration, A. Bondar *et al.*, “Observation of two charged bottomonium-like resonances in  $Y(5S)$  decays,” *Phys. Rev. Lett.* **108** (2012) 122001, [arXiv:1110.2251 \[hep-ex\]](#).
- [7] Belle Collaboration, K. Chilikin *et al.*, “Observation of a new charged charmoniumlike state in  $\bar{B}^0 \rightarrow J/\psi K^- \pi^+$  decays,” *Phys. Rev. D* **90** no. 11, (2014) 112009, [arXiv:1408.6457 \[hep-ex\]](#).
- [8] BESIII Collaboration, M. Ablikim *et al.*, “Observation of a charged charmoniumlike structure in  $e^+e^- \rightarrow (D^* \bar{D}^*)^\pm \pi^\mp$  at  $\sqrt{s} = 4.26$  GeV,” *Phys. Rev. Lett.* **112** no. 13, (2014) 132001, [arXiv:1308.2760 \[hep-ex\]](#).
- [9] BESIII Collaboration, M. Ablikim *et al.*, “Observation of a Charged Charmoniumlike Structure  $Z_c(4020)$  and Search for the  $Z_c(3900)$  in  $e^+e^- \rightarrow \pi^+\pi^- h_c$ ,” *Phys. Rev. Lett.* **111** no. 24, (2013) 242001, [arXiv:1309.1896 \[hep-ex\]](#).
- [10] BESIII Collaboration, M. Ablikim *et al.*, “Observation of a charged  $(D\bar{D}^*)^\pm$  mass peak in  $e^+e^- \rightarrow \pi D\bar{D}^*$  at  $\sqrt{s} = 4.26$  GeV,” *Phys. Rev. Lett.* **112** no. 2, (2014) 022001, [arXiv:1310.1163 \[hep-ex\]](#).

- [11] **BESIII** Collaboration, M. Ablikim *et al.*, “Observation of  $e^+e^- \rightarrow \pi^0\pi^0h_c$  and a Neutral Charmoniumlike Structure  $Z_c(4020)^0$ ,” *Phys. Rev. Lett.* **113** no. 21, (2014) 212002, [arXiv:1409.6577 \[hep-ex\]](#).
- [12] **LHCb** Collaboration, R. Aaij *et al.*, “Observation of the resonant character of the  $Z(4430)^-$  state,” *Phys. Rev. Lett.* **112** no. 22, (2014) 222002, [arXiv:1404.1903 \[hep-ex\]](#).
- [13] S. L. Olsen, “XYZ Meson Spectroscopy,” *PoS Bormio2015* (2015) 050, [arXiv:1511.01589 \[hep-ex\]](#).
- [14] A. Esposito, A. Pilloni, and A. D. Polosa, “Multiquark Resonances,” *Phys. Rept.* **668** (2017) 1–97, [arXiv:1611.07920 \[hep-ph\]](#).
- [15] R. F. Lebed, R. E. Mitchell, and E. S. Swanson, “Heavy-Quark QCD Exotica,” *Prog. Part. Nucl. Phys.* **93** (2017) 143–194, [arXiv:1610.04528 \[hep-ph\]](#).
- [16] J.-M. Richard, “Exotic hadrons: review and perspectives,” *Few Body Syst.* **57** no. 12, (2016) 1185–1212, [arXiv:1606.08593 \[hep-ph\]](#).
- [17] S. L. Olsen, T. Skwarnicki, and D. Zieminska, “Nonstandard heavy mesons and baryons: Experimental evidence,” *Rev. Mod. Phys.* **90** no. 1, (2018) 015003, [arXiv:1708.04012 \[hep-ph\]](#).
- [18] N. Brambilla, S. Eidelman, C. Hanhart, A. Nefediev, C.-P. Shen, C. E. Thomas, A. Vairo, and C.-Z. Yuan, “The XYZ states: experimental and theoretical status and perspectives,” *Phys. Rept.* **873** (2020) 1–154, [arXiv:1907.07583 \[hep-ex\]](#).
- [19] H.-X. Chen, W. Chen, X. Liu, Y.-R. Liu, and S.-L. Zhu, “An updated review of the new hadron states,” [arXiv:2204.02649 \[hep-ph\]](#).
- [20] **LHCb** Collaboration, R. Aaij *et al.*, “Study of the doubly charmed tetraquark  $T_{cc}^+$ ,” [arXiv:2109.01056 \[hep-ex\]](#).
- [21] **LHCb** Collaboration, R. Aaij *et al.*, “Observation of an exotic narrow doubly charmed tetraquark,” [arXiv:2109.01038 \[hep-ex\]](#).
- [22] M. Luscher, “Two particle states on a torus and their relation to the scattering matrix,” *Nucl. Phys. B* **354** (1991) 531–578.
- [23] R. A. Briceno, J. J. Dudek, and R. D. Young, “Scattering processes and resonances from lattice QCD,” *Rev. Mod. Phys.* **90** no. 2, (2018) 025001, [arXiv:1706.06223 \[hep-lat\]](#).
- [24] S. Meinel, M. Pflaumer, and M. Wagner, “Search for  $\bar{b}\bar{b}us$  and  $\bar{b}\bar{c}ud$  tetraquark bound states using lattice QCD,” *Phys. Rev. D* **106** no. 3, (2022) 034507, [arXiv:2205.13982 \[hep-lat\]](#).

- 
- [25] J. Carlson, L. Heller, and J. A. Tjon, “Stability of Dimesons,” *Phys. Rev. D* **37** (1988) 744.
- [26] A. V. Manohar and M. B. Wise, “Exotic  $QQ\bar{q}\bar{q}$  states in QCD,” *Nucl. Phys. B* **399** (1993) 17–33, [arXiv:hep-ph/9212236](#).
- [27] E. J. Eichten and C. Quigg, “Heavy-quark symmetry implies stable heavy tetraquark mesons  $Q_i Q_j \bar{q}_k \bar{q}_l$ ,” *Phys. Rev. Lett.* **119** no. 20, (2017) 202002, [arXiv:1707.09575 \[hep-ph\]](#).
- [28] **European Twisted Mass** Collaboration, P. Bicudo and M. Wagner, “Lattice QCD signal for a bottom-bottom tetraquark,” *Phys. Rev. D* **87** no. 11, (2013) 114511, [arXiv:1209.6274 \[hep-ph\]](#).
- [29] Z. S. Brown and K. Orginos, “Tetraquark bound states in the heavy-light heavy-light system,” *Phys. Rev. D* **86** (2012) 114506, [arXiv:1210.1953 \[hep-lat\]](#).
- [30] P. Bicudo, K. Cichy, A. Peters, B. Wagenbach, and M. Wagner, “Evidence for the existence of  $ud\bar{b}\bar{b}$  and the non-existence of  $ss\bar{b}\bar{b}$  and  $cc\bar{b}\bar{b}$  tetraquarks from lattice QCD,” *Phys. Rev. D* **92** no. 1, (2015) 014507, [arXiv:1505.00613 \[hep-lat\]](#).
- [31] P. Bicudo, K. Cichy, A. Peters, and M. Wagner, “ $BB$  interactions with static bottom quarks from Lattice QCD,” *Phys. Rev. D* **93** no. 3, (2016) 034501, [arXiv:1510.03441 \[hep-lat\]](#).
- [32] P. Bicudo, J. Scheunert, and M. Wagner, “Including heavy spin effects in the prediction of a  $\bar{b}b\bar{u}d$  tetraquark with lattice QCD potentials,” *Phys. Rev. D* **95** no. 3, (2017) 034502, [arXiv:1612.02758 \[hep-lat\]](#).
- [33] P. Bicudo, M. Cardoso, A. Peters, M. Pflaumer, and M. Wagner, “ $ud\bar{b}\bar{b}$  tetraquark resonances with lattice QCD potentials and the Born-Oppenheimer approximation,” *Phys. Rev. D* **96** no. 5, (2017) 054510, [arXiv:1704.02383 \[hep-lat\]](#).
- [34] J. Hoffmann, A. Zimmermann-Santos, and M. Wagner, “Inclusion of heavy spin effects in the  $ud\bar{b}\bar{b}$   $I(J^P)=0(1^-)$  four-quark channel in the Born-Oppenheimer approximation,” *PoS LATTICE2022* (2023) 262, [arXiv:2211.15765 \[hep-lat\]](#).
- [35] A. Francis, R. J. Hudspith, R. Lewis, and K. Maltman, “Lattice Prediction for Deeply Bound Doubly Heavy Tetraquarks,” *Phys. Rev. Lett.* **118** no. 14, (2017) 142001, [arXiv:1607.05214 \[hep-lat\]](#).

- [36] P. Junnarkar, N. Mathur, and M. Padmanath, “Study of doubly heavy tetraquarks in Lattice QCD,” *Phys. Rev. D* **99** no. 3, (2019) 034507, [arXiv:1810.12285 \[hep-lat\]](#).
- [37] L. Leskovec, S. Meinel, M. Pflaumer, and M. Wagner, “Lattice QCD investigation of a doubly-bottom  $\bar{b}b\bar{u}d$  tetraquark with quantum numbers  $I(J^P) = 0(1^+)$ ,” *Phys. Rev. D* **100** no. 1, (2019) 014503, [arXiv:1904.04197 \[hep-lat\]](#).
- [38] P. Mohanta and S. Basak, “Construction of  $bb\bar{u}\bar{d}$  tetraquark states on lattice with NRQCD bottom and HISQ up and down quarks,” *Phys. Rev. D* **102** no. 9, (2020) 094516, [arXiv:2008.11146 \[hep-lat\]](#).
- [39] T. Aoki, S. Aoki, and T. Inoue, “Lattice study on a tetra-quark state  $T_{bb}$  in the HAL QCD method,” [arXiv:2306.03565 \[hep-lat\]](#).
- [40] R. J. Hudspith and D. Mohler, “Exotic Tetraquark states with two  $\bar{b}$ -quarks and  $J^P = 0^+$  and  $1^+$   $B_s$  states in a nonperturbatively-tuned Lattice NRQCD setup,” [arXiv:2303.17295 \[hep-lat\]](#).
- [41] A. Francis, R. J. Hudspith, R. Lewis, and K. Maltman, “Evidence for charm-bottom tetraquarks and the mass dependence of heavy-light tetraquark states from lattice QCD,” *Phys. Rev. D* **99** no. 5, (2019) 054505, [arXiv:1810.10550 \[hep-lat\]](#).
- [42] R. J. Hudspith, B. Colquhoun, A. Francis, R. Lewis, and K. Maltman, “A lattice investigation of exotic tetraquark channels,” *Phys. Rev. D* **102** (2020) 114506, [arXiv:2006.14294 \[hep-lat\]](#).
- [43] N. Mathur and M. Padmanath, “ $\bar{b}\bar{c}q_1q_2$  four-quark states from Lattice QCD,” *PoS LATTICE2021* (2022) 443, [arXiv:2111.01147 \[hep-lat\]](#).
- [44] M. A. Moinester, “How to search for doubly charmed baryons and tetraquarks,” *Z. Phys. A* **355** (1996) 349–362, [arXiv:hep-ph/9506405](#).
- [45] A. Ali, A. Y. Parkhomenko, Q. Qin, and W. Wang, “Prospects of discovering stable double-heavy tetraquarks at a Tera-Z factory,” *Phys. Lett. B* **782** (2018) 412–420, [arXiv:1805.02535 \[hep-ph\]](#).
- [46] A. Ali, Q. Qin, and W. Wang, “Discovery potential of stable and near-threshold doubly heavy tetraquarks at the LHC,” *Phys. Lett. B* **785** (2018) 605–609, [arXiv:1806.09288 \[hep-ph\]](#).
- [47] M. Padmanath and S. Prelovsek, “Evidence for a doubly charm tetraquark pole in  $DD^*$  scattering on the lattice,” [arXiv:2202.10110 \[hep-lat\]](#).



- 
- [48] D. Mohler, C. B. Lang, L. Leskovec, S. Prelovsek, and R. M. Woloshyn, “ $D_{s0}^*$ (2317) Meson and  $D$ -Meson-Kaon Scattering from Lattice QCD,” *Phys. Rev. Lett.* **111** no. 22, (2013) 222001, [arXiv:1308.3175 \[hep-lat\]](#).
- [49] C. B. Lang, L. Leskovec, D. Mohler, S. Prelovsek, and R. M. Woloshyn, “ $D_s$  mesons with  $DK$  and  $D^*K$  scattering near threshold,” *Phys. Rev. D* **90** no. 3, (2014) 034510, [arXiv:1403.8103 \[hep-lat\]](#).
- [50] C. Gattringer and C. B. Lang, *Quantum chromodynamics on the lattice*, vol. 788. Springer, Berlin, 2010.
- [51] H. J. Rothe, *Lattice Gauge Theories : An Introduction (Fourth Edition)*, vol. 43. World Scientific Publishing Company, 2012.
- [52] M. Luscher and P. Weisz, “On-Shell Improved Lattice Gauge Theories,” *Commun. Math. Phys.* **97** (1985) 59. [Erratum: *Commun.Math.Phys.* 98, 433 (1985)].
- [53] M. Luscher and P. Weisz, “Computation of the Action for On-Shell Improved Lattice Gauge Theories at Weak Coupling,” *Phys. Lett. B* **158** (1985) 250–254.
- [54] Y. Iwasaki and T. Yoshie, “Renormalization Group Improved Action for SU(3) Lattice Gauge Theory and the String Tension,” *Phys. Lett. B* **143** (1984) 449–452.
- [55] Y. Iwasaki, “Renormalization group analysis of lattice theories and improved lattice action: Two-dimensional non-linear O(N) sigma model,” *Nucl. Phys. B* **258** (1985) 141–156.
- [56] H. B. Nielsen and M. Ninomiya, “Absence of Neutrinos on a Lattice. 1. Proof by Homotopy Theory,” *Nucl. Phys. B* **185** (1981) 20. [Erratum: *Nucl.Phys.B* 195, 541 (1982)].
- [57] H. B. Nielsen and M. Ninomiya, “Absence of Neutrinos on a Lattice. 2. Intuitive Topological Proof,” *Nucl. Phys. B* **193** (1981) 173–194.
- [58] H. B. Nielsen and M. Ninomiya, “No Go Theorem for Regularizing Chiral Fermions,” *Phys. Lett. B* **105** (1981) 219–223.
- [59] P. H. Ginsparg and K. G. Wilson, “A Remnant of Chiral Symmetry on the Lattice,” *Phys. Rev. D* **25** (1982) 2649.
- [60] M. Luscher, “Exact chiral symmetry on the lattice and the Ginsparg-Wilson relation,” *Phys. Lett. B* **428** (1998) 342–345, [arXiv:hep-lat/9802011](#).
- [61] R. Narayanan and H. Neuberger, “Infinitely many regulator fields for chiral fermions,” *Phys. Lett. B* **302** (1993) 62–69, [arXiv:hep-lat/9212019](#).

- [62] R. Narayanan and H. Neuberger, “Chiral fermions on the lattice,” *Phys. Rev. Lett.* **71** no. 20, (1993) 3251, [arXiv:hep-lat/9308011](#).
- [63] R. Narayanan and H. Neuberger, “Chiral determinant as an overlap of two vacua,” *Nucl. Phys. B* **412** (1994) 574–606, [arXiv:hep-lat/9307006](#).
- [64] R. Narayanan and H. Neuberger, “A Construction of lattice chiral gauge theories,” *Nucl. Phys. B* **443** (1995) 305–385, [arXiv:hep-th/9411108](#).
- [65] H. Neuberger, “Exactly massless quarks on the lattice,” *Phys. Lett. B* **417** (1998) 141–144, [arXiv:hep-lat/9707022](#).
- [66] K. Symanzik, “Continuum Limit and Improved Action in Lattice Theories. 1. Principles and  $\varphi^4$  Theory,” *Nucl. Phys. B* **226** (1983) 187–204.
- [67] K. Symanzik, “Continuum Limit and Improved Action in Lattice Theories. 2. O(N) Nonlinear Sigma Model in Perturbation Theory,” *Nucl. Phys. B* **226** (1983) 205–227.
- [68] M. Luscher, S. Sint, R. Sommer, and P. Weisz, “Chiral symmetry and O(a) improvement in lattice QCD,” *Nucl. Phys. B* **478** (1996) 365–400, [arXiv:hep-lat/9605038](#).
- [69] M. Luscher, S. Sint, R. Sommer, P. Weisz, and U. Wolff, “Nonperturbative O(a) improvement of lattice QCD,” *Nucl. Phys. B* **491** (1997) 323–343, [arXiv:hep-lat/9609035](#).
- [70] **ALPHA** Collaboration, K. Jansen and R. Sommer, “O(a) improvement of lattice QCD with two flavors of Wilson quarks,” *Nucl. Phys. B* **530** (1998) 185–203, [arXiv:hep-lat/9803017](#). [Erratum: *Nucl.Phys.B* 643, 517–518 (2002)].
- [71] G. P. Lepage and P. B. Mackenzie, “On the viability of lattice perturbation theory,” *Phys. Rev. D* **48** (1993) 2250–2264, [arXiv:hep-lat/9209022](#).
- [72] D. B. Kaplan, “A Method for simulating chiral fermions on the lattice,” *Phys. Lett. B* **288** (1992) 342–347, [arXiv:hep-lat/9206013](#).
- [73] Y. Shamir, “Chiral fermions from lattice boundaries,” *Nucl. Phys. B* **406** (1993) 90–106, [arXiv:hep-lat/9303005](#).
- [74] V. Furman and Y. Shamir, “Axial symmetries in lattice QCD with Kaplan fermions,” *Nucl. Phys. B* **439** (1995) 54–78, [arXiv:hep-lat/9405004](#).
- [75] P. M. Vranas, “Chiral symmetry restoration in the Schwinger model with domain wall fermions,” *Phys. Rev. D* **57** (1998) 1415–1432, [arXiv:hep-lat/9705023](#).

- 
- [76] D. B. Kaplan, “Chiral Symmetry and Lattice Fermions,” in *Les Houches Summer School: Session 93: Modern perspectives in lattice QCD: Quantum field theory and high performance computing*, pp. 223–272. 12, 2009. [arXiv:0912.2560 \[hep-lat\]](#).
- [77] P. Vranas, “Domain wall fermions and MC simulations of vector theories,” *Nucl. Phys. B Proc. Suppl.* **53** (1997) 278–282, [arXiv:hep-lat/9608078](#).
- [78] J. B. Kogut and L. Susskind, “Hamiltonian Formulation of Wilson’s Lattice Gauge Theories,” *Phys. Rev. D* **11** (1975) 395–408.
- [79] F. Gliozzi, “Spinor Algebra of the one Component Lattice Fermions,” *Nucl. Phys. B* **204** (1982) 419–428.
- [80] H. Kluberg-Stern, A. Morel, O. Napoly, and B. Petersson, “Flavors of Lagrangian Susskind Fermions,” *Nucl. Phys. B* **220** (1983) 447–470.
- [81] G. P. Lepage, “Flavor symmetry restoration and Symanzik improvement for staggered quarks,” *Phys. Rev. D* **59** (1999) 074502, [arXiv:hep-lat/9809157](#).
- [82] **HPQCD, UKQCD** Collaboration, E. Follana, Q. Mason, C. Davies, K. Hornbostel, G. P. Lepage, J. Shigemitsu, H. Trottier, and K. Wong, “Highly improved staggered quarks on the lattice, with applications to charm physics,” *Phys. Rev. D* **75** (2007) 054502, [arXiv:hep-lat/0610092](#).
- [83] S. Naik, “On-shell Improved Lattice Action for QCD With Susskind Fermions and Asymptotic Freedom Scale,” *Nucl. Phys. B* **316** (1989) 238–268.
- [84] K. Cichy, G. Herdoiza, and K. Jansen, “Continuum Limit of Overlap Valence Quarks on a Twisted Mass Sea,” *Nucl. Phys. B* **847** (2011) 179–196, [arXiv:1012.4412 \[hep-lat\]](#).
- [85] K. Cichy, V. Drach, E. Garcia-Ramos, G. Herdoiza, and K. Jansen, “Overlap valence quarks on a twisted mass sea: a case study for mixed action Lattice QCD,” *Nucl. Phys. B* **869** (2013) 131–163, [arXiv:1211.1605 \[hep-lat\]](#).
- [86] **PNDME** Collaboration, T. Bhattacharya, V. Cirigliano, S. Cohen, R. Gupta, A. Joseph, H.-W. Lin, and B. Yoon, “Iso-vector and Iso-scalar Tensor Charges of the Nucleon from Lattice QCD,” *Phys. Rev. D* **92** no. 9, (2015) 094511, [arXiv:1506.06411 \[hep-lat\]](#).
- [87] **Particle Data Group** Collaboration, R. L. Workman *et al.*, “Review of Particle Physics,” *PTEP* **2022** (2022) 083C01.
- [88] B. A. Thacker and G. P. Lepage, “Heavy quark bound states in lattice QCD,” *Phys. Rev. D* **43** (1991) 196–208.

- [89] S. Hashimoto and T. Onogi, “Heavy quarks on the lattice,” *Ann. Rev. Nucl. Part. Sci.* **54** (2004) 451–486, [arXiv:hep-ph/0407221](#).
- [90] S. Meinel, *Heavy quark physics on the lattice with improved nonrelativistic actions*. PhD thesis, Cambridge U., DAMTP, 3, 2010.
- [91] J. G. Korner and G. Thompson, “The Heavy mass limit in field theory and the heavy quark effective theory,” *Phys. Lett. B* **264** (1991) 185–192.
- [92] M. Pflaumer, *Investigation of the Heavy-Light Tetraquark System  $\bar{b}bud$  Using Lattice NRQCD*. Master’s thesis, Goethe-Universität, Frankfurt am Main, 9, 2018. [https://itp.uni-frankfurt.de/~mwagner/theses/MA\\_Pflaumer.pdf](https://itp.uni-frankfurt.de/~mwagner/theses/MA_Pflaumer.pdf).
- [93] A. Peters, *Investigation of heavy-light four-quark systems by means of Lattice QCD*. PhD thesis, Goethe-Universität, Frankfurt am Main, 7, 2017. [https://itp.uni-frankfurt.de/~mwagner/theses/PHD\\_Peters.pdf](https://itp.uni-frankfurt.de/~mwagner/theses/PHD_Peters.pdf).
- [94] G. P. Lepage, L. Magnea, C. Nakhleh, U. Magnea, and K. Hornbostel, “Improved nonrelativistic QCD for heavy quark physics,” *Phys. Rev. D* **46** (1992) 4052–4067, [arXiv:hep-lat/9205007](#).
- [95] N. H. Shakespeare and H. D. Trottier, “Tadpole renormalization and relativistic corrections in lattice NRQCD,” *Phys. Rev. D* **58** (1998) 034502, [arXiv:hep-lat/9802038](#).
- [96] A. X. El-Khadra, A. S. Kronfeld, and P. B. Mackenzie, “Massive fermions in lattice gauge theory,” *Phys. Rev. D* **55** (1997) 3933–3957, [arXiv:hep-lat/9604004](#).
- [97] M. B. Oktay and A. S. Kronfeld, “New lattice action for heavy quarks,” *Phys. Rev. D* **78** (2008) 014504, [arXiv:0803.0523 \[hep-lat\]](#).
- [98] P. Chen, “Heavy quarks on anisotropic lattices: The Charmonium spectrum,” *Phys. Rev. D* **64** (2001) 034509, [arXiv:hep-lat/0006019](#).
- [99] S. Aoki, Y. Kuramashi, and S.-i. Tominaga, “Relativistic heavy quarks on the lattice,” *Prog. Theor. Phys.* **109** (2003) 383–413, [arXiv:hep-lat/0107009](#).
- [100] S. Aoki, Y. Kayaba, and Y. Kuramashi, “A Perturbative determination of mass dependent  $O(a)$  improvement coefficients in a relativistic heavy quark action,” *Nucl. Phys. B* **697** (2004) 271–301, [arXiv:hep-lat/0309161](#).
- [101] N. H. Christ, M. Li, and H.-W. Lin, “Relativistic Heavy Quark Effective Action,” *Phys. Rev. D* **76** (2007) 074505, [arXiv:hep-lat/0608006](#).
- [102] H.-W. Lin and N. Christ, “Non-perturbatively Determined Relativistic Heavy Quark Action,” *Phys. Rev. D* **76** (2007) 074506, [arXiv:hep-lat/0608005](#).

- 
- [103] T. Burch, C. DeTar, M. Di Pierro, A. X. El-Khadra, E. D. Freeland, S. Gottlieb, A. S. Kronfeld, L. Levkova, P. B. Mackenzie, and J. N. Simone, “Quarkonium mass splittings in three-flavor lattice QCD,” *Phys. Rev. D* **81** (2010) 034508, [arXiv:0912.2701 \[hep-lat\]](#).
- [104] **Fermilab Lattice, MILC** Collaboration, C. Bernard *et al.*, “Tuning Fermilab Heavy Quarks in 2+1 Flavor Lattice QCD with Application to Hyperfine Splittings,” *Phys. Rev. D* **83** (2011) 034503, [arXiv:1003.1937 \[hep-lat\]](#).
- [105] **RBC, UKQCD** Collaboration, Y. Aoki, N. H. Christ, J. M. Flynn, T. Izubuchi, C. Lehner, M. Li, H. Peng, A. Soni, R. S. Van de Water, and O. Witzel, “Nonperturbative tuning of an improved relativistic heavy-quark action with application to bottom spectroscopy,” *Phys. Rev. D* **86** (2012) 116003, [arXiv:1206.2554 \[hep-lat\]](#).
- [106] D. Mohler, S. Prelovsek, and R. M. Woloshyn, “ $D\pi$  scattering and  $D$  meson resonances from lattice QCD,” *Phys. Rev. D* **87** no. 3, (2013) 034501, [arXiv:1208.4059 \[hep-lat\]](#).
- [107] M. Luscher, “Volume Dependence of the Energy Spectrum in Massive Quantum Field Theories. 1. Stable Particle States,” *Commun. Math. Phys.* **104** (1986) 177.
- [108] J. J. Dudek, “Recent progress on hadron spectroscopy from lattice QCD,” in *13th Conference on the Intersections of Particle and Nuclear Physics*. 9, 2018. [arXiv:1809.07350 \[hep-lat\]](#).
- [109] M. Luscher, “Volume Dependence of the Energy Spectrum in Massive Quantum Field Theories. 2. Scattering States,” *Commun. Math. Phys.* **105** (1986) 153–188.
- [110] M. Luscher and U. Wolff, “How to Calculate the Elastic Scattering Matrix in Two-dimensional Quantum Field Theories by Numerical Simulation,” *Nucl. Phys. B* **339** (1990) 222–252.
- [111] M. Luscher, “Signatures of unstable particles in finite volume,” *Nucl. Phys. B* **364** (1991) 237–251.
- [112] K. Rummukainen and S. A. Gottlieb, “Resonance scattering phase shifts on a nonrest frame lattice,” *Nucl. Phys. B* **450** (1995) 397–436, [arXiv:hep-lat/9503028](#).
- [113] X. Feng, K. Jansen, and D. B. Renner, “Resonance Parameters of the  $\rho$ -Meson from Lattice QCD,” *Phys. Rev. D* **83** (2011) 094505, [arXiv:1011.5288 \[hep-lat\]](#).

- [114] **ETM** Collaboration, X. Feng, K. Jansen, and D. B. Renner, “A new moving frame to extract scattering phases in lattice QCD,” PoS **LATTICE2010** (2010) 104, [arXiv:1104.0058 \[hep-lat\]](#).
- [115] Z. Fu, “Rummukainen-Gottlieb’s formula on two-particle system with different mass,” *Phys. Rev. D* **85** (2012) 014506, [arXiv:1110.0319 \[hep-lat\]](#).
- [116] L. Leskovec and S. Prelovsek, “Scattering phase shifts for two particles of different mass and non-zero total momentum in lattice QCD,” *Phys. Rev. D* **85** (2012) 114507, [arXiv:1202.2145 \[hep-lat\]](#).
- [117] C. h. Kim, C. T. Sachrajda, and S. R. Sharpe, “Finite-volume effects for two-hadron states in moving frames,” *Nucl. Phys. B* **727** (2005) 218–243, [arXiv:hep-lat/0507006](#).
- [118] R. C. Johnson, “Angular momentum on a lattice,” *Phys. Lett.* **114B** (1982) 147–151.
- [119] S. He, X. Feng, and C. Liu, “Two particle states and the S-matrix elements in multi-channel scattering,” *JHEP* **07** (2005) 011, [arXiv:hep-lat/0504019](#).
- [120] M. Doring, U.-G. Meissner, E. Oset, and A. Rusetsky, “Unitarized Chiral Perturbation Theory in a finite volume: Scalar meson sector,” *Eur. Phys. J. A* **47** (2011) 139, [arXiv:1107.3988 \[hep-lat\]](#).
- [121] **HAL QCD** Collaboration, S. Aoki, N. Ishii, T. Doi, T. Hatsuda, Y. Ikeda, T. Inoue, K. Murano, H. Nemura, and K. Sasaki, “Extraction of Hadron Interactions above Inelastic Threshold in Lattice QCD,” *Proc. Japan Acad. B* **87** (2011) 509–517, [arXiv:1106.2281 \[hep-lat\]](#).
- [122] R. A. Briceno and Z. Davoudi, “Moving multichannel systems in a finite volume with application to proton-proton fusion,” *Phys. Rev. D* **88** no. 9, (2013) 094507, [arXiv:1204.1110 \[hep-lat\]](#).
- [123] M. T. Hansen and S. R. Sharpe, “Multiple-channel generalization of Lellouch-Luscher formula,” *Phys. Rev. D* **86** (2012) 016007, [arXiv:1204.0826 \[hep-lat\]](#).
- [124] P. Guo, J. Dudek, R. Edwards, and A. P. Szczepaniak, “Coupled-channel scattering on a torus,” *Phys. Rev. D* **88** no. 1, (2013) 014501, [arXiv:1211.0929 \[hep-lat\]](#).
- [125] R. A. Briceno, “Two-particle multichannel systems in a finite volume with arbitrary spin,” *Phys. Rev. D* **89** no. 7, (2014) 074507, [arXiv:1401.3312 \[hep-lat\]](#).

- 
- [126] C. E. Thomas, R. G. Edwards, and J. J. Dudek, “Helicity operators for mesons in flight on the lattice,” *Phys. Rev. D* **85** (2012) 014507, [arXiv:1107.1930 \[hep-lat\]](#).
- [127] J. J. Dudek, R. G. Edwards, M. J. Peardon, D. G. Richards, and C. E. Thomas, “Toward the excited meson spectrum of dynamical QCD,” *Phys. Rev. D* **82** (2010) 034508, [arXiv:1004.4930 \[hep-ph\]](#).
- [128] J. J. Dudek, R. G. Edwards, and C. E. Thomas, “ $S$  and  $D$ -wave phase shifts in isospin-2  $\pi\pi$  scattering from lattice QCD,” *Phys. Rev. D* **86** (2012) 034031, [arXiv:1203.6041 \[hep-ph\]](#).
- [129] D. J. Wilson, J. J. Dudek, R. G. Edwards, and C. E. Thomas, “Resonances in coupled  $\pi K, \eta K$  scattering from lattice QCD,” *Phys. Rev. D* **91** no. 5, (2015) 054008, [arXiv:1411.2004 \[hep-ph\]](#).
- [130] S. Prelovsek, U. Skerbis, and C. B. Lang, “Lattice operators for scattering of particles with spin,” *JHEP* **01** (2017) 129, [arXiv:1607.06738 \[hep-lat\]](#).
- [131] M. Padmanath, S. Collins, D. Mohler, S. Piemonte, S. Prelovsek, A. Schäfer, and S. Weishaupl, “Identifying spin and parity of charmonia in flight with lattice QCD,” *Phys. Rev. D* **99** no. 1, (2019) 014513, [arXiv:1811.04116 \[hep-lat\]](#).
- [132] M. Gell-Mann, “The Eightfold Way: A Theory of strong interaction symmetry,”
- [133] Y. Ne’eman, “Derivation of strong interactions from a gauge invariance,” *Nucl. Phys.* **26** (1961) 222–229.
- [134] R. L. Jaffe, “Exotica,” *Phys. Rept.* **409** (2005) 1–45, [arXiv:hep-ph/0409065](#).
- [135] **Hadron Spectrum** Collaboration, G. K. C. Cheung, C. E. Thomas, J. J. Dudek, and R. G. Edwards, “Tetraquark operators in lattice QCD and exotic flavour states in the charm sector,” *JHEP* **11** (2017) 033, [arXiv:1709.01417 \[hep-lat\]](#).
- [136] P. Bicudo, A. Peters, S. Velten, and M. Wagner, “Importance of meson-meson and of diquark-antidiquark creation operators for a  $\bar{b}bud$  tetraquark,” *Phys. Rev. D* **103** no. 11, (2021) 114506, [arXiv:2101.00723 \[hep-lat\]](#).
- [137] Z. S. Brown, W. Detmold, S. Meinel, and K. Orginos, “Charmed bottom baryon spectroscopy from lattice QCD,” *Phys. Rev. D* **90** no. 9, (2014) 094507, [arXiv:1409.0497 \[hep-lat\]](#).
- [138] C. Michael, “Fitting correlated data,” *Phys. Rev. D* **49** (1994) 2616–2619, [arXiv:hep-lat/9310026](#).



- [139] B. Blossier, M. Della Morte, G. von Hippel, T. Mendes, and R. Sommer, “On the generalized eigenvalue method for energies and matrix elements in lattice field theory,” *JHEP* **04** (2009) 094, [arXiv:0902.1265 \[hep-lat\]](#).
- [140] S. Meinel, *User manual for QMBF and MBF*.  
[http://www.stefanmeinel.com/software/QMBF\\_MBF/](http://www.stefanmeinel.com/software/QMBF_MBF/).
- [141] R. Barrett, M. Berry, T. F. Chan, J. Demmel, J. Donato, J. Dongarra, V. Eijkhout, R. Pozo, C. Romine, and H. van der Vorst, *Templates for the Solution of Linear Systems: Building Blocks for Iterative Methods*. Society for Industrial and Applied Mathematics, 1994.
- [142] H. A. van der Vorst, “Bi-cgstab: A fast and smoothly converging variant of bi-cg for the solution of nonsymmetric linear systems,” *SIAM Journal on Scientific and Statistical Computing* **13** no. 2, (1992) 631–644.
- [143] M. Luscher, “Local coherence and deflation of the low quark modes in lattice QCD,” *JHEP* **07** (2007) 081, [arXiv:0706.2298 \[hep-lat\]](#).
- [144] J. Brannick, R. C. Brower, M. A. Clark, J. C. Osborn, and C. Rebbi, “Adaptive Multigrid Algorithm for Lattice QCD,” *Phys. Rev. Lett.* **100** (2008) 041601, [arXiv:0707.4018 \[hep-lat\]](#).
- [145] R. Babich, J. Brannick, R. C. Brower, M. A. Clark, T. A. Manteuffel, S. F. McCormick, J. C. Osborn, and C. Rebbi, “Adaptive multigrid algorithm for the lattice Wilson-Dirac operator,” *Phys. Rev. Lett.* **105** (2010) 201602, [arXiv:1005.3043 \[hep-lat\]](#).
- [146] A. Frommer, K. Kahl, S. Krieg, B. Leder, and M. Rottmann, “Adaptive Aggregation Based Domain Decomposition Multigrid for the Lattice Wilson Dirac Operator,” *SIAM J. Sci. Comput.* **36** (2014) A1581–A1608, [arXiv:1303.1377 \[hep-lat\]](#).
- [147] M. A. Clark, B. Joó, A. Strelchenko, M. Cheng, A. Gambhir, and R. Brower, “Accelerating Lattice QCD Multigrid on GPUs Using Fine-Grained Parallelization,” [arXiv:1612.07873 \[hep-lat\]](#).
- [148] S. Bernardson, P. McCarty, and C. Thron, “Monte Carlo methods for estimating linear combinations of inverse matrix entries in lattice QCD,” *Comput. Phys. Commun.* **78** (1993) 256–264.
- [149] S.-J. Dong and K.-F. Liu, “Stochastic estimation with Z(2) noise,” *Phys. Lett. B* **328** (1994) 130–136, [arXiv:hep-lat/9308015](#).
- [150] J. Foley, K. Jimmy Juge, A. O’Cais, M. Peardon, S. M. Ryan, and J.-I. Skullerud, “Practical all-to-all propagators for lattice QCD,” *Comput. Phys. Commun.* **172** (2005) 145–162, [arXiv:hep-lat/0505023](#).



- 
- [151] A. Abdel-Rehim, C. Alexandrou, J. Berlin, M. Dalla Brida, J. Finkenrath, and M. Wagner, “Investigating efficient methods for computing four-quark correlation functions,” *Comput. Phys. Commun.* **220** (2017) 97–121, [arXiv:1701.07228 \[hep-lat\]](#).
- [152] **UKQCD** Collaboration, M. Foster and C. Michael, “Quark mass dependence of hadron masses from lattice QCD,” *Phys. Rev. D* **59** (1999) 074503, [arXiv:hep-lat/9810021](#).
- [153] **UKQCD** Collaboration, C. McNeile and C. Michael, “Decay width of light quark hybrid meson from the lattice,” *Phys. Rev. D* **73** (2006) 074506, [arXiv:hep-lat/0603007](#).
- [154] M. Kalinowski and M. Wagner, “Masses of  $D$  mesons,  $D_s$  mesons and charmonium states from twisted mass lattice QCD,” *Phys. Rev. D* **92** no. 9, (2015) 094508, [arXiv:1509.02396 \[hep-lat\]](#).
- [155] **LHPC** Collaboration, R. G. Edwards, G. T. Fleming, B. Joo, K. J. Juge, A. C. Lichtl, C. J. Morningstar, D. G. Richards, and S. J. Wallace, “Group theoretical construction of nucleon operators using all-to-all quark propagators,” *PoS LATTICE2007* (2007) 108, [arXiv:0710.3571 \[hep-lat\]](#).
- [156] **APE** Collaboration, M. Albanese *et al.*, “Glueball Masses and String Tension in Lattice QCD,” *Phys. Lett. B* **192** (1987) 163–169.
- [157] A. Hasenfratz and F. Knechtli, “Flavor symmetry and the static potential with hypercubic blocking,” *Phys. Rev. D* **64** (2001) 034504, [arXiv:hep-lat/0103029](#).
- [158] C. Morningstar and M. J. Peardon, “Analytic smearing of SU(3) link variables in lattice QCD,” *Phys. Rev. D* **69** (2004) 054501, [arXiv:hep-lat/0311018](#).
- [159] S. Gusken, U. Low, K. H. Mutter, R. Sommer, A. Patel, and K. Schilling, “Nonsinglet Axial Vector Couplings of the Baryon Octet in Lattice QCD,” *Phys. Lett. B* **227** (1989) 266–269.
- [160] S. Gusken, “A Study of smearing techniques for hadron correlation functions,” *Nucl. Phys. B Proc. Suppl.* **17** (1990) 361–364.
- [161] **European Twisted Mass** Collaboration, C. Alexandrou *et al.*, “Light baryon masses with dynamical twisted mass fermions,” *Phys. Rev. D* **78** (2008) 014509, [arXiv:0803.3190 \[hep-lat\]](#).
- [162] M. Della Morte, B. Jager, T. D. Rae, and H. Wittig, “Improved interpolating fields for hadrons at non-vanishing momentum,” *PoS LATTICE2012* (2012) 260, [arXiv:1211.1288 \[hep-lat\]](#).

- [163] G. S. Bali, B. Lang, B. U. Musch, and A. Schäfer, “Novel quark smearing for hadrons with high momenta in lattice QCD,” *Phys. Rev. D* **93** no. 9, (2016) 094515, [arXiv:1602.05525 \[hep-lat\]](#).
- [164] **ETM** Collaboration, K. Jansen, C. Michael, A. Shindler, and M. Wagner, “The Static-light meson spectrum from twisted mass lattice QCD,” *JHEP* **12** (2008) 058, [arXiv:0810.1843 \[hep-lat\]](#).
- [165] S. R. Beane, W. Detmold, K. Orginos, and M. J. Savage, “Nuclear Physics from Lattice QCD,” *Prog. Part. Nucl. Phys.* **66** (2011) 1–40, [arXiv:1004.2935 \[hep-lat\]](#).
- [166] G. Moir, M. Peardon, S. M. Ryan, C. E. Thomas, and D. J. Wilson, “Coupled-Channel  $D\pi$ ,  $D\eta$  and  $D_s\bar{K}$  Scattering from Lattice QCD,” *JHEP* **10** (2016) 011, [arXiv:1607.07093 \[hep-lat\]](#).
- [167] C. B. Lang, D. Mohler, S. Prelovsek, and M. Vidmar, “Coupled channel analysis of the  $\rho$  meson decay in lattice QCD,” *Phys. Rev. D* **84** no. 5, (2011) 054503, [arXiv:1105.5636 \[hep-lat\]](#). [Erratum: *Phys.Rev.D* 89, 059903 (2014)].
- [168] G. Silvi *et al.*, “ $P$ -wave nucleon-pion scattering amplitude in the  $\Delta(1232)$  channel from lattice QCD,” *Phys. Rev. D* **103** no. 9, (2021) 094508, [arXiv:2101.00689 \[hep-lat\]](#).
- [169] P. Guo, R. Mitchell, and A. P. Szczepaniak, “The Role of  $P$ -wave inelasticity in  $J/\psi\to\pi\pi^+\pi^-\pi^0$ ,” *Phys. Rev. D* **82** (2010) 094002, [arXiv:1006.4371 \[hep-ph\]](#).
- [170] **Hadron Spectrum** Collaboration, J. J. Dudek, R. G. Edwards, and D. J. Wilson, “An  $a_0$  resonance in strongly coupled  $\pi\eta$ ,  $K\bar{K}$  scattering from lattice QCD,” *Phys. Rev. D* **93** no. 9, (2016) 094506, [arXiv:1602.05122 \[hep-ph\]](#).
- [171] A. Woss, C. E. Thomas, J. J. Dudek, R. G. Edwards, and D. J. Wilson, “Dynamically-coupled partial-waves in  $\rho\pi$  isospin-2 scattering from lattice QCD,” *JHEP* **07** (2018) 043, [arXiv:1802.05580 \[hep-lat\]](#).
- [172] G. F. Chew and S. Mandelstam, “Theory of low-energy pion pion interactions,” *Phys. Rev.* **119** (1960) 467–477.
- [173] D. J. Wilson, R. A. Briceño, J. J. Dudek, R. G. Edwards, and C. E. Thomas, “Coupled  $\pi\pi$ ,  $K\bar{K}$  scattering in  $P$ -wave and the  $\rho$  resonance from lattice QCD,” *Phys. Rev. D* **92** no. 9, (2015) 094502, [arXiv:1507.02599 \[hep-ph\]](#).
- [174] M.-L. Du, A. Filin, V. Baru, X.-K. Dong, E. Epelbaum, F.-K. Guo, C. Hanhart, A. Nefediev, J. Nieves, and Q. Wang, “Role of left-hand cut contributions on pole extractions from lattice data: Case study for  $T_{cc}(3875)^+$ ,” [arXiv:2303.09441 \[hep-ph\]](#).

- 
- [175] V. Baru, E. Epelbaum, A. A. Filin, and J. Gegelia, “Low-energy theorems for nucleon-nucleon scattering at unphysical pion masses,” *Phys. Rev. C* **92** no. 1, (2015) 014001, [arXiv:1504.07852 \[nucl-th\]](#).
- [176] V. Baru, E. Epelbaum, and A. A. Filin, “Low-energy theorems for nucleon-nucleon scattering at  $M_\pi = 450$  MeV,” *Phys. Rev. C* **94** no. 1, (2016) 014001, [arXiv:1604.02551 \[nucl-th\]](#).
- [177] A. B. a. Raposo and M. T. Hansen, “The Lüscher scattering formalism on the t-channel cut,” *PoS LATTICE2022* (2023) 051, [arXiv:2301.03981 \[hep-lat\]](#).
- [178] S. M. Dawid, M. H. E. Islam, and R. A. Briceño, “Analytic continuation of the relativistic three-particle scattering amplitudes,” [arXiv:2303.04394 \[nucl-th\]](#).
- [179] **RBC, UKQCD** Collaboration, Y. Aoki *et al.*, “Continuum Limit Physics from 2+1 Flavor Domain Wall QCD,” *Phys. Rev. D* **83** (2011) 074508, [arXiv:1011.0892 \[hep-lat\]](#).
- [180] **RBC, UKQCD** Collaboration, T. Blum *et al.*, “Domain wall QCD with physical quark masses,” *Phys. Rev. D* **93** no. 7, (2016) 074505, [arXiv:1411.7017 \[hep-lat\]](#).
- [181] R. C. Brower, H. Neff, and K. Orginos, “The Möbius domain wall fermion algorithm,” *Comput. Phys. Commun.* **220** (2017) 1–19, [arXiv:1206.5214 \[hep-lat\]](#).
- [182] T. Blum, T. Izubuchi, and E. Shintani, “New class of variance-reduction techniques using lattice symmetries,” *Phys. Rev. D* **88** no. 9, (2013) 094503, [arXiv:1208.4349 \[hep-lat\]](#).
- [183] E. Shintani, R. Arthur, T. Blum, T. Izubuchi, C. Jung, and C. Lehner, “Covariant approximation averaging,” *Phys. Rev. D* **91** no. 11, (2015) 114511, [arXiv:1402.0244 \[hep-lat\]](#).
- [184] T. C. Hammant, A. G. Hart, G. M. von Hippel, R. R. Horgan, and C. J. Monahan, “Radiative improvement of the lattice NRQCD action using the background field method and application to the hyperfine splitting of quarkonium states,” *Phys. Rev. Lett.* **107** (2011) 112002, [arXiv:1105.5309 \[hep-lat\]](#). [Erratum: *Phys.Rev.Lett.* 115, 039901 (2015)].
- [185] **Flavour Lattice Averaging Group** Collaboration, S. Aoki *et al.*, “FLAG Review 2019: Flavour Lattice Averaging Group (FLAG),” *Eur. Phys. J. C* **80** no. 2, (2020) 113, [arXiv:1902.08191 \[hep-lat\]](#).

- [186] MILC Collaboration, A. Bazavov *et al.*, “Lattice QCD Ensembles with Four Flavors of Highly Improved Staggered Quarks,” *Phys. Rev. D* **87** no. 5, (2013) 054505, [arXiv:1212.4768 \[hep-lat\]](#).
- [187] HPQCD Collaboration, A. Hart, G. M. von Hippel, and R. R. Horgan, “Radiative corrections to the lattice gluon action for HISQ improved staggered quarks and the effect of such corrections on the static potential,” *Phys. Rev. D* **79** (2009) 074008, [arXiv:0812.0503 \[hep-lat\]](#).
- [188] T. Bhattacharya, S. D. Cohen, R. Gupta, A. Joseph, H.-W. Lin, and B. Yoon, “Nucleon Charges and Electromagnetic Form Factors from 2+1+1-Flavor Lattice QCD,” *Phys. Rev. D* **89** no. 9, (2014) 094502, [arXiv:1306.5435 \[hep-lat\]](#).
- [189] R. Gupta, Y.-C. Jang, B. Yoon, H.-W. Lin, V. Cirigliano, and T. Bhattacharya, “Isovector Charges of the Nucleon from 2+1+1-flavor Lattice QCD,” *Phys. Rev. D* **98** (2018) 034503, [arXiv:1806.09006 \[hep-lat\]](#).
- [190] HPQCD Collaboration, R. J. Dowdall *et al.*, “The Upsilon spectrum and the determination of the lattice spacing from lattice QCD including charm quarks in the sea,” *Phys. Rev. D* **85** (2012) 054509, [arXiv:1110.6887 \[hep-lat\]](#).
- [191] B. Colquhoun, R. J. Dowdall, J. Koponen, C. T. H. Davies, and G. P. Lepage, “ $B \rightarrow \pi \ell \nu$  at zero recoil from lattice QCD with physical u/d quarks,” *Phys. Rev. D* **93** no. 3, (2016) 034502, [arXiv:1510.07446 \[hep-lat\]](#).
- [192] C. Alexandrou, J. Berlin, J. Finkenrath, T. Leontiou, and M. Wagner, “Tetraquark interpolating fields in a lattice QCD investigation of the  $D_{s0}^*(2317)$  meson,” *Phys. Rev. D* **101** no. 3, (2020) 034502, [arXiv:1911.08435 \[hep-lat\]](#).
- [193] M. Pflaumer, L. Leskovec, S. Meinel, and M. Wagner, “Existence and Non-Existence of Doubly Heavy Tetraquark Bound States,” *PoS LATTICE2021* (2022) 392, [arXiv:2108.10704 \[hep-lat\]](#).
- [194] S. González-Solís, P. Masjuan, and C. Rojas, “Padé approximants to  $B \rightarrow \pi \ell \nu_\ell$  and  $B_s \rightarrow K \ell \nu_\ell$  and determination of  $|V_{ub}|$ ,” *Phys. Rev. D* **104** no. 11, (2021) 114041, [arXiv:2110.06153 \[hep-ph\]](#).
- [195] B. Blok, J. G. Korner, D. Pirjol, and J. C. Rojas, “Spectator effects in the heavy quark effective theory,” *Nucl. Phys. B* **496** (1997) 358–374, [arXiv:hep-ph/9607233](#).
- [196] S. H. Lee and S. Yasui, “Stable multiquark states with heavy quarks in a diquark model,” *Eur. Phys. J. C* **64** (2009) 283–295, [arXiv:0901.2977 \[hep-ph\]](#).

- 
- [197] W. Chen, T. G. Steele, and S.-L. Zhu, “Exotic open-flavor  $bc\bar{q}\bar{q}$ ,  $bc\bar{s}\bar{s}$  and  $qc\bar{q}\bar{b}$ ,  $sc\bar{s}\bar{b}$  tetraquark states,” *Phys. Rev. D* **89** no. 5, (2014) 054037, [arXiv:1310.8337 \[hep-ph\]](#).
- [198] M. Karliner and J. L. Rosner, “Discovery of doubly-charmed  $\Xi_{cc}$  baryon implies a stable  $(bb\bar{u}\bar{d})$  tetraquark,” *Phys. Rev. Lett.* **119** no. 20, (2017) 202001, [arXiv:1707.07666 \[hep-ph\]](#).
- [199] S. Sakai, L. Roca, and E. Oset, “Charm-beauty meson bound states from  $B(B^*)D(D^*)$  and  $B(B^*)\bar{D}(\bar{D}^*)$  interaction,” *Phys. Rev. D* **96** no. 5, (2017) 054023, [arXiv:1704.02196 \[hep-ph\]](#).
- [200] C. Deng, H. Chen, and J. Ping, “Systematical investigation on the stability of doubly heavy tetraquark states,” *Eur. Phys. J. A* **56** no. 1, (2020) 9, [arXiv:1811.06462 \[hep-ph\]](#).
- [201] S. S. Agaev, K. Azizi, B. Barsbay, and H. Sundu, “Weak decays of the axial-vector tetraquark  $T_{bb;\bar{u}\bar{d}}^-$ ,” *Phys. Rev. D* **99** no. 3, (2019) 033002, [arXiv:1809.07791 \[hep-ph\]](#).
- [202] T. F. Caramés, J. Vijande, and A. Valcarce, “Exotic  $bc\bar{q}\bar{q}$  four-quark states,” *Phys. Rev. D* **99** no. 1, (2019) 014006, [arXiv:1812.08991 \[hep-ph\]](#).
- [203] G. Yang, J. Ping, and J. Segovia, “Doubly-heavy tetraquarks,” *Phys. Rev. D* **101** no. 1, (2020) 014001, [arXiv:1911.00215 \[hep-ph\]](#).
- [204] Y. Tan, W. Lu, and J. Ping, “Systematics of  $QQ\bar{q}\bar{q}$  in a chiral constituent quark model,” *Eur. Phys. J. Plus* **135** no. 9, (2020) 716, [arXiv:2004.02106 \[hep-ph\]](#).
- [205] T. Guo, J. Li, J. Zhao, and L. He, “Mass spectra of doubly heavy tetraquarks in an improved chromomagnetic interaction model,” *Phys. Rev. D* **105** no. 1, (2022) 014021, [arXiv:2108.10462 \[hep-ph\]](#).
- [206] J.-M. Richard, A. Valcarce, and J. Vijande, “Doubly-heavy tetraquark bound states and resonances,” in *25th International Conference in Quantum Chromodynamics*. 9, 2022. [arXiv:2209.07372 \[hep-ph\]](#).
- [207] X.-Y. Liu, W.-X. Zhang, and D. Jia, “Doubly heavy tetraquarks: heavy quark bindings and chromomagnetically mixings,” [arXiv:2303.03923 \[hep-ph\]](#).
- [208] D. Ebert, R. N. Faustov, V. O. Galkin, and W. Lucha, “Masses of tetraquarks with two heavy quarks in the relativistic quark model,” *Phys. Rev. D* **76** (2007) 114015, [arXiv:0706.3853 \[hep-ph\]](#).

- [209] W. Park, S. Noh, and S. H. Lee, “Masses of the doubly heavy tetraquarks in a constituent quark model,” *Nucl. Phys. A* **983** (2019) 1–19, [arXiv:1809.05257 \[nucl-th\]](#).
- [210] E. Braaten, L.-P. He, and A. Mohapatra, “Masses of doubly heavy tetraquarks with error bars,” *Phys. Rev. D* **103** no. 1, (2021) 016001, [arXiv:2006.08650 \[hep-ph\]](#).
- [211] Q.-F. Lü, D.-Y. Chen, and Y.-B. Dong, “Masses of doubly heavy tetraquarks  $T_{QQ'}$  in a relativized quark model,” *Phys. Rev. D* **102** no. 3, (2020) 034012, [arXiv:2006.08087 \[hep-ph\]](#).
- [212] Y. Song and D. Jia, “Mass spectra of doubly heavy tetraquarks in diquark–antidiquark picture,” *Commun. Theor. Phys.* **75** no. 5, (2023) 055201, [arXiv:2301.00376 \[hep-ph\]](#).
- [213] T. Iritani, S. Aoki, T. Doi, T. Hatsuda, Y. Ikeda, T. Inoue, N. Ishii, H. Nemura, and K. Sasaki, “Are two nucleons bound in lattice QCD for heavy quark masses? Consistency check with Lüscher’s finite volume formula,” *Phys. Rev. D* **96** no. 3, (2017) 034521, [arXiv:1703.07210 \[hep-lat\]](#).
- [214] G. Rendon, L. Leskovec, S. Meinel, J. Negele, S. Paul, M. Petschlies, A. Pochinsky, G. Silvi, and S. Syritsyn, “ $I = 1/2$   $S$ -wave and  $P$ -wave  $K\pi$  scattering and the  $\kappa$  and  $K^*$  resonances from lattice QCD,” *Phys. Rev. D* **102** no. 11, (2020) 114520, [arXiv:2006.14035 \[hep-lat\]](#).
- [215] **Hadron Spectrum** Collaboration, J. J. Dudek, R. G. Edwards, and C. E. Thomas, “Energy dependence of the  $\rho$  resonance in  $\pi\pi$  elastic scattering from lattice QCD,” *Phys. Rev. D* **87** no. 3, (2013) 034505, [arXiv:1212.0830 \[hep-ph\]](#). [Erratum: *Phys.Rev.D* 90, 099902 (2014)].
- [216] C. Alexandrou, L. Leskovec, S. Meinel, J. Negele, S. Paul, M. Petschlies, A. Pochinsky, G. Rendon, and S. Syritsyn, “ $P$ -wave  $\pi\pi$  scattering and the  $\rho$  resonance from lattice QCD,” *Phys. Rev. D* **96** no. 3, (2017) 034525, [arXiv:1704.05439 \[hep-lat\]](#).
- [217] B. Silvestre-Brac and C. Semay, “Systematics of  $L = 0$   $q$ -2 anti- $q$ -2 systems,” *Z. Phys. C* **57** (1993) 273–282.
- [218] D. M. Brink and F. Stancu, “Tetraquarks with heavy flavors,” *Phys. Rev. D* **57** (1998) 6778–6787.
- [219] J. Vijande, F. Fernandez, A. Valcarce, and B. Silvestre-Brac, “Tetraquarks in a chiral constituent quark model,” *Eur. Phys. J. A* **19** (2004) 383, [arXiv:hep-ph/0310007](#).



- 
- [220] D. Janc and M. Rosina, “The  $T_{cc} = DD^*$  molecular state,” *Few Body Syst.* **35** (2004) 175–196, [arXiv:hep-ph/0405208](#).
- [221] J. Vijande, A. Valcarce, and K. Tsushima, “Dynamical study of  $QQ - \bar{u}\bar{d}$  mesons,” *Phys. Rev. D* **74** (2006) 054018, [arXiv:hep-ph/0608316](#).
- [222] F. S. Navarra, M. Nielsen, and S. H. Lee, “QCD sum rules study of  $QQ - \bar{u}\bar{d}$  mesons,” *Phys. Lett. B* **649** (2007) 166–172, [arXiv:hep-ph/0703071](#).
- [223] M. Zhang, H. X. Zhang, and Z. Y. Zhang, “ $QQ\bar{q}\bar{q}$  four-quark bound states in chiral SU(3) quark model,” *Commun. Theor. Phys.* **50** (2008) 437–440, [arXiv:0711.1029 \[nucl-th\]](#).
- [224] Z.-G. Wang, “Analysis of the axialvector doubly heavy tetraquark states with QCD sum rules,” *Acta Phys. Polon. B* **49** (2018) 1781, [arXiv:1708.04545 \[hep-ph\]](#).
- [225] B. Wang, Z.-W. Liu, and X. Liu, “ $\bar{B}^{(*)}\bar{B}^{(*)}$  interactions in chiral effective field theory,” *Phys. Rev. D* **99** no. 3, (2019) 036007, [arXiv:1812.04457 \[hep-ph\]](#).
- [226] M.-Z. Liu, T.-W. Wu, M. Pavon Valderrama, J.-J. Xie, and L.-S. Geng, “Heavy-quark spin and flavor symmetry partners of the X(3872) revisited: What can we learn from the one boson exchange model?,” *Phys. Rev. D* **99** no. 9, (2019) 094018, [arXiv:1902.03044 \[hep-ph\]](#).
- [227] Y. Kim, M. Oka, and K. Suzuki, “Doubly heavy tetraquarks in a chiral-diquark picture,” *Phys. Rev. D* **105** no. 7, (2022) 074021, [arXiv:2202.06520 \[hep-ph\]](#).
- [228] M. Praszalowicz, “Doubly heavy tetraquarks in the chiral quark soliton model,” *Phys. Rev. D* **106** no. 11, (2022) 114005, [arXiv:2208.08602 \[hep-ph\]](#).
- [229] T.-W. Wu and Y.-L. Ma, “Doubly heavy tetraquark multiplets as heavy antiquark-diquark symmetry partners of heavy baryons,” *Phys. Rev. D* **107** no. 7, (2023) L071501, [arXiv:2211.15094 \[hep-ph\]](#).
- [230] L. Maiani, A. Pilloni, A. D. Polosa, and V. Riquer, “Doubly heavy tetraquarks in the Born-Oppenheimer approximation,” *Phys. Lett. B* **836** (2023) 137624, [arXiv:2208.02730 \[hep-ph\]](#).
- [231] T. Iritani *et al.*, “Mirage in Temporal Correlation functions for Baryon-Baryon Interactions in Lattice QCD,” *JHEP* **10** (2016) 101, [arXiv:1607.06371 \[hep-lat\]](#).
- [232] R. N. Faustov, V. O. Galkin, and E. M. Savchenko, “Heavy tetraquarks in the relativistic quark model,” *Universe* **7** no. 4, (2021) 94, [arXiv:2103.01763 \[hep-ph\]](#).

- [233] L. R. Dai, E. Oset, A. Feijoo, R. Molina, L. Roca, A. M. Torres, and K. P. Khemchandani, “Masses and widths of the exotic molecular  $B_{(s)}^{(*)}B_{(s)}^{(*)}$  states,” *Phys. Rev. D* **105** no. 7, (2022) 074017, [arXiv:2201.04840 \[hep-ph\]](#).  
[Erratum: *Phys.Rev.D* 106, 099904 (2022)].
- [234] X. Chen, F.-L. Wang, Y. Tan, and Y. Yang, “Double-heavy tetraquarks with strangeness in the chiral quark model,” *Chin. Phys. C* **47** no. 2, (2023) 023102, [arXiv:2206.10917 \[hep-ph\]](#).
- [235] R. A. Briceño, M. T. Hansen, and S. R. Sharpe, “Relating the finite-volume spectrum and the two-and-three-particle  $S$  matrix for relativistic systems of identical scalar particles,” *Phys. Rev. D* **95** no. 7, (2017) 074510, [arXiv:1701.07465 \[hep-lat\]](#).
- [236] T. D. Blanton, F. Romero-López, and S. R. Sharpe, “Implementing the three-particle quantization condition for  $\pi^+\pi^+K^+$  and related systems,” *JHEP* **02** (2022) 098, [arXiv:2111.12734 \[hep-lat\]](#).
- [237] M. T. Hansen, F. Romero-López, and S. R. Sharpe, “Decay amplitudes to three hadrons from finite-volume matrix elements,” *JHEP* **04** (2021) 113, [arXiv:2101.10246 \[hep-lat\]](#).
- [238] **LHCb** Collaboration, “Future physics potential of LHCb,”
- [239] M. Wagner, *Gruppentheoretische Methoden in der Physik*. Cambridge University Press, 1985.
- [240] C. Alexandrou, S. Gusken, F. Jegerlehner, K. Schilling, and R. Sommer, “The Static approximation of heavy - light quark systems: A Systematic lattice study,” *Nucl. Phys. B* **414** (1994) 815–855, [arXiv:hep-lat/9211042](#).



---

# ACKNOWLEDGEMENTS

---

First of all, I thank Marc Wagner for his extraordinary support. He was not only my supervisor but also a mentor for many years who always provided useful advice. His inspirations and patience in our numerous discussions were an essential assistance behind my progress. I am very grateful for his trust and the opportunity to take on responsibility in teaching and research.

My thanks also go to Stefan Meinel for being my second supervisor and for our long-lasting and productive collaboration. I am very grateful to him for sharing his enormous experience with me and for his valuable suggestions during our frequent discussions. I learned a lot from him.

I also thank all other members of our collaboration, first of all Constantia Alexandrou, for many fruitful discussions and providing computing resources without which this work would not have been possible. Special thanks go to Jacob Finkenrath, who was always available whenever I was poking him with questions. His advice and knowledge of high-performance computing helped me a lot, and I really enjoyed our conversations. Moreover, I would like to thank Theodoros Leontiou, who verified parts of my results using a different evaluation scheme.

I acknowledge the support of Simone Bacchio for introducing me to the code framework PLEGMA. Furthermore, I would like to thank Luka Leskovec for useful discussions and helpful advice. I am also grateful to Dirk Rischke for our regular PhD Committee meetings in an enjoyable atmosphere. Further thanks go to our lattice group for a pleasant time and interesting discussions.

Finally, I thank my family and my girlfriend for their enduring support and patience. Their constant backing has been an incredible encouragement throughout the years.

I thank the Helmholtz Graduate School for Hadron and Ion Research “HGS-HIRE” for exciting courses and financial support via a GSI F&E scholarship. I acknowledge funding by the Deutsche Forschungsgemeinschaft (DFG, project number 457742095). I thank the MILC collaboration and the RBC and UKQCD collaborations for providing their gauge field ensembles. Parts of my computations were done at the Cyclone High Performance Computer at The Cyprus Institute. Results were also obtained from calculations on the GOETHE-HLR high-performance computers of the Frankfurt University, and I would like to thank HPC-Hessen, funded by the State Ministry of Higher Education. I also used resources of the National Energy Research Scientific Computing Center (NERSC), a U.S. Department of Energy Office of Science User Facility (Contract No. DE-AC02-05CH11231), and resources at the Texas Advanced Computing Center being part of the Extreme Science and Engineering Discovery Environment (XSEDE), supported by National Science Foundation grant number ACI-1548562.